

University of Alberta
Department of Civil &
Environmental Engineering



Structural Engineering Report No. 223

Strip Model For Capacity of Slab-Column Connections

by
Shahab Afhami
Scott D. B. Alexander
and
Sidney H. Simmonds

August 1998

Structural Engineering Report 223

Strip Model for Capacity of Slab-Column Connections

by

Shahab Afhami

Scott D.B. Alexander

Sidney H. Simmonds

Department of Civil and Environmental Engineering

University of Alberta

Edmonton, Alberta

August 1998

Acknowledgements

This report is a reprint of a thesis by the same name, written by the first author under the co-supervision of the remaining authors.

Financial support was provided by the Natural Sciences and Engineering Research Council of Canada (NSERC), through operating grant NSERC-A1691, and by the Ministry of Culture and Higher Education of Iran (MCHE), through its scholarship.

Abstract

This report presents the results of tests on a full-scale two-span flat plate supported by one interior and two edge columns with rotational restraint provided at the plate boundaries. The test was designed to examine how well the Bond Model, as proposed by Alexander and Simmonds, describes the mechanics of shear transfer in flat plates. It also examines the validity of North American Standards and the Bond Model in predicting the behavior of edge connections. Internal vertical shears were calculated from strain measurements on the flexural reinforcing bars.

The Bond Model describes a connection as radial strips attached to the column. The mechanism of shear transfer described by this model results in a lower bound solution for the capacity of a single radial strip, referred to as nominal capacity. The capacity of the connection is assumed equal to the sum of the capacity of its radial strips.

Test results strongly support the mechanics of shear transfer described by the Bond Model. However, at failure, not all radial strips were loaded to their nominal capacities. Such behavior in which some radial strips do not reach their nominal capacities is called non-proportional behavior. Non-proportional behavior is prevalent in edge connections and eccentrically loaded interior connections, and may occur in concentrically loaded interior connections as a result of, for example, column or panel rectangularity.

On the basis of these tests and the extensive test results available in the literature, a model, called Strip Model, is proposed to describe the behaviour of both interior and edge connections. The Strip Model addresses the non-proportional behavior and provides a reliable estimate of the ultimate capacity of flat plate-column connections.

Moment-shear interaction diagrams for the capacity of edge and eccentrically loaded interior connections are developed. The Strip Model and the North American Standards are compared to 40 tests on the edge connections and 43 tests on the eccentrically loaded interior connections reported in the literature. Both approaches provide a safe prediction of the ultimate capacity. However, the Strip Model is considerably more reliable. The behavior of the two tested edge connections was consistent with the Strip Model and not with the code prediction.

Table of Contents

1. Introduction	1
1.1 The Goal	1
1.2 Objectives and Scope	1
1.3 Outline	2
2. Background	4
2.1 Mechanics of Shear Transfer	4
2.1.1 Shear Transfer in One-way Flexural Systems	4
2.1.2 Shear Transfer in Flat Plates	4
2.2 Observed Behavior	5
2.2.1 Description of Punching Failure	5
2.2.2 Types of Failure	5
2.2.3 Effect of Reinforcement	6
2.3 Methods of Estimating Punching Capacities	6
2.4 The Bond Model	8
2.4.1 Description of the Model	8
2.4.2 Shear Capacity of Radial Strips	8
2.4.2.1 Equilibrium of a Radial Strip	8
2.4.2.2 Simplified Model	9
2.4.3 Comparison of A23.3 and ACI 318 Values of One-way Critical Shear	10
2.4.4 Bond Model and Building Code Procedures	10
2.5 Methods of Testing	11
2.6 Measuring the Distribution of Internal Shears	12
2.6.1 General	12
2.6.2 Comments	13
2.6.2.1 Validity of Assumptions in Equations 2.14 and 2.15	13
2.6.2.2 Alternative Solution for Equation 2.16	14
2.6.2.3 Alternative Approach for the Derivation of Equation 2.17	14
3. Prototype, Specimen, Apparatus, Fabrication Procedure, and Ancillary Tests	24
3.1 Objectives of Experimental Program	24
3.2 Design Considerations of Specimen	24
3.3 Test Specimen	25
3.3.1 Geometry of the Specimen	25
3.3.2 Design Load and Flexural Design of Specimen	25
3.3.2.1 Target Design Moments	25
3.3.2.2 Minimum Reinforcement and Integrity Steel	26
3.3.2.3 Position of Reinforcement in Cross-Section of the Plate	26
3.3.2.4 Service and Factored Loads	26
3.3.2.5 Area and Detailing of Reinforcement	27
3.3.3 Assessing the Specimen for Shear	28
3.3.3.1 Factored Shear at the Connections	28
3.3.3.2 Shear Calculation According to the Canadian Standard	28
3.3.3.3 Shear Capacity According to the Bond Model	29

3.3.4 Other Detailing	29
3.4 Test Apparatus	30
3.4.1 Supports	30
3.4.2 Edge Restraining System	30
3.4.2.1 Design Considerations	30
3.4.2.2 Extension Arms	30
3.4.2.3 Transverse Ties	31
3.4.3 Loading System	31
3.5 Instrumentation	31
3.5.1 Strain Measurements	31
3.5.2 Load Measurements	32
3.5.3 Deformation Measurements	32
3.5.4 Recording and Monitoring Data and Loads	32
3.6 Fabrication Procedure	32
3.7 Ancillary Tests	33
3.7.1 Reinforcement	33
3.7.2 Concrete	33
3.7.3 Tests on Reinforced Concrete	34
3.8 Predicted Capacity of the Specimen Based on the Tested Material Property	35
3.8.1 Predicted Shear Capacity of the Specimen Based on the Bond Model	35
3.8.2 Predicted Yield Line Capacity of the Specimen and Related Shear Forces	35
3.8.3 Predicted Shear Capacity by North American Standards	35
4. Observations and Test Results	64
4.1 Test Procedure	64
4.1.1 Self-weight and Super Imposed Loads	64
4.1.2 Preliminary Loading	64
4.1.3 Loading to Service Load	65
4.1.4 Loading to Failure of Interior Connection	65
4.1.5 Retest of the Edge Connections	65
4.2 Flexural Behavior	66
4.3 Stress Resultants and M-V Diagrams	67
4.3.1 External Measurement of Stress Resultants, and M-V Diagrams	67
4.3.2 Moment at Critical Sections Based on Strain Gauge Measurement	68
4.3.2.1 Negative Bending Moments at the South Connection	68
4.3.2.2 Negative Bending Moments at the North Connection	69
4.3.2.3 Bending Moments at the Interior Connection	69
4.3.2.4 Positive Moments in the x Direction	69
4.3.3 Validity of Gauge Readings	69
4.4 Deformation along Continuous Edges	70
4.5 Yielding of Steel Perpendicular to the Free Edges	71
4.6 Serviceability Considerations	71
4.6.1 Deflections	71
4.6.2 Crack Widths	72
4.7 Disposal of the Specimen	72

5. Internal Shear Forces and Torsional Moments Measured by Strain Gauges	105
5.1 Test Results	105
5.1.1 Force Gradient in Reinforcement	105
5.1.2 Internal Shear Forces, and Torsional Moments - General	105
5.1.2.1 Equations to Calculate Internal Shears	105
5.1.2.2 Equations for Internal Shears and Torsions	106
5.1.3 Internal Shear Forces, and Torsional Moments - Interior Connection	107
5.1.4 Internal Shear Forces, and Torsional Moments - South Edge Connection	108
5.2 Discussion	109
5.2.1 General	109
5.2.1.1 Comparison of Different Test Methods	109
5.2.1.2 Shear Transfer in Plates with Different Stiffness in Two Directions	109
5.2.2 Interior Connection	110
5.2.2.1 Different Behavior of the Radial Strips	110
5.2.2.2 Interaction of a Radial Strip and its Adjacent Quadrant	111
5.2.2.3 Ductility of the Interior Connection	111
5.2.3 Edge Connection	111
6. Behavior of Radial Strips in Flat Plate Structures	122
6.1 Finite Elements, Background	122
6.1.1 General	122
6.1.2 Finite Element Program NISA 90	123
6.2 Finite Element Study	123
6.2.1 Scope	123
6.2.2 Plates under Study, General	124
6.2.3 Interior Connections	125
6.2.3.1 Interior Connection INT01	125
6.2.3.2 Interior Connection INT02	125
6.2.3.3 Interior Connection INT03	126
6.2.4 Exterior Connections	126
6.2.4.1 Edge Connection EXT01	126
6.2.4.2 Edge Connection EXT02	127
6.2.5 Discussion	127
6.3 Distribution of Shear and Torsion along Side Faces of Radial Strips	128
6.3.1 General	129
6.3.1.1 Shear Intensity	129
6.3.1.2 Torsional Moments	129
6.3.1.3 Torsional Shear	129
6.3.1.4 Torsional Moment at the Corner of the Column	130
6.3.2 Interior Radial Strips Reaching or Exceeding Their Nominal Capacities	130
6.3.3 Radial Strips Not Reaching Their Nominal Capacities	131
6.3.4 Interior Radial Strips in an Edge Connection	131

7. Strip Model for the Capacity of Interior and Edge Connections	156
7.1 Shear Capacity of Concentrically Loaded Interior Connections	156
7.1.1 General	156
7.1.2 Derivation of a Lower Bound Estimate for the Shear Capacity of a Concentrically Loaded Interior Connection	157
7.1.3 Comparison of P_{bond} , P_{max} , and P_{min}	159
7.2 Moment - Shear Interaction for the Capacity of the Edge Connections	160
7.2.1 General	160
7.2.2 Point 4 on the Interaction Diagram	160
7.2.3 Points 3a and 3b on the Interaction Diagram	161
7.2.4 Point 2 on the Interaction Diagram	162
7.2.5 Point 1 on the Interaction Diagram	162
7.3 Moment-Shear Interaction Diagram for the Capacity of the Eccentrically Loaded Interior Connections	162
7.4 Non-Proportional Behavior in the Presence of Unbalanced Moments	164
7.4.1 Edge Connections	164
7.4.2 Interior Connections	164
7.5 Other Considerations Regarding Capacity of Plate-Column Connections	164
7.5.1 Non-uniform Distribution of Reinforcement	164
7.5.2 Considerations Regarding M_s^+	165
7.5.3 Cases Where Shear Capacity of the Connection is Smaller than the Yield Line Mechanism Load	165
8. Strip Model, North American Standards, and Tests in Literature	174
8.1 General	174
8.2 Applying the Strip Model to Tests in the Literature	174
8.2.1 Strip Model and Tests on Edge Connections	174
8.2.2 Strip Model and Eccentrically Loaded Interior Connections	175
8.3 North American Standards in the Presence of the Unbalanced Moments	175
8.3.1 Strength of the Connection	175
8.3.2 Moment-Shear Interaction Diagrams	176
8.3.3 Comparison with the Tests in the Literature	177
8.4 Comparison of Strip Model, North American Standards, and Test Results	177
9. Summary and Conclusions	191
9.1 Summary	191
9.2 Conclusion	193
References	194
Appendix A Pictures of the Test Specimen	197
Appendix B Force gradient in bars	200

Appendix C Tests in Literature-Edge Connections	204
C1 Stamenkovic and Chapman	204
C2 Zaghlool	205
C3 Kane, Hanson and Hanson	205
C4 Current Study	205
C5 Scavuzzo / Gosselin / Lamb	206
C6 Regan, Walker, and Zakaria	207
Appendix D Tests in Literature-Eccentrically Loaded Interior Connections	220
D1 Regan, Walker, and Zakaria	220
D2 Stamenkovic and Chapman	220
D3 Hanson and Hanson	221
D4 Moe	221

List of Tables

Table 3.1	Shear Calculations According to the Bond Model; $\phi_c = 0.6$, $\phi_s = 0.85$, $f'_c = 30$ MPa, and $f_y = 400$ MPa	36
Table 3.2	Properties of Reinforcing Bars	37
Table 3.3	Concrete Properties	37
Table 3.4	Shear Calculation According to the Bond Model; $f'_c = 34.8$ MPa, and $f_y = 420$ MPa	38
Table 3.5	Yield Line Capacities of the Specimen; $f'_c = 34.8$ MPa, and $f_y = 420$ MPa	39
Table 3.6	Shear Capacity of the Specimen; $f'_c = 34.8$ MPa, and $f_y = 420$ MPa	39
Table 4.1	Selected Data-Description of Load Cases, and Deformation of the Plate	73
Table 4.2	Selected Data - Shear, Negative Moments at Column Center, and Positive Moments (based on load cells)	74
Table 4.3	Selected Data - Negative Moments at the Face of Columns	75
Table 4.4	Moment-Strain Relationships used at Different Locations of the Specimen	76
Table 6.1	Reinforcement of Simulation INT01	133
Table 6.2	Reinforcement of Simulations INT02 and INT03	133
Table 6.3	Reinforcement of Simulation EXT01	134
Table 6.4	Reinforcement of Simulation EXT02	134
Table 6.5	Average out of Plane Shear Intensity, INT01 at 15 kPa	135
Table 6.6	Average out of Plane Shear Intensity, INT02 at 14 kPa	135
Table 6.7	Average out of Plane Shear Intensity, INT03 at 13 kPa	135
Table 6.8	Average out of Plane Shear Intensity, INT03 at 9 kPa	136
Table 6.9	Average out of Plane Shear Intensity, EXT01 at 10 kPa	136
Table 6.10	Average out of Plane Shear Intensity, EXT02 at 9 kPa	136
Table 7.1	Comparison of P_{Bond} , P_{max} , and P_{min} (Equations 7.13, 7.14, and 7.16)	166
Table 8.1	Comparison of Strip Model, North American Standards, and test results	178

Table C1	Summary of Test Results, Geometry, and Material Properties of Edge Connections Reported in the Literature	208
Table C2	Information Regarding Reinforcement of Tests on the Edge Connection	210
Table C3	Parameters Required for Constructing Interaction Diagram of the Edge Connections Reported in the Literature	212
Table C4	Analytical Results (Points on Interaction Diagram, Failure Load, and Test to Calculated Ratio) for Edge Connection Tests - Strip Model	214
Table C5	Analytical Results (Points on Interaction Diagram, Failure Load, and Test to Calculated Ratio) for Edge Connection Tests - North American Standards	217
Table D1	Summary of Test Results, Geometry, and Material Properties of the Interior Connections Reported in the Literature	222
Table D2	Information Regarding Reinforcement of Tests on the Interior Connections	224
Table D3	Parameters Required for Constructing Interaction Diagram of the Interior Connections Reported in Literature	226
Table D4	Analytical Results (Points on Interaction Diagram, Failure Load, and Test to Calculated Ratio) for Interior Connection Tests - Strip Model	228
Table D5	Analytical Results (Points on Interaction Diagram, Failure Load, and Test to Calculated Ratio) for Interior Connection Tests - North American Standards	230

List of Figures

Figure 2.1	Typical Punching Failure of an Interior Connection	16
Figure 2.2	Typical Punching Failure of an Edge Connection	16
Figure 2.3	Typical Punching Failure of Plate-Column Connections with Unbalanced Moments	17
Figure 2.4	Brittle and Ductile Punching Failures	17
Figure 2.5	Layout of Radial Strips	18
Figure 2.6	Shear Transfer in Flat Plate-Column Connections	19
Figure 2.7	Actual Loading on Radial Strips	19
Figure 2.8	Free Body Diagram of Radial Strips in a Simplified Model	20
Figure 2.9	Code-Defined Critical Sections	21
Figure 2.10	Bond Model Critical Section	21
Figure 2.11	Bond Model Results Using ACI 318 One-way Shear	22
Figure 2.12	ACI 318 Building Code Predictions	22
Figure 2.13	BS8110 Building Code Predictions	22
Figure 2.14	Definition and Free Body Diagram of Bar Strips	23
Figure 3.1	Prototype	40
Figure 3.2	Specimen	41
Figure 3.3	Target Design Moments	42
Figure 3.4	Reinforcement Area and Related Moment	43
Figure 3.5	Cross Section of Slab	44
Figure 3.6	Top Reinforcement Around Interior Column	44
Figure 3.7	Top Reinforcement Around Exterior Columns	45
Figure 3.8	Bottom Reinforcement Around Interior Column	46
Figure 3.9	Bottom Bars Around North Edge Column	47

Figure 3.10	Bottom Bars Around South Edge Column	48
Figure 3.11	Dimensions and Reinforcement of Columns	49
Figure 3.12	Supports and Overall Stability of the Specimen	50
Figure 3.13	Schematic Plan of Transverse Ties	51
Figure 3.14	Restraint Details for Continuous Edge	52
Figure 3.15	Connections of Load Distributing Beams	52
Figure 3.16	Loading System	53
Figure 3.17	Load Application System	54
Figure 3.18	Strain Gauges on Top Mat Around Center Column	55
Figure 3.19	Strain Gauges on Top Reinforcement Around Exterior Columns	56
Figure 3.20	Strain Gauges on Bottom Bars in North Panel	57
Figure 3.21	Strain Gauges on Bottom Bars in South Panel	58
Figure 3.22	Position of Linear Variable-Differential Transformers (LVDTs)	59
Figure 3.23	Typical Load-Strain Plot for Reinforcement	60
Figure 3.24	Tests on Reinforced Concrete Beams	61
Figure 3.25	Moment-Strain Relationship for Beam 1	62
Figure 3.26	Moment-Strain Relationship for Beam 2	62
Figure 3.27	Moment-Strain Relationship for Beam 3	63
Figure 3.28	Moment-Strain Relationship for Beam 4	63
Figure 4.1a	Load-Deflection Diagram - Full Loading History	77
Figure 4.1b	Load-Deflection Diagram - Enlarged Portion	78
Figure 4.2	Load in Jack # 1 Versus Deflection of the Specimen	79
Figure 4.3	Load in Jack # 4 Versus Deflection of the Specimen	79
Figure 4.4	Load-Deflection Diagram - Ideal Edge Restraint	80
Figure 4.5	Load in Jacks Versus Deflection of the Specimen	80

Figure 4.6	Definition and Position of Loads and Moments	81
Figure 4.7	Free Body Diagrams	82
Figure 4.8	Moment-Shear Diagrams of the North Connection	83
Figure 4.9	Moment-Shear Diagrams of the South Connection	83
Figure 4.10	Moment-Shear Diagrams of the Interior Connection	84
Figure 4.11	Negative Moment in the x Direction at the Face of the Interior Column Versus the Deflection of the Specimen	84
Figure 4.12	Negative Moment in the x Direction at the Face of the North Column Versus the Deflection of the Specimen	85
Figure 4.13	Negative Moment in the x Direction at the Face of the South Column Versus the Deflection of the Specimen	85
Figure 4.14	Positive Moment in the x Direction - North Panel	86
Figure 4.15	Positive Moment in the x Direction - South Panel	86
Figure 4.16	Negative Moment in the y Direction at the Face of the North Column Versus the Deflection of the Specimen	87
Figure 4.17	Negative Moment in the y Direction at the Face of the South Column Versus the Deflection of the Specimen	87
Figure 4.18	Negative Moment in the y Direction at the face of the Interior Column Versus the Deflection of the Specimen	88
Figure 4.19	Positive Moment in the y Direction at the Continuous Edge Versus the Deflection of the Specimen	88
Figure 4.20	Comparison of the External Measurements with the Internal Measurements in the North Connection	89
Figure 4.21	Comparison of the External Measurements with the Internal Measurements in the South Connection	89
Figure 4.22	Comparison of the External Measurements with the Internal Measurements in the Interior Connection	90
Figure 4.23	Overall Expansion at Mid-Height of the Continuous Edge	90
Figure 4.24	Sum of Rotation of the Corresponding Continuous Edges	91
Figure 4.25	Average Load in Jacks Versus the Rotation of the Continuous Edge	91

Figure 4.26	Stress and Strain Distribution for Bars Normal to the Free Edge-South Connection	92
Figure 4.27	Stress and Strain Distribution for Bars Normal to the Free Edge-North Connection	93
Figure 4.28	Crack Widths in mm at Service Load, $q = 10.1$ kPa, Top Surface	94
Figure 4.29	Crack Widths in mm at the Load of 13.06 kPa, Top Surface	95
Figure 4.30	Crack Pattern on Bottom Surface of the Slab at Service Load, $q = 10.1$ kPa	96
Figure 4.31	Crack Pattern on Bottom Surface of the Slab at the Load of 13.06 kPa	97
Figure 4.32	Deflection of the Specimen Prior to Punching of the Interior Connection	98
Figure 4.33	Deflection of the Specimen	99
Figure 4.34	Cutting Specimen into Pieces	100
Figure 4.35	Crack Pattern Around Interior Column, Load Stage 2	101
Figure 4.36	Punching of the Interior Connection	101
Figure 4.37	Crack Pattern Around the North Column, Load Stage 2	102
Figure 4.38	Punching of the North Connection	102
Figure 4.39	Crack Pattern Around the South Column, Load Stage 2	103
Figure 4.40	Punching of the South Connection	103
Figure 4.41	Side View of the Punching of the North Connection	104
Figure 4.42	Side View of the Punching of the South Connection	104
Figure 5.1	Force Gradient in Bars Running N-S, Interior Connection, $(T1-T3)/2s$	113
Figure 5.2	Force Gradient in Bars Running E-W, Interior Connection, $(T1-T3)/2s$	113
Figure 5.3	Force Gradient in Bars Running N-S, South Connection, $(T1-T3)/2s$	114
Figure 5.4	Force Gradient in Bars Running E-W, South Connection, $(T1-T3)/2s$	114
Figure 5.5	Mathematical Comparison of Equations 5.1, 5.2, and 5.3	115
Figure 5.6	Suggested Equations (5.4 and 5.5) for V_{bar}	115
Figure 5.7	Shear Attributed to Individual Bars Running N-S, Interior Connection	116

Figure 5.8	Shear Attributed to Individual Bars Running E-W, Interior Connection	116
Figure 5.9	Measured Shear at the Interior Connection Based on the Load Cells and Strain Gauges	117
Figure 5.10	Torsion Along Each Side Face of Radial Strips of the Interior Connection	117
Figure 5.11	Shear Attributed to Individual Bars Running N-S, South Connection	118
Figure 5.12	Shear Attributed to Individual Bars Running E-W, South Connection	118
Figure 5.13	Measured Shear at the South Connection by Load Cells and Strain Gauges	119
Figure 5.14	Torsion Along Each Side Face of the Radial Strips of the South Connection	119
Figure 5.15	Ratio of Measured Shear by Strain Gauges to Measured Shear by Load Cell in the Interior Connection	120
Figure 5.16	Ratio of Measured Shear by Strain Gauges to Measured Shear by Load Cell in the South Connection	120
Figure 5.17	An Example of Possible Mechanisms of Failure	121
Figure 5.18	Description of the Third Mechanism	121
Figure 6.1	Geometry of Slab INT01	137
Figure 6.2	Geometry of Slab INT02	138
Figure 6.3	Geometry of Slab INT03	139
Figure 6.4	Geometry of Slabs EXT01 and EXT02	140
Figure 6.5	Shear Intensity at a Load of 15 kPa, Slab INT01	141
Figure 6.6	Torsional Moment Intensity at a Load of 15 kPa, Slab INT01	141
Figure 6.7	Torsional Moment Along Each Side Face of Radial Strips, Slab INT01	141
Figure 6.8	Shear Intensity at a Load of 14 kPa, Slab INT02	142
Figure 6.9	Torsional Moment Intensity at a Load of 14 kPa, Slab INT02	142
Figure 6.10	Torsional Moment Along Each Side Face of Radial Strips, Slab INT02	142
Figure 6.11	Shear Intensity at a Load of 13 kPa, Slab INT03	143
Figure 6.12	Torsional Moment Intensity at a Load of 13 kPa, Slab INT03	143

Figure 6.13	Torsional Moment Along Each Side Face of Radial Strips, Slab INT03	143
Figure 6.14	Shear Intensity at a Load of 10 kPa, Slab EXT01	144
Figure 6.15	Torsional Moment Intensity at a Load of 10 kPa, Slab EXT01	144
Figure 6.16	Torsional Moment Along Each Side Face of Radial Strip, Slab EXT01	144
Figure 6.17	Shear Intensity at a Load of 9 kPa, Slab EXT02	145
Figure 6.18	Torsional Moment Intensity at a Load of 9 kPa, Slab EXT02	145
Figure 6.19	Torsional Moment Along Each Side Face of Radial Strips, Slab EXT02	145
Figure 6.20	Load Transferred Through Each Radial Strip, Interior Connections	146
Figure 6.21	Load Transferred Through Each Radial Strip, Exterior Connections	146
Figure 6.22	Key Plan for Figures 6.21 through 6.35	147
Figure 6.23	Typical Shear Intensity Diagram Along Section ABF	147
Figure 6.24	Typical Torsional Moment Intensity Along Side Faces of Strip 1	148
Figure 6.25	Typical Torsional Shear Intensity Diagram Along Side Faces of Strip 1	148
Figure 6.26	Torsional Moments at the Corner of the Column	149
Figure 6.27	Typical Shear Intensity Diagram Along Side Faces of Interior Radial Strips, Case a	150
Figure 6.28	Idealized Torsional Moment Intensity Diagram Along Side Faces of Interior Radial Strips, Case a	151
Figure 6.29	Idealized Torsional Shear Intensity Diagram Along Side Faces of Interior Radial Strips, Case a	151
Figure 6.30	Typical Shear Intensity Diagram Along Side Faces of Interior Radial Strips not Loaded in Proportion to Their Capacity, Case b	152
Figure 6.31	Idealized Torsional Moment Intensity Diagram Along Side Faces of Interior Radial Strips, Case b	153
Figure 6.32	Idealized Torsional Shear Intensity Diagram Along Side Faces of Interior Radial Strips, Case b	153
Figure 6.33	Typical Shear Intensity Diagram Along Side Face of a Spandrel Strip	154

Figure 6.34	Typical Shear Intensity Diagram Along Side Faces of an Interior Radial Strip of an Edge Connection	154
Figure 6.35	Idealized Torsional Moment Intensity Diagram Along Side Faces of Spandrel Strips	155
Figure 6.36	Idealized Torsional Shear Intensity Diagram Along Side Faces of Spandrel Strips	155
Figure 7.1	Distribution of Shear in Simplified Models	167
Figure 7.2	Free Body Diagram of a Concentrically Loaded Interior Connection	168
Figure 7.3	Relation Between Loads Transferred Through Each Half Radial Strip	169
Figure 7.4	Free Body Diagram of an Edge Connection	170
Figure 7.5	Moment-Shear Diagram for the Capacity of Edge Connections	171
Figure 7.6	Moment-Shear Diagram for the Capacity of Interior Connections	172
Figure 7.7	Shear Transfer in Edge Connections	173
Figure 7.8	Moment-Shear Diagram for the Capacity of Interior Connections - Non-Proportional Behavior	173
Figure 8.1	Test to Calculated Ratio for the Edge Connections Reported in the Literature	179
Figure 8.2	Test to Calculated Ratios of Edge Connections Reported in the Literature Versus the Reinforcement Ratio of the Top Bars in the Interior Radial Strip	180
Figure 8.3	Test to Calculated Ratios of Edge Connections Reported in the Literature Versus the Compressive Strength of the Concrete, f'_c	180
Figure 8.4	Test to Calculated Ratio of the Interior Connections Reported in Literature	181
Figure 8.5	Test to Calculated Ratios of Eccentrically Loaded Interior Connections Reported in the Literature Versus the Reinforcement Ratio	182
Figure 8.6	Test to Calculated Ratios of Eccentrically Loaded Interior Connections Reported in the Literature Versus the Compressive Strength of the Concrete	182
Figure 8.7	Moment-Shear Interaction Diagrams for the Interior Connections - North American Building Codes	183
Figure 8.8	Moment-Shear Interaction Diagrams for the Edge Connections - North American Building Codes	183

Figure 8.9	Shear Distribution Along the Critical Section of an Edge Connection Based on the North American Standards	184
Figure 8.10	Test to Calculated Ratio for the Edge Connections Reported in the Literature - North American Standards	185
Figure 8.11	Test to Calculated Ratios of the Edge Connections Reported in the Literature Versus the Reinforcement Ratio of the Top Bars in the Interior Radial Strip	186
Figure 8.12	Test to Calculated Ratios of the Edge Connections Reported in the Literature Versus the Compressive Strength of the Concrete, f'_c	186
Figure 8.13	Test to Calculated Ratio for the Interior Connections Reported in the Literature- North American Standards	187
Figure 8.14	Test to Calculated Ratios of Eccentrically Loaded Interior Connections Reported in the Literature Versus the Reinforcement Ratio	188
Figure 8.15	Test to Calculated Ratios of Eccentrically Loaded Interior Connections Reported in the Literature Versus the Compressive Strength of the Concrete	188
Figure 8.16	Comparison of North American Standards, Bond Model, and the Test Results of the North Edge Connection in the Current Study	189
Figure 8.17	Comparison of North American Standards, Bond Model, and the Test Results of the South Edge Connection in the Current Study	190
Figure A1	Scaffolding and Formwork	197
Figure A2	Casting	197
Figure A3	Finishing the Surface	198
Figure A4	Loading System	198
Figure A5	Overall View	199
Figure A6	Overall View	199
Figure B1	Force Gradient in Bars Running N-S, Interior connection, 1st interval	200
Figure B2	Force Gradient in Bars Running N-S, Interior Connection, 2nd Interval	200
Figure B3	Force Gradient in Bars Running E-W, Interior Connection, 1st Interval	201
Figure B4	Force Gradient in Bars Running E-W, Interior Connection, 2nd Interval	201
Figure B5	Force Gradient in Bars Running N-S, South Edge Connection, 1st Interval	202
Figure B6	Force Gradient In Bars Running N-S, South Edge Connection, 2nd Interval	202
Figure B7	Force Gradient in Bars Running E-W, South Edge Connection, 1st Interval	203
Figure B8	Force Gradient in Bars Running E-W, South Edge Connection, 2nd Interval	203

List of Symbols

A_1, A_2	Side faces of a radial strip
A_b	Area of single reinforcing bar
A_g	Gross area of concrete
A_s	Area of flexural reinforcement
A_v	Area of contributing concrete
b	Width of plate strip
c	Distance from centroid of the critical section for shear to extreme points on the critical section
$c_1, c_2;$ c_x, c_y	Width of radial strips
C	Force at compression block
d	Flexural depth of reinforcement
d_{avg}	Average effective depth of reinforcement
d'	Clear cover of reinforcement
D	Force equal to $\sqrt{P_1^2 + P_2^2}$
e	Eccentricity of the load M/V
E	Modulus of elasticity of steel
E_c	Modulus of elasticity of concrete
E_s	Slope of strain hardening of steel
f_{cu}	Cube strength of concrete
f_y	Yield stress of steel
f'_c	Cylinder strength of concrete
f'_t	Concrete tensile strength from split cylinder test

F	Force measured by horizontal load cells
G_{\max}	Maximum strain for reinforcement
h	Thickness of the plate
j	Ratio of internal flexural moment arm to d
J	Polar moment of inertia of the critical section in shear
J_i	Load in Jack # i
$l; l_1; l_2;$ $l_x; l_y$	Loaded length of radial strip
$l_n; l_{nx}; l_{ny}$	Clear span length
m_b	Bending moment intensity
m_t	Torsional moment intensity
M	Unbalanced moment at the center line of the columns
$M_1; M_2;$ $M_3; M_4$	M corresponding to points on M-V interaction diagram according to the Strip Model
$M_1; M_2;$ M_3	Moment in bar strip at gauge rows 1, 2, and 3
$M_a; M_b;$ $M_c; M_d$	M corresponding to points on M-V interaction diagram according to the North American Standard
M_f	Factored moment
M_{face}	Moment at the column face
$M_o; M_{ox};$ M_{oy}	Total static moment
$M_r; M_r^+;$ M_r^-	Flexural resistances

M_s	Flexural capacity of radial strips equal to $M_s^+ + M_s^-$
M_s^+	Positive moment in radial strips at failure
M_s^-	Negative flexural capacity of radial strips
$M_{tx}; M_{ty}; M_{tz};$ $M_{tx}; M_{ty}$	Torsion along each side face of radial strips
M_{tc}	Torsion along side face of the column
M_{tr}	Torsional resistance
M_u	Unbalanced moment at the centroid of the critical section
p	Perimeter of the critical section
P	Column reaction
P_f	Shear capacity corresponding to the flexural limitation of codes
$P_{s1}; P_{s2}; P_{s3};$ $P_{sx}; P_{sy}$	Shear capacity of radial strips
$P_1; P_2;$ $P_x; P_y$	Load transferred through radial strips 1, 2, x, and y
$P_1; P_2;$ $P_3; P_4$	Load corresponding to points on M-V interaction diagram according to the Strip Model
$P_{min}; P_{max}$	Minimum and maximum capacity of an interior connection
P_{bond}	Capacity of an interior connection in proportional behavior
P_v	Shear capacity of the connection according to the Bond Model or Strip Model
P_y	Shear associated with the yield line mechanism load
$q; q_f$	Uniformly distributed load; factored distributed load
s	Spacing of the reinforcement
s_{avg}	Average spacing of reinforcement
T_i	Tensile force of reinforcement at row i of gauges

v_b	Bending shear intensity
v_c	Factored distributed shear resistance
v_i	Distributed shear at connection i
v_t	Torsional shear intensity
V	Shear force
V_i	Shear at connection i, also shear corresponding to M-V interaction diagrams according to the bond model
$V_a; V_b;$ $V_c; V_j$	Shear corresponding to M-V interaction diagrams according to the codes
V_j	Factored shear
V_u	Shear at the centroid of the critical section
$w; w_1; w_2;$ $w_x; w_y$	Bond model loading term from one adjacent quadrant of plate
W	Total load
ϕ	Shear resistance factor (ACI)
ϕ_c	Resistance factor for concrete (A23.3)
ϕ_s	Resistance factor for reinforcing bars (A23.3)
ρ	Flexural reinforcement ratio (A_s/bd)
γ_v	Fraction of unbalanced moment transferred by Eccentricity of shear
Δs	Dimension of a small segment

1. Introduction

1.1 The Goal

Reinforced concrete flat plate slabs are a common economical form of high rise construction. The absence of capitals, drop panels, or projecting beams simplifies formwork, and allows the application of interior finishes directly to the soffit of the slab. The ultimate strength of such structures is governed by the ultimate capacity of their connections. Failure of the column-plate connection is called punching failure.

The goal of the study is to develop a general mechanical model capable of explaining the ultimate behavior of slab-column connections over a wide range of relevant parameters such as geometry (including plate perforations), flexural reinforcement, concrete properties, and load combinations. Such model should lead to a simple design procedure without significant loss of accuracy in its ability to predict the ultimate load. The assessment of existing structures requires an accurate model as the decision to strengthen or not carries a significant cost.

Building code procedures for evaluating the punching capacity of plate-column connections are empirically based. Defined critical sections, allowable shear stresses, and the effect of reinforcement differ from one standard to another. Although these procedures lead to safe designs, they do not predict failure loads, especially for cases with unbalanced moments, with any consistency.

The Bond Model, as proposed by Alexander and Simmonds (1991) is an attempt to develop such a model. It describes the transfer of shear between the plate and the column in terms of the available mechanisms of moment gradient. The model combines strut and tie behavior with the concept of a limiting one way shear stress, and provides a reliable lower bound prediction of the ultimate capacity of a single radial strip (a strip of the plate attached to the column). In the Bond Model, the shear capacity of a plate-column connection is assumed to be equal to the sum of the capacities of all of its radial strips.

The Bond Model, originally developed for the interior column-plate connections, has the potential of providing a general solution to the problem of estimating the strength of any type of flat plate-column connections under any combination of loads. However, it has been compared only to tests on the concentrically loaded interior column-plate connections reported in the literature (Alexander, 1996).

The combination of shear and unbalanced moment is inevitable at edge column-plate connections, and may occur at interior column-plate connections as the result of unequal spans, unequal loads on adjacent panels, or as a result of lateral loads. Extending the Bond Model to these issues is the problem addressed in this study.

1.2 Objectives and Scope

The primary objective of this study is to examine how well the Bond Model explains the behavior of the flat plates, especially in cases with unbalanced moment, and to make modifications to the model, where necessary. Of particular interest is to see whether at failure all radial strips can be loaded to their shear capacity. Secondary objective is the comparison of failure loads predicted by the modified bond model (called Strip Model), and ACI 318 and A23.3 (referred to as North American Standards) with the test results on

both the edge column-plate connections and the eccentrically loaded interior column-plate connections reported in the literature.

Certain column-plate connections that would be deemed unsatisfactory to resist a given shear-moment loading using North American Standards may be deemed satisfactory using the Bond Model. Not surprisingly, no tests could be found in literature that were designed specifically to examine this contradiction. To provide such data, a test on one full-scale two span specimen consisting of two edge column-plate connections and one interior column-plate connection was undertaken. Slab continuity was modeled with rotational restraints on the boundary of the test specimen. The specimen was loaded monotonically to failure with 32 point loads stimulating uniform load on the slab. The flexural reinforcement of the plate was designed and detailed in compliance with A23.3-M84. A total of 116 strain gauges were installed on the flexural reinforcement to provide data to verify the Bond Model.

The gross geometry and the effective depth of the two edge connections were the same. However, the design moments and hence the reinforcement ratios were different. This results in a contradiction between the Bond Model and the North American Standards, and permits the study of the effect of the reinforcement on the punching capacity of the edge connections. Among other objectives of the experimental work were the study of the performance at the service load, and also yielding of bars perpendicular to the free edge.

This study is limited to interior and edge column-plate connections and does not include corner column-plate connections. Only plates orthogonally reinforced for flexure are considered. The behavior of the plates with shear reinforcement is also outside the scope of this study.

1.3 Outline

Mechanics of shear transfer in flat plates as described by the Bond Model, and how to determine the internal vertical shears based on the strain measurements of the flexural reinforcement are presented in chapter two.

In chapter three, the experimental program is described. Details of the specimen, the apparatus, and the ancillary tests are explained. Finally, predictions of the ultimate capacity of the specimen by the Bond Model and by the North American Standards are determined.

Test results and observed behavior are presented in two chapters. Test procedure, flexural results, yielding of steel perpendicular to the free edges, and serviceability considerations are explained in chapter four. Internal shears and torsional moments are determined in chapter five.

Measurement of internal shear shows that even for the interior connection, not all of the radial strips were loaded to their maximum capacity. Test results also revealed new facts about the distribution of the torsional moments in flat plates. These observations resulted in the discovery of a substantial difference between the tests in which loads are applied through a load distributing system and tests with enforced deformation.

In chapter six, a non-linear finite element analysis is used to verify some of the test outcomes based on the strain measurements. On the basis of the test results and the finite

element analysis, behavior of the radial strips and the distribution of shear and torsional moments along their side faces are discussed in detail.

In chapter seven, a modification of the Bond Model, called Strip Model, is proposed. First, a general lower bound solution for the capacity of the concentrically loaded interior connections is derived. Then, moment-shear interaction diagram for the capacity of both the edge and the interior column-plate connections are derived. Also, other considerations regarding the evaluation of the flexural capacity of the radial strips are presented.

Finally, in chapter eight, predictions based on the Strip Model and the North American Standards are compared to the tests on the edge and interior connections reported in the literature.

2. Background

2.1 Mechanics of Shear Transfer

2.1.1 Shear Transfer in One-way Flexural Systems

In a reinforced concrete flexural member, neglecting the tensile force of the concrete, bending moment is expressed as the product of the steel force, T , and an effective moment arm, jd . One-way shear is the gradient of bending moment along the length of the member, and consists of two components (Equation 2.1).

$$V = \frac{dM}{dx} = \frac{d(T \times jd)}{dx} = jd \times \frac{dT}{dx} + T \times \frac{d(jd)}{dx} \quad [2.1]$$

Shear resulting from a gradient in tensile force acting on a constant moment arm is referred to as beam action. It requires bond force between steel and concrete, and is reasonably modeled by a critical nominal shear stress. Beam action is characteristic of slender flexural members (B-regions).

Shear resulting from a constant tensile force acting on a varying moment arm is called arching action. It requires only remote anchorage of the reinforcement and, unlike beam action, the transfer of shear flow will not be prevented by the inclined cracks. Shear transfer by means of arching action is usually associated with deep beams and regions adjacent to discontinuities or disturbances in either the loading or the geometry of the member (D-regions).

2.1.2 Shear Transfer in Flat Plates

In a two-way flexural system, shear is transferred by two mechanisms, namely bending shear and torsional shear. Bending shear, produced by gradient in the bending moment, is directly analogous to shear in a one-way flexural member, and plate-column connections have the characteristics of both D and B regions. Torsional shear, produced by gradient in the torsional moment, is unique to two-way flexural systems. Alexander et. al. (1995), studying the behavior of flat plate-column connections, emphasize the importance of the torsional moments on the redistribution of shear in the vicinity of a plate-column connection.

It is generally agreed that arching is the dominant mechanism of shear transfer in the radial direction. At the column face, a D-region, the nominal shear intensity by far exceeds the critical stress that would be consistent with slender behavior. Measuring compressive strains of concrete, Kinnunen and Nylander (1960) conclude that any model of a slab column connection must have an equivalent of arching action in the radial direction in order to be consistent with concrete strain measurements. Strain measurements by Shehata, reported by Regan and Braestrup (1985), also suggest arching action in the radial direction. In tests conducted at the University of Alberta, strain measurements of reinforcement passing through the column are consistent with a curved compression strut rather than a straight line (Alexander and Simmonds, 1992).

In the circumferential direction, the distribution of strain measured by Shehata was linear, and consistent with the strains in a slender beam, B-region. It is believed that shearing forces are transferred mostly by beam action in the circumferential direction.

2.2 Observed Behavior

Based on the observations of the other investigators (Masterson and Long (1974), Regan (1984), and Broms (1990)), the following stages in the punching failure of a plate-column connection are identified:

- (1) Vertical flexural cracks open at the face of the column in the early stages of loading.
- (2) Tension reinforcement close to the column yields.
- (3) The vertical flexural cracks spread out to a relatively large area around the column.
- (4) Diagonal cracks form at a load of about 50-70 percent of the ultimate load.
- (5) Eventually, the slab splits apart at these previously formed diagonal cracks.

2.2.1 Description of Punching Failure

Localized failure of a reinforced concrete flat plate-column connection is described by the term punching failure. It is associated with a particular collapse mechanism in which the column together with an attached portion of plate push through the surrounding plate. Failure of the connection may occur in a brittle manner before a complete yield line mechanism, or it may progress gradually after a considerable amount of deformation and extensive yielding of all the reinforcement.

Whether or not a folding mechanism has developed, all failure surfaces look about the same. For concentric loading, the failure surface is usually a truncated cone or pyramid with the fracture surface inclined at an angle of about 25 to 35 degrees with a horizontal plane. Figure 2.1 shows a section sawn through a typical punching failure of an interior connection.

Figure 2.2 shows a typical punching failure of an edge connection. There is a striking similarity between the failure of an interior connection under combined shear and unbalanced moment, and that of an edge connection as illustrated in Figure 2.3. The two adjacent side regions show extensive torsional cracking. In an interior connection, the punched region is confined to the area near the more heavily loaded face of the column, and the area near the opposite face may show little or no distress.

2.2.2 Types of Failure

For two-way plates, flexural capacities are based on a yield-line analysis. Test results on simply supported plates routinely exceed these upper bound estimates by as much as 30 percent due to membrane forces, boundary restraints and second order effects which allow the slab to act as a folded plate.

Punching failure may occur before or after the formation of the yield lines, and almost all flat plate-column connections appear to fail by punching. Clyde and Carmichael (1974) suggest that the terms "punching failure" and "shear failure" are synonymous, while Gesund (1975) states that many tests, reported in the literature as punching failures, were actually local flexural failures. Criswell (1974) discusses a gradual transition between flexural and shear failures of slab-column connections. He tries to separate shear and flexural failures on the basis of how much ductility is evident prior to fracture and whether or not the flexural capacity of the plate is reached.

Alexander and Simmonds (1991) state that the question of whether a specimen fails in flexure or shear should be replaced with the question of whether the failure was concerned with the mechanism of moment capacity or moment gradient. In a reinforced

concrete flexural member, shear is the resultant of gradient in bending moments and can be achieved either by beam action, which requires a force gradient in the reinforcement, or by arching action, which requires a changing internal flexural moment arm.

Force gradient in the reinforcement may be controlled by the bond strength at the reinforcement to concrete interface, or by extensive yielding of the reinforcing bars. Bond failure would introduce brittle quality to the failure mechanism.

Figure 2.4 shows a typical load-deflection curve for a reinforced concrete flat plate. The shear and flexural capacities of the connection are referred to as P_v and P_y respectively. Where P_v is less than P_y , loss of bond between the reinforcement and its surrounding concrete causes a brittle punching failure. Where P_v is greater than P_y , the spread of yielding away from the column reduces the force gradient in the reinforcement and hence, the shear capacity of the connection. As shown in Figure 2.4, failure is reached when the declining shear strength becomes less than the available flexural strength.

Alexander and Simmonds (1991) then conclude that punching failure may always be explained in terms of shear failure (loss of force gradient in reinforcement). Those reported in the literature as flexural failures are interpreted as ductile shear failures in which the loss of force gradient is brought about by the spread of yielding. Those that were considered "proper" are categorized as either shear failures due to the loss of bond, or over-reinforced flexural failures. This explanation is consistent with the observation that almost all flat plate connections fail by punching and that the failure surfaces look about the same.

2.2.3 Effect of Reinforcement

The importance of top reinforcement in increasing the shear capacity of both edge and interior connections is well established in the literature. In virtually all realistically reinforced connections, steel through the column yields prior to punching. Steel strains are highest in bars which pass through the column, although there may be sufficient strains to yield the bars outside the column. In edge connections, bars normal to the free edge and outside the column face may not yield unless they are anchored and their correspondent bending moment is less than the torsional capacity of plate at column side-faces.

Bottom reinforcement also improves both the ultimate capacity and the ductility of a connection. Clyde and Carmichael (1974) showed that the ultimate deflection doubled and the ultimate load increased by 25 percent as bottom steel content went from 0 to 100 percent of the top mat. The reinforcement ratio of the top mat was set at 0.84 percent in all their tests.

2.3 Methods of Estimating Punching Capacities

Analytical models may be categorized in four groups based on their failure criterion; concrete rupture models (including most code procedures and plasticity approaches), flexural models, the Truss Model, and the Bond Model.

Concrete rupture models assume that something similar to diagonal tension failure in beams governs punching failure in plates. Due to the appearance of punching failures, diagonal tension may seem to be important in limiting shear strength. However, these cracks typically form at loads less than 70 percent of the ultimate loads (Broms, 1990) and the connection is stable in this crack condition and may be repeatedly loaded and unloaded

(Regan and Braestrup, 1985). These observations are supported by tests by Kinnunen and Nylander (1960). Test specimens that were fabricated with pre-formed conical punching surfaces completely surrounding the column showed at most only about 25 percent reduction in capacity.

In upper bound plasticity approaches, concrete fracture is described by some yield criterion for concrete. The plasticity approach assumes a fracture surface of a particular form and derives an energy expression that describes rupture along this surface. This expression is then minimized by employing variational calculus. Regan and Braestrup (1985) note that the plasticity approach predicts that a critical vertical shear stress on a critical section should be a good parameter for describing punching failure.

The position of this critical section and the value of critical shear stress vary from one code to another. It is not clear how concrete rupture models can be reconciled with the test observation that diagonal cracking does not lead to punching. However, the fact that code procedures work is evidence that something like beam action is at work within the plate. The concept of a critical, nominal shear stress is easily justified if the ultimate load is governed by the horizontal shear stresses resulting from bond.

Flexural punching models for plate-column connections assume a fan-like mechanism of wedge-shaped sections of slab. The failure criterion may be based on a yield-line analysis, as in Gesund (1975) or it may be based on a critical condition in the concrete compressive block, as in Kinnunen and Nylander. The yield line approach is criticized by Long (1975) as not being consistent with the observed behavior of plate-column connections. The limiting strains proposed by Kinnunen and Nylander have been criticized as not being realistic. In addressing some of these concerns, Broms (1990) uses a variation of the Kinnunen and Nylander model incorporating failure criteria for the concrete that are more justifiable. The model, however, remains essentially a flexural mechanism that is controlled by rupture of the compressive block near the face of column. Very little attention has been given to the location where the failure surface intercepts the tension reinforcement of the plate (Alexander and Simmonds, 1991).

The Truss Model (Alexander and Simmonds, 1986) assumes that a slab column connection can be idealized as a space truss composed of steel tension ties and straight-line inclined concrete compressive struts. The Truss Model is most like a flexural model, except that it assumes failure to be governed by conditions where a concrete strut meets its steel tie and not where the strut meets the column. The rationale behind this model is that punching failure results from the failure of the plate to confine the out-of-plate component of a compression fan. In principle, the Truss Model can handle a wide variety of problems, including the shear-moment interaction of edge column-slab connections. However, estimates based on this model rely on an empirical prediction of the angle of the compression strut. To remove the empiricism from the estimate of the angle of the compression strut, Alexander and Simmonds (1991) reexamined the Truss Model approach. Test results showed that the geometry of the compression strut was a curved arch rather than a straight line. This led to the development of a new mechanical model called the Bond Model that retains the desirable characteristics of the Truss Model, and is consistent with the experimental measurements of strain.

2.4 The Bond Model

2.4.1 Description of the Model

Bond Model describes the transfer of load between the plate and the column in terms of the two fundamental mechanisms of shear transfer; beam action, and arching action. For convenience, as defined in Figure 2.5, the plate is divided into radial strips and quadrants. In the quadrant, consistent with the test observations, shear transfer is governed by beam action as illustrated in Figure 2.6. Inside the radial strips, shear is carried by a compression arch, and varies from a maximum at the face of the column where the slope of the arch is large to a minimum, perhaps zero, at the intersection of the arch and the reinforcing steel where the slope is small. The shear that was carried by the arch at the face of column must be dissipated in a direction perpendicular to the arch at some distance away from the column. The rate at which shear can be dissipated determines the curvature of the arch.

The capacity of a radial strip is limited by two independent quantities, namely the flexural capacity of the radial strip and the ability of the plate to generate bar force gradient by which the strip is loaded. Anything that reduces or limits either of these quantities will affect the capacity of the radial strip.

Since beam action requires a force gradient in the reinforcement, failure may occur if the force gradient exceeds its limitation. The term Bond Model is used because bond strength is the most important limitation on force gradient for those connections that fail prior to widespread yielding. However, the model describes a complete load path, and does not preclude other possible failure modes such as loss of bond due to extensive yielding of reinforcement, failure of concrete compression strut at the face of the column, or the anchorage failure of the tensile tie of the arch.

Shear capacity of a connection is assumed to be equal to the sum of the shear capacities of its radial strips. The ultimate capacity of the connection is governed by the lesser of the two independent capacities; the yield line mechanism load, P_y , and the shear capacity of the connection, P_v , as shown in Figure 2.4.

2.4.2 Shear Capacity of Radial Strips

The most important distinction between the Bond Model and most other models is that the Bond Model provides a lower bound estimate for the capacity of a radial strip. There are three requirements for a lower bound solution: (1) equilibrium must be satisfied at every point, (2) no element may be loaded beyond its relevant capacity and (3) there must be sufficient ductility to allow redistribution of load.

2.4.2.1 Equilibrium of a Radial Strip

Figure 2.7 presents the free body diagram of a radial strip in an interior connection. It is convenient to define the total strip moment, M_s , as the sum of the M_s^- and M_s^+ , the bending moments at column end and remote end, respectively. The total load transferred by the radial strip to the column is P_s . Side face of the strip, forming the boundary between the strip and the adjacent quadrant of the two way plate, is loaded by bending moment, m_b , torsional moment, m_t , and shear, v . These are related by the equations of equilibrium of a two-way flexural system ;

$$v = \frac{\partial m_b}{\partial n} + \frac{\partial m_t}{\partial r} = v_b + v_t$$

The quantities v_b and v_t are the bending and torsional shear, respectively. The vertical and rotational equilibrium of the strip result in the following equations.

$$P_s = 2 \int_0^L (v_b + v_t) dr = 2 \int_0^L v_b dr + 2 [m_t]_0^L \quad [2.2]$$

$$M_s + 2 \int_0^L m_t dr = 2 \int_0^L (v_b + v_t) r dr = 2 \int_0^L v_b r dr + 2 [m_t \times r]_0^L - 2 \int_0^L m_t dr$$

In the latter, the torsional shear component is integrated by parts, and $\int_0^L m_t dr$ is the net torsion, M_p , along each side face of the radial strip. Therefore,

$$M_s + 4M_t = 2 \int_0^L v_b r dr + 2 [m_t \times r]_0^L \quad [2.3]$$

The actual distribution of shear forces and torsional moments on the side faces of radial strips are not known. Bending shear always adds to the loads on the strip. However, torsional shear removes the load from middle parts of the strip and applies it directly to the radial compressive arch.

2.4.2.2 Simplified Model

It is convenient to consider the load, q , directly on the radial strip as part of the load, v , on the side faces of the radial strip as shown in Figure 2.8a. In a simplified model, Figures 2.8b and 2.8c respectively show the free body diagrams of an interior radial strip and a spandrel strip. The direct effect of torsional moments in rotational equilibrium of the radial strip is neglected. However, part of the effect of torsional shear is being considered in the assumption of uniformly distributed load acting on the arch. Shear capacity in this simplified model is referred to as nominal capacity of the radial strip. Solving the equations of equilibrium, the loaded length, l , and the shear capacity of each radial strip, P_s , are as following:

$$l = \sqrt{M_s / w} \quad (\text{Interior Radial Strips}) \quad [2.4]$$

$$P_s = 2 \times \sqrt{M_s \times w} \quad (\text{Interior Radial Strips}) \quad [2.5]$$

$$l = \sqrt{2 \times M_s / w} \quad (\text{Spandrel Strips}) \quad [2.6]$$

$$P_s = \sqrt{2 \times M_s \times w} \quad (\text{Spandrel Strips}) \quad [2.7]$$

Where M_s is the flexural capacity of the radial strip and w is one way shear acting on each side face of the radial strip. Results of 115 tests on interior connections in the literature

show that limiting w to the one-way critical shear of ACI 318 (Equation 2.8) gives the least scattered results (Alexander and Simmonds 1991).

$$w = 0.167 \times \sqrt{f'_c} \times \quad (\text{SI units}) \quad [2.8]$$

2.4.3 Comparison of A23.3 and ACI 318 Values of One-way Critical Shear

The factored shear resistance currently used in Canadian Standard, A23.3, is about 85 percent of that of American code, ACI 318 (compare Equations 2.9 and 2.10). This leads to almost equal central factors of safety (ratio of load factor to the resistance factor), since the average load factor in A23.3 is about 89 percent of that in ACI code.

$$v_c = \Phi_c \times 0.4 \times \sqrt{f'_c} = 0.6 \times 0.4 \times \sqrt{f'_c} = 0.24 \times \sqrt{f'_c} \quad (\text{CAN-A23.3}) \quad [2.9]$$

$$v_c = \Phi \times 0.333 \times \sqrt{f'_c} = 0.85 \times 0.333 \times \sqrt{f'_c} = 0.283 \times \sqrt{f'_c} \quad (\text{ACI 318}) \quad [2.10]$$

In the design of flat plate-column connections by the Bond Model, using the resistance factors of the Canadian Standard results in a shear capacity which is about 84 percent of the shear capacity using the ACI shear resistance factors (compare Equations 2.11 and 2.12). This also results in an almost equal central factor of safety.

$$\begin{aligned} P_{s,CAN} &= 2 \times \sqrt{(\Phi_s \times M_s) \times (\Phi_c \times w)} \\ &= 2 \times \sqrt{(0.85M_s) \times (0.6w)} = 1.428 \times \sqrt{M_s \times w} \quad (\text{CAN-A23.3}) \quad [2.11] \end{aligned}$$

$$\begin{aligned} P_{s,ACI} &= 2 \times \Phi \times \sqrt{M_s \times w} \\ &= 2 \times 0.85 \times \sqrt{M_s \times w} = 1.7 \times \sqrt{M_s \times w} \quad (\text{ACI 318}) \quad [2.12] \end{aligned}$$

Observing that the ratio of $P_{s,CAN}$ to $P_{s,ACI}$ equals to the ratio of $v_{c,CAN}$ to $v_{c,ACI}$, the same one way critical shear may be used in the Bond Model, regardless of the governing code. Hence, Equation 2.8 will be used as the critical one-way shear throughout this study.

2.4.4 Bond Model and Building Code Procedures

Building codes and the Bond Model share the concept of a limiting shear acting on a critical section. What distinguishes them in part is the shape, position, and size of the critical section.

The code critical sections surround the column at a fixed distance from the column faces. This distance differs from one code to another (Figure 2.9). The Bond Model, however, defines shear arms that cantilever from the column, resulting in a critical section with a cruciform shape (Figure 2.10). Where as the size of the critical sections defined by codes are fixed, the size of the critical section used by the Bond Model is variable, being a

function of both the flexural reinforcement of the radial strip and the ability of slab to carry one way shear (Equations 2.4 and 2.6).

The effect of reinforcement ratio on shear capacity of the plate-column connection is ignored by the North American Standards. British code, BS 8110, accounts for the effect of reinforcement ratio by changing its allowable shear stress with the ratio of top reinforcement. The Bond Model, however, accounts for the effect of both top and bottom reinforcement since loaded length of radial strip is a function of flexural capacity of the radial strip. To compare test results to the Bond Model and code procedures, Alexander and Simmonds (1991) plotted the test to predicted values for 115 tests on concentrically loaded interior connections in the literature (Figures 2.11 to 2.13).

In the presence of unbalanced moment, North American Standards assume that a certain fraction of the unbalanced moment is carried by a linear distribution of vertical shear stresses around the critical section. The combined effect of vertical shear and moment is estimated as follows:

$$v_{max} = \frac{V_u}{p \times d} \pm \frac{\gamma_v \times M_u \times c}{J} \quad [2.13]$$

where v_{max} is critical stress for concrete in shear, V_u is shear force transferred between slab and column, M_u is unbalanced moment, d is effective depth of reinforcement, p is perimeter of the critical section, c is the distance from the centroid to extreme points on the critical section, and J is the polar moment of inertia of the critical section.

Consider two edge connections with the same gross geometry and effective depth, but with different design moments. Parameters p , d , γ_v , c and J are functions of geometry only, and therefore are the same for both connections. According to the North American Standards, the connection designed for the larger moment requires more flexural reinforcement. However, based on Equation 2.13, its shear capacity is assumed to be smaller. This contradicts the Bond Model which predicts that the more heavily reinforced connection can be designed in a way that it also transfers more shear.

2.5 Methods of Testing

In this section, test setups reported in the literature are briefly described and evaluated with respect to how the setup effects the observed results. Three independent features of testing are considered; (a) whether positive moments can be generated, (b) how loads are applied to the specimen, and (c) how realistic is the amount of reinforcement.

By far the greatest number of tests have been performed on isolated column-slabs. The edges of the plate may or may not be rotationally restrained. The size of the rotationally restrained test specimens is determined by the position of maximum positive moment (or zero shear line) of a prototype structure. The size of rotationally unrestrained plates, however, is determined by the approximate position of radial contra-flexure of a prototype structure.

Isolated column tests with rotationally unrestrained edges fail to model such features as moment redistribution. They also do not consider the effect of the positive reinforcement on the punching capacity of the flat plate-column connections.

Based on the method of the load application, there are two types of the isolated column tests. With the first type, the load is applied through the column and the slab is supported at fixed positions. In effect, the supports control the displacement of the slab relative to the column. With the second type, the magnitude of the individual loads applied to the slab are controlled directly.

Tests with controlled load on the plate are not equivalent to enforced deformation tests, in which load is applied through the column and displacements on the plate are controlled. Assume two identical plates for which the flexural capacity in one direction is smaller. Plate A is loaded uniformly along all the edges, and fails at the load related to the smaller flexural capacity. Plate B, however, is loaded through the column and is supported by line supports along all the edges. Flexural failure of this plate occurs at a larger load than that of plate A, simply because of the redistribution of the forces along the edges.

Enforced deformation tests allow the slab a freedom in determining its own internal force distribution that is not available to the prototype structures. The distribution of forces along the boundary is statically indeterminate, and may be unrealistic, especially for eccentrically loaded specimens. Yet, in most cases, these forces are not measured.

It is concluded that controlling the load distribution rather than the displacements is always a better representative of the prototype slab. This is especially true in cases where one expects different behavior in the two directions, as with the rectangular column or panels.

Load in multi-column tests is always applied on the slab. Hence, similar to the prototype structures, their flexural capacity is governed by the smaller capacity in the two directions. Also, in multi-column tests, positive moments are generated in at least one direction. This permits the study of the effect of positive reinforcement and redistribution of moments on the capacity of the plate-column connections.

It has been observed that some investigators provide an excessive amount of reinforcement in their test specimen to avoid flexural failure and to ensure that punching failure occurs first. In these specimens, the steel might not even yield. However, in almost all buildings, only the flexural reinforcement necessary to provide the required flexural capacity is provided. Therefore, to reflect real life structures, it is very important to keep the reinforcement ratio in a reasonable range. Ideally, the test specimens should be flexurally designed so that no reinforcement in excess of that required for flexural equilibrium is provided.

2.6 Measuring the Distribution of Internal Shears

2.6.1 General

The first attempt to measure the internal shear forces in a flat plate structure was based on the mechanism of shear transfer described in the Bond Model. Alexander, Lu, and Simmonds (1995) estimated the internal shear distribution in two tests using strain gauges on the reinforcement. The total internal shear was in excellent agreement with the measured external load. The results provided strong support for the mechanics of shear transfer in an interior column-plate connection, and led to a unique insight into the importance of the contribution of torsion in shear transfer at a plate-column connection.

It is assumed that the magnitude of the torsional moment is zero at both remote and column ends. This assumption is discussed in Section 2.6.2. As a result, sum of the

torsional shear over the full length of each face of the radial strip becomes zero, and Equations 2.2 and 2.3 reduce to Equations 2.14 and 2.15, respectively.

$$P_s = 2 \int_0^L v_b dr \quad [2.14]$$

$$M_s + 4M_t = 2 \int_0^L v_b r dr \quad [2.15]$$

The location of the radial strip is such that v_b is dominated by beam action. Therefore, estimates of integrals on the right hand side of Equations 2.14 and 2.15 can be made based on strain measurements of the reinforcement perpendicular to the radial strip.

In cases where shear is transferred by beam action only (i.e. constant j throughout the interval), bending shear can be measured from readings of only two strain gauges, using Equation 2.16, in which s is the distance between the gauges, and T is the force in the bar. Subscripts 1 and 2 reflect the position of the gauge from the center line of the column.

$$V_{bar} = \frac{T_1 - T_2}{s} \times j d_1 \quad [2.16]$$

However, some limited arching action might exist in the first interval. In this case, a third strain gauge is required. It is assumed that all shear in the second interval is carried by beam action, and that the shear in the first and second intervals are equal. This results in Equation 2.17;

$$\begin{aligned} V_{bar} &= \frac{M_1 - M_2}{s} = \frac{T_1 \times j d_1 - T_2 \times j d_2}{s} && \text{First Interval} \\ V_{bar} &= \frac{T_2 - T_3}{s} \times j d_2 && \text{Second Interval} \\ V_{bar} &= \frac{T_1 \times j d_1}{s} \times \frac{T_2 - T_3}{2T_2 - T_3} && \text{Basic Equation} \end{aligned} \quad [2.17]$$

All strain gauges must lie at fully cracked sections so that $T \times j d$ will be an accurate representation of the bending moment. Otherwise (e.g. in early stages of loading), part of the tensile force is carried by adjacent concrete, and the forces measured based on the gauge readings are smaller than the actual tensile forces.

2.6.2 Comments

2.6.2.1 Validity of Assumptions in Equations 2.14 and 2.15

In the derivation of Equations 2.14 and 2.15, two basic assumptions were made; first, torsional moment on the side face of a radial strip at the remote end equals zero, and second, the torsional moment at the column end equals zero. The first assumption is always valid because both shear and torsion are zero on any axis of symmetry. However, the second assumption is not necessarily true, and m_t may have non-zero value at column

corners. This has no effect on Equation 2.15, since $(m_t \times r)$ is always zero at $r = 0$. However, a term of $-2 m_t(0)$ should be added to the right side of Equation 2.14.

It will be discussed in chapter 6 that at the ultimate capacity of a radial strip, the torsional moment at the corner of a column is most likely about zero. It is worth mentioning that it is not clear how to measure this torsional moment experimentally nor how to predict it analytically.

2.6.2.2 Alternative Solution for Equation 2.16

Where the gauges are spaced closely, the concrete might not crack right at the position of the second gauge. This would result in a smaller value of T_2 , and leads to an unrealistically high estimate of the bar shear when using Equation 2.16.

As an alternative solution, in cases where readings of three strain gauges on one reinforcing bar are available, Equation 2.18 which is based on the readings of the first and the third gauges may be used.

$$V_{bar} = \frac{T_1 - T_3}{2 \times s} \times j d_1 \quad [2.18]$$

Equation 2.18, in turn, may overestimate the shear if the concrete is not cracked at the position of the third gauge. To avoid overestimation of the shear, the smaller value from Equations 2.16 and 2.18 should be used as the bar shear.

2.6.2.3 Alternative Approach for the Derivation of Equation 2.17

Figure 2.14a shows the definition of a bar strip (a strip of plate attributed to the bar for which shear is being measured), and Figure 2.14b shows the free body diagram of this strip. In deriving Equation 2.17, it was assumed that the torsional moments on the side faces of a bar strip are equal, and therefore the only mechanisms of shear transfer are the beam action and limited arching action. In general, torsional moments on opposite side faces of bar strip are not equal, resulting in ΔM_t as obtained from Equation 2.19.

$$\Delta M_t = \int_{A_1} (m_t + \Delta m_t) dA - \int_{A_2} m_t dA = \int_{A_1} \Delta m_t dA \quad [2.19]$$

In this part it is assumed that the only mechanisms of shear transfer are the beam action and the gradient in torsional moments. The moment arm becomes almost constant in the bar strip since no arching action exists. As shown in Figure 2.14c, the tensile stress in reinforcement at critical section A is about yield stress, and is needed to satisfy the bending requirement for the equilibrium of the plate. Tensile force at a distance "x" from section "A" is equal to $T(x)$. Part of this force, $\alpha T(x)$, is generated due to ΔM_t , in which α is a coefficient between zero and one, and is assumed to be constant along each bar.

Considering the free body diagrams in Figures 2.14d and 2.14e, rotational equations of equilibrium result in Equations 2.20 and 2.21, respectively.

$$V_{bar} \times s = (T_1 - T_2) \times j d_1 + \alpha T_2 \times j d_1 \quad [2.20]$$

$$2 \times V_{bar} \times s = (T_1 - T_3) \times j d_1 + \alpha T_3 \times j d \quad [2.21]$$

Combining Equations 2.20 and 2.21 and eliminating α results in V_{bar} as in Equation 2.22. This equation is exactly the same as Equation 2.17, although the assumptions made are different. It is concluded that in the circumferential direction, where the dominant mechanism of shear transfer is beam action, Equation 2.17 results in good estimates of V_{bar} in the existence of gradient in torsional moments, as well as in the presence of limited arching action.

$$V_{bar} = \frac{j d_1}{s} \times T_1 \times \frac{T_2 - T_3}{2T_2 - T_3} \quad [2.22]$$



Figure 2.1 Typical punching failure of an interior connection

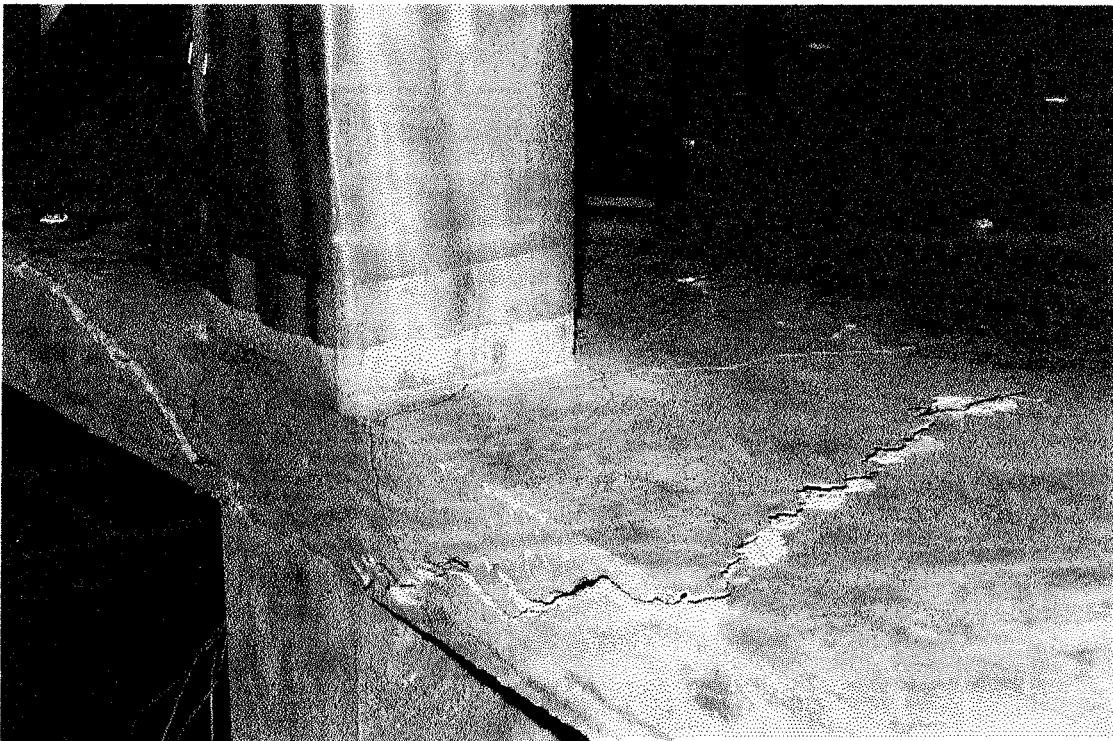


Figure 2.2 Typical punching failure of an edge connection

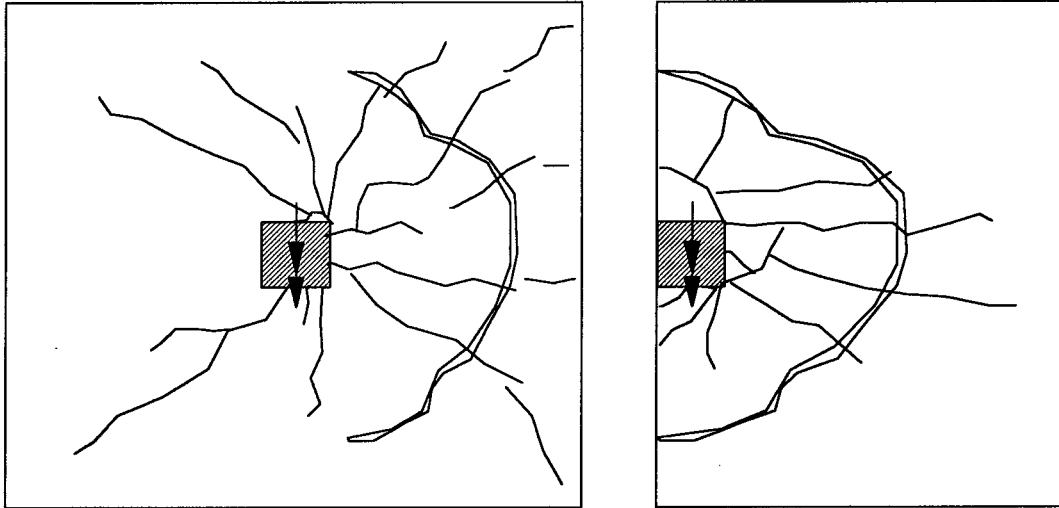


Figure 2.3 Typical punching failure of plate-column connections with unbalanced moments

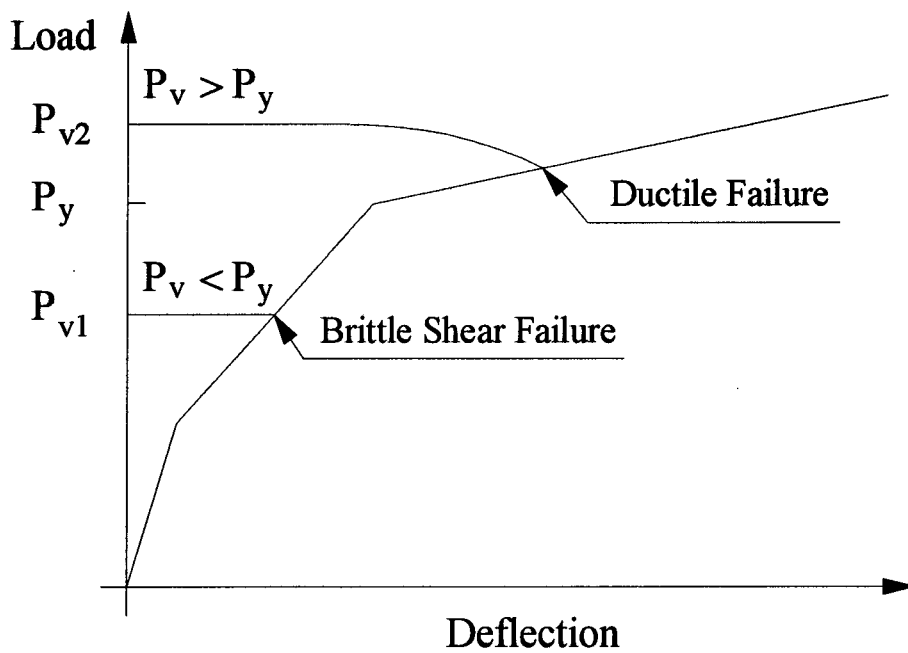
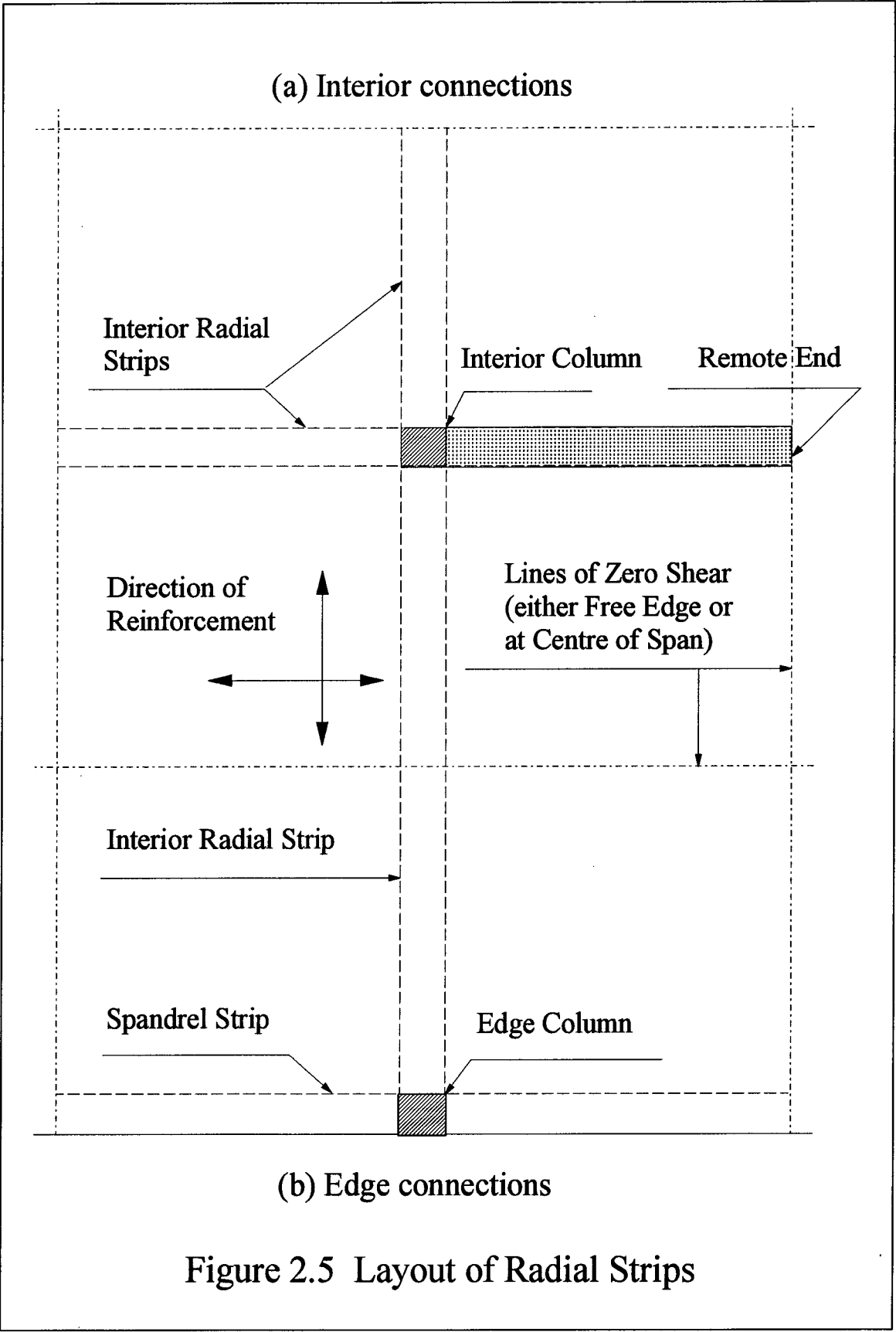


Figure 2.4 Brittle and Ductile Punching Failures



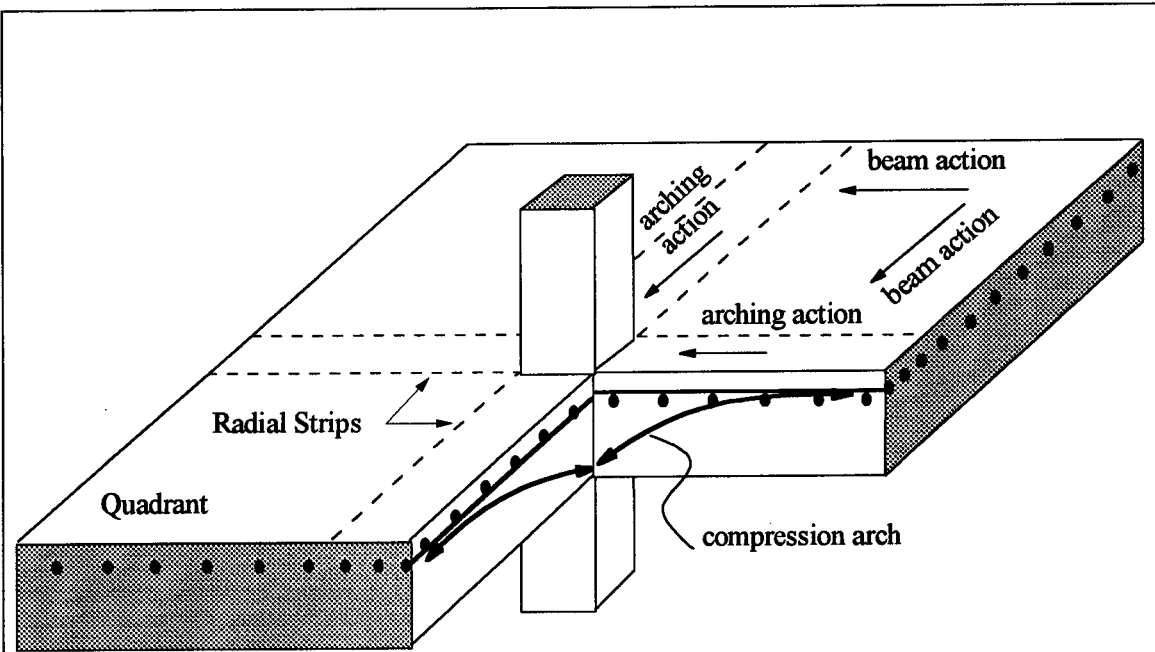


Figure 2.6 Shear transfer in flat plate-column connections

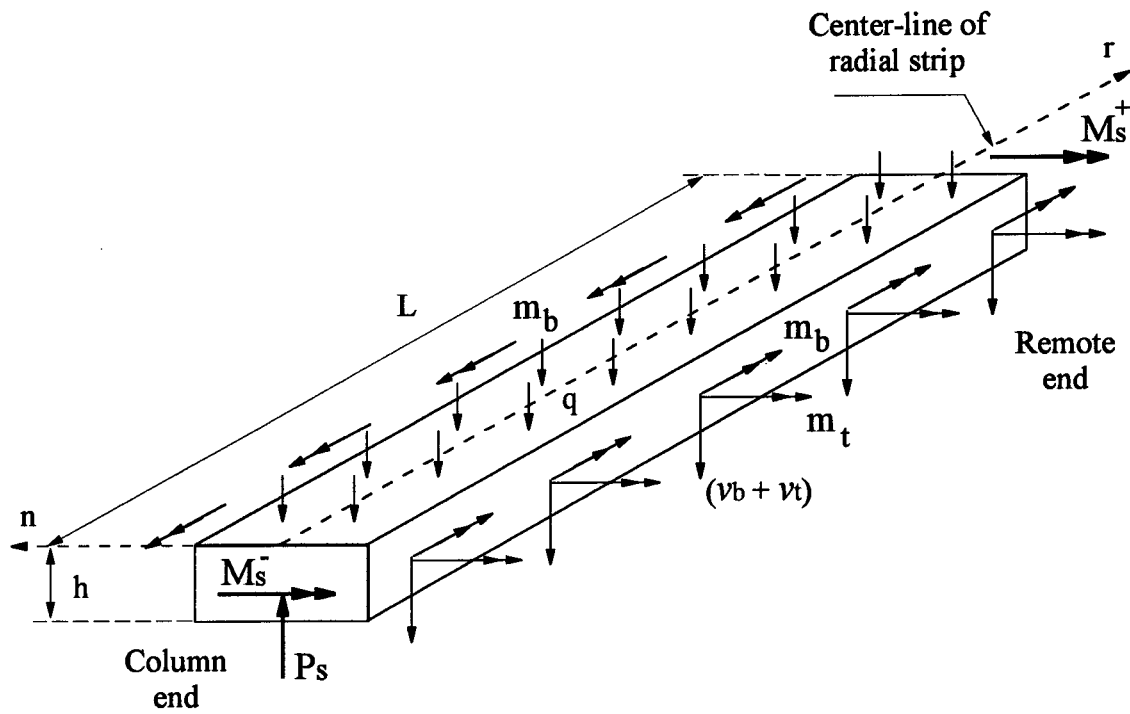


Figure 2.7 Actual Loading on Radial Strips

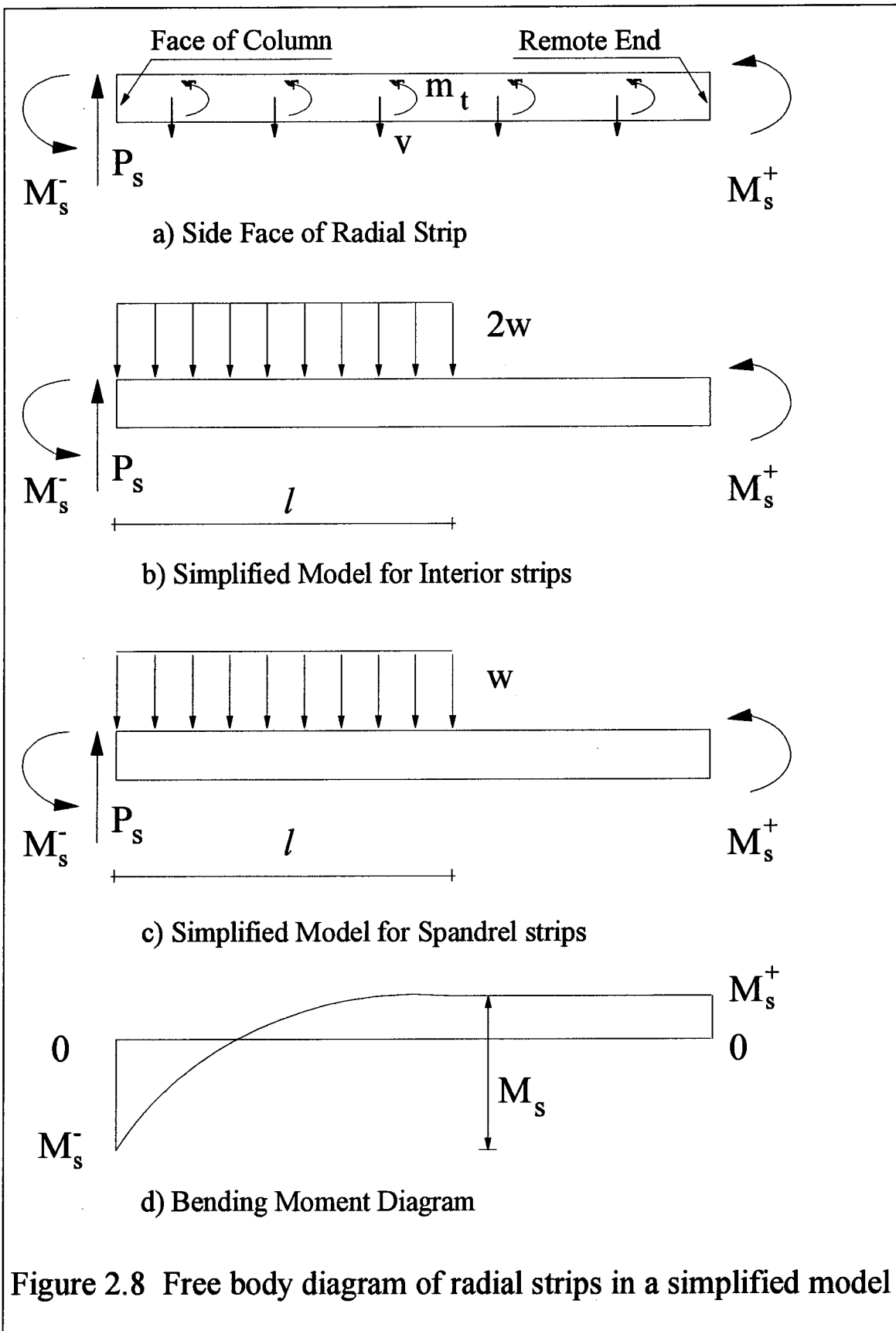


Figure 2.8 Free body diagram of radial strips in a simplified model

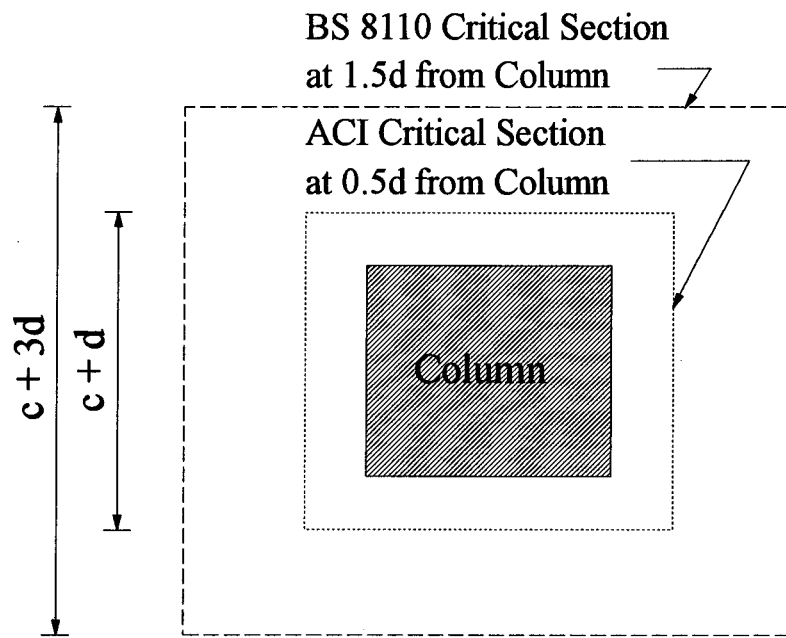


Figure 2.9 Code-defined Critical Sections

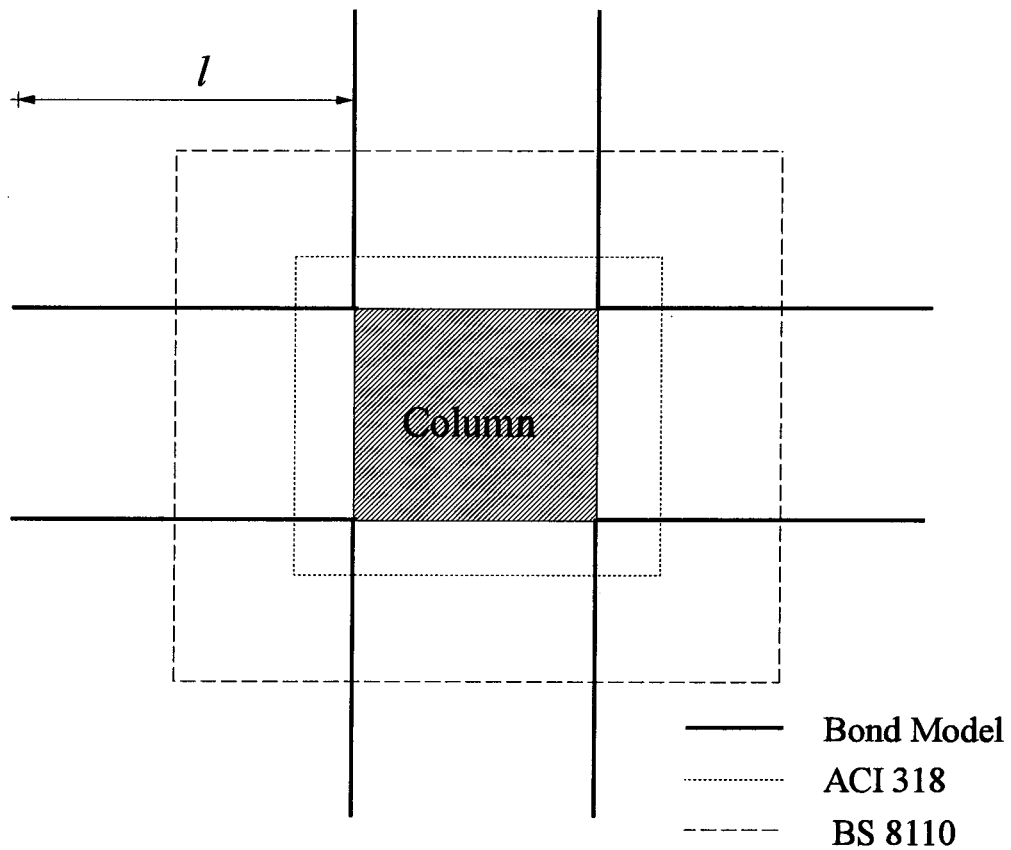


Figure 2.10 Bond Model Critical Section

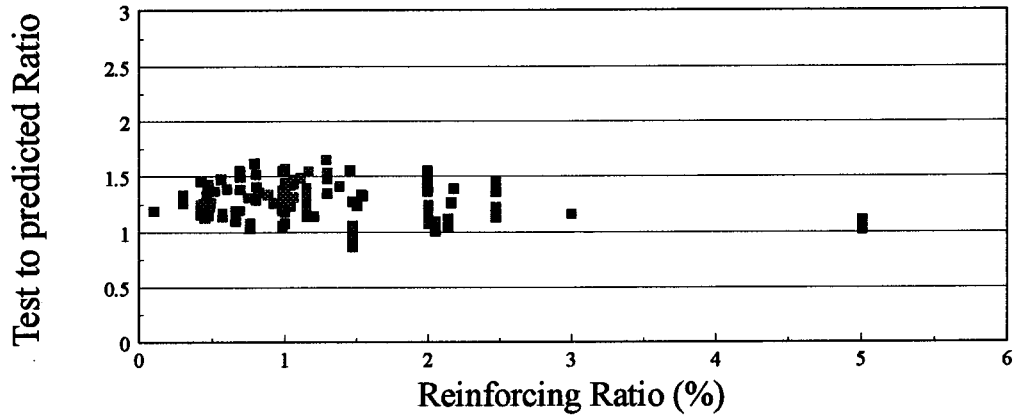


Figure 2.11 Bond model results using ACI 318 one way shear

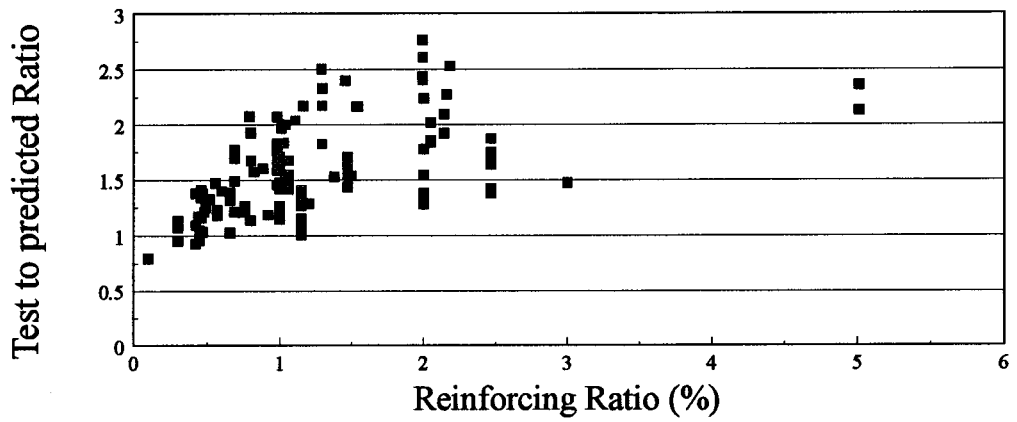


Figure 2.12 ACI 318 Building Code predictions

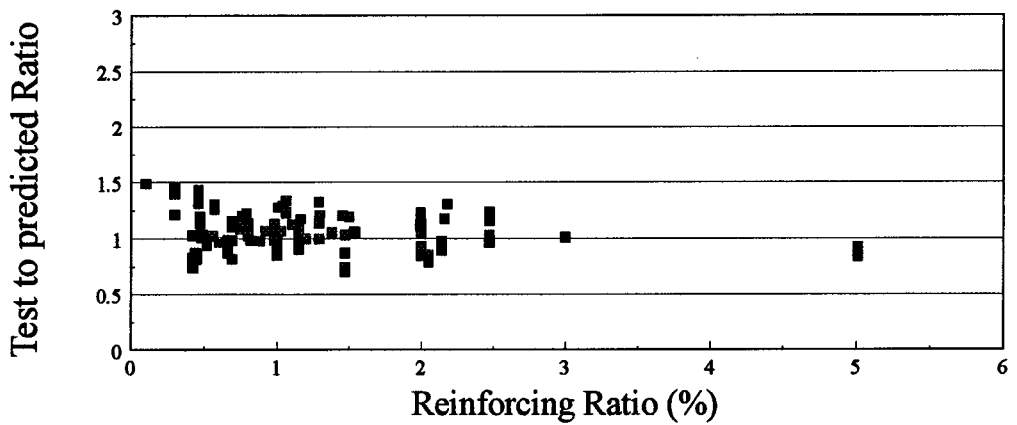


Figure 2.13 BS8110 Building Code predictions

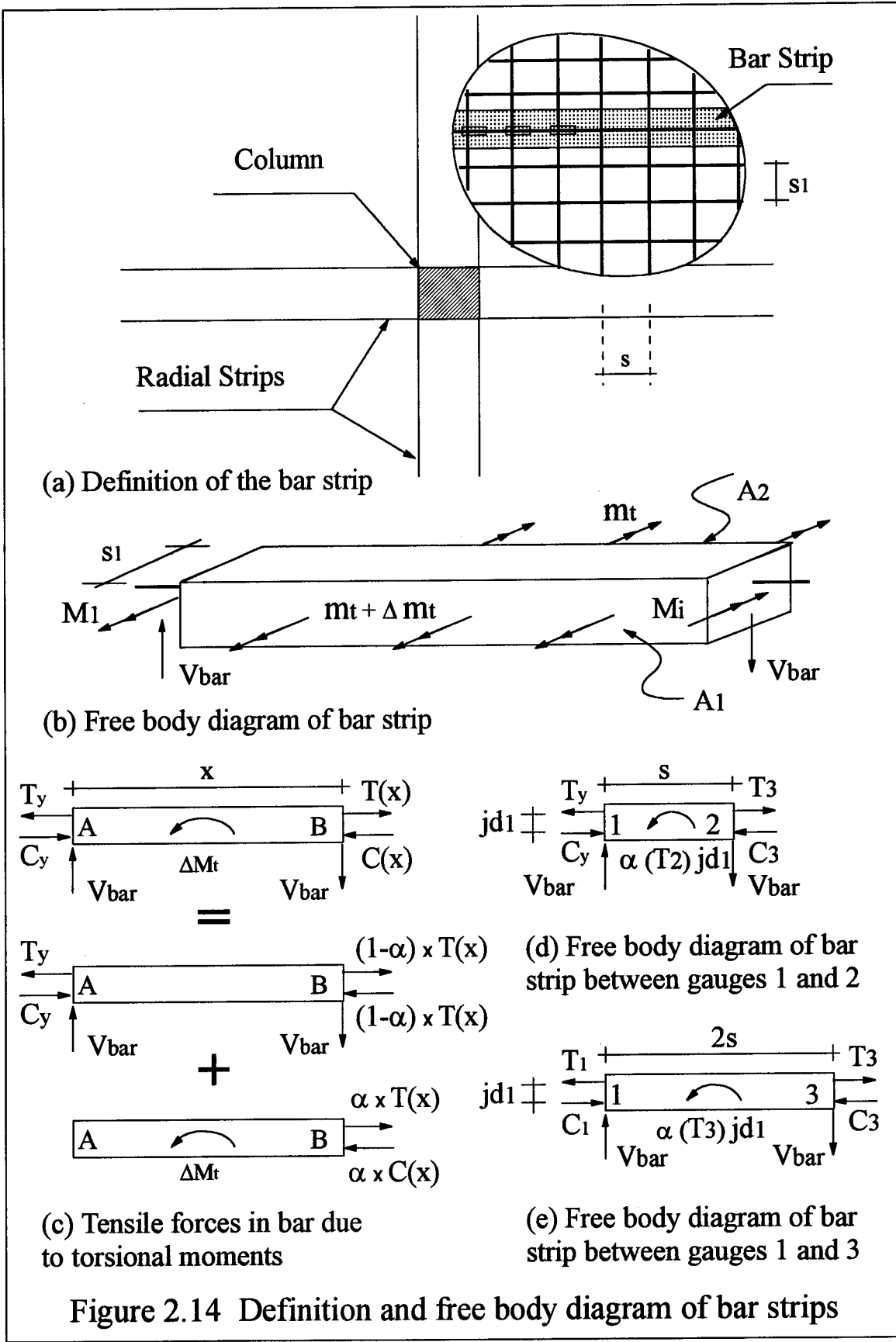


Figure 2.14 Definition and free body diagram of bar strips

3. Prototype, Specimen, Apparatus, Fabrication Procedure, and Ancillary Tests

Figure 3.1 illustrates the prototype and the region modeled by the test specimen. The prototype is assumed to be a flat plate structure with two spans in one direction and at least four spans in the other direction. A span length of 4877 mm (16') was selected in both directions. Two geometrically similar edge column-plate connections and one interior column-plate connection will be examined.

3.1 Objectives of Experimental Program

There are two main objectives for the test program. The first is to create the data so that the distribution of the internal shear and torsional moments in both edge and interior connections can be determined. Subsequently, this data is used for verification and/or improvement of the Bond Model. The second is to examine how well the Bond Model and the North American Standards predict the behavior of edge connections with different design moments.

By determining the distribution of internal shears, two main assumptions of the Bond Model can be verified, namely, that w can be treated as a uniformly distributed one-way shear, and that at failure, all radial strips reach their ultimate capacity. Also, of interest is the contribution of the torsional moments to the flexural capacity of the radial strips.

Negative moment transferred to the edge column is one of the variables to be investigated. Two edge connections with the same geometry, the same effective depth of reinforcement and the same concrete properties, but with different design moments, will have different flexural reinforcement. For properly detailed connections, the Bond Model predicts an increase in both vertical shear and moment transfer with the increased reinforcement. North American Standards, however, suggest that the ability of the connection to transfer shear would diminish as the connection transfers larger moments.

One of the edge connections was designed for 30 percent of the panel moment. Most designers prefer to reduce the amount of moment transferred through the edge connections because it results in a considerable reduction in the size of the edge columns. The other connection was designed for only 10 percent of the panel moment. Of interest is the comparison, at service load, of these edge connections with the two extreme values of negative design moment.

The flexural capacity of the connection is directly related to the yielding of the bars perpendicular to the free edge, including those not passing through the column. A23.3-M84 required that a fraction, $1 - \gamma_v$, of the total reinforcement be placed within $c_2 + 3h$. This requirement has been revised in A23.3-94 so that currently all reinforcement required for the flexural resistance must be placed within this distance. Among the objectives of the test is to examine how effective is the top steel outside of the column.

3.2 Design Considerations of Specimen

The amount and the distribution of the flexural reinforcement was selected so that the yield-line mechanisms would almost occur simultaneously in both directions. The test specimen satisfied all the flexural requirements of A23.3-M84 regarding the details of reinforcement such as cut off points, splices, hook development length, integrity steel, and

minimum reinforcement. Comments are given where relevant provisions have been changed in A23.3-1994 (not available at the time of specimen fabrication).

The shear requirements of the Standard, however, are not satisfied. All column dimensions were selected so that, according to the North American Standards, the factored shears would exceed the capacities of the connections. Spacing of the reinforcement was selected so that according to the Bond Model, a complete yield line mechanism would form prior to the punching failure.

To model the true behavior of a flat plate-column connection, it is important to test a full scale specimen with accurate boundary conditions. An accurate boundary condition is the one in which deformations and forces are measured and, their distributions are reasonably close to that in the prototype building. Tests in which loads are distributed over a large number of points are preferred to tests with enforced deformation. Rotational restraints should be provided at the continuous edges to consider the effect of the bottom reinforcement.

The testing facility introduced some limitations or certain preferences on the size of the specimen. To facilitate setting up the test apparatus, especially those of the loading system, span length of specimen was chosen to be modular with laboratory strong floor .

3.3 Test Specimen

3.3.1 Geometry of the Specimen

The test specimen consisted of a two panel flat plate, 4270 mm wide and 10008 mm long, supported by three concrete columns as shown in Figure 3.2. Interior column had a 305 mm square cross section. Cross sectional dimensions of the edge columns were 305 and 255 mm with the shorter side perpendicular to the free edge. Pictures of the test specimen and the test setup are presented in Appendix A.

So that deflection computations are not required, a slab thickness of 152 mm (6") was selected to satisfy the requirements of clause 9.5.3 of CSA A23.3-M84. This minimum thickness has been increased in A23.3-94 to 170 mm, a 13 percent increase.

Nominal values of $f'_c = 30$ MPa for the specified compressive strength of concrete and $f_y = 400$ MPa for the yield strength of the reinforcing bars have been used in the design of the plate. The average height of stories has been assumed to be 3.2 m.

3.3.2 Design Load and Flexural Design of Specimen

3.3.2.1 Target Design Moments

Target design moments are presented in Figure 3.3. These moments are similar to those required by Direct Design Method, but were modified to demand increased ductility especially in the interior connection.

Negative yield lines are the first ones to occur. According to the Bond Model, due to the extensive yielding of bars in the vicinity of the column, the shear capacity of the connection declines. An important issue is to observe whether the interior connection is ductile enough to maintain its shear capacity while moments are redistributed (i.e. until all positive yield lines form).

In an edge panel with at least three spans, the negative moment at the interior connection is frequently taken to be 70 percent of the panel moment. The magnitude of the negative moment at the interior column might be even 25 percent more than this value,

if there are only two spans (Mulenga and Simmonds, 1993). However, in the N-S direction, the interior connection is designed for only 65 percent of the panel moment, M_{ox} . This demands an extremely high ductility at the interior plate-column connection.

As described in Section 3.1, the negative design moments at the north and the south edge columns were selected as 10 and 30 percent of the panel moment, M_{ox} , respectively. To satisfy equation of equilibrium, the positive moments at north and south panels should be about 68.5 and 56.6 percent of the panel moment, respectively. The effect of jack loads being concentrated loads rather than uniformly distributed loads has been accounted for. Actual moment capacity provided was determined by the selection of reinforcement as described later and are shown in Figure 3.4.

3.3.2.2 Minimum Reinforcement and Integrity Steel

Minimum flexural reinforcement is established by one of two criteria. First, steel area of $0.002 A_g$ is required to satisfy minimum requirements in A23.3 for shrinkage and temperature reinforcement. For a 152 mm slab, this corresponds to 304 mm^2 of reinforcement per meter width of the slab.

Second, the maximum allowable spacing of reinforcing bars given by A23.3-M84 is twice the thickness of the plate or 305 mm. Placing 10M bars ($A_b = 100 \text{ mm}^2$) at the maximum spacing provides reinforcement of $328 \text{ mm}^2 / \text{m}$, which is greater than that obtained from shrinkage and temperature considerations. Therefore, the maximum spacing of bottom steel will be 305 mm (12"). Note that A23.3-94 allows a maximum spacing of three times the plate thickness for bottom bars.

To satisfy provisions for the integrity steel in the direction with two spans, two 15M reinforcing bars are provided. These bars pass through interior column and have standard end hooks at the edge columns. In the transverse direction, two 15M and two 10M reinforcing bars pass through the interior column and each edge column, respectively.

As shown in Figure 3.3, the positive moment in the E-W direction ($0.4 M_{oy}$) is the smallest positive design moment of the plate. Hence, the minimum reinforcement is placed in this direction. Area of the bottom reinforcement, including the integrity steel, is presented in Figure 3.4.

3.3.2.3 Position of Reinforcement in Cross-Section of the Plate

As shown in Figure 3.5, top and bottom reinforcing bars running in the N-S direction were placed in outer layers to give the maximum effective depth in this direction. The decision was based on two factors. First, as shown in Figure 3.3, the positive moments in this direction were higher. Second, at the edge connections, a smaller number of top reinforcing bars running perpendicular to the free edge is desired as these bars must be fully anchored. A minimum clear cover of 20 mm is used for both top and bottom steel.

3.3.2.4 Service and Factored Loads

The factored load is calculated under the assumption that all bottom reinforcement will yield at ultimate. The corresponding flexural resistance, M_{ry}^+ , is calculated using Equation 3.1.

$$M_r = \Phi_s \times A_s \times f_y \times d - \left(\frac{\Phi_s \times A_s \times f_y}{1.7 \times \Phi_c \times f'_c \times b} \right) \quad [3.1]$$

For $d = 110$ mm, $f_y = 400$ MPa, $f'_c = 30$ MPa, $\phi_s = 0.85$, and $\phi_c = 0.6$, M_{ry}^+ becomes equal to 71.8 kNm for each panel. The corresponding factored moment is as following:

$$M_f^+ = 0.4 M_{oy} = 0.4 \times 0.125 \times q_f \times l_x \times l_{ny}^2 = 5.107 \times q_f$$

where $l_x = 4877$ mm and $l_{ny} = 4575$ mm. Equating M_{ry}^+ and M_f^+ , the value of factored distributed load, q_f , equals 14.0 kN/m².

The service load is estimated to be 10.1 kPa, which corresponds to 3.6, 1.0, and 5.5 kPa for the self-weight, superimposed dead load, and live load, respectively. Dead and live load factors are, respectively, 1.25 and 1.5 in the Canadian Standards.

3.3.2.5 Area and Detailing of Reinforcement

For the factored load of 14.0 kN/m², the span moments required to satisfy the flexural equilibrium are determined;

$$M_{ox} = 0.125 \times q_f \times l_{nx}^2 \times l_y = 180.7 \quad kNm$$

$$M_{oy} = 0.125 \times q_f \times l_{ny}^2 \times l_x = 178.7 \quad kNm$$

Where $l_x = l_y = 4877$ mm, $l_{nx} = 4600$ mm, and $l_{ny} = 4575$ mm. The area of reinforcement was based on the share of the panel moment assigned to the different critical sections. A summary of the steel areas provided and the corresponding share of panel moments at different critical sections of the plate is shown in Figure 3.4. Details of the reinforcement are presented in Figures 3.5 through 3.11.

A23.3-M84 requires a fraction of the unbalanced moment to be transferred by flexure over an effective slab width of $c_2 + 3h$, where A23.3-94 requires that all the reinforcing steel be placed within this width. For both edge connections, the reinforcement was placed within this defined width.

To facilitate construction, a few straight bars perpendicular to the free edge were added to the top mat of the edge connections outside the region of $c_2 + 3h$. Since these bars were not hooked at the free edge, they could generate limited negative moment and were ignored in the calculations.

In an edge connection, top bars perpendicular to the free edge but not passing through the column must be adequately anchored to the column through a study of their mechanism (Alexander and Simmonds, 1987). To accomplish this, two 15M bars parallel to the free edge (anchorage bars) were added to the top mat of the south edge connection (Figure 3.7).

Top bars at the interior and the south edge connections are labeled as shown in Figures 3.18 and 3.19, respectively. Each label is given as a fraction, with the numerator equal to the number of the bar counted from the center line of the column, and the

denominator equal to one-half of the total number of the bars in that direction (e.g. at the interior connection, 8 bars running N-S and 9 bars running E-W).

3.3.3 Assessing the Specimen for Shear

3.3.3.1 Factored Shear at the Connections

For a load of 14 kN/m², the total load on each span, W , equals $q_x \times l_x \times l_y = 333.4$ kN. Because of unequal negative moments at edge and interior connections, the reaction at the edge columns is less than $W/2$, while the load transferred from each panel to the interior column is more than $W/2$. The change in column reaction, ΔV , due to unequal negative moments is calculated as follows:

$$\Delta V_{f1} = \frac{(0.64 - 0.12) M_{ox}}{l_{nx}} = 20.4 \text{ kN} \quad (\text{North Panel})$$

$$\Delta V_{f1} = \frac{(0.64 - 0.30) M_{ox}}{l_{nx}} = 13.7 \text{ kN} \quad (\text{South Panel})$$

The factored shears at north edge connection, V_{f1} , at interior connection, V_{f2} , and at south edge connection, V_{f3} , are as followings:

$$V_{f1} = W/2 - \Delta V_{f1} = 146.3 \text{ kN} \quad (\text{North Edge Connection})$$

$$V_{f2} = W + \Delta V_{f1} + \Delta V_{f2} = 367.1 \text{ kN} \quad (\text{Interior Connection})$$

$$V_{f3} = W/2 - \Delta V_{f3} = 153.4 \text{ kN} \quad (\text{South Edge Connection})$$

3.3.3.2 Shear Calculation According to the Canadian Standard

In a flat plate-column connection with no shear reinforcement the factored shear stress at the critical section must be smaller than the allowable shear resistance of concrete, v_c , given by Equation 3.2. For $\phi_c = 0.6$, and $f'_c = 30$ MPa, the factored shear resistance is 1.31 MPa.

$$v_c = \Phi_c \times 0.4 \times \sqrt{f'_c} \quad [3.2]$$

In the interior connection, the average shear stress at the critical section defined by the standard (at a distance of $d/2$ from column) is calculated as follows:

$$v_{f2} = \frac{V_{f2}}{p \times d_{avg}} \quad [3.3]$$

Where $d_{avg} = 116$ mm and $P = 2(c_1 + c_2 + 2d) = 1684$ mm. The average calculated shearing stress is 1.88 MPa, approximately 43 percent more than the allowable shear specified in A23.3.

Substituting $p = 1047$ mm, $d_{\text{avg}} = 116$ mm, $\gamma_v = 0.365$, $c = 93.6$ mm, and $J = 1.389$ (10^9) mm⁴ into Equation 2.13 gives the factored shear stress for either edge connections.

$$v_f = \frac{V_f}{121.0} + \frac{M_f}{40.66} \quad [3.4]$$

Where V_f and M_f are in kN and kNm, respectively. At the north edge connection, $V_{f_n} = 146$ kN and $M_{f_n} = 21.68$ kNm. The factored shearing stress, v_{f_n} , becomes 1.74 MPa, about 33 percent more than the factored shearing resistance of concrete.

At the south edge connection, $V_{f_s} = 153$ kN and $M_{f_s} = 54.2$ kNm. The factored shear stress, v_{f_s} , is 2.60 MPa, about twice the factored resistance of concrete.

3.3.3.3 Shear Capacity According to the Bond Model

According to the Bond Model, the shear capacity of a flat plate-column connection is assumed to be equal to the sum of the shear capacity of the radial strips attached to the column. The shear capacity of each radial strip is a function of its flexural capacity, M_s , and the ability of the slab to transfer one way shear, w , and is calculated from Equations 2.5, 2.7, and 2.86. Shear calculations according to the Bond Model are summarized in Table 3.1.

The factored shear resistance of the north and south edge connections are 185 kN and 198 kN respectively, which are greater than the calculated factored shears ($V_{f_n} = 146$ kN and $V_{f_s} = 153$ kN). The factored shear resistance of interior connection is 352 kN which is slightly less than the factored shear $V_{f_i} = 367$ kN.

3.3.4 Other Detailing

The loading system required a total of 12 holes in the test specimen as shown in Figure 3.2. A row of four 90 mm diameter holes along the center line of the columns allowed long rods to pass through the slab. The function of these rods is explained in Section 3.4.3. No additional reinforcement was required around these holes.

The remaining eight holes had a diameter of 75 mm, and were located in two rows 1220 mm on either side of the center line of the specimen. These holes accommodated load rods that were used to support the slab after punching of its connections. Two 15M reinforcing bars per hole were placed in the top layer and in each direction to provide the required negative moment resistance.

Figure 3.14 shows the details of the rotational restraint provided to the continuous edge. Reinforcing bars of the bottom mat aligned in the E-W direction were extended 400 mm (16") beyond the concrete edge of the specimen so that the edge restraining system could be mounted. To prevent crushing of concrete, 45 by 30 mm angles anchored with #3 US bars were embedded at concrete along the continuous edges. To avoid acting as reinforcement in negative moment region, these angles were discontinuous in the middle of the plate. Also, to avoid stiffening the slab, the vertical legs of the angles were cut in 1 m intervals.

3.4 Test Apparatus

3.4.1 Supports

The lower end of the columns, representing mid-height of the columns of the prototype were designed to act as hinges. This was accomplished by a series of knife edges, load cells, and rollers as illustrated in Figure 3.12. These rollers were used so that horizontal load cells would measure the full horizontal reaction of the columns.

While horizontal compressive load cells were used in the lower end of all three columns, horizontal tensile load cells were used in the top ends of the two edge columns. To minimize the second order effects in the measurement of the vertical loads, the compression load cells at the base had spherical heads, and each tensile load cell was connected to its concrete column and to the steel frame by a relatively long pin-end member.

Lateral stability was provided by bracing the lower half of the edge columns with a Watts mechanism located at 550 mm below the mid-height of the slab.

3.4.2 Edge Restraining System

3.4.2.1 Design Considerations

The continuous edge of the specimen, representing mid-span of the prototype, must be rotationally restrained, ideally to provide the angle of rotation of zero. The edge restraint system was designed so that its capacity would be at least 1.5 times the bending capacity of the continuous edge.

The edge restraint system consisted of two main parts; extension arms and transverse ties. These are shown in Figures 3.13 and 3.14. This restraint system will work for any combination of loads where the positive moments along opposite restrained edges are equal.

So that the specimen would not be flexurally stiffened by the edge restraining system in the direction parallel to the continuous edge, extension arms were connected to the transverse ties by relatively long threaded rods.

3.4.2.2 Extension Arms

Extension arms consisted of C 150 x 12 sections mounted on either a pair of 10M bars or on one 15M integrity bar as shown in Figure 3.14. An angle (L 125 x 125 x 8) was welded to the channel to work as the compressive support. A hollow section (HSS 102 x 51 x 4.8) was used to transfer the tensile force in the reinforcing bars to the channel. Reinforcing bars were passed through holes in the hollow section and were welded to a plate bearing on the hollow section. Tests on the weld detail were conducted to ensure that the reinforcing bar could reach its ultimate strength before weld failure.

To transfer the weight of the extension arm directly to the slab, the angle was spot welded to an embedded angle (L 35 x 30 x 4) at the edge of the specimen. The extension arms were connected by transverse ties to the corresponding ones along the opposite edge at a level of 810 mm (32") above the top surface of the slab.

3.4.2.3 Transverse Ties

Transverse ties included tensile load cells to measure the force in the ties to determine the positive moment along the continuous edges, and a method for adjusting the force in the ties to maintain zero rotation along the continuous edges. The corresponding positive moment could be calculated from the measured force.

Each transverse tie consisted of a round hollow section (HSS 48 x 2.8) in series with a load cell and a 560 x 50 x 6.3 plate, illustrated schematically in Figure 3.13. The ties connected opposing groups of two or three extension arms, linked together by HSS 127 x 51 x 4.8 sections as shown in Figure 3.13. Wooden chairs supported the self-weight of the ties. Forces in the ties could be controlled by adjusting threaded rods that connected the extension arms to the HSS 127 x 51 x 4.8 sections.

3.4.3 Loading System

Figure 3.16 shows a schematic plan of the loading system. Load was applied by means of four 900 kN actuators each in series with a compressive load cell supported by a steel frame, as shown in Figure 3.17. Each jack applied load to a distributing beam (member A in Figure 3.16). The distributing beam could be tied to the strong floor by means of long threaded rods, permitting repair or adjustment of a jack while maintaining the same level of deflections of the specimen. The compression load cells were prestressed with a force of 50 kN so that a tensile load up to 50 kN could also be measured.

A statically determinate system was used to distribute the load of each jack equally to eight load points. Figure 3.15 shows the details of the connections, and Figure 3.16 shows the position of the load points. Since all connections are hinged, the load distributing system can adapt to differential displacements in the slab over the loaded area. For any vertical displacements, the horizontal distance between the points on the slab will change. Rubber pads and ball bearings were used at the load points to allow for this relatively small horizontal movement of the plate between the load points.

3.5 Instrumentation

3.5.1 Strain Measurements

Figures 3.18 to 3.21 show the layout of the strain gauges. Gauges placed on the top bars at the interior and the south edge connections are labeled in Figures 3.18 and 3.19. One hundred and sixteen electrical resistance foil strain gauges with a nominal resistance of 120 ohms and a gauge length of 5 mm were used. At each gauge location, the deformations of the reinforcement were ground smooth. Grinding was restricted to the smallest area that would permit placement of the gauge. All gauges on the top mat were attached with an epoxy adhesive prior to tying the reinforcement and placing it in the forms. Gauges on the bottom mat, however, were installed after tying the bottom steel in the form. This avoided damage the strain gauges while handling the long bottom bars. M-Bond 200, a fast hardening glue containing methyl-2-cyanoacrylate, was used for these gauges.

After soldering of lead wires, all gauges were covered with a layer of flowable silicon to provide electrical insulation. This was followed by a thick patch of conventional silicon sealant being confined to the immediate area of the gauge in order to lessen the effect on the steel-concrete bond.

3.5.2 Load Measurements

All vertical loads and reactions were measured, thereby allowing an overall equilibrium check. A total of seven load cells were used for vertical loads. Five more load cells were used to measure horizontal reactions of the columns. In addition to the above commercial load cells, eight load cells were fabricated for use in the transverse ties of the edge restraining system. These fabricated load cells each consisted of a full bridge arrangement of strain gauges installed on coupon shaped steel plate.

3.5.3 Deflection Measurements

Twenty-six vertical and sixteen horizontal Linear Variable Differential Transformers (LVDTs) were used to measure the deformations of the specimen. Figure 3.22 illustrates the location of these LVDTs.

Vertical LVDTs were used to measure the deflection of the slab. These LVDTs were placed on the laboratory floor. Wires were strung to the bottom surface of the plate.

Horizontal LVDTs were used to monitor the rotation and the overall expansion of the plate. These LVDTs were mounted on eight wooden extension arms hanging down from the west edge of the plate and were located at two levels; 152 and 456 mm from the bottom surface of the plate. Wires were strung across to the corresponding positions on the extension arms of the east edge of the plate.

All LVDTs were installed after stripping the bottom forms and the removal of the scaffolding. Therefore, they measured only the deformations due to jack loads. The rotation at the continuous edges and the overall expansion of the plate under the self-weight and the superimposed dead loads were not measured. However, the vertical deflections of the plate under the dead loads were determined by surveying 57 points on the slab. These points were different from LVDT points because of the interference of the bench marks with the location of the loading system. Results of the survey were interpolated to establish the initial deflections at the location of the LVDTs.

3.5.4 Recording and Monitoring Data and Loads

Two Fluke 2400B data acquisition units, each connected to a personal computer, were used to record the readings of strain gauges, load cells, and LVDTs. A third computer was used to monitor the jack loads graphically. Jack loads were also monitored by four separate gauges responding to the oil pressure.

3.6 Fabrication Procedure

The bottom portions of the columns were cast up to the level of the plate soffit. These were then placed on top of the supports, and were braced against steel columns connected to the strong floor. The slab formwork was erected and supported by scaffolding, which consisted of steel frames with adjustable legs and heads, aluminum joists, and aluminum beams. Forming plywood was used for both side and bottom forms. Holes were drilled in bottom form to pass the strain gauge wires through, and in the side forms to let the bars pass through.

A professional crew was hired to place and finish the concrete for the slab to ensure uniformity of the slab thickness. Extra care was taken to make sure that the top and bottom mats were tightly fixed in position and that the strain gauges were well protected

prior to concreting. After finishing, the test specimen was sprayed with a curing compound.

The upper portion of the columns were cast, the load distributing beams were assembled and placed on top of the slab, the edge restraining system was installed, and horizontal column supports were assembled.

Just prior to the removal of the scaffolds, the load cells and strain gauges were connected to the data acquisition system. An initial set of readings was taken to establish reference zero values for strain and load. At this point, the entire test specimen rested solely on the scaffolds, and the three columns were not bearing on their supports. Using a level, a survey of the slab established the undeflected shape. The strain gauges were then disconnected and the form was stripped.

Forms were removed at 28 days from casting. After stripping, the strain gauges were reconnected to the data acquisition system and a set of readings was taken. A second survey of the slab established dead load deflections.

The steel loading frame was built over the specimen. Jacks and related load cells were installed and the hydraulic system was connected. The LVDTs were positioned and connected to the data acquisition system. A third survey of the slab established reference deflections for the LVDTs.

3.7 Ancillary tests

3.7.1 Reinforcement

The plate was reinforced with 10M and 15M deformed reinforcing bars with nominal area of 100 and 200 mm², respectively. All steel was cut and bent from 12 m long bars of one heat so that the material properties for all bars of the same size were the same. Tension tests were performed on two sample coupons for each size. As presented in Table 3.2, on the basis of nominal area, 10M and 15M bars had static yield stress of 423 and 426 MPa and ultimate strength of 614 and 624 MPa, respectively. For convenience, a yield stress of 420 MPa will be used. The modulus of elasticity was 194000 MPa for 10M and 187500 MPa for 15M bars. Typical load-strain plot of the coupon tests is shown in Figure 3.23.

Columns were reinforced with 20M reinforcing bars with nominal area of 300 mm² and the nominal yield stress of 400 MPa. Stirrups were made from #3 US deformed bar with nominal area of 70 mm². No testing was required on column reinforcement.

3.7.2 Concrete

Normal density concrete with a specified slump of 70 mm and a specified design strength, f'_c , of 30 MPa was obtained from a local supplier. Results of the compression and split cylinder tests at different ages of the concrete are shown in Table 3.3. Cylinders were nominally 150 mm in diameter and 300 mm in length.

Concrete for the columns was mixed at the laboratory and had a nominal 28 day compressive strength of 30 MPa.

3.7.3 Tests on Reinforced Concrete

To predict the bending moments at different cross sections of the plate based on the strain gauge readings, four narrow beams with the same concrete thickness and reinforcement ratio as the test specimen were tested with the load configuration shown in Figure 3.24. Details of the arrangement of the steel in each beam are also illustrated in this figure.

For each beam, two strain gauges were mounted on each bottom reinforcement. These gauges were located at two cross sections in the constant moment region. Transverse bars were placed at these sections as crack initiators.

All beams were tested at 56 or 57 days from casting, before the start of the main test. Moment-strain diagrams for these beams are illustrated in Figures 3.25 to 3.28. The moment-strain relationship for each beam is modeled with a bilinear or trilinear curve.

For each beam, the yield moment was calculated based on the yield strain determined in the tension tests on the reinforcing bars, and is plotted on the moment-strain diagram. These points are in close agreement with the beam test results, except in the case of beam 3, the shortest and the widest of all, which shows much higher yield moment than the predicted value. The second relationship in Equation 3.7 is revised in accordance with the calculated yield moment.

Beam 1 (2M15, s = 150 mm, outer layer): [3.5]

$$\text{strain} < 2154 \quad M = 0.00936 \times (\text{strain}) \quad (\text{kNm})$$

$$\text{strain} > 2154 \quad M = 0.00046 \times (\text{strain}) + 19.17 < 25.49$$

Beam 2 (2M15, s = 150 mm, inner layer): [3.6]

$$\text{strain} < 1998 \quad M = 0.00883 \times (\text{strain}) \quad (\text{kNm})$$

$$\text{strain} > 1998 \quad M = 0.00053 \times (\text{strain}) + 16.59 < 22.73$$

Beam 3 (2M15, s = 200 mm, outer layer): [3.7]

$$\text{strain} < 1933 \quad M = 0.01043 \times (\text{strain}) \quad (\text{kNm})$$

$$1993 < \text{strain} < 4838 \quad M = 19.6 \quad (\text{kNm})$$

$$\text{strain} > 4838 \quad M = 0.00053 \times (\text{strain}) + 17.04 < 26.65$$

Beam 4 (2M15, s = 100 mm, outer layer): [3.8]

$$\text{strain} < 2045 \quad M = 0.00885 \times (\text{strain}) \quad (\text{kNm})$$

$$2045 < \text{strain} < 8791 \quad M = 0.00044 \times (\text{strain}) + 17.19$$

$$8791 < \text{strain} < 15300 \quad M = -0.00021 \times (\text{strain}) + 22.9$$

3.8 Predicted Capacity of Specimen Based on Tested Material Properties

Based on the measured material properties and with resistance factors equal to one, the shear capacities calculated by the Bond Model and by ACI 318 are compared to the shears corresponding to the yield line mechanism loads.

3.8.1 Predicted Shear Capacity of Specimen Based on the Bond Model

The shear capacities of the connections of the specimen based on the Bond Model are summarized in Table 3.4. Because of 15M integrity steel, passing through the columns, the bottom mesh of reinforcement was not uniform. Determination of M_s^+ , hence, requires an appropriate estimate of the average spacing of the reinforcement involved in the positive moment of the radial strips. The area of steel used in Table 3.4 is based on the average ratio of steel within the column width plus 1.5 h on each side of the column.

3.8.2 Predicted Yield Line Capacity of Specimen and Related Shear Forces

The yield line capacity of the specimen is calculated based on three independent flexural capacities: (a) of both panels in the y direction, $2M_{oy}$, (b) of the north panel in the x direction, M_{ox1} , and (c) of the south panel in the x direction, M_{ox2} . Table 3.5 summarizes these calculations. The predicted yield line load, q, is the smallest load calculated based on these three flexural capacities, 18.8 kPa. The corresponding shear at each connection is;

$$V_1 = 196.8 \text{ kN} \quad (\text{North Edge Connection})$$

$$V_2 = 492.2 \text{ kN} \quad (\text{Interior Connection})$$

$$V_3 = 206.5 \text{ kN} \quad (\text{South Edge Connection})$$

3.8.3 Predicted Shear Capacity by North American Standards

The shear capacity of the interior connection based on the ACI model is 384 kN. For the north edge connection, the shear and the moment at the yield line mechanism are equal to 196.8 kN and 29.5 kNm, respectively. Hence, the eccentricity, e, is equal to 0.15 m, and M in Equation 3.7 may be replaced with 0.15 V. This results in a shear capacity for north connection, V_1 , equal to 164 kN. Similarly, for the south connection $e = 73.9 / 206.5 = 0.358$ m, resulting in a shear capacity of 115 kN.

Table 3.1 Shear Calculations According to the Bond Model; $\phi_c = 0.6$, $\phi_s = 0.85$, $f'_c = 30$ MPa, and $f_y = 400$ MPa

Connection	Radial Strip	Width of Strip (mm)	Position of reinforcement	A_s^* (mm ²)	effective depth (mm)	Moment (kNm)	M_s (kNm)	w^{**} (N / mm)	P_s^{***} (kN)	Shear Capacity (kN)		
North	Spandrel	255	Top	400	108	12.3	19.2	67.0	50.7	185.1		
			Bottom	200	110	6.89						
	Interior	305	Top	300	122	11.5	29.5	59.3	83.7			
			Bottom	500	124	18						
Interior	North Panel N-S	305	Top	400	124	14.9	32.9	59.3	88.3	352.2		
			Bottom	500	124	18						
	E-W	305	Top	400	108	12.7	28.3	68.1	87.8			
			Bottom	500	110	15.6						
	South Panel N-S	305	Top	400	124	14.9	32.9	59.3	88.3			
			Bottom	500	124	18						
	South	Interior	305	Top	600	124	20.8	38.8	59.3		95.9	198.2
				Bottom	500	124	18					
Spandrel		255	Top	400	108	12.3	19.2	68.1	51.1			
			Bottom	200	110	6.89						

* Area of steel within the strip

** Includes ϕ_c

*** Equation 2.5 for interior radial strips and Equation 2.7 for spandrel strips.

Table 3.2 Properties of Reinforcing Bars

	Nominal Area	Yield Stress	Ultimate Strength	Modulus of Elasticity
Bar Size	mm ²	MPa	MPa	MPa
10M	100	423	614	194000
15M	200	426	624	187500

Table 3.3 Concrete Properties

Age (days):	7	14	21	28	56
Compressive strength (MPa)	f'_c 27.3	31.1	33.9	34.8	37.4
Tensile strength (MPa)	f'_t 2.25	-----	2.71	-----	2.65
Modulus of elasticity (MPa)	E_c -----	-----	24660	25440	27210

Table 3.4 Shear Calculations According to the Bond Model; $f'_c = 34.8$ MPa, $f_y = 420$ MPa

Connection	Radial Strip	Width of Strip (mm)	Position of reinforcement	Area of Steel (mm^2)	effective depth (mm)	Moment* (kNm)	M_s (kNm)	w^{**} (N/mm)	P_s^{***} (kN)	Shear Capacity (kN)
North	Spandrel	255	Top	286	108	12.02	19.8	119.5	68.8	256
			Bottom	176	110	7.77				
	Interior	305	Top	300	122	14.49	33.1	105.8	118.4	
			Bottom	386	124	18.65				
Interior	North Panel N-S	305	Top	400	124	19.27	37.9	105.8	126.7	
			Bottom	386	124	18.65				
	E-W	305	Top	400	108	16.58	29.3	121.4	119.3	
			Bottom	300	110	12.73				
South	South Panel N-S	305	Top	400	124	19.27	36.0	105.8	123.4	
			Bottom	343	124	16.71				
	Interior	305	Top	600	124	27.73	44.4	105.8	137.1	
			Bottom	343	124	16.71				
Spandrel	255	Top	286	108	12.02	19.8	121.4	69.3		
		Bottom	176	110	7.77					

* Resistance factors equal to 1.0

** Equation 2.8

*** Equation 2.5 for interior radial strips and Equation 2.7 for spandrel strips.

Table 3.5 Yield Line Capacities of the Specimen; $f'_c = 34.8$ MPa, $f_y = 420$ MPa

	Position of Reinforcement	Area of Steel (mm ²)	Width b (mm)	effective depth (mm)	Moment* (kNm)	Panel Moment (kNm)	Load q (kPa)
Both Panels y Direction	Top	7200	6249	108	301.9	2 M _{oy}	q _y
	Bottom	4000	10000	110	180	481.9	18.87
North Panel x Direction	North Connection	600	124	610	29.5	M _{ox1} 248.6	q _{x1} 19.26
	Mid-span	3200	122	4270	156.8		
	Interior Connection	3200	124	2438	154.1		
South Panel x Direction	Interior Connection	3200	124	2438	154.1	M _{ox2} 242.5	q _{x2} 18.78
	Mid-span	2600	122	4270	128.5		
	South Connection	1600	124	812	73.9		

* Resistance factors equal to 1.0

Table 3.6 Shear Capacity of the Specimen in kN; $f'_c = 34.8$ MPa, $f_y = 420$ MPa

	Yield line Mechanism q = 18.8 kPa	North American Standards	The Bond Model
North Connection	197	164	256
Interior Connection	492	384	489
South Connection	206.5	115	276

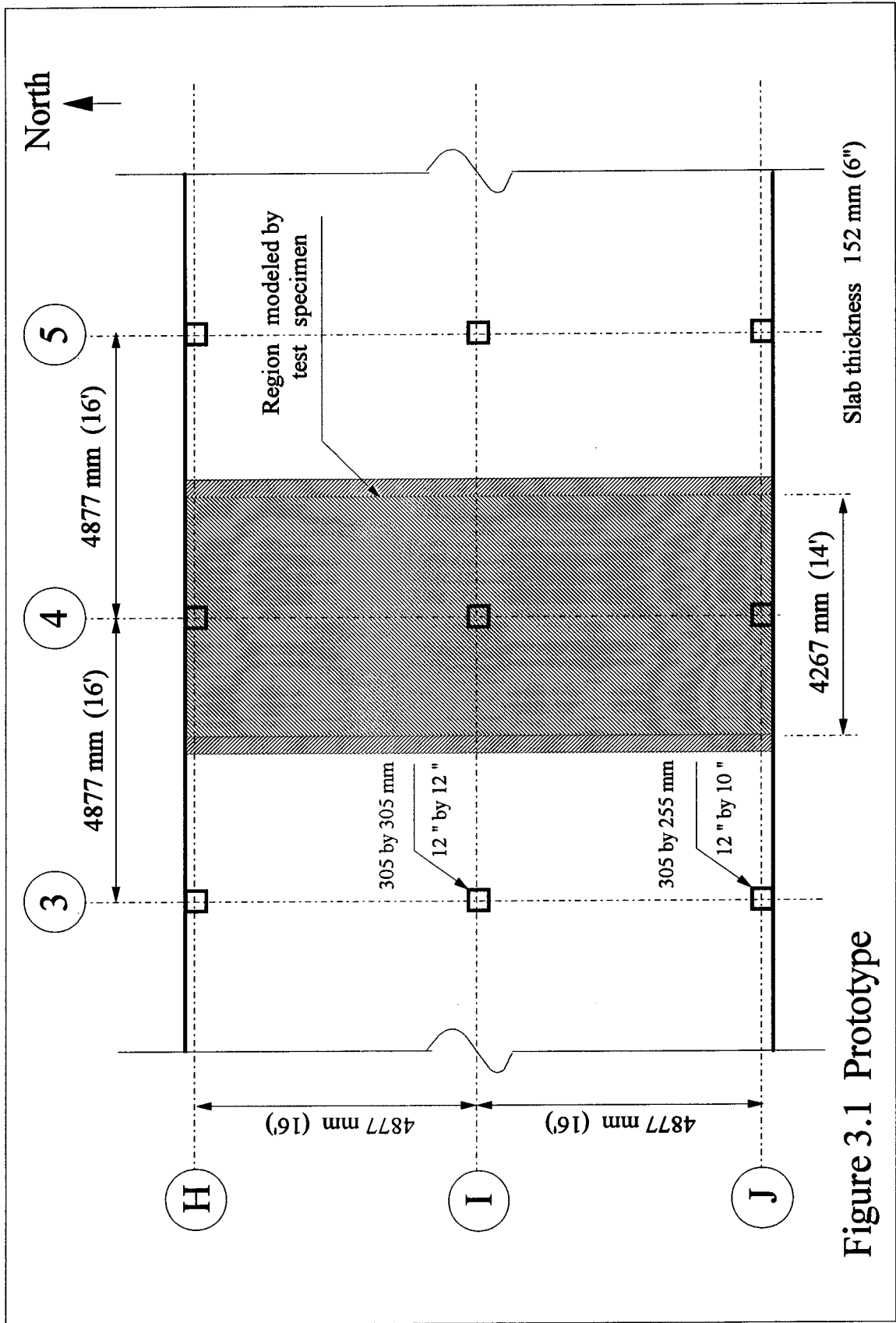


Figure 3.1 Prototype

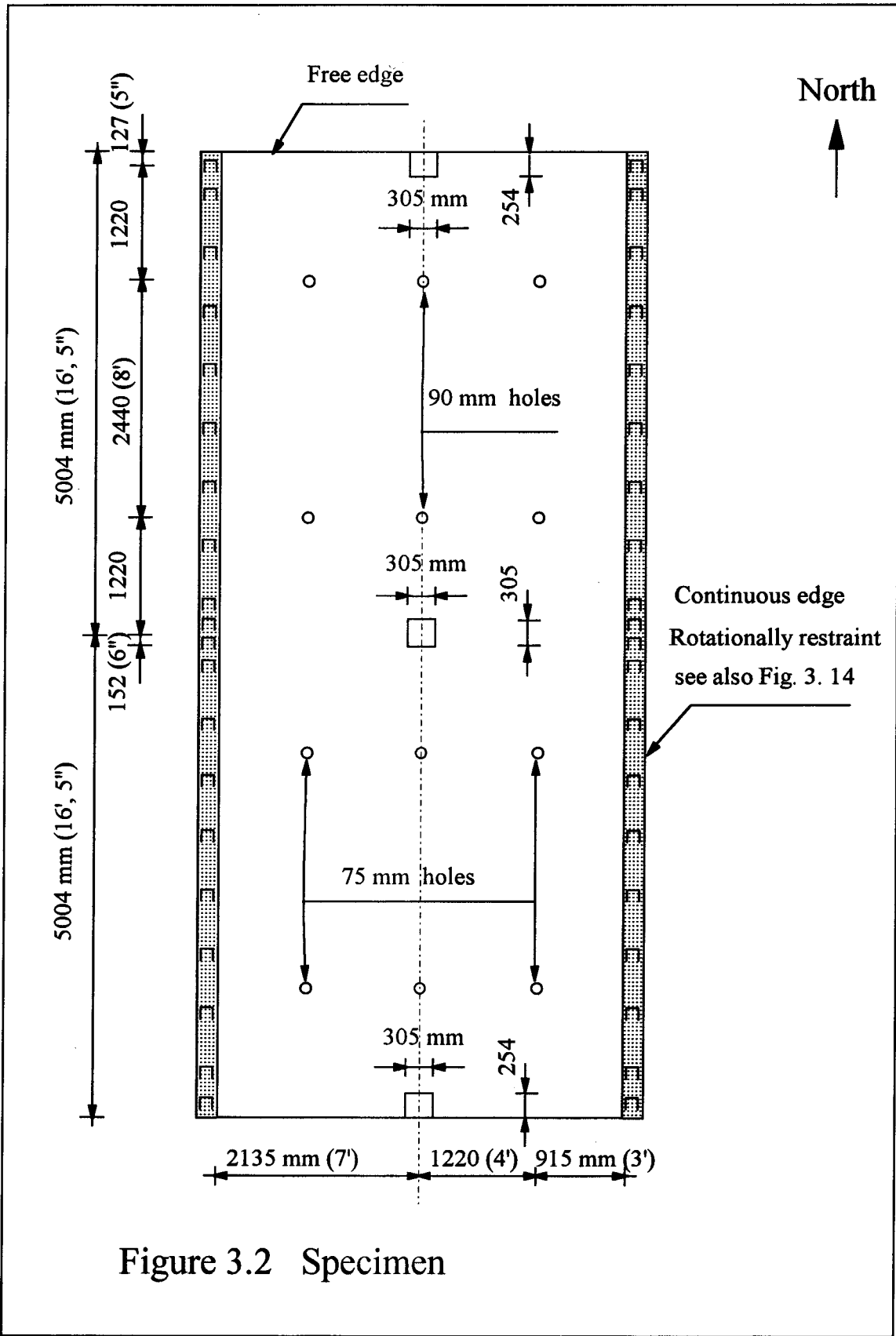


Figure 3.2 Specimen

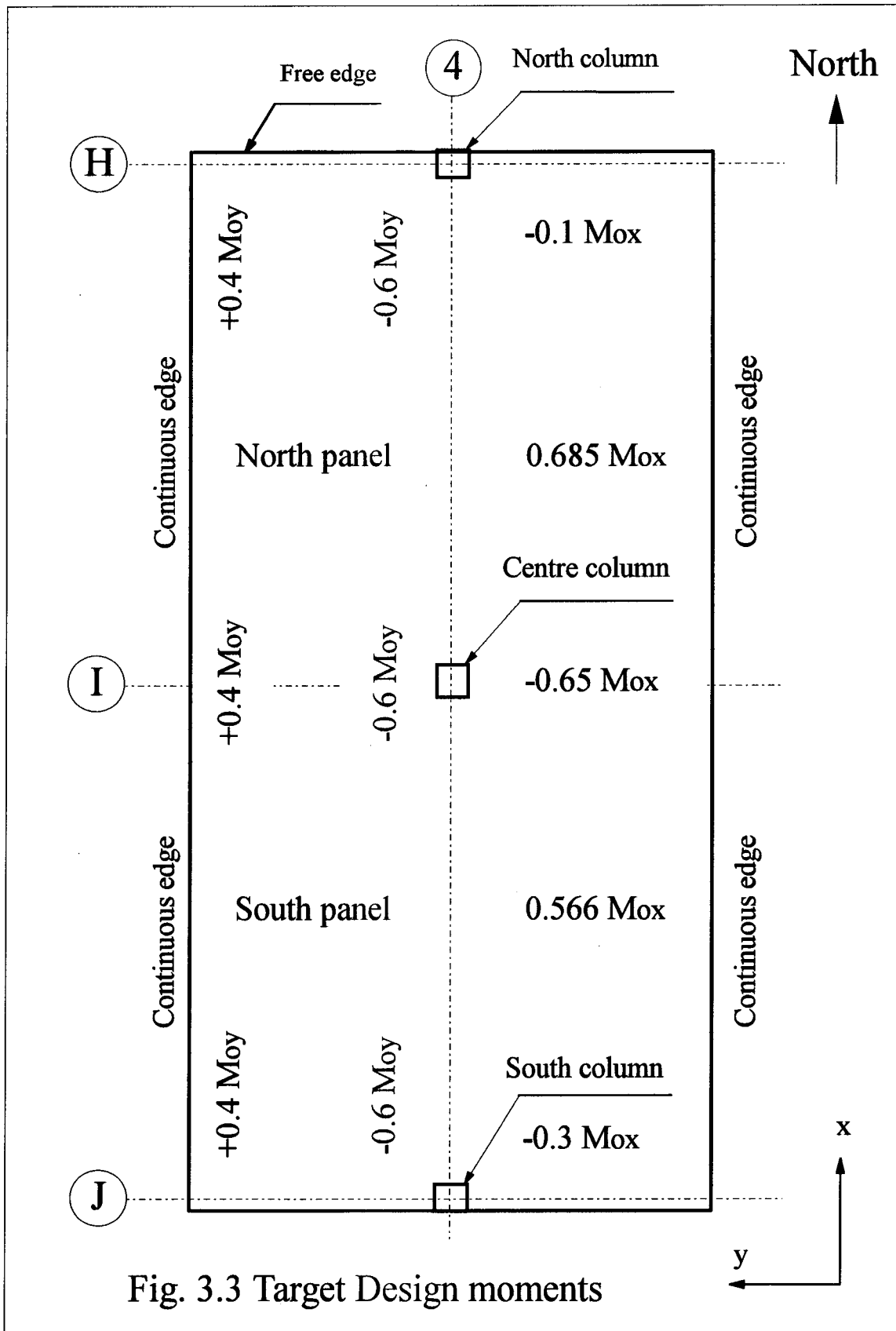


Fig. 3.3 Target Design moments

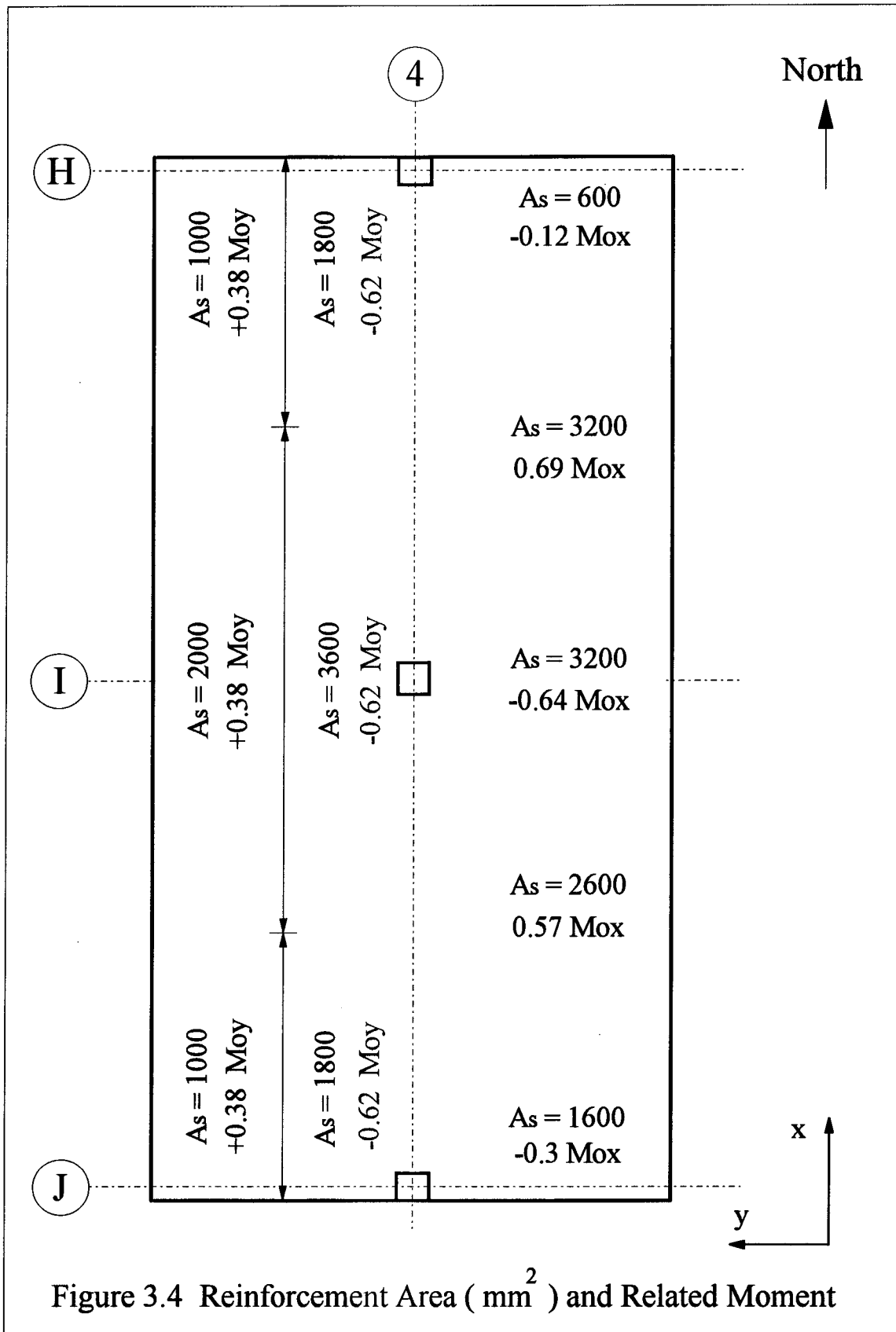


Figure 3.4 Reinforcement Area (mm^2) and Related Moment

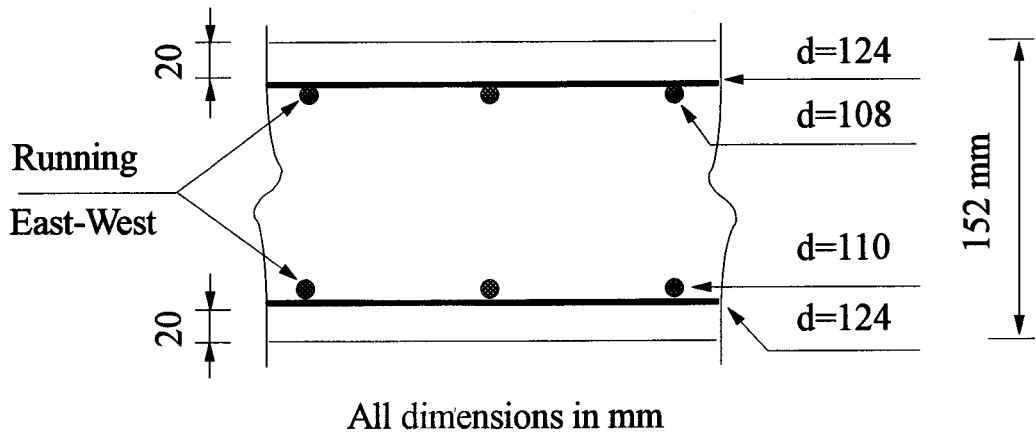


Figure 3.5 Cross section of slab

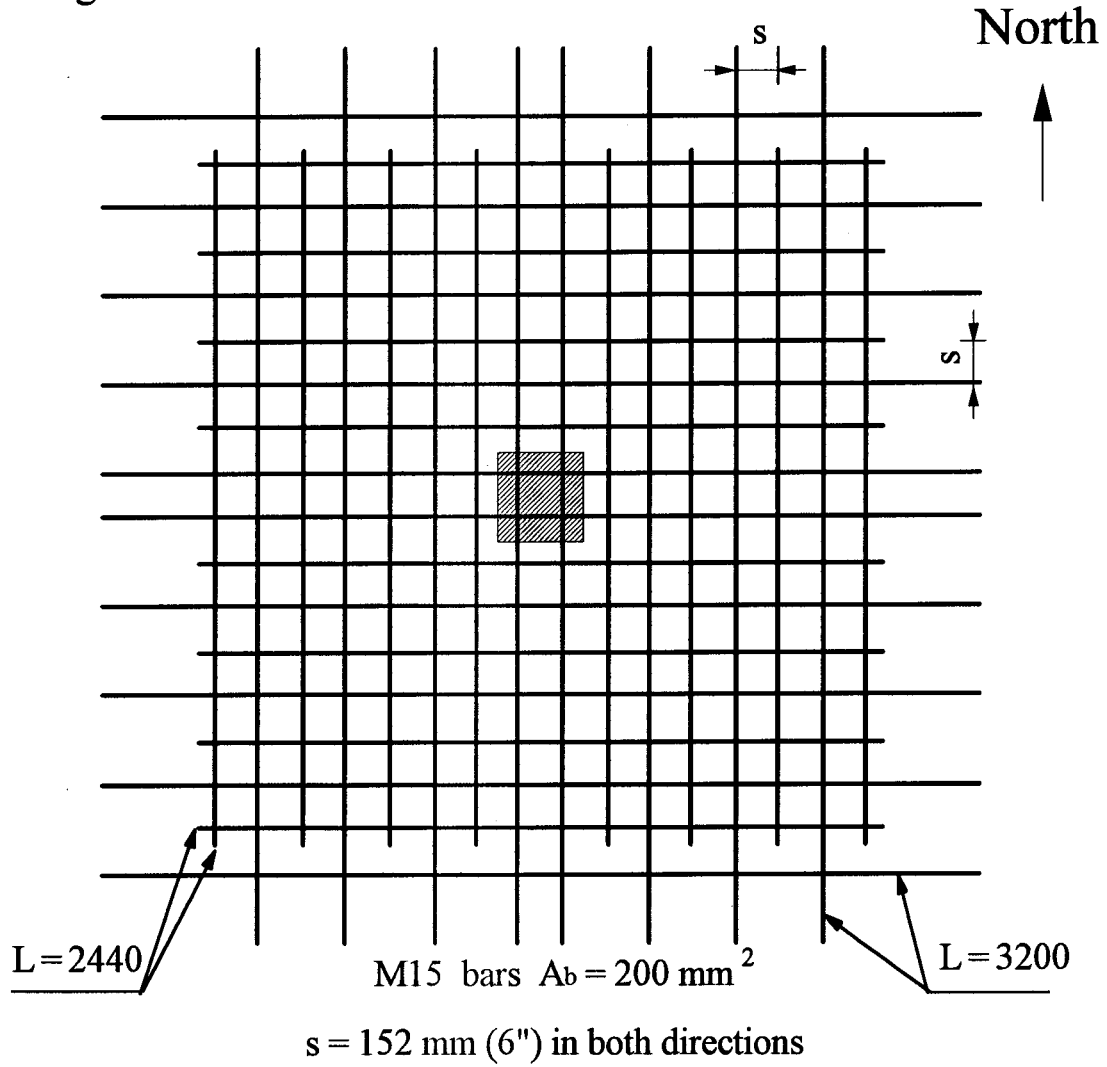
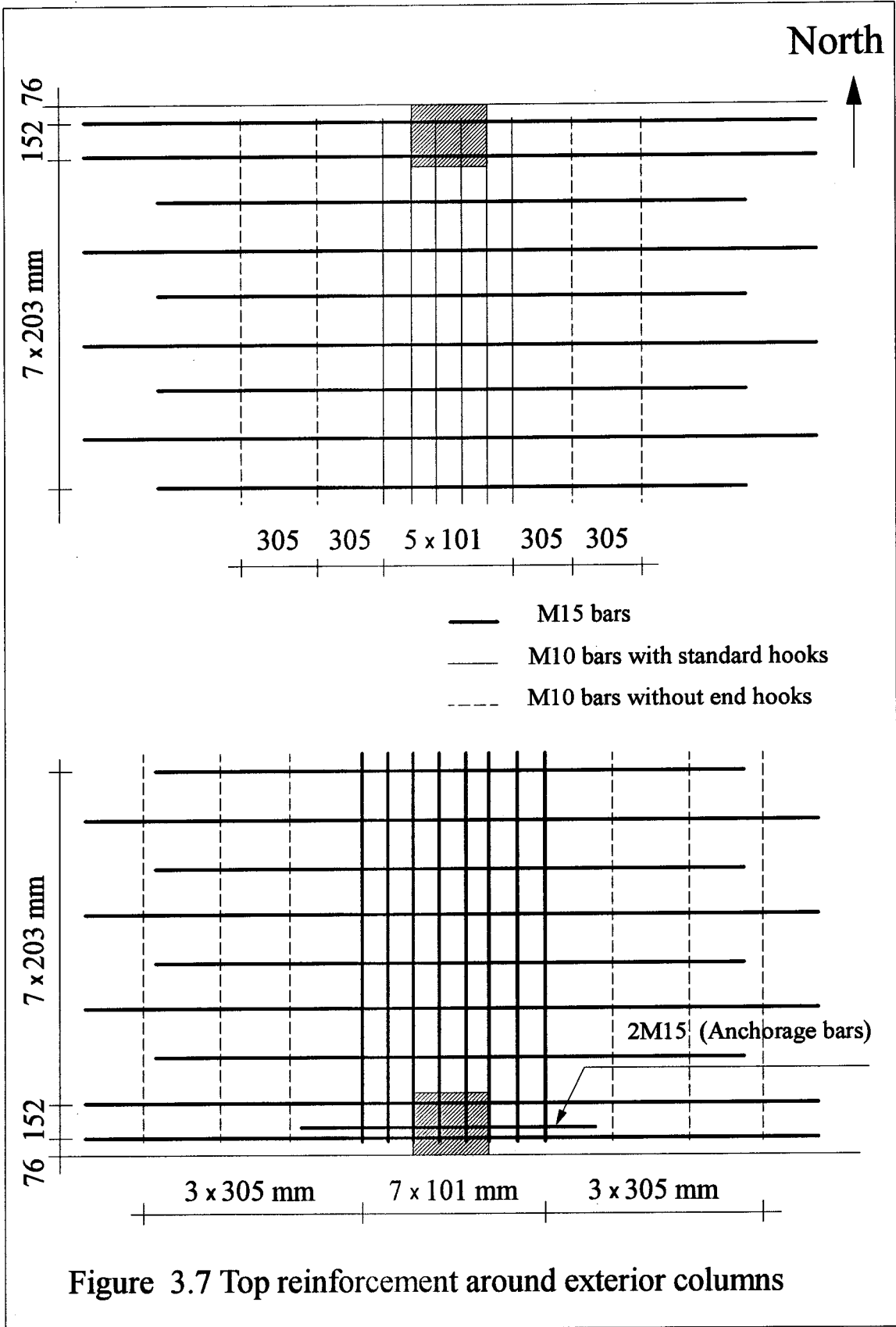
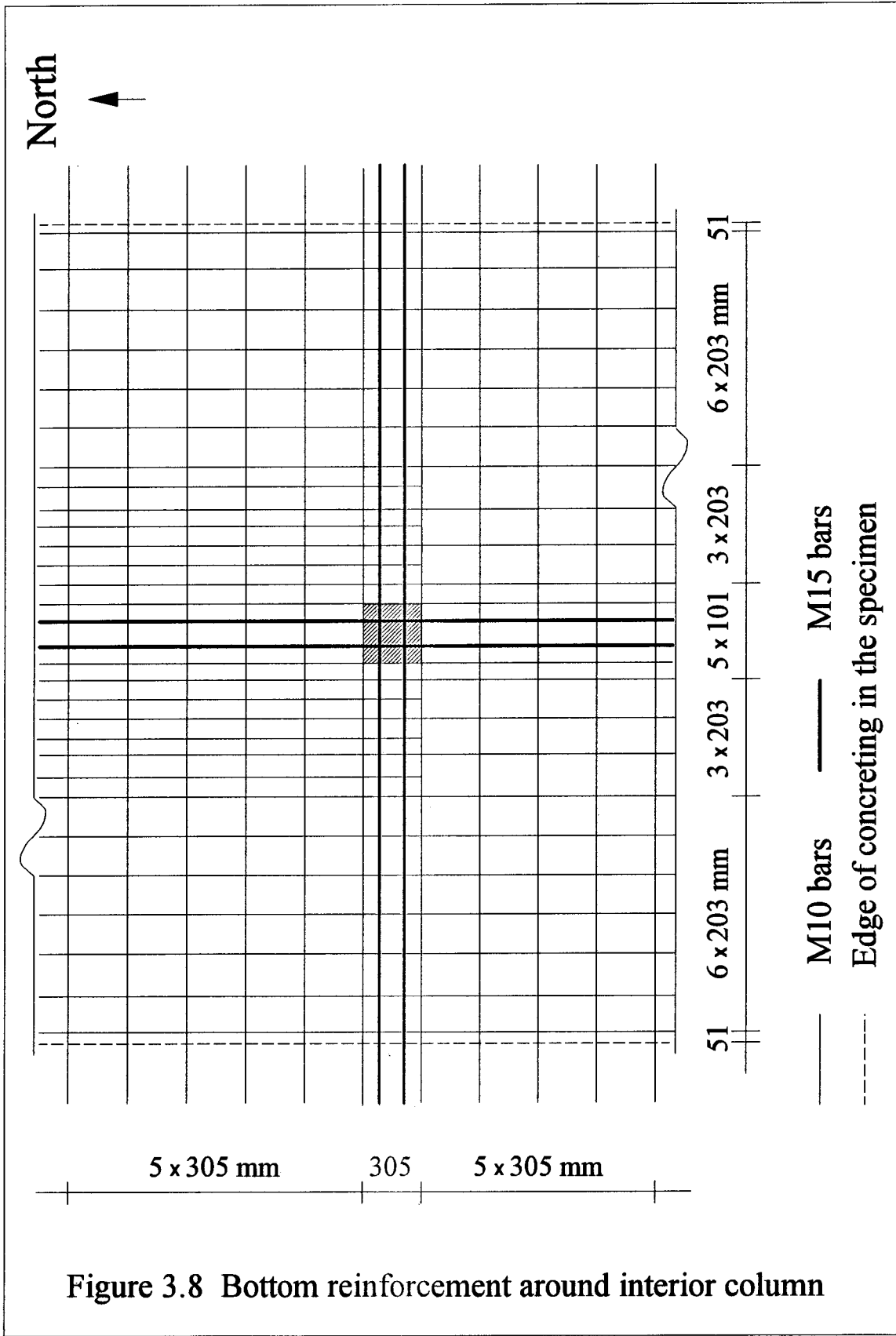


Figure 3.6 Top reinforcement around interior column





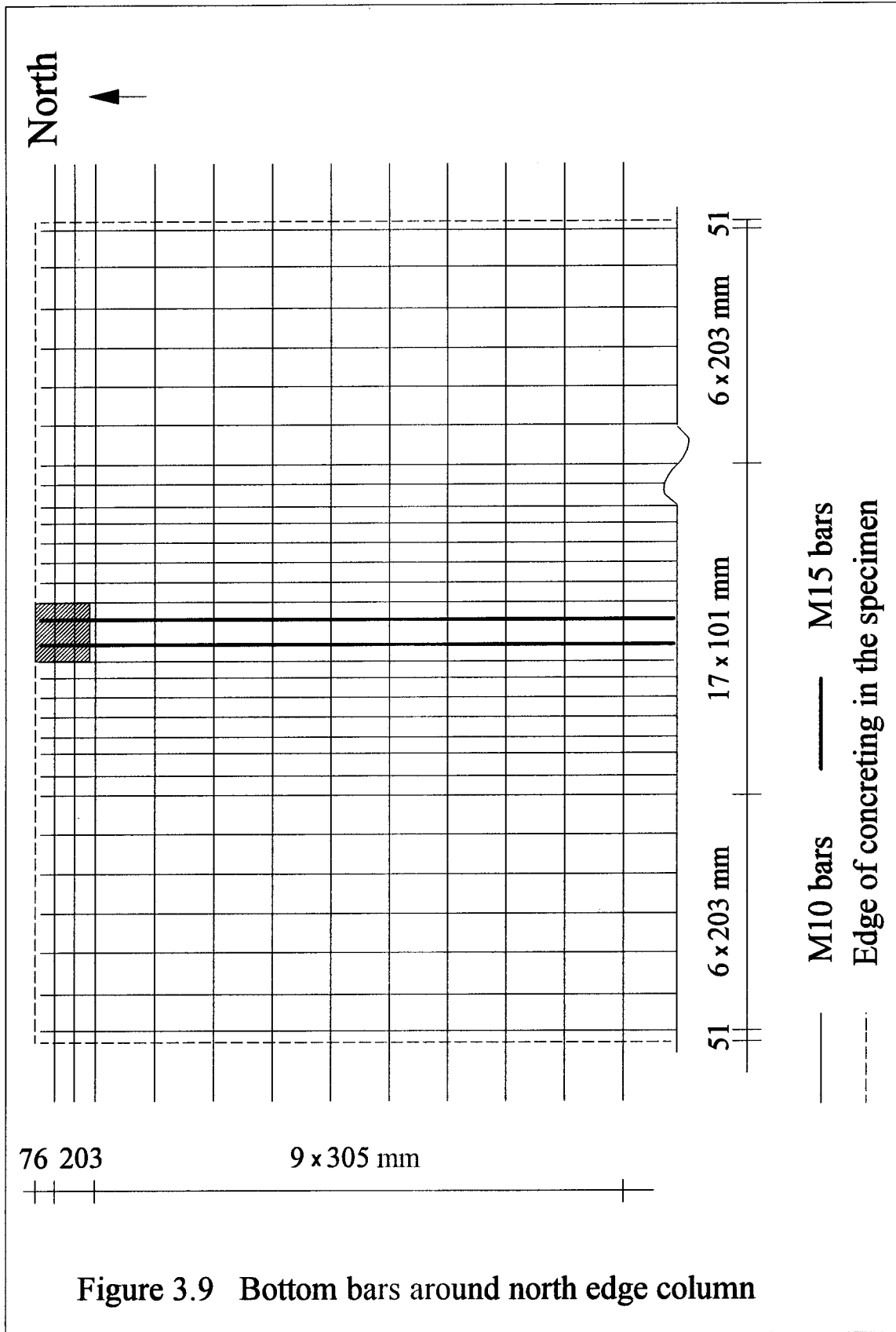


Figure 3.9 Bottom bars around north edge column

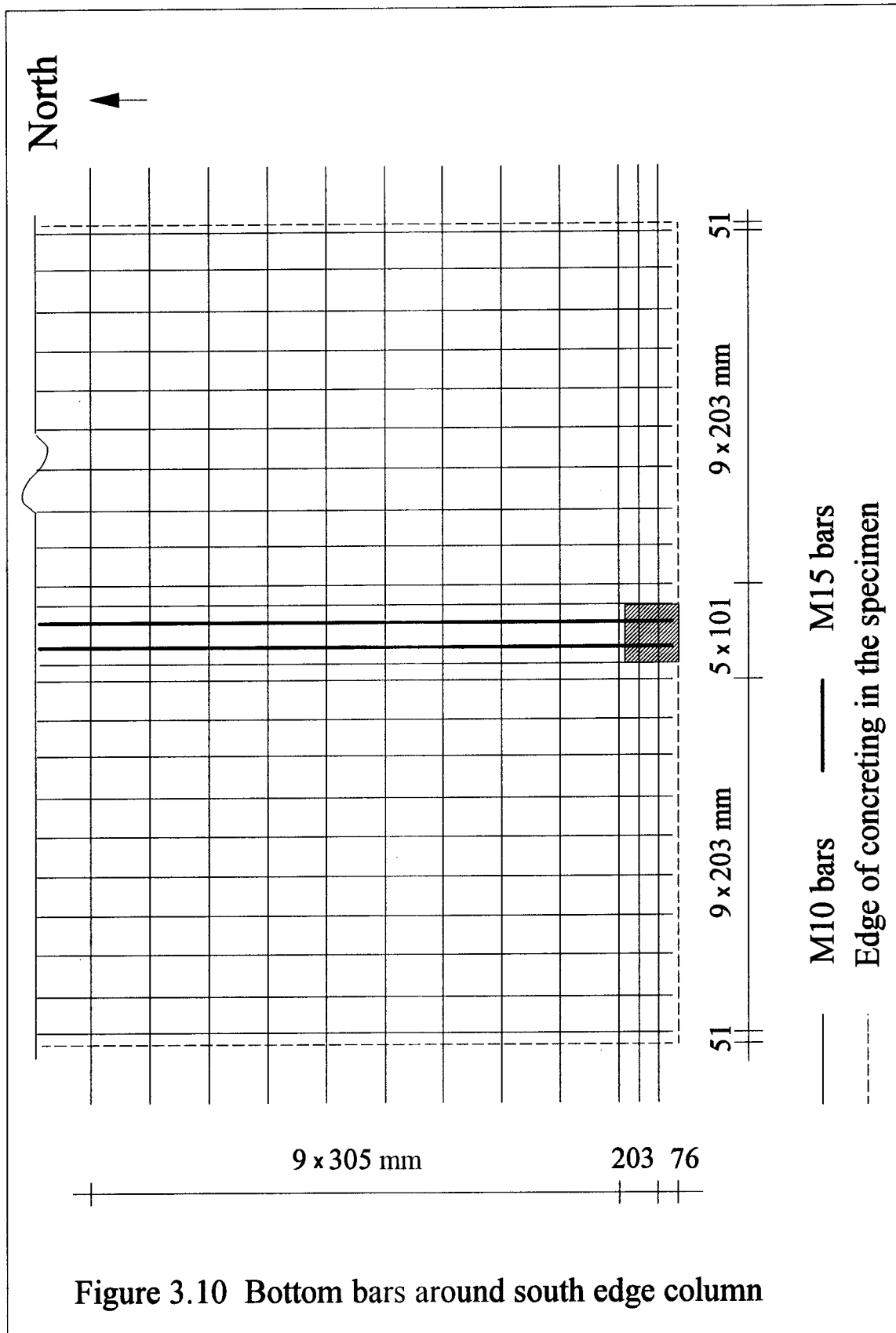
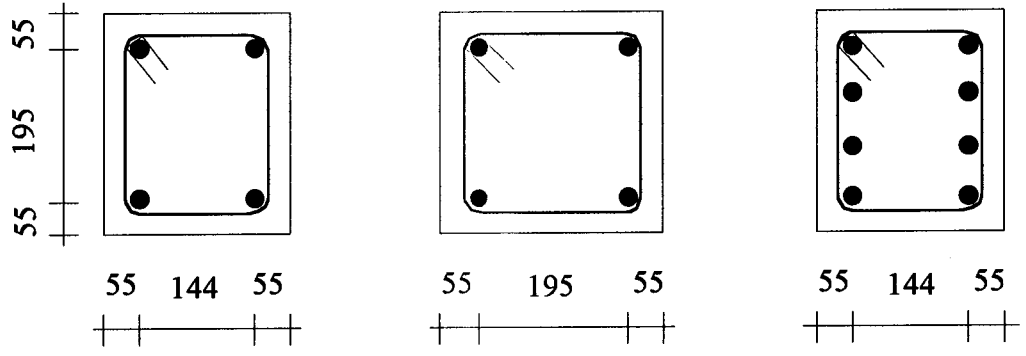
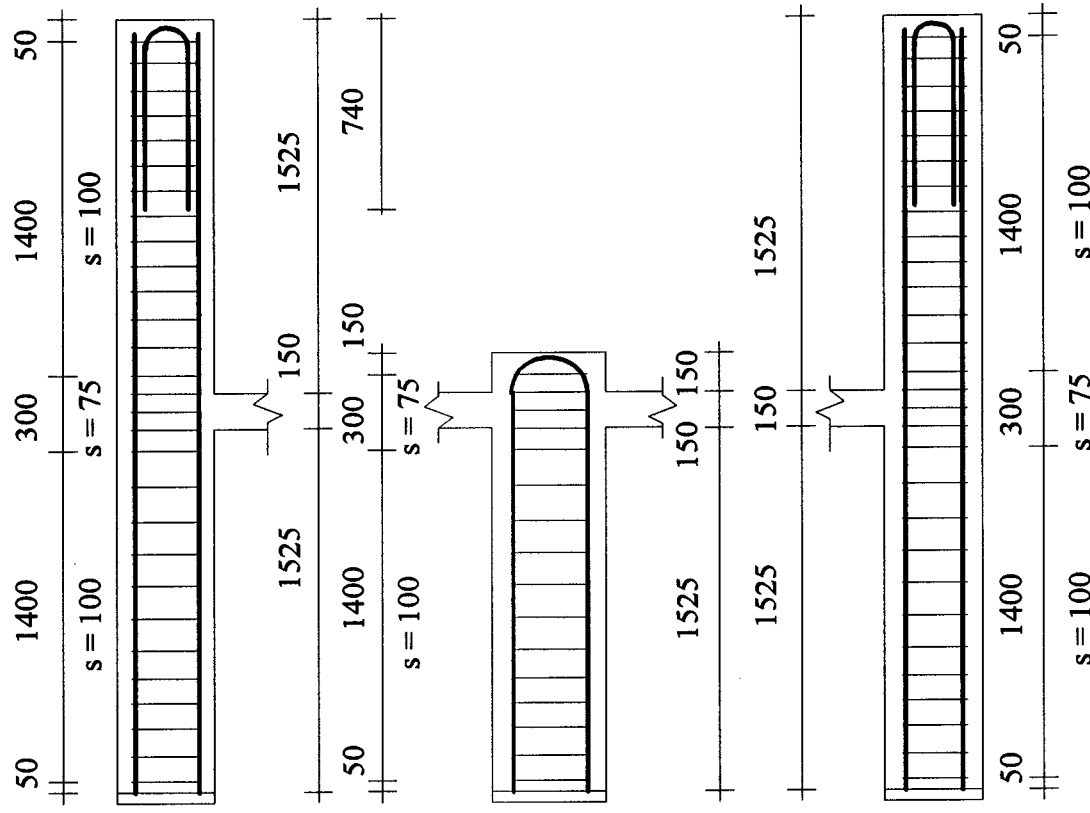


Figure 3.10 Bottom bars around south edge column



North column

Centre column

South column

● 20M bars — #3 US bars

All dimensions in mm

Figure 3.11 Dimensions and reinforcement of columns

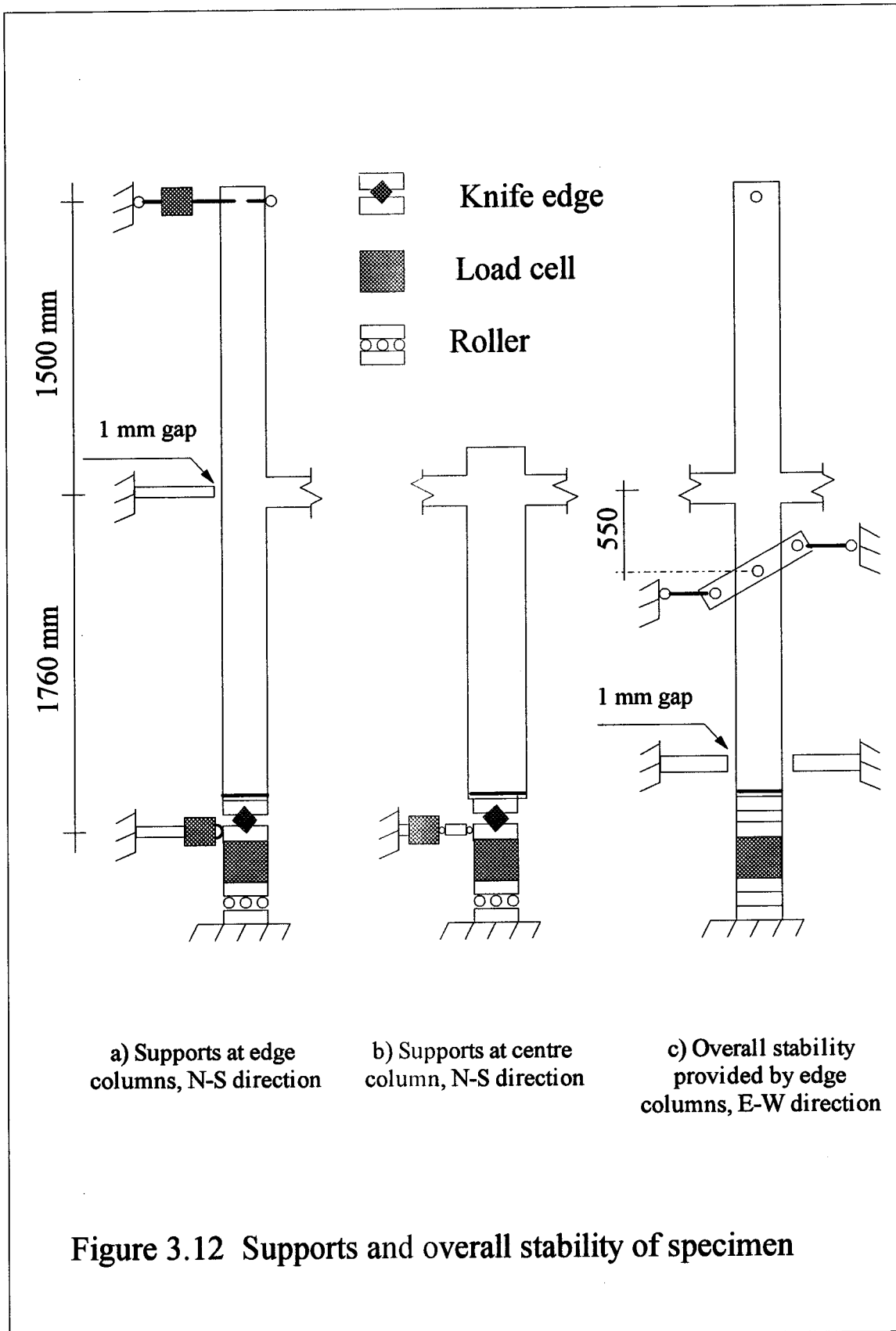


Figure 3.12 Supports and overall stability of specimen

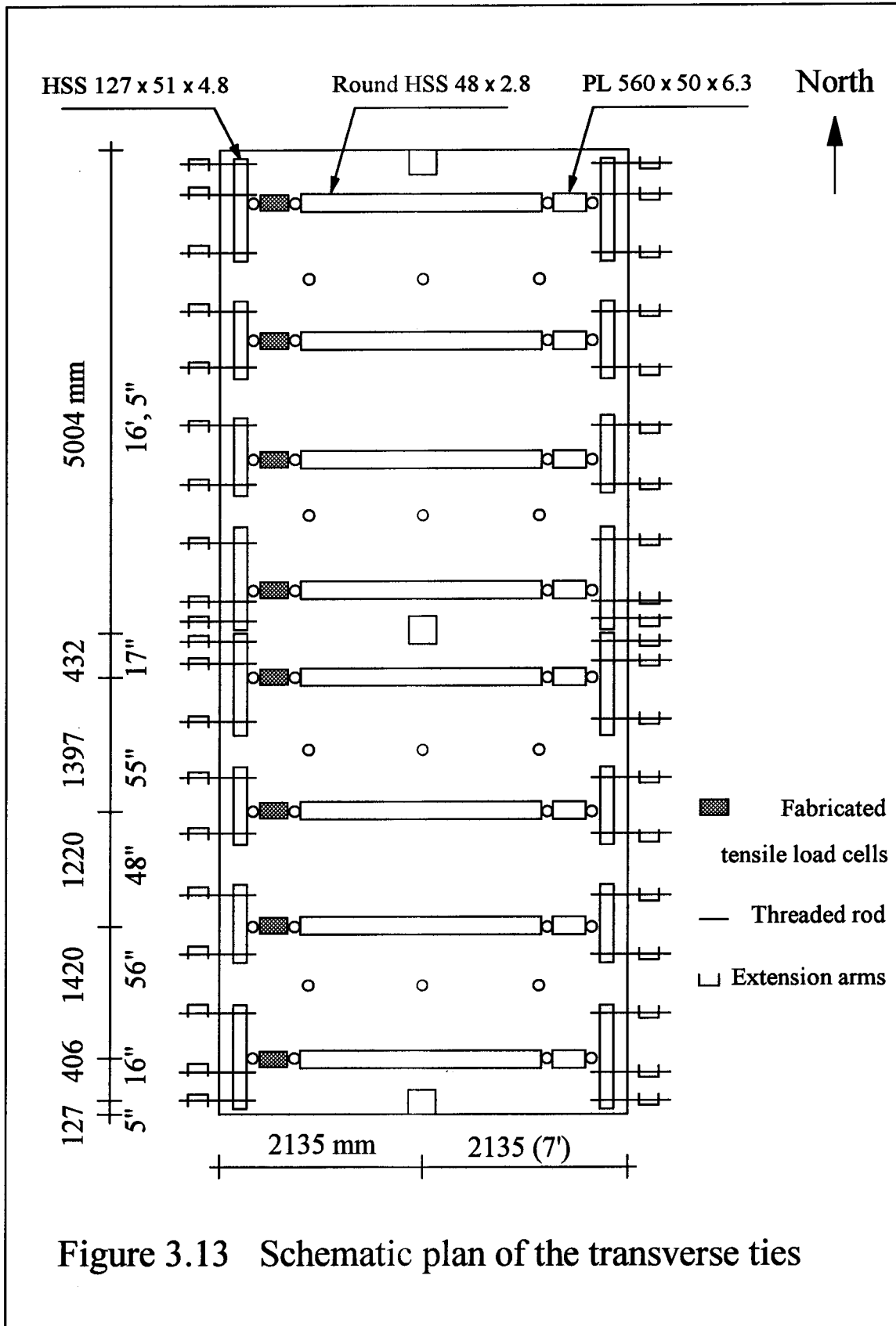


Figure 3.13 Schematic plan of the transverse ties

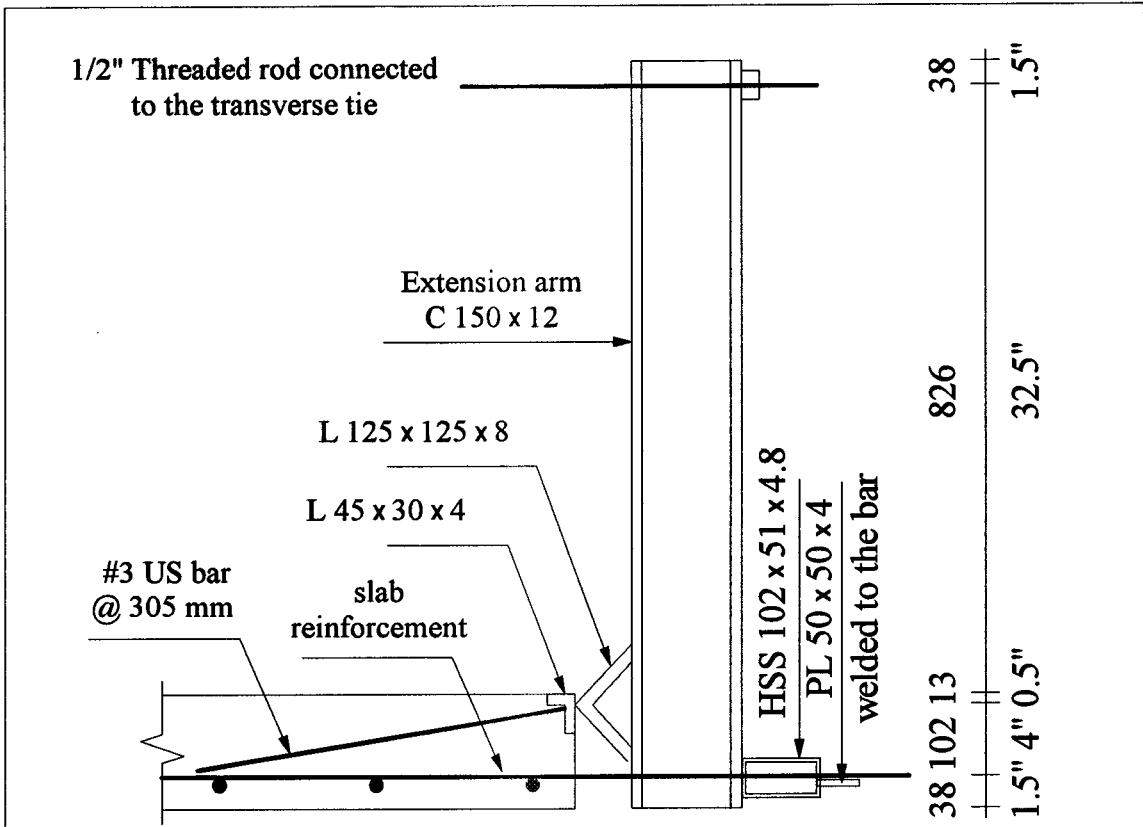


Figure 3.14 Restraint Details for continuous edge

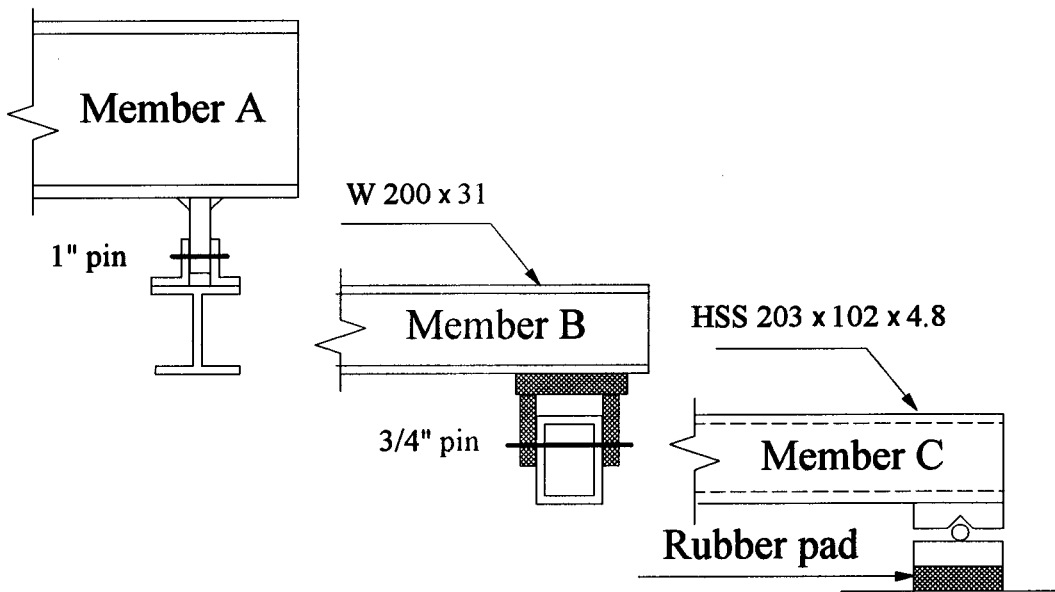


Figure 3.15 Connections of load distributing beams

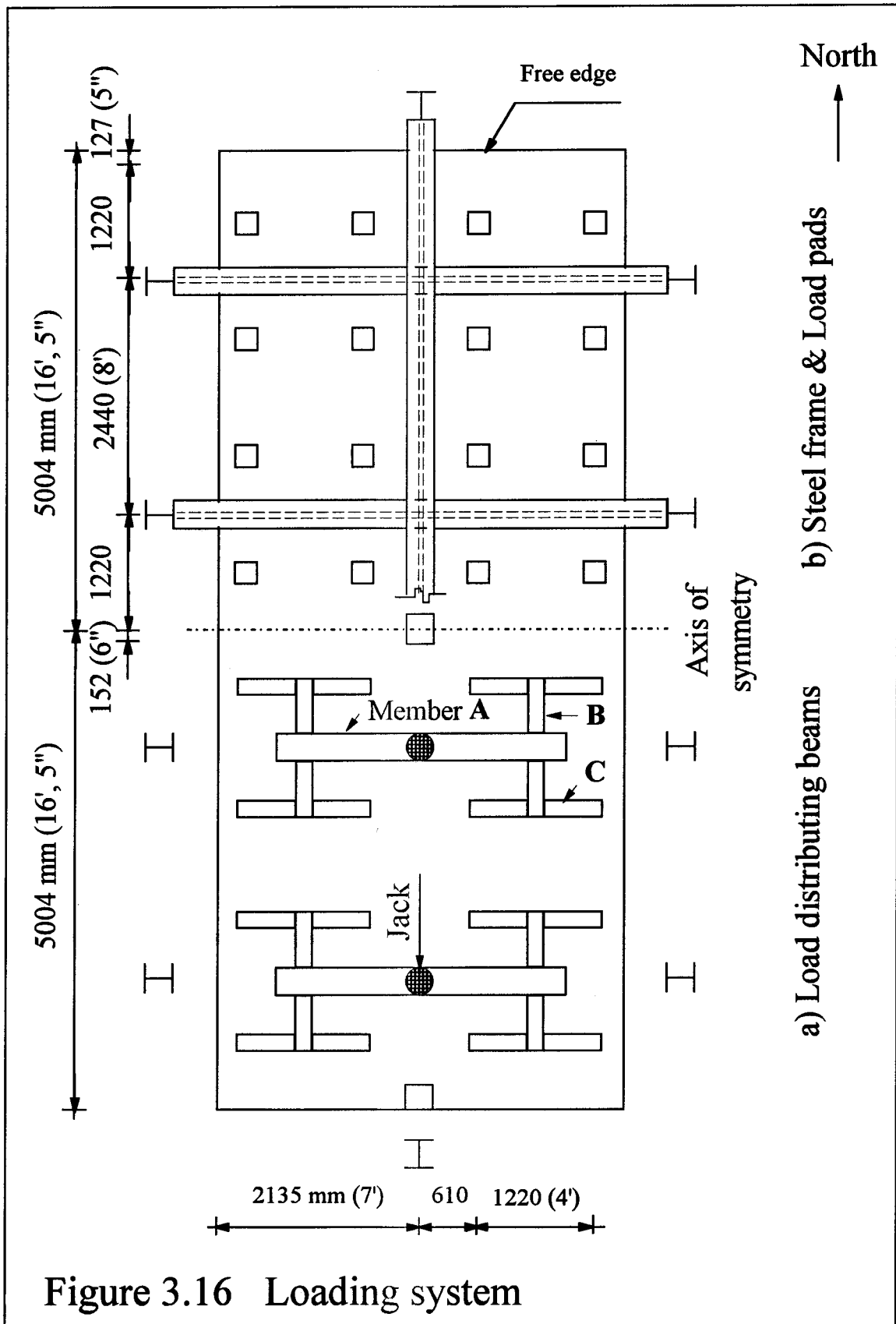
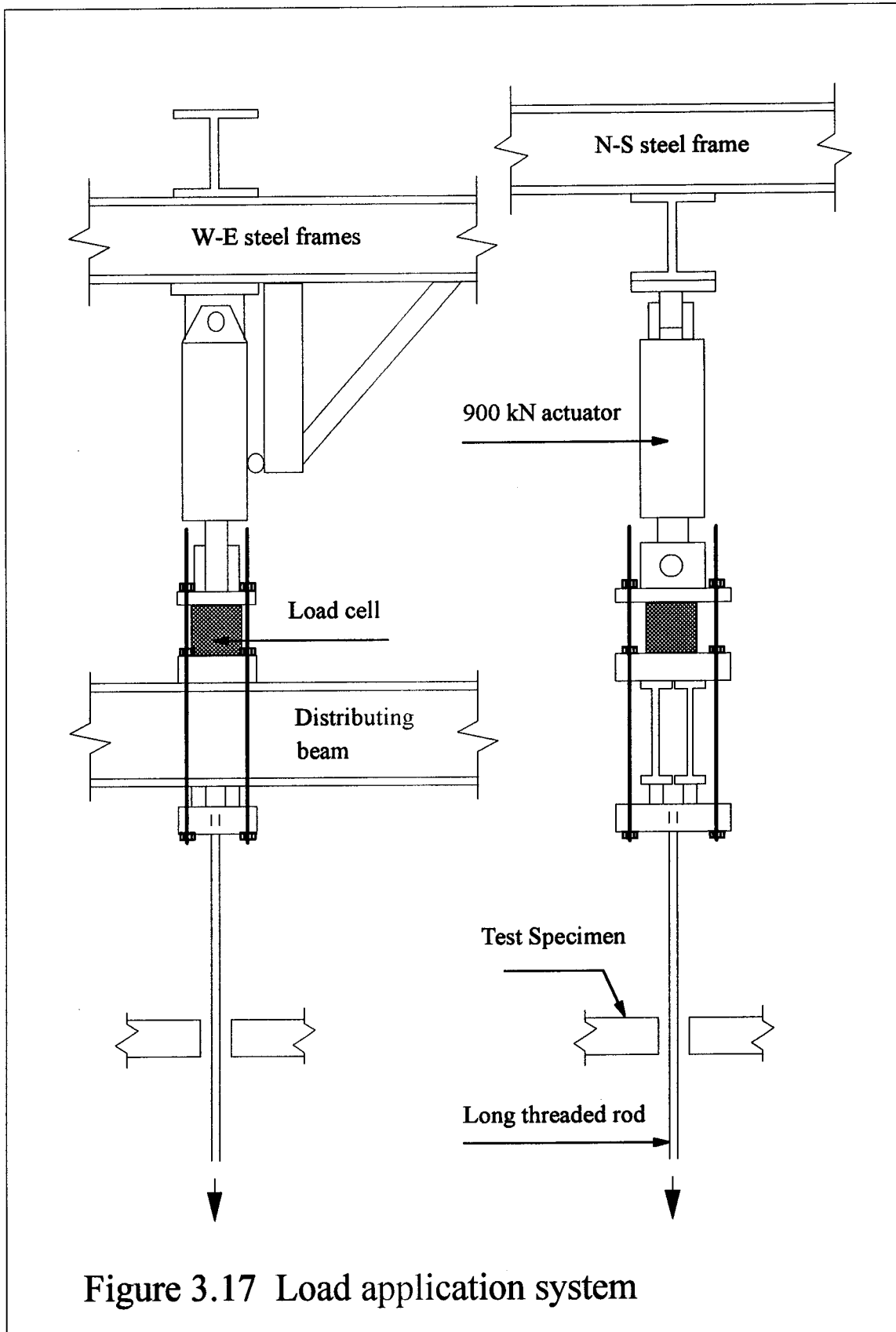


Figure 3.16 Loading system



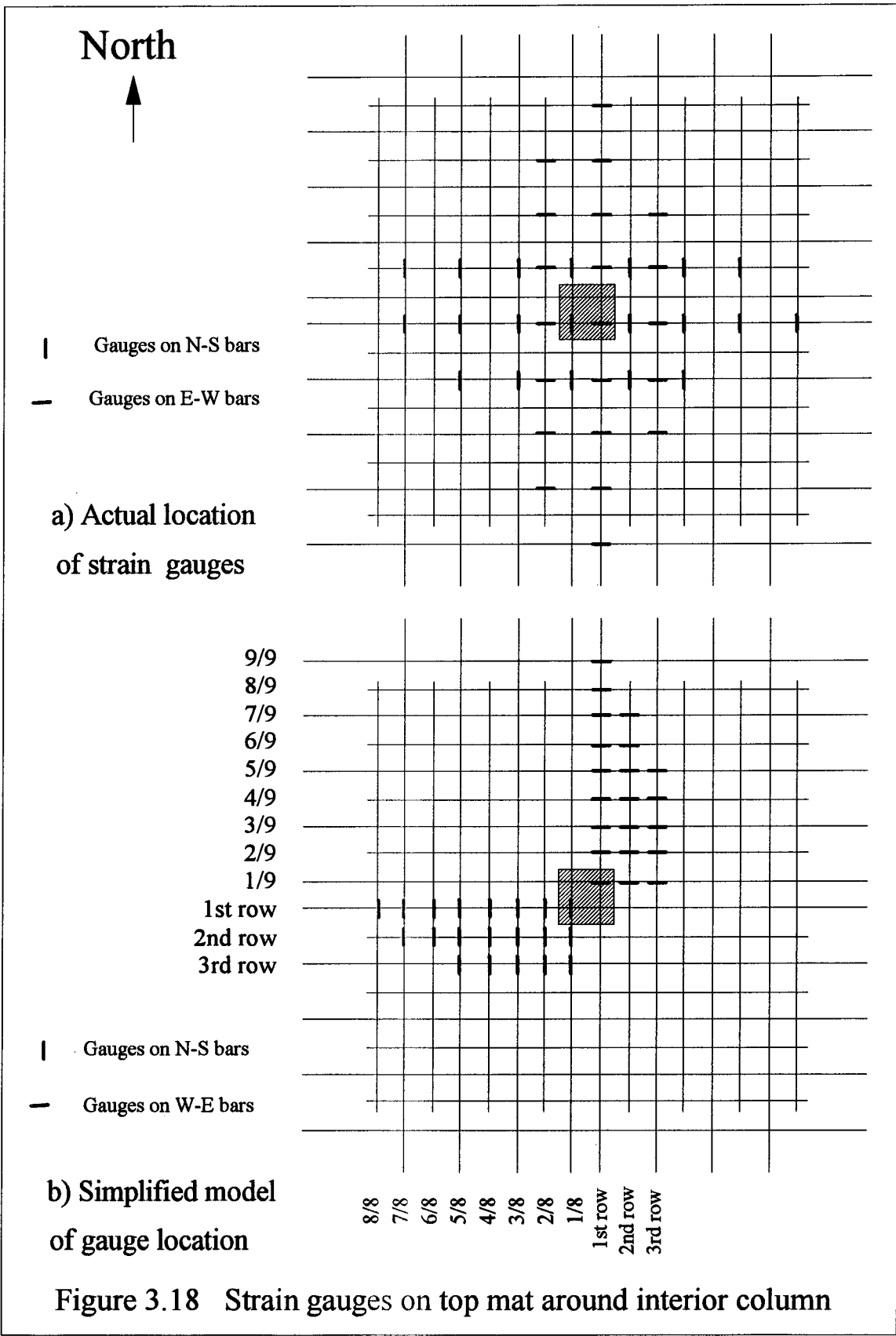


Figure 3.18 Strain gauges on top mat around interior column

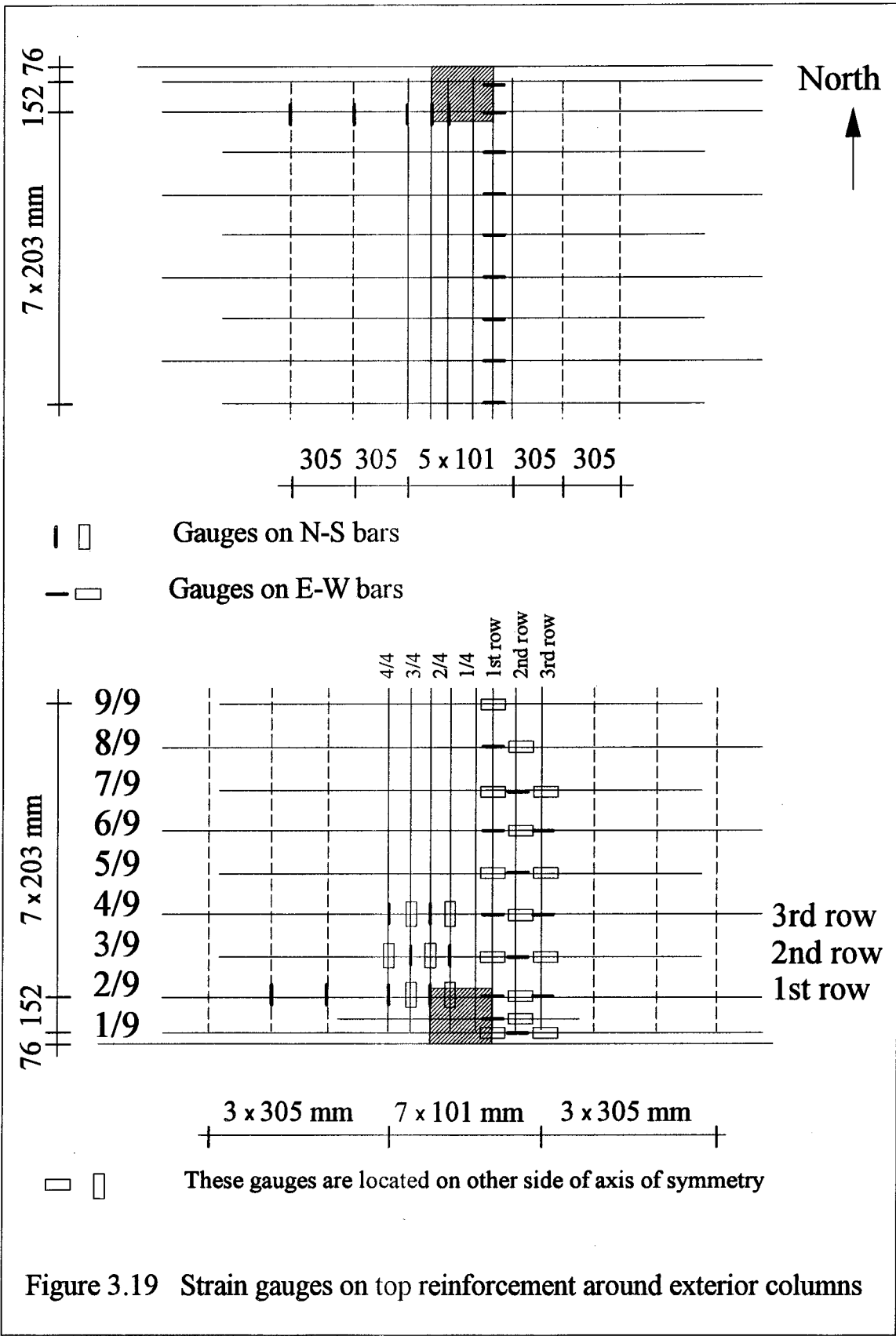
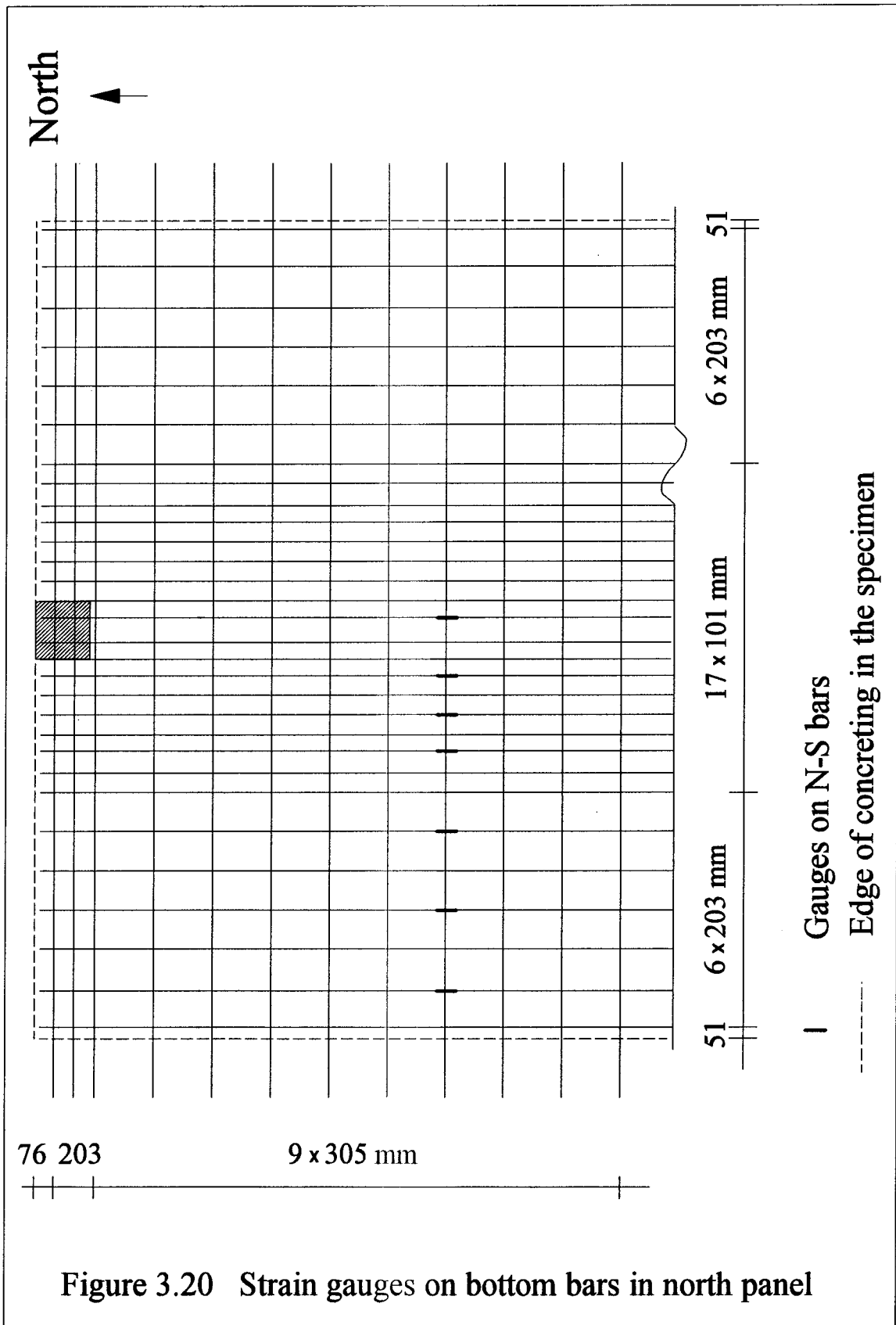


Figure 3.19 Strain gauges on top reinforcement around exterior columns



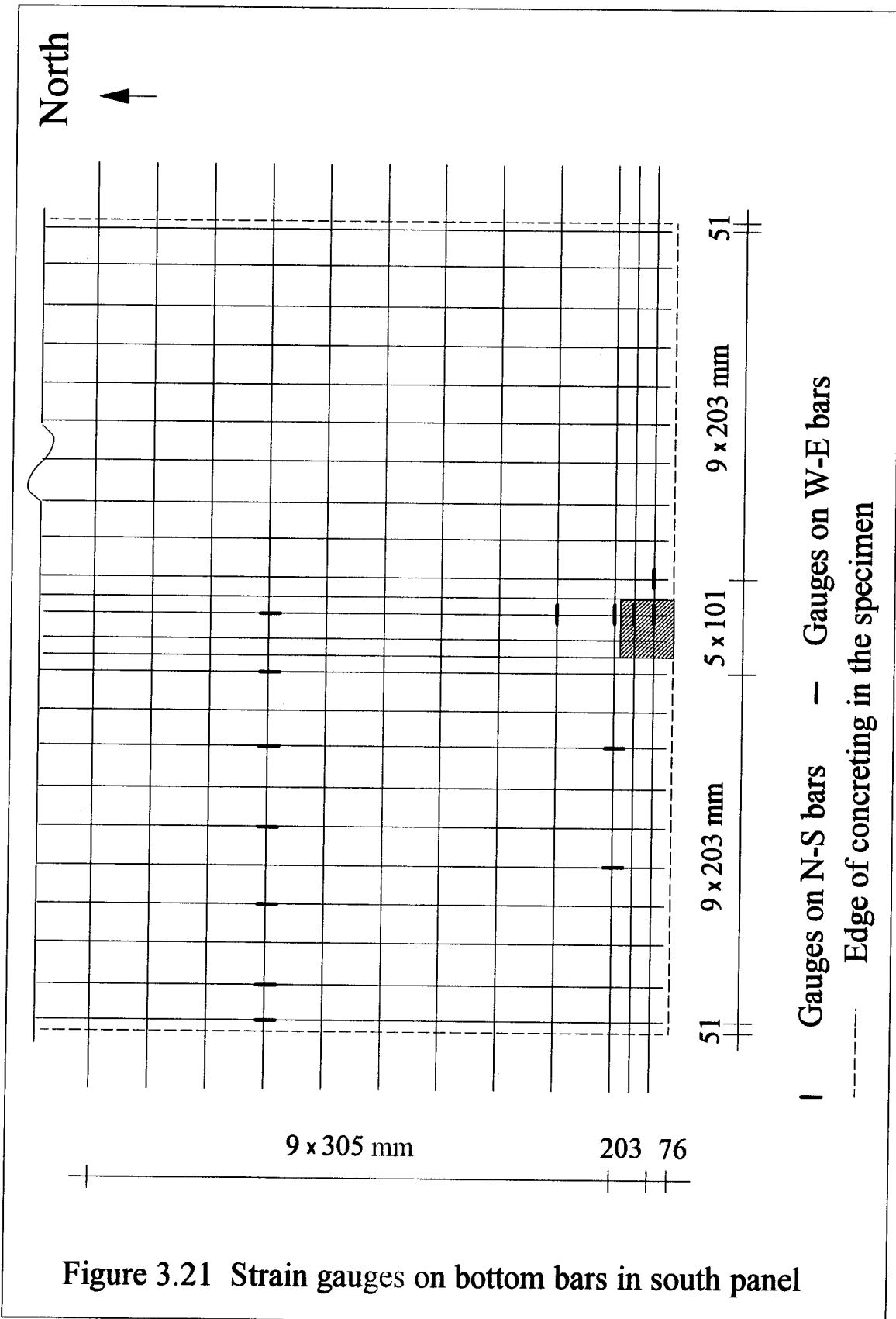
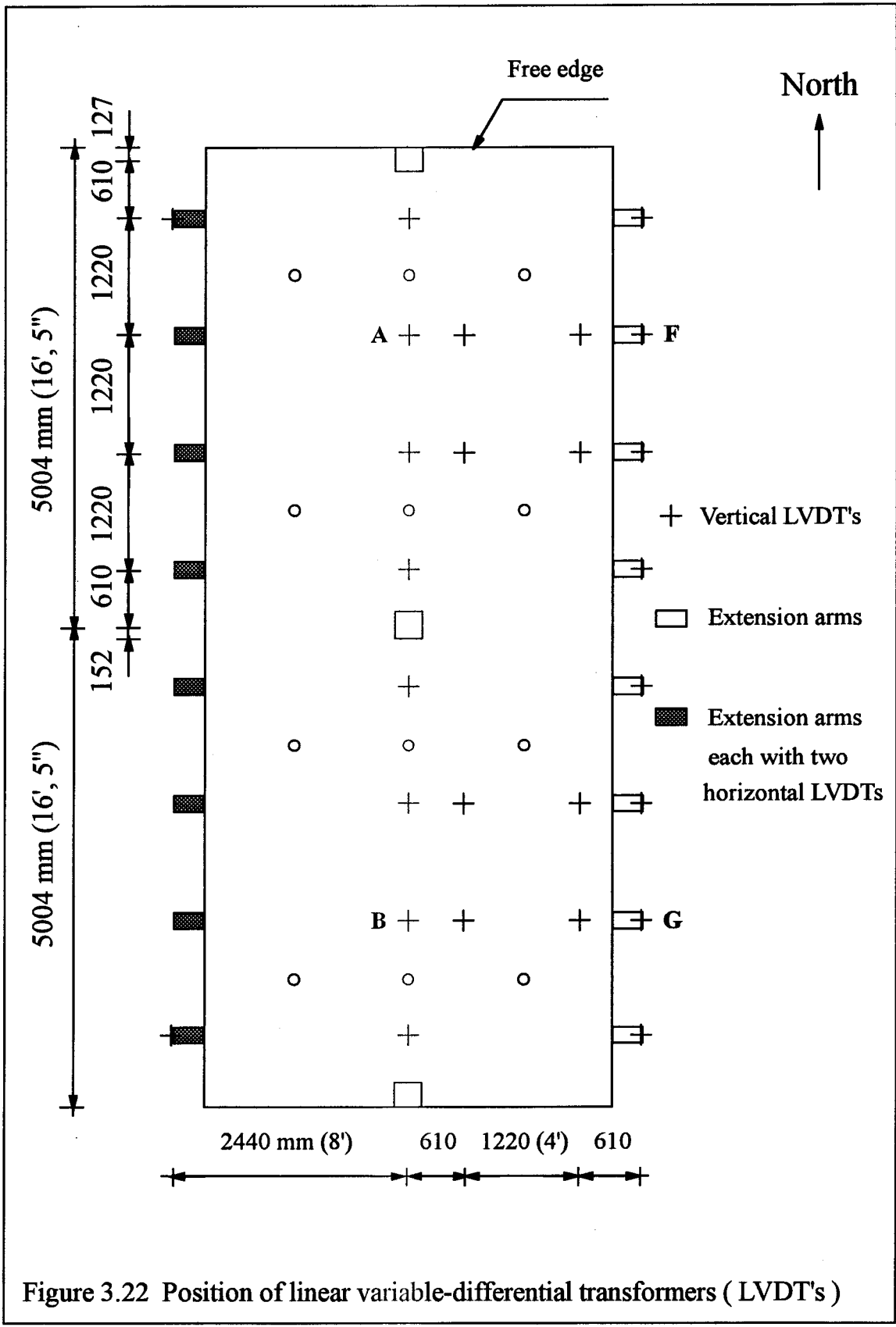
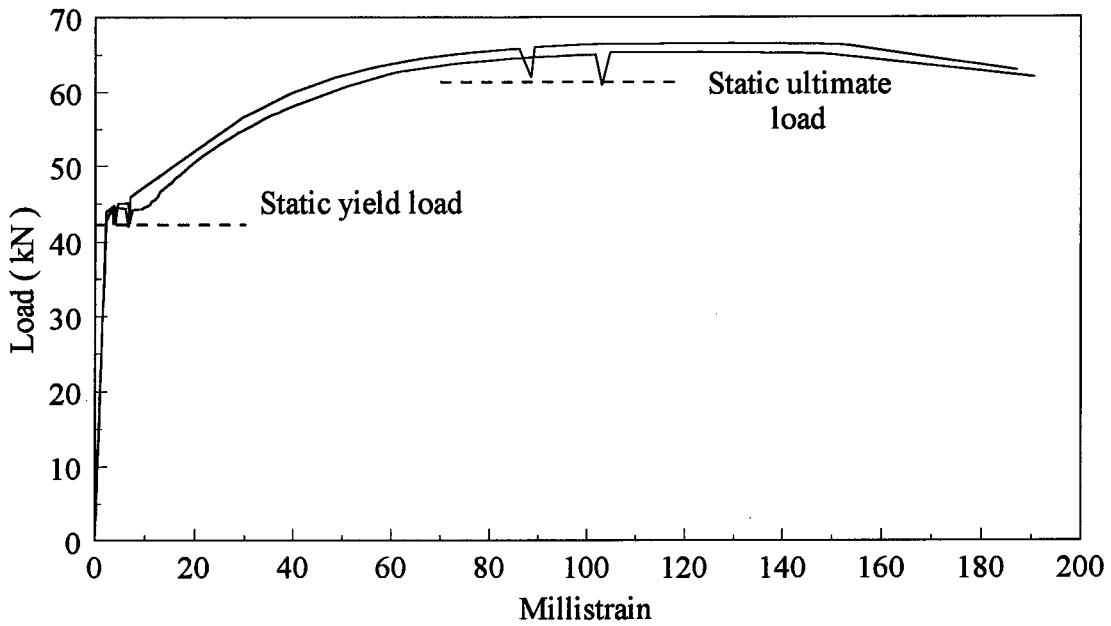
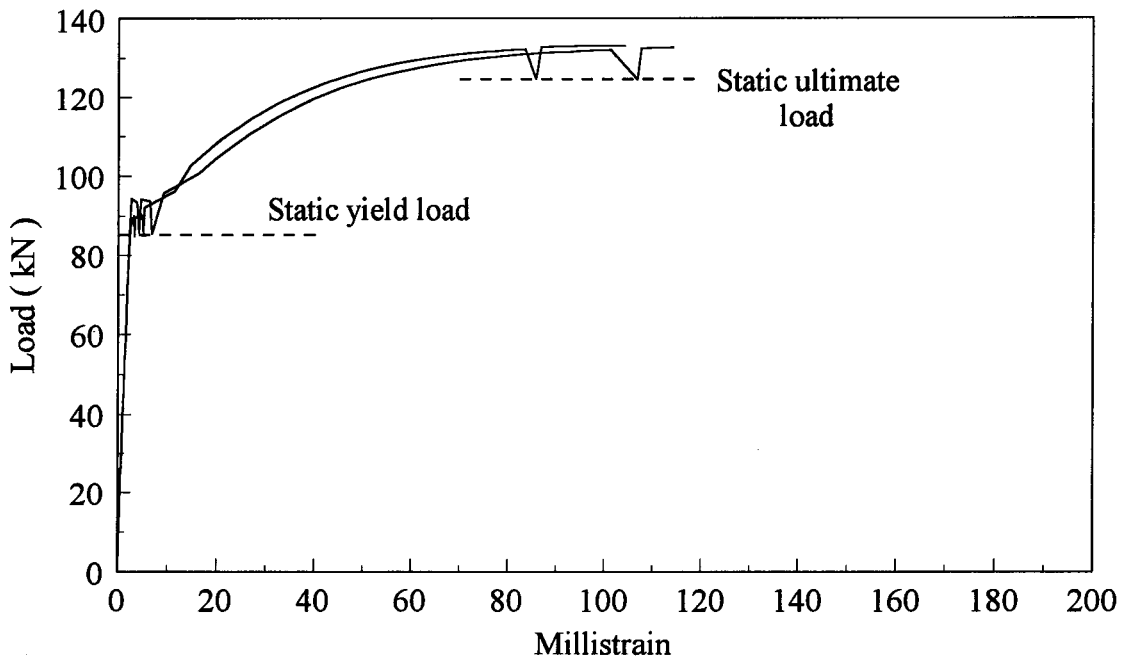


Figure 3.21 Strain gauges on bottom bars in south panel



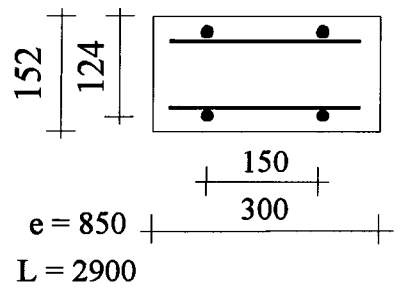
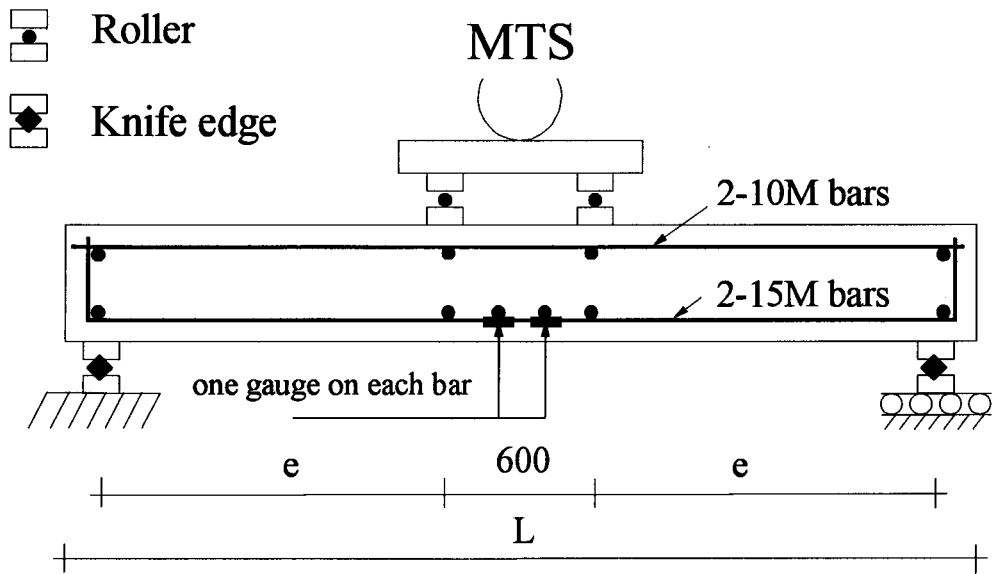


(a) 10M deformed bars with nominal area of 100 mm²

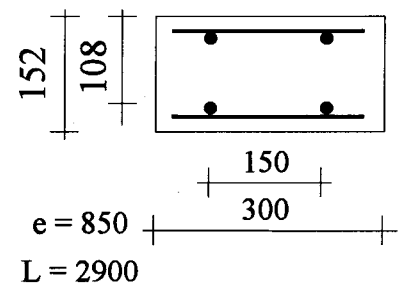


(b) 15M deformed bars with nominal area of 200 mm²

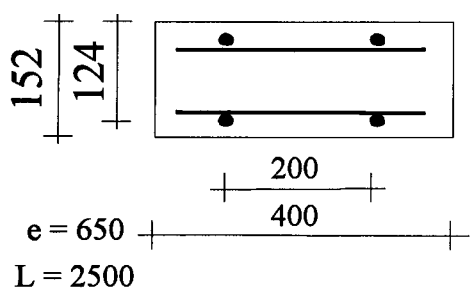
Figure 3.23 Typical load-strain plot for reinforcement



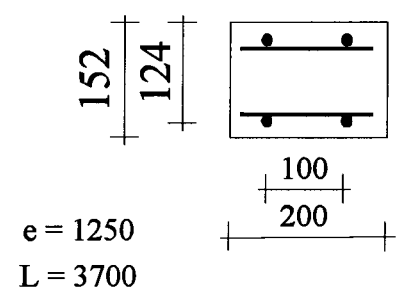
Beam 1



Beam 2



Beam 3



Beam 4

All dimensions in mm

Figure 3.24 Tests on reinforced concrete beams

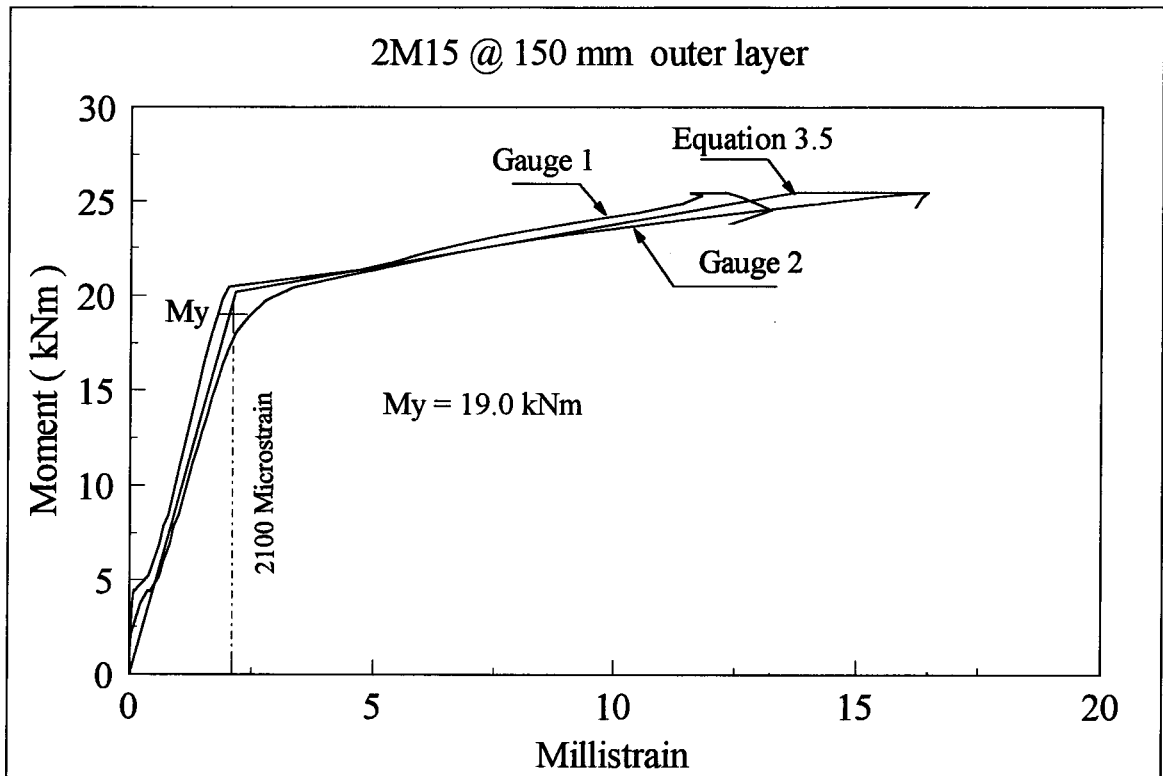


Figure 3.25 Moment-Strain Relationship for Beam 1

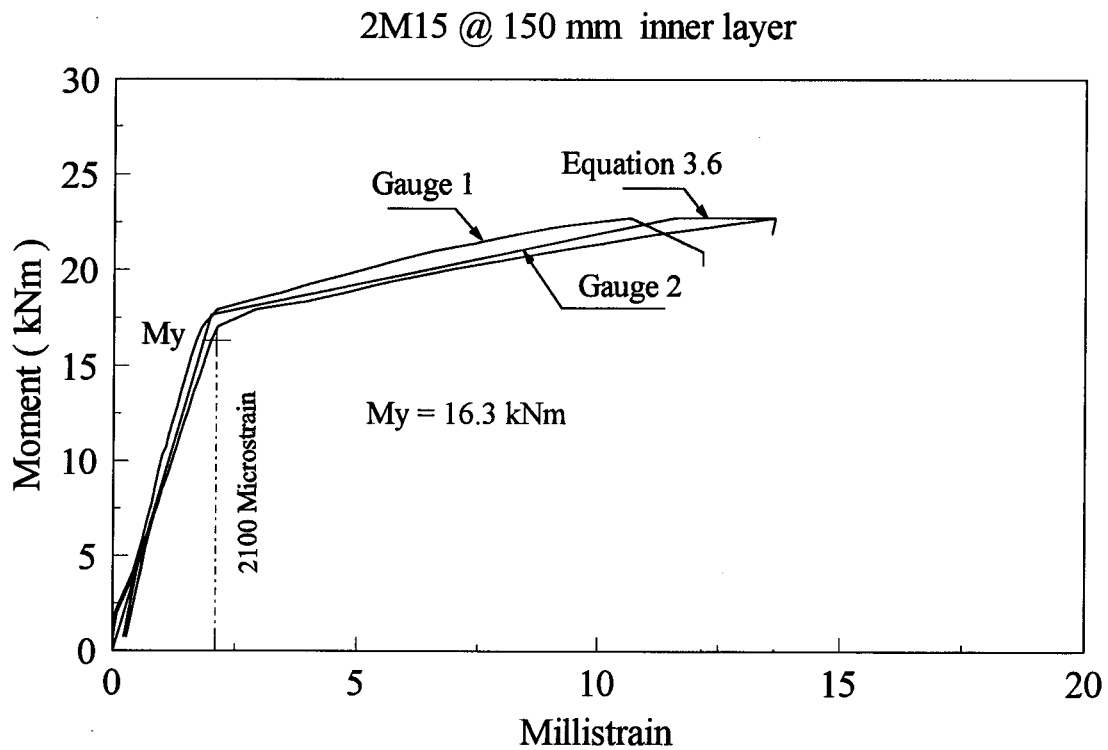


Figure 3.26 Moment-Strain Relationship for Beam 2

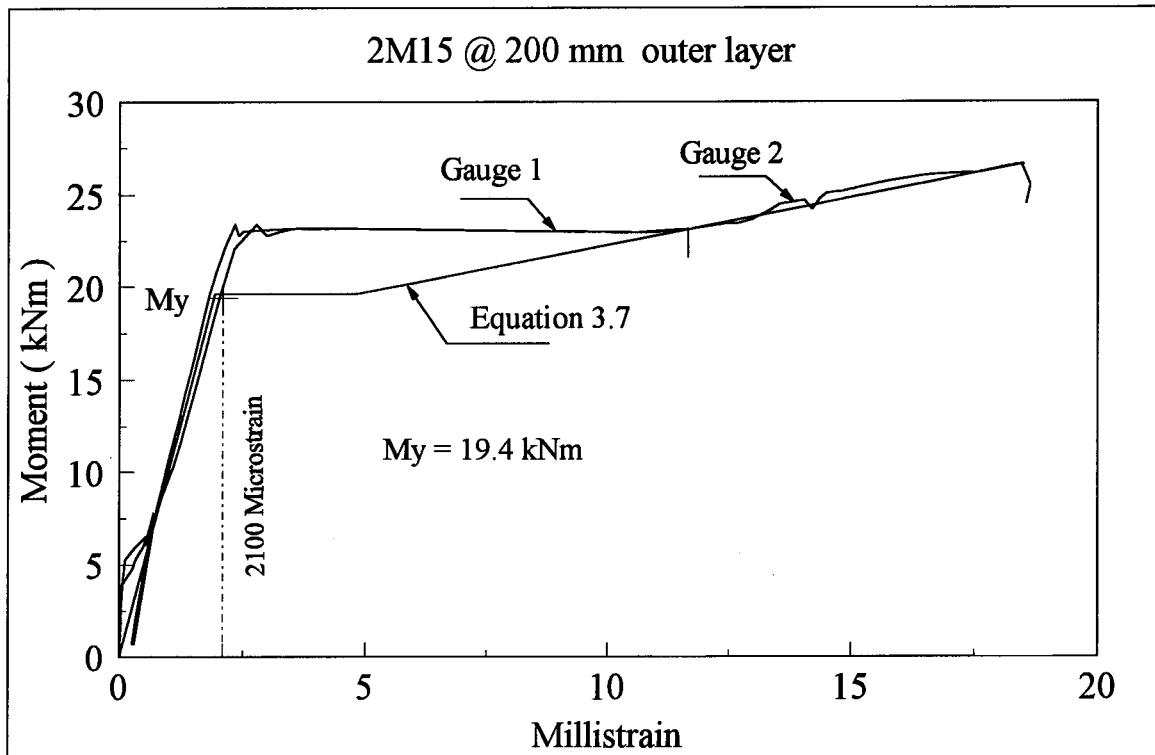


Figure 3.27 Moment-Strain Relationship for Beam 3

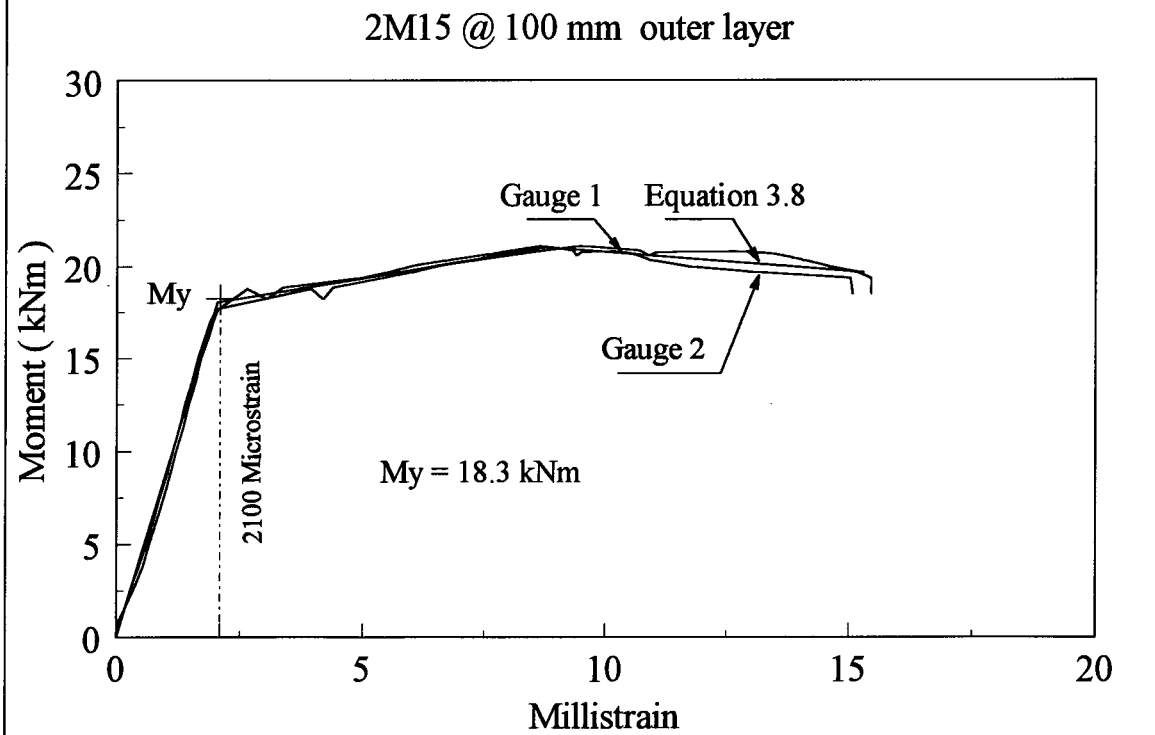


Figure 3.28 Moment-Strain Relationship for Beam 4

4. Observations and Test Results

4.1 Test Procedure

The test specimen was loaded in five stages: (1) self-weight and super imposed loads, (2) preliminary loading, (3) loading up to the service load, (4) loading up to the failure of the interior column-plate connection, and (5) retest to failure of the edge column-plate connections.

4.1.1 Self-weight and Super Imposed Loads

Figures 4.1a and 4.1b show the equivalent uniformly distributed load versus the deflection of the specimen measured by LVDT at point F (Figure 3.22). Point 1 on these diagrams relates to the dead load (3.48 kPa) at 28 days from casting. Deflections at this point were measured by surveying the slab. Deflections at point 2, correspond to the self-weight of the slab plus the weight of all the apparatus (4.32 kPa) and were measured at day 65. Therefore, a part of the deflection between points 1 and 2 is due to the creep. Deflections at point 2 established the reference values for the LVDTs.

4.1.2 Preliminary Loading

The purpose of the preliminary loading was to make sure that all the apparatus and instrumentation were working. Preliminary loading started at day 65, with load increments of about 11.9 kN per jack, equivalent to a distributed load of 1 kPa. Shortly after reaching an average jack load of 22 kN (point 4, 6.17 kPa), the load suddenly dropped to 20 kN (point 5, 6.0 kPa). The load was then increased to 24 kN per jack (point 6, 6.3 kPa). At this load, all jack loads suddenly dropped to 21 kN (point 7, 6.08 kPa), and a long continuous crack in the north-south direction was observed on the top surface. This crack was close to the west side face of the columns, resulting in more deflection in the west part of the plate. No crack was visible on the bottom surface. Load was then increased to 24 kN per jack (point 8, 6.32 kPa). After an hour, no further load drop was observed. The slab was then tied down to the strong floor to make sure that the displaced configuration would remain constant until the test resumed after the weekend.

At day 68, ties to the strong floor were released, and as anticipated, the load was decreased (point 9) due to the creep of the specimen. The load was then brought back to 24 kN per jack (point 10, 6.32 kPa). Because cracking in the N-S direction was more extensive than that in the E-W direction, it was felt that the specimen was not behaving as planned. Since reinforcement strains were well below yield, the specimen was unloaded (point 11) to take the corrective action.

Further investigation showed that the N-S crack was accompanied by considerable rotation and deflection at the continuous edges. Also, positive moment at the continuous edge did not increase as much as expected, showing that the edge restraint system was not stiff enough (positive moment was only about 13 percent of the panel moment). A decision was made to adjust the edge restraint manually.

At day 69, the edge restraint was adjusted to generate a positive moment of about 46 percent of the panel moment (point 13). The specimen was then loaded to 28 kN per jack (point 14, 6.67 kPa). The ratio of positive to panel moment reduced to 36 percent. To maintain the desired ratio of the positive to panel moment, the edge restraint would have to be adjusted manually prior to each load step. By reducing the jack loads to zero

(point 15), the prestressing force remained in the edge restraint system, and the specimen was ready for the third stage of loading.

4.1.3 Loading to Service Load

At day 70, the specimen was loaded to its full service load. Prior to each load step, edge restraint was adjusted so that the positive moment at the continuous edge was about 40 to 45 percent of the panel moment.

First, load was increased to 27 kN per jack (point 17, 6.58 kPa). Then loads were applied in increments of about 6 kN per jack (0.5 kPa). At an average jack load of 50 kN (point 18, 8.5 kPa), cracks at the top surface extended from center to the edge, on both sides of the interior column.

The last adjustment of the edge restraint was made at point 20 to give a positive moment of 40 percent of the panel moment at the service load level (point 21). Due to bending of the reinforcing bars extending out of the edge of the concrete, further adjustment of the edge restraint was not practical.

At service load (68 kN per jack, 10.1 kPa), the main cracks were measured (presented in Section 4.6.2). The first flexural cracks on the bottom surface of the plate were observed. The load was increased to 73 kN per jack (point 22, 10.47 kPa), and the load system was tied down to the strong floor.

4.1.4 Loading to Failure of the Interior Connection

Loading the specimen continued on day 71. At a jack load of 104 kN (point 24, 13.06 kPa, 70 percent of the predicted yield line mechanism load), the width of the main cracks was measured (presented in Section 4.6.2).

At an average jack load of 152 kN (point 25, 17.1 kPa), spalling of flakes of concrete on the top surface of the slab and about 500 mm from the interior face of the north column was observed, indicating that the north connection was near failure. The corresponding shear and moment at the center of the north column were 176 kN, and 51.1 kNm, respectively (Section 4.3.1). At this load no spalling of concrete was observed in the south edge connection, and shear and moment at the center of the south column were 181.5 kN and 81.0 kNm, respectively.

With a small increase in load, however, it was the interior connection that failed in punching without any warning. Immediately after the failure of the interior connection, a set of readings was taken (point 26 in Figures 4.2 and 4.3). At this point, what was to become the punching failure intercepted the top surface of the slab 500 mm from the interior face of the north column.

4.1.5 Retest of the Edge Connections

To continue testing on the exterior connections, the middle connection was supported by the two interior jacks and a set of reading was taken (point 27). First, the north edge connection was loaded. The load in jack #1 was gradually increased up to the load of 185 kN, at which the north connection failed (shear of 181 kN, and a moment of 46.5 kNm). The shape of failure was almost symmetric in this connection (Figures 4.38 and 4.41).

The same day, the south edge connection was loaded to failure. The load in jack #4 was gradually increased up to 248 kN, at which the south edge connection failed (shear of 220 kN, and a moment of 88.0 kNm). Unlike the north connection, the shape of failure of this connection was not symmetric (Figures 4.40 and 4.42).

4.2 Flexural Behavior

Based on the slope of the load-deflection curves, three stages of behavior can be distinguished for the specimen. These stages of behavior are shown in Figure 4.1 where total uniform load, including the self weight of slab, is plotted versus the deflection of the slab. Throughout stage (1), the slab was generally uncracked, although there may have been a few undetected shrinkage cracks. Part of the deflection at this stage was due to the creep under the self-weight of slab and the weight of the load distributing system during the period from 28 to 66 days.

Stage (2) begins with cracking around the column perimeters at the top surface. At the beginning of this stage, the load-deflection behavior is linear and the specimen may be described as a cracked elastic slab.

Longitudinal crack along the column line running in the N-S direction occurred earlier than expected (point 4), causing a considerable deflection without substantial change in load (point 10). Between steps 4 and 10, the edge restraint was not adjusted. The ratio, α , of the negative moment to the panel moment in the E-W direction was 0.87, considerably greater than expected (0.6 to 0.7).

Based on the load cell measurements of the negative moment in the E-W direction, theoretical panel moments corresponding to given values of α (i.e. 0.6, 0.65, and 0.7) are calculated. Their associated loads, called load in a specimen with ideal edge restraint, together with the test results are plotted in Figure 4.4.

As illustrated in this figure, at the stage 2, by adjusting the edge restraint system and therefore applying positive moment to the continuous edge manually, the specimen was brought back to its expected range of behavior.

The plastic behavior between points 4 and 10 caused a residual displacement, between points 16 and 2 in Figure 4.1b. The gradual adjustment of the positive moment from point 16 and 18, recovered almost all of this residual displacement. The load-deflection behavior became non-linear after point 18 for two reasons; (1) transverse cracks running E-W extended to the edges, and (2) the adjustment of the edge restraint system was stopped.

Stage (3) of the flexural behavior started with the initiation of the cracks in the positive moment region on the bottom surface. At the beginning of this stage, the load-deflection behavior was linear. With the development of these cracks, the slope of the load-deflection curve decreased. This stage ended with the punching of the interior column-plate connection at 17.1 kPa, 91 percent of the predicted yield line mechanism load.

Figure 4.5 shows the actual load in different jacks versus the deflection of the specimen at point F due to the jack loads. In part of the test, a plotter was connected to the jack #1. The malfunction of this plotter caused an error in monitoring the load in this jack. As a result, the load in jack #1 was slightly greater than that in the other jacks. To correct the data, loading system #1 was tied down to the strong floor so that the actual

load on the slab never decreased. With the decrease of the load in jack #1, at different load levels, loads were measured once with the plotter connected and once without it. The reported data are the corrected data so obtained. After the removal of the plotter, first the load in jack #2, and then the load in the other jacks were increased to the level of the load in jack #1. Loads in all jacks were at the same level, until the failure of the interior column-plate connection (point 25).

As illustrated in Figures 4.2 and 4.3, right after the failure of the interior connection (point 26), the load in the exterior jacks increased. This load (point 27) was decreased because of seating of the supports at the position of jacks 2 and 3. The increase in the slope of the load-deflection curve at the retest is due to the change in boundary conditions; Jacks 2 and 3 are no longer applying load, and are acting as a supports, reducing the span length. Compared to the north connection, the south connection sustained considerable deflection and load capacity after the failure of the interior connection as would be anticipated as it had heavier reinforcement.

4.3 Stress Resultants and M-V Diagrams

4.3.1 External Measurement of Stress Resultants, and M-V Diagrams

Based on load cell measurements, moments and shears at critical sections are calculated. Selected data is presented in Tables 4.1 through 4.3. Figure 4.6 defines the terms used, and Figure 4.7 shows free body diagrams of the specimen.

The value of the shear at each connection is equal to the column reaction minus the weight of the column and the knife edge, about 5.0 and 7.0 kN for exterior and middle columns, respectively.

Negative moments at the edge connections are calculated using the horizontal load cells at the top and bottom of the exterior columns (shown in Figure 3.12);

$$M_{1x}^- = 1.76 \times F_{1,bot} + 1.5 \times F_{1,top} \quad (\text{North connection}) \quad [4.1]$$

$$M_{3x}^- = 1.76 \times F_{3,bot} + 1.5 \times F_{3,top} \quad (\text{South connection}) \quad [4.2]$$

As expected, the horizontal load cell at the bottom of the interior connection showed a negligible value throughout the test. Based on the free body diagram in Figure 4.7a, the negative moment at the interior connection was obtained from Equation 4.3, where q is the equivalent uniformly distributed load for the self-weight of the plate and the superimposed dead loads.

$$M_{2x}^- = \frac{M_{1x} + M_{3x}}{2} + \frac{V_2 \times L}{2} - \frac{q \times L}{8} - \frac{(J_1 + J_4)}{16} - \frac{3 \times (J_2 + J_3)}{16} \quad [4.3]$$

The negative moment at the face of the columns, shown in Figures 4.7c and 4.7d, can be calculated for both exterior and interior column-plate connections according to Equations 4.4 to 4.6.

$$M_{1x,face}^- = M_{1x}^- - V_1 \times c_1 / 2 - q \times c_1^2 / 2 \quad (\text{North connection}) \quad [4.4]$$

$$M_{2x,face}^- = M_{2x}^- - V_2 \times c / 4 - q \times c^2 / 8 \quad (\text{Interior connection}) \quad [4.5]$$

$$M_{3x,face}^- = M_{3x}^- - V_3 \times c_1 / 2 - q \times c_1^2 / 2 \quad (\text{South connection}) \quad [4.6]$$

Figures 4.8 to 4.10 show the moment at the center of the column and the moment at the column face versus the shear. The shear V_2 in these figures and in Equation 4.5 is one-half of the total column shear.

The maximum span moment can be approximated by the positive moment at the position shown in Figure 4.7a (Equations 4.7 and 4.8).

$$M_{1x}^+ = 3 \times L \times V_1 / 8 - M_{1x}^- - L \times J_1 / 16 - q \times L_1^2 / 2 \quad (\text{North panel}) \quad [4.7]$$

$$M_{2x}^+ = 3 \times L \times V_3 / 8 - M_{3x}^- - L \times J_4 / 16 - q \times L_1^2 / 2 \quad (\text{South panel}) \quad [4.8]$$

In the other direction, positive moment M_y (at the continuous edge) is equal to the force in cross ties multiplied by the distance from tensile load cell to the center of the slab, 0.90 m. Then the negative moment at the face of the column, as shown in Figure 4.7b, is calculated by Equation 4.9.

$$M_{y,face}^- = M_y^+ - q \times b_2^2 / 2 - J \times b_1 / 2 \quad [4.9]$$

Equation 4.9 is valid until the failure of the interior connection. After punching of the interior connection, middle jacks are used as supports. Hence, the free body diagram shown in Figure 4.7b changes, and it is impossible to calculate $M_{y,face}^-$ based on the load cell readings.

Moments at the critical sections are plotted versus the deflections measured by the LVDTs in Figures 4.11 through 4.19. For the edge connections and for the mid-span moments, the deflection at the position of the exterior jacks is used, while for the interior connection and the continuous edge, the deflection at point F (Figure 3.22) is used.

4.3.2 Moment at Critical Sections Based on Strain Gauge Measurements

Moments at different critical sections of the slab were calculated using the strain gauge readings and the moment-strain equations developed from the beam tests described in Section 3.7.3. Moment-strain equations used for different locations of the specimen are listed in Table 4.4. Moments based on strain measurements are listed with those based on the load cell measurements for selected load levels in Tables 4.2 and 4.3, and are illustrated in Figures 4.8 through 4.18.

4.3.2.1 Negative Bending Moments at the South Connection

The negative moment at the column face, $M_{3x,face}^-$, was extrapolated from moments calculated from the measured strains of the second and the third row of gauges using the beam 4 moment-strain relationship expressed by Equation 3.8. These moments are plotted in Figures 4.9 and 4.13 versus the shear and the deflection under jack 4, respectively.

Figure 4.17 shows the negative moment in the y direction at the face of the south column, $M_{3y,face}^-$. This moment was estimated using the strain-moment relationship of beam

2, adjusted to account for the change in bar spacing from 150 mm to 200 mm. Beam 2 was used for the negative moment in the y direction, as it was the only beam with tension reinforcement in the inner layer.

4.3.2.2 Negative Bending Moments at the North Connection

Bars perpendicular to the free edge were M10 @ 100 mm, providing the same reinforcement ratio as M15 @ 200 mm. Therefore, Equation 3.7 was used to find the negative moment at the column face. The only available strain gauges were located 25 mm inside the column face, where the E-W bars would initiate the cracks (Figure 3.19). Bending moment using these gauges is referred to as negative moment at the column face, $M_{1x,face}$, although it is slightly different. This moment is plotted in Figures 4.8 and 4.12 versus the shear and the deflection under jack 1, respectively. In the other direction, like the south connection, Equation 3.6, with a minor adjustment for spacing was used for $M_{1y,face}$ (Figure 4.16).

4.3.2.3 Bending Moments at the Interior Connection

Second row of gauges, 75 mm outside the column face (refer to Figure 3.18), was used to calculate the negative moment at the face of the interior column, $M_{2,face}$. Since the amount of shear, V_2 , is known by the vertical load cell, the amount of negative moment at the column face can be calculated by Equation 4.10.

$$M_{2,face} = M_{2nd\ set\ of\ gauges} + V \times e \quad [4.10]$$

Where e is the distance between the two sections. Equations 3.5 and 3.6 were used to calculate moment in the x and y directions, respectively.

4.3.2.4 Positive Moments in the x Direction

The spacing of the reinforcing bars in the bottom mat in the x direction varied in column and middle strips (Figures 3.20 to 3.21). To calculate the positive moments in the north panel, M_{1x}^+ , and in the south panel, M_{2x}^+ , both Equations 3.7 and 3.8 were used. Note that Equation 3.8 is valid for 15M bars at 100 mm (e.g. integrity steel), and Equation 3.7 is good for 15M bars at 200 mm, or 10M bars at 100 mm. Equation 3.7 is also good for larger spacing of the reinforcement because of the small size of the compression block and hence insignificant change of the internal moment arm. Positive moments at the north and the south panels are presented in Figures 4.14 and 4.15, respectively.

4.3.3 Validity of Gauge Readings

Accuracy of the moment calculations based on the strain measurement of reinforcement is directly affected if the gauge is located at an uncracked section. In such sections, since part of the tensile force of the internal force couple is transferred by the concrete, the tensile force and hence the bending moment is underestimated. At low load levels, cracking has not spread to a large area, and many gauges lie at uncracked sections. With increase in load, the cracked region expands to include a larger number of the gauges, and calculated moments become more realistic.

All strain gauges were functional during the course of the test. Validity of the moments calculated based on the strain measurements can be determined by comparison to the load cell measurements. Comparisons of internal measurement of bending moments with their corresponding external measurement at selected loads are listed in Tables 4.2 and 4.3. Figures 4.20, 4.21, and 4.22 illustrate the ratio of moments calculated from strain gauge readings to the moments measured by load cells for the north, the south, and the interior connections, respectively.

As anticipated, after sufficient cracking, this ratio was less than one with the exceptions of the negative moments in the x direction at the face of the north column, where this moment was calculated from strain gauges that were 25 mm inside the column face, and at the face of the south column where this moment was extrapolated from the results of the second and the third row of the gauges.

Near the end of the test, or more accurately speaking, near the formation of a yield line mechanism, the ratio of internal measurement to the external measurement of moments becomes very close to one. The only case that this ratio is more than one is the moment at the column face of the north connection, $M_{1x,face}$. This is due mainly to the position of the gauges in this connection (25 mm inside the column face).

Near or at failure of any given connection, moments based on the internal measurements were in excellent agreement with those based on load cell measurements as listed in Tables 4.2 and 4.3. At the sections where yield line mechanism formed, these moments are very close to the predicted yield line moments based on the tested material properties.

4.4 Deformations along Continuous Edges

Deformations along the continuous edges were measured to define the boundary condition and to examine how well the edges of the specimen represent the midspan of the prototype building, especially at the service load level.

The overall expansion of the plate and the end rotation was calculated at eight points along the continuous edge (Figure 3.22) from the readings of 16 LVDTs. Deformations calculated this way are due only to the jack loads, because these LVDTs were installed after stripping the forms.

The top row of the LVDTs was located 229 mm (9") below mid-height of the plate, and the bottom row was 305 mm (12") below the top row. As a result, overall expansion at the mid-height of slab is calculated by the following equation;

$$\text{Mid-height overall Expansion} = 1.75 \times \text{Top LVDT} - 0.75 \times \text{Bottom LVDT}$$

Average of the overall expansions along the edge is plotted in Figure 4.23 versus the vertical deflection. A negative sign means that the distance between two corresponding points on the continuous edges decreased during the test.

The difference between readings of the top and the bottom LVDTs divided by the distance between them (305 mm) gives the sum of the rotation of both edges in radians. This total rotation is averaged along the continuous edge, and is plotted in Figure 4.24 versus the deflection of the specimen. Also, in Figure 4.25 the average jack load is plotted versus the average total rotation along the continuous edge.

4.5 Yielding of Steel Perpendicular to the Free Edges

As shown in Table 4.3, the maximum negative moment (load step 25) at the interior face of the north edge column reaches the predicted yield moment. At the south edge connection, the maximum moment (load step 30) was 60.6 kNm, only 82 percent of the predicted yield moment.

In Figure 4.26, the distributions of strain and stress of the steel perpendicular to the free edge of the south edge connection are plotted for selected stages of loading, at a section 25 mm inside the column (first row of gauges). At service load levels, the reinforcement was not yielded. Ultimately, all reinforcing bars inside the column width yielded, while those outside the column width did not yield. Based on the strain gauge readings, the maximum moment associated with bars on each side of the column was 14.7 kNm. Similar results, illustrated in Figure 4.27, were observed at the north edge connection. The maximum moment associated with the reinforcing bars on each side of the column was 11.7 kNm. This value is slightly smaller than that of the south connection, as two 15M bars were provided in the south connection as anchorage bars.

The area of anchored steel placed outside of the column perpendicular to the free edge was four times greater in the south connection than in the north connection. The fact that the maximum moments generated by these bars were more or less the same in both connections and were really limited by the torsional capacity of the plate at the side face of the column, suggests that the moment capacity of an edge connection might be independent of the area of the steel provided outside the column width. This is not considered in the North American Standards.

Another observation in the north column-plate connection is the large strains, approximately 14500 microstrain at ultimate, in the two bars within the column width. This strain was large even before punching of the interior connection (approximately, 13000 microstrain). The strains shown in Figure 4.27 increased slightly after the failure of the interior connection (load step 26), and then decreased significantly (load steps 27 and 28). This decrease in strains required a complete unloading of the two bars within the column width.

4.6 Serviceability Considerations

4.6.1 Deflections

In general, two deflections must be considered; (a) immediate deflection due to specified live load, and (b) deflections due to sustained load and live load. The latter, however, can not be considered in this study.

The maximum deflection of the specimen due to loads between the stages 16 (the self-weight and other superimposed dead loads) and 21 (specified service live load), given in Table 4.1, is equal to $(16.9 - 6.1) = 10.8$ mm for the north panel and $(14.4 - 6.1) = 8.3$ mm for the south panel. The maximum deflection can be expressed as $L / 450$, and is less than the requirement given in A23.3 of $L / 360$, where $L = 4880$ mm is the span length.

4.6.2 Crack Widths

According to the commentary to the Canadian Standard, at service loads and for interior exposure, crack widths should be less than 0.4 mm.

Crack widths on the top surface of the slab measured at the service load of $q = 10.1$ kPa, and at a load of 13.06 kPa are shown in Figures 4.28 and 4.29, respectively. As shown in Figure 4.28, at service loads, the maximum crack width in regions with top reinforcement was about 0.4 mm for the north and the interior connections, and 0.25 mm for the south connection. These cracks are considered satisfactory according to the Standard.

In regions of negative curvature but without top reinforcement, the crack widths were as high as 1.0 mm. To avoid such wide cracks, it is recommended that, in addition to the flexural reinforcement, some minimum top steel be placed in these regions. Whether this additional steel is effective in resisting bending moments is not clear and requires further investigation.

In Figures 4.30 and 4.31, crack patterns at the bottom surface of the slab are shown at service load (10.1 kPa) and at 13.06 kPa load, respectively. The width of these cracks was less than 0.1 mm.

4.7 Disposal of the Specimen

After failure of all three connections, the instrumentation underneath the slab was removed. Scaffolding was placed under the slab. The lateral supports were removed. The edge restraining system was dismantled. Using the loading system with jacks pulling the slab slightly upward, the knife edge assembly, load cell, and roller underneath each column was removed and replaced with steel.

The load system, and the steel frames were dismantled, leaving the specimen resting on the scaffolding. The slab was then cut into four parts by a local contractor, because it was too heavy for the existing 10 ton crane and too large for a truck load. This also allowed observing the crack pattern at different cross sections of the punched area. Figure 4.34 shows the position of the cut lines.

Table 4.1 Selected Data - Description of Load Cases, and Deformations of the Plate

Load stage	Average jack load		Description of the load cases	Deflections due to jack loads (mm)				Continuous Edge	
	kN	Uniform load kPa		Max. in North panel	Max. in South panel	At the position of jack #1	At the position of jack #4	Overall expansion (mm)	sum of end rotations 10 ⁻³ Rad
2	0	4.32	Self-weight and super imposed loads	0	0	0	0	0	0
16	0	4.32	After adjusting the edge restraint	6.1	6.1	2.6	1.8	-0.1	1.52
18	50	8.27	Extension of E-W cracks to the edges	10.3	9.1	4.8	3.6	-0.54	3.87
21	72	10.1	Service load, crack width measured	16.9	14.4	8.6	6.4	-1.17	7.84
24	104	13.06	Crack width measured	28	26.3	15	13	-2.36	16.4
25	152	17.1	Punching failure of interior connections	55.2	56.1	26.5	27	-4.76	33.9
27	-----	-----	Retest of the exterior connections	62.5	63.5	30.8	29.1		
28	Jack #1	185 kN	Failure of the north edge connection	64.1	63.6	32.6	29.1		
29	Jack #4	188 kN			64.3		30.8		
30	Jack #4	238 kN	Max. moment at south edge connection		67.6		34.1		
31	Jack #4	248 kN	Failure of the south edge connection		69.5		37.8		
Predicted yield moment using tested material properties									

Table 4.2 Selected Data - Shear, Negative Moments at Column Center, and Positive Moments (based on load cells)

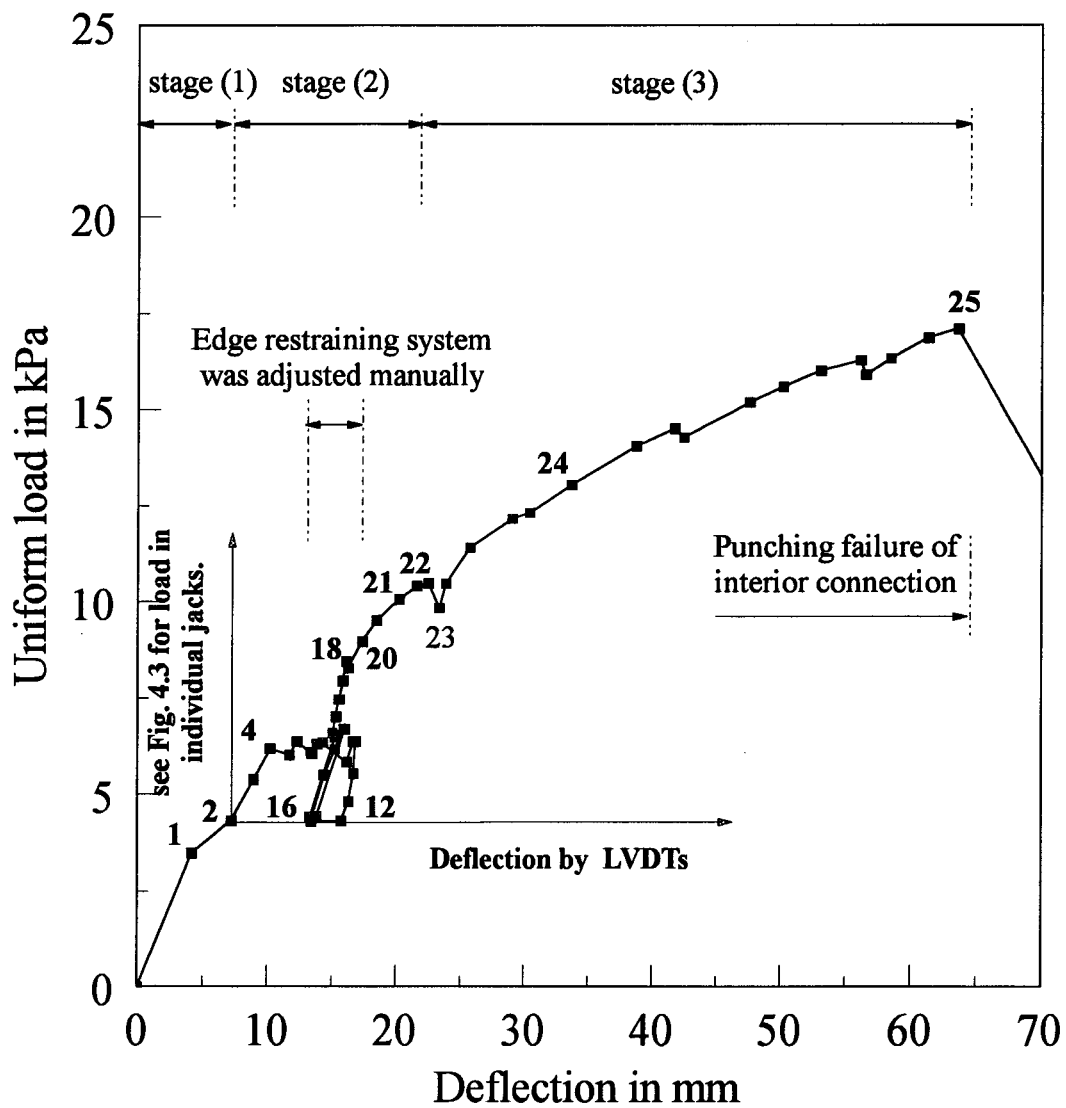
Load stage	shear (kN)			Negative moments at column center (kNm)			Positive moment at north panel		Positive moment at south panel		Positive moments at continuous edge (kNm)		
	North	Interior	South	North	Interior	South	M^+_{1x} (kNm)		M^+_{2x} (kNm)		North	Interior	South
	V_1	V_2	V_3	M^-_{1x}	M^-_{2x}	M^-_{3x}	load cell	gauge	load cell	gauge	M^+_{1y}	M^+_{2y}	M^+_{3y}
2	49.1	115.1	46.4	17	42	17.8	31.5	-----	27	-----	2.4	5.7	3.3
16	49.8	117.9	47.9	13.2	41	14.9	35.8	-----	30.8	-----	15	30.7	15.4
18	94.9	216.5	87.8	29.8	77.5	32	70.3	11.5	60.5	14	23.8	47.1	23.9
21	118.5	273	109.2	40.2	106.3	44.4	85.2	59.5	72	41.8	24.9	49.3	24.9
24	147.9	346.4	132.6	46.8	145.2	56.6	109.5	89.6	85.5	64.3	26.9	53.1	26.7
25	176.1	461.8	181.5	51.1	193.5	81	138.1	124.3	116.6	104	29.9	60.4	30.2
27	155.7		161.3	41.5		72.7	116	113.5	95.9	97.6	25.6		26.3
28	181		161.3	46.5		72.1	134.4	124	95.5	97.5	29.6		26.3
29			189.4			79.2			112.5	107.2			30.8
30			219.9			88			128.8	120.2			31.5
31			222			76.7			138.1	127.8			31.7
Predicted yield moment using tested material properties							159.5		130.7		45	90	45

Table 4.3 Selected Data - Negative Moments at the Face of Columns (kNm)

Load	x direction						y direction					
	north connection		interior connection		south connection		north connection		interior connection		south connection	
	load cell	gauge	load cell	gauge	load cell	gauge	load cell	gauge	load cell	gauge	load cell	gauge
2	11.3	5	33.4	15.5	12.4	8.4	22.9	5.8	46.9	12.9	22.9	7.3
16	7.4	7.4	32.2	18.6	9.3	14	12.3	17.6	22.8	27.4	12.3	13.9
18	18.2	12.2	61.2	39.4	21.3	18.7	26.7	27.2	54.2	43.9	26.7	19.4
21	25.7	21.1	85.7	68.6	31	27.7	39.2	39.7	78.1	61.6	39.2	26.5
24	28.5	29.7	119	102.2	40.2	40.3	52.4	58.6	105.5	92.4	52.4	42.5
25	29.3	33	158.5	155.1	58.5	57.8	78.5	73.6	155.5	155.8	78.5	69.6
27	22.2	21.8			52.7	53.4		64.6				61.5
28	24	22.6			52.2	53.3		68.7				61.4
29					55.6	53.8						65.3
30					60.6	55.4						74.2
31					49	46.8						76.6
Predicted yield values	30		154.1		73.9		76.2		149.2		76.2	

Table 4.4 Moment -Strain Relationships used at Different Locations of the Specimen

Location of moment to be determined	Slab reinforcing bar	Beam	Equation	Comment
Negative moment at south connection perpendicular to the free edge	M15 @ 100 mm d = 124	beam 4	3.8	
Negative moment at south connection parallel to the free edge	M15 @ 200 mm d = 108	beam 2	3.6	Adjusted for bar spacing
Negative moment at north connection perpendicular to the free edge	M10 @ 100 mm d = 122	beam 3	3.7	Same reinforcement ratio as M15 @ 200 mm
Negative moment at north connection parallel to the free edge	M15 @ 200 mm d = 108	beam 2	3.6	Adjusted for bar spacing
Negative moment at the interior connection, N-S direction	M15 @ 150 mm d = 124	beam 1	3.5	
Negative moment at the interior connection, E-W direction	M15 @ 150 mm d = 108	beam 2	3.6	
Positive moment in the N-S direction north panel	see Fig. 3.9 d = 124	beam 3 beam 4	3.7 3.8	Different bar spacing at the column and middle strips
Positive moment in the N-S direction south panel	see Fig. 3.10 d = 124	beam 3 beam 4	3.7 3.8	Different bar spacing at the column and middle strips

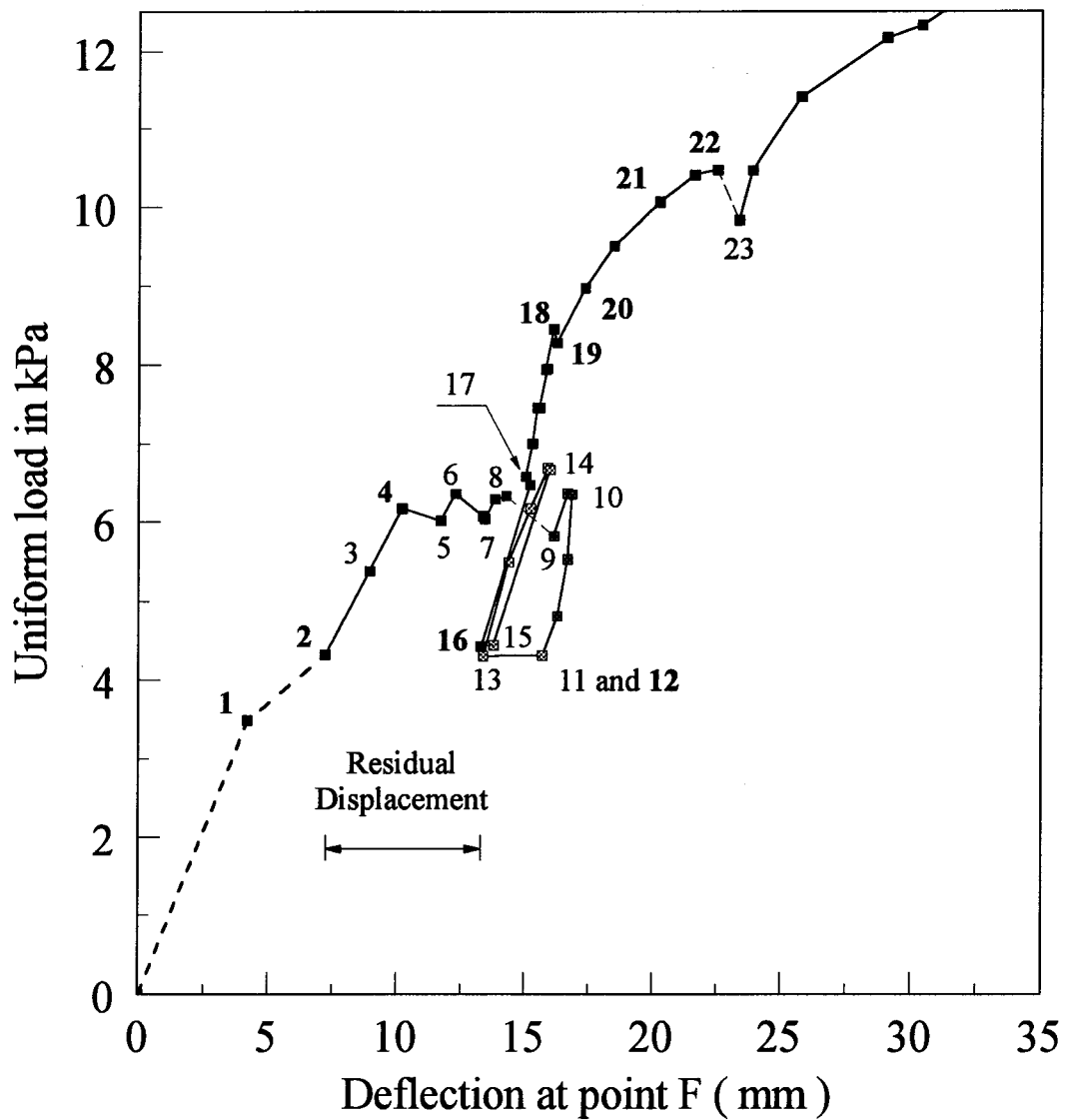


1	day 28	Dead load at the time of removing forms
2	day 65	Self-weight plus superimposed dead load
4	day 65	Longitudinal crack running N-S formed.
12	day 69	Adjusting the edge restraining system started
18	day 70	Transverse crack running E-W formed.
20	day 70	Last adjustment of the edge restraint
21	day 70	service load; Positive cracks formed.
25	day 71	Failure of interior connection

* Deflections are at point F in figure 3.22.

** Effects of self-weight of specimen and superimposed dead loads are included in both axes.

Figure 4.1a Load-deflection diagram - full loading history



1	day 28	Dead load at the time of removing forms
2	day 65	Self-weight plus superimposed dead load
3-8	day 65	Preliminary loading
9-11	day 68	Unloading
12-15	day 69	Preliminary loading after adjusting the edge restraint
16-22	day 70	Loading to about service load
23-25	day 71	Loading up to failure of interior connection

* All dates are after casting the specimen

Figure 4.1b Load-deflection diagram - enlarged portion

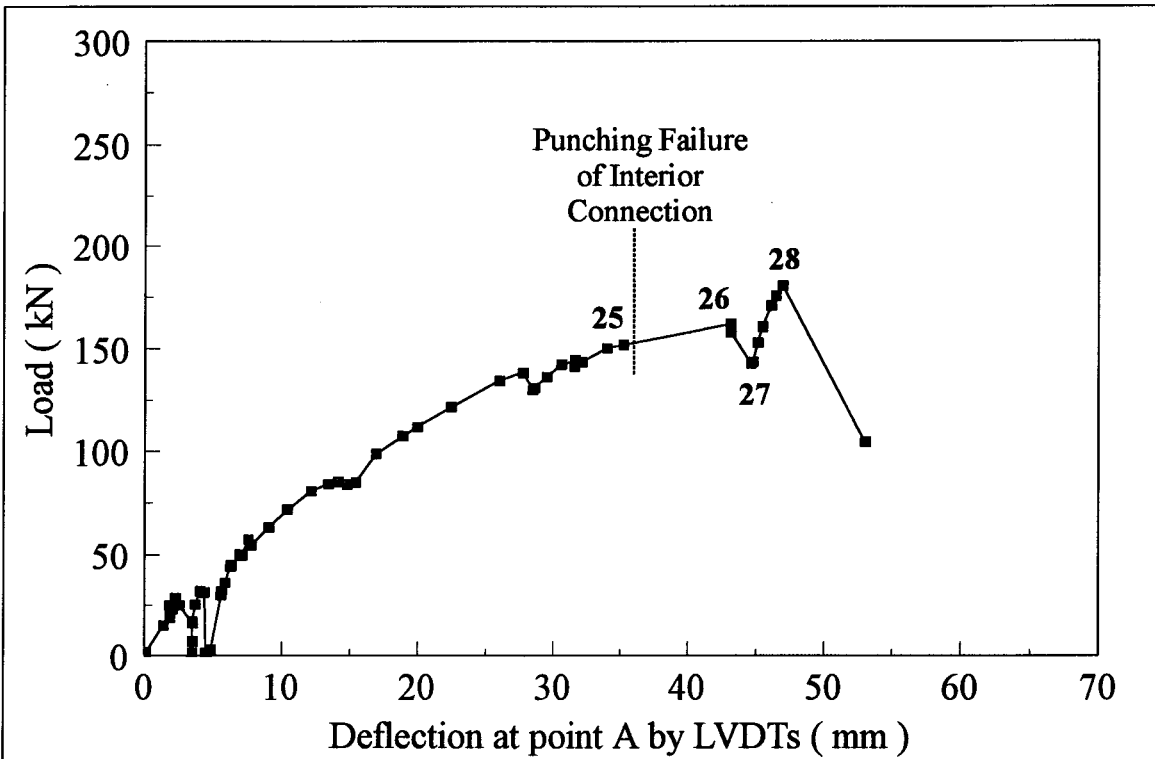


Figure 4.2 Load in jack #1 versus the deflection of the specimen

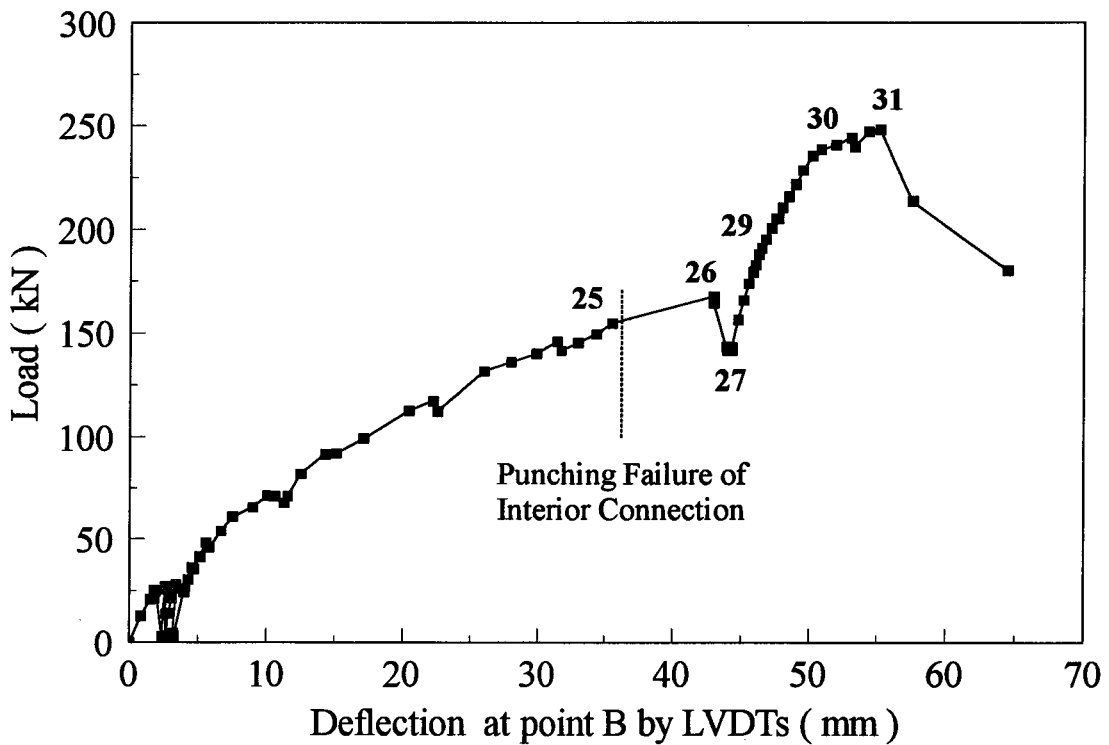


Figure 4.3 Load in jack #4 versus the deflection of the specimen

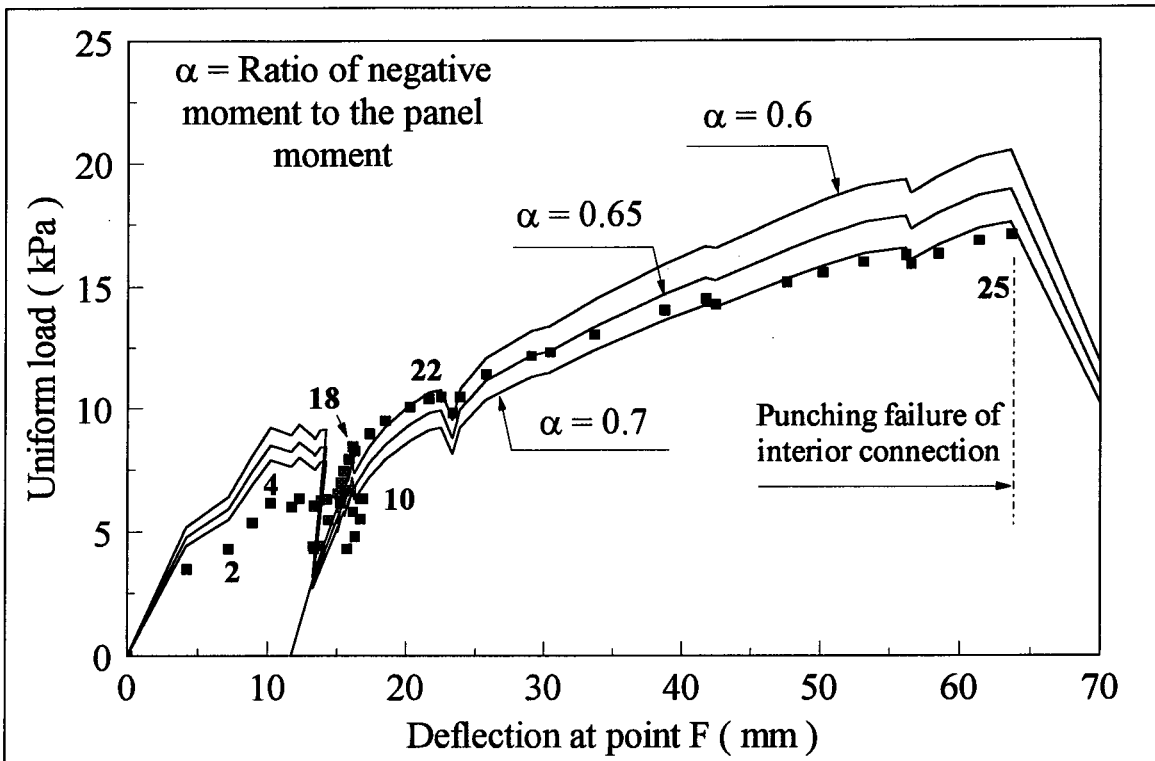


Figure 4.4 Load-Deflection Diagram - Ideal Edge Restraint

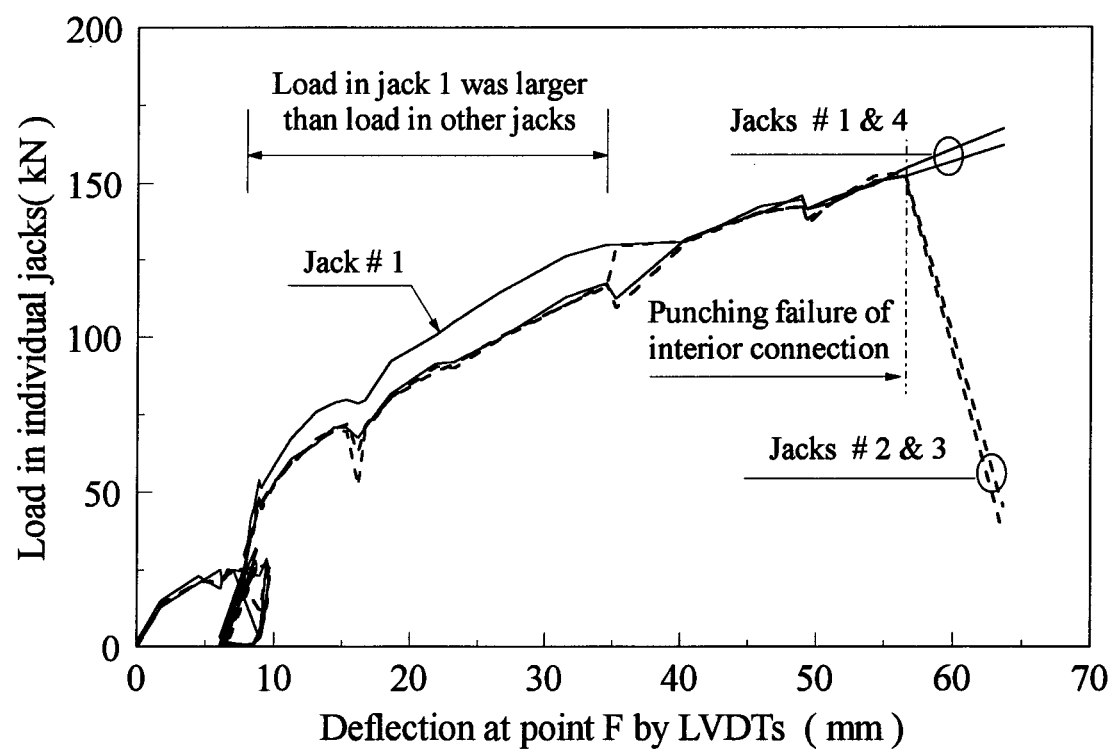


Figure 4.5 Load in jacks versus deflection of specimen

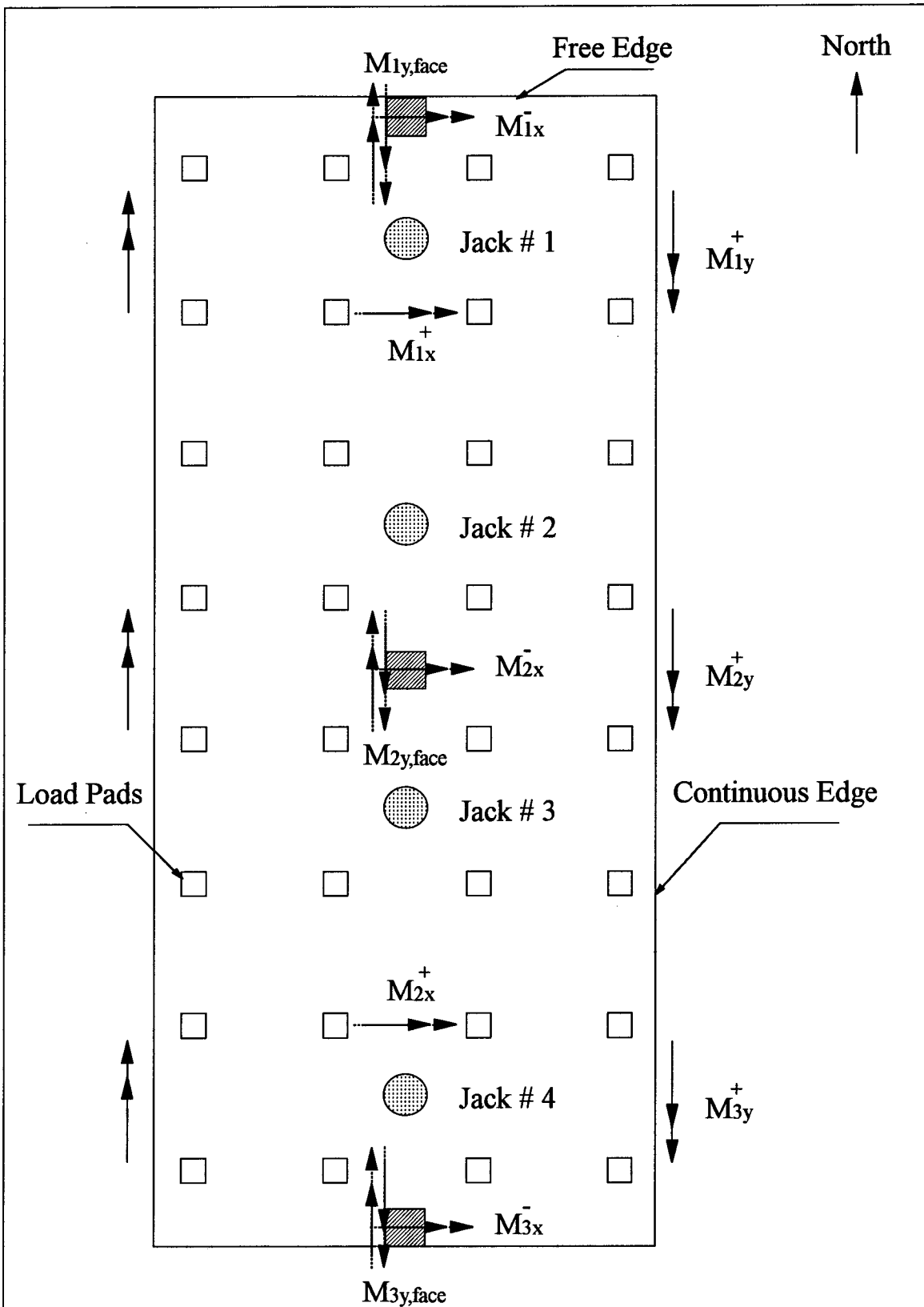
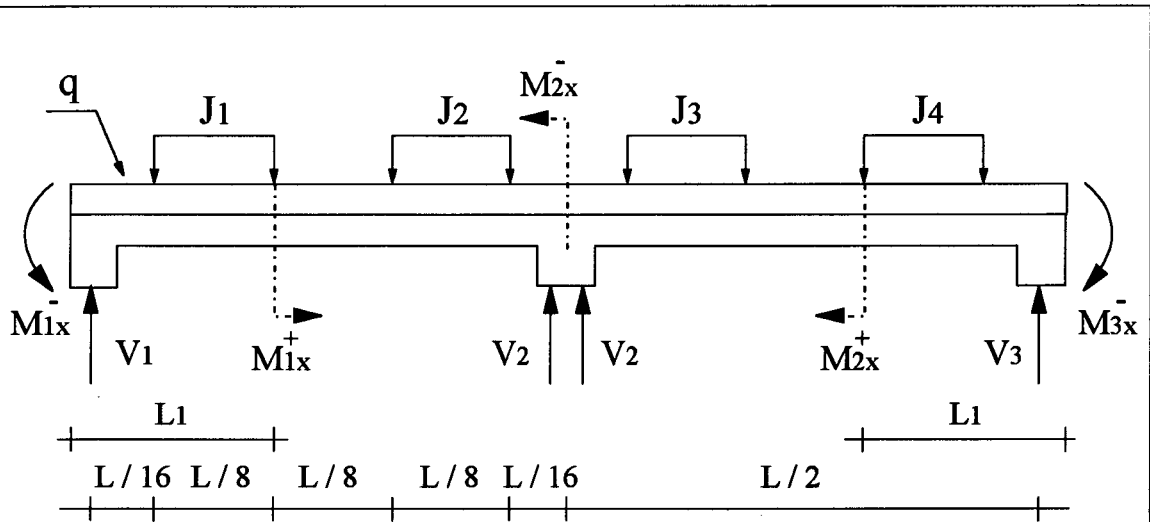
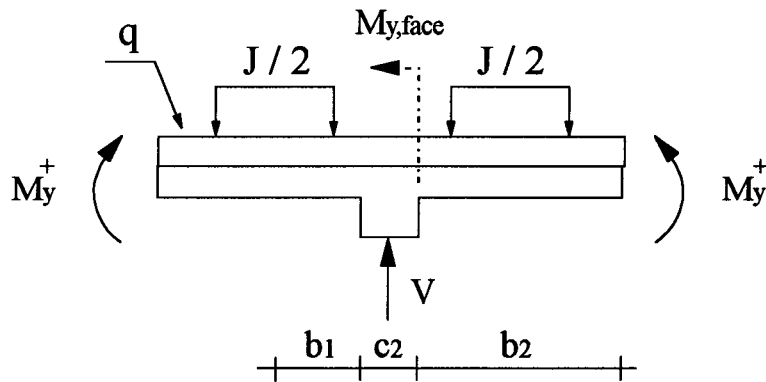


Figure 4.6 Definition and position of loads and moments

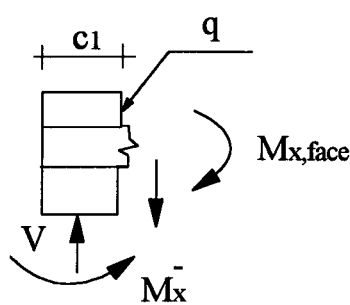


$J_i = \text{Force in Jack \#}i$

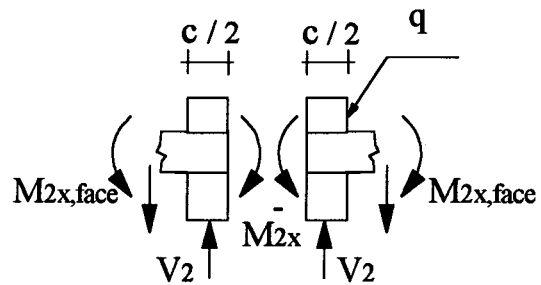
(a) In North-South Direction



(b) In East-West Direction



(c) Edge Connections



(d) Interior Connection

Figure 4.7 Free Body Diagrams

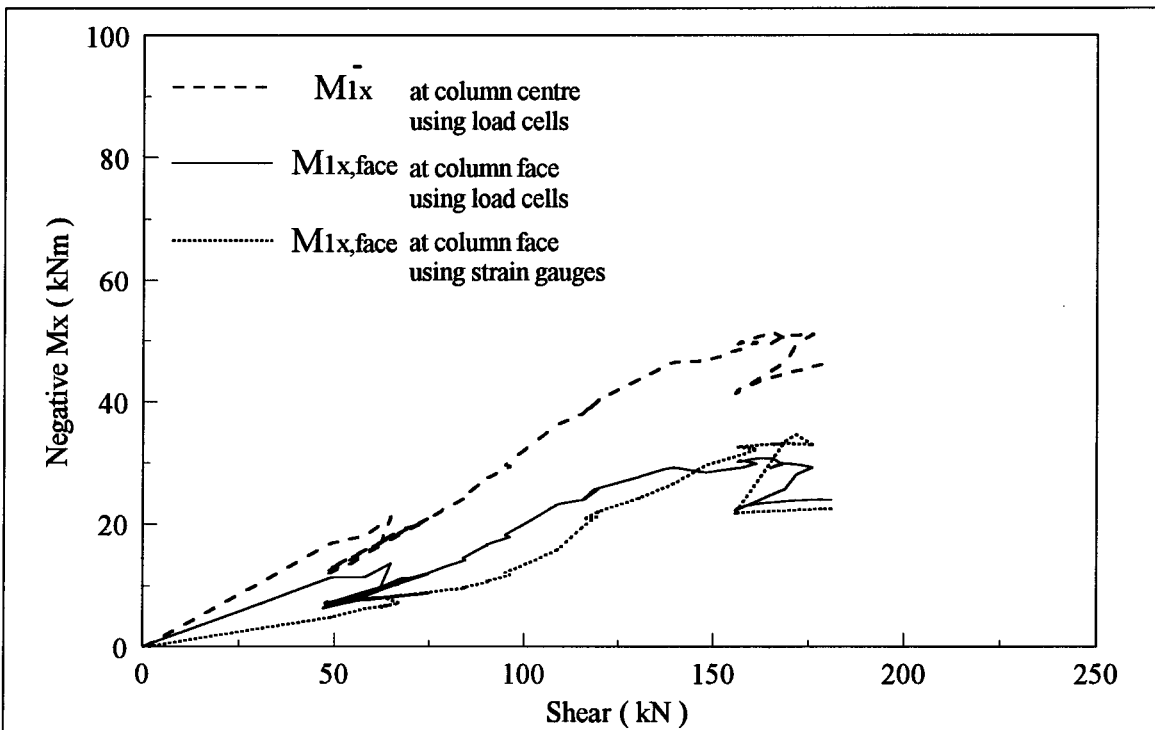


Figure 4.8 Moment -shear diagrams of the north connection

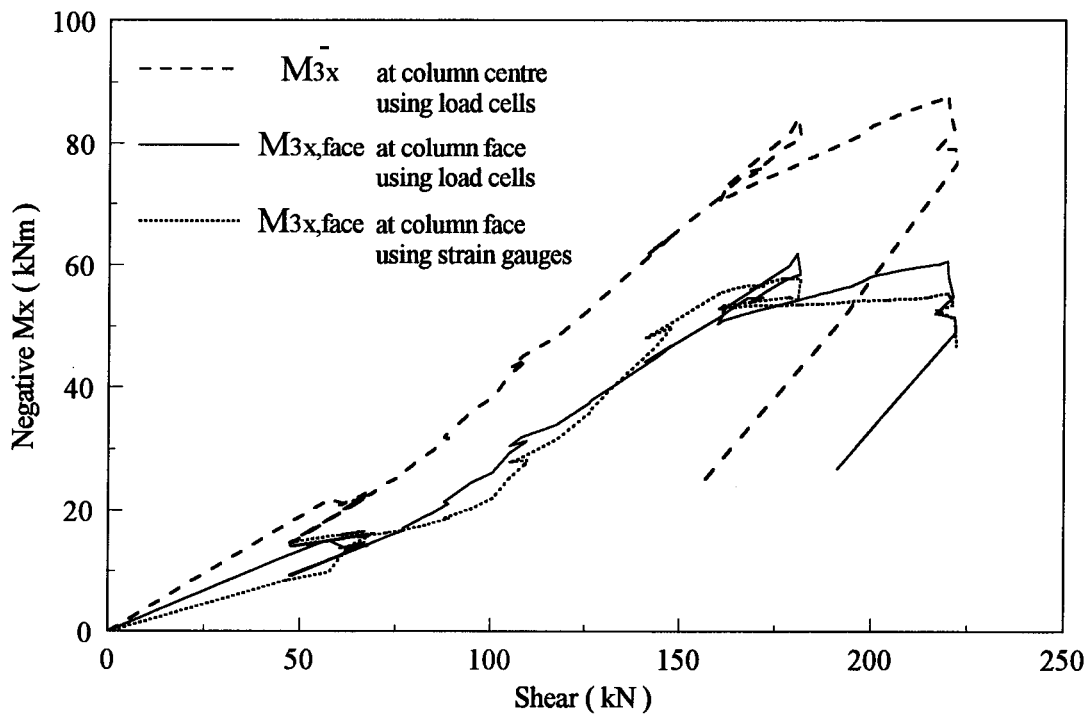


Figure 4.9 Moment -shear diagrams of the south connection

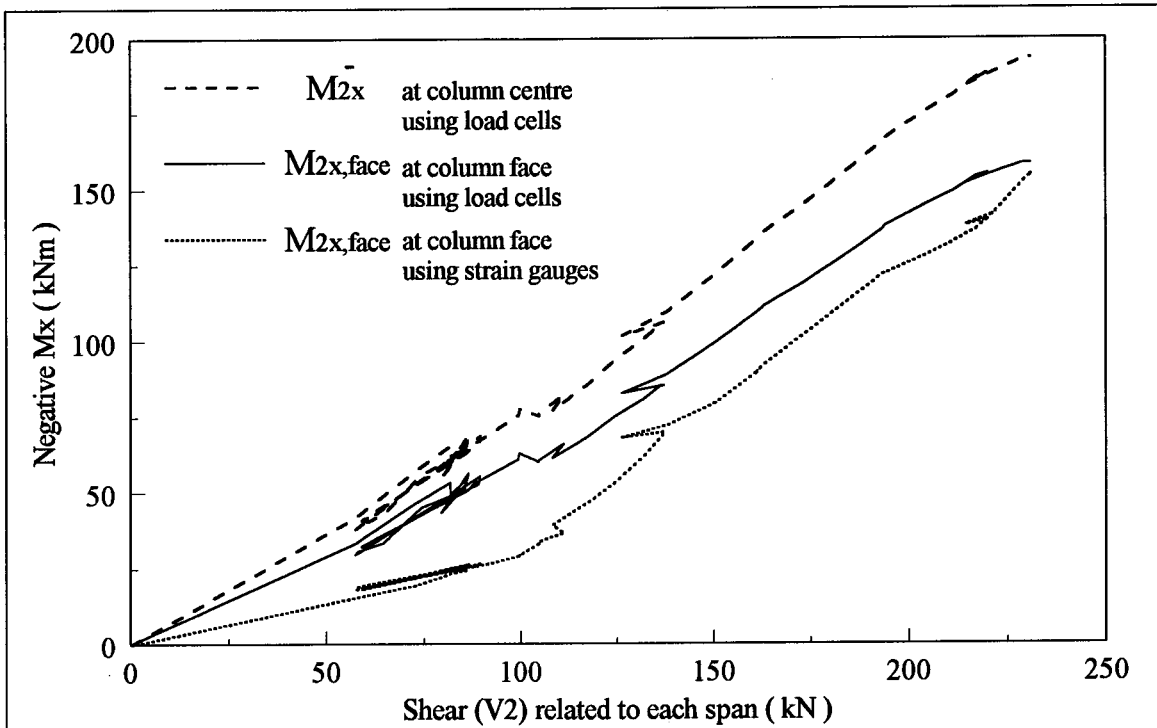


Figure 4.10 Moment-shear diagrams of the interior connection

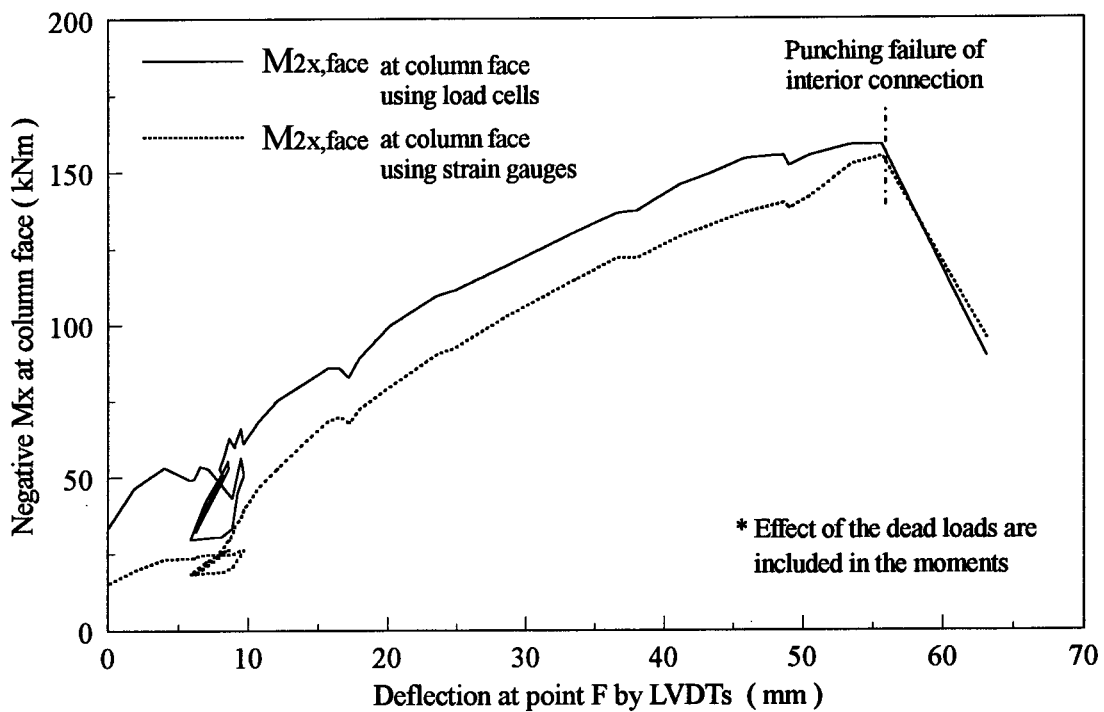


Figure 4.11 Negative moment in the x direction at the face of the interior column versus deflection of the specimen

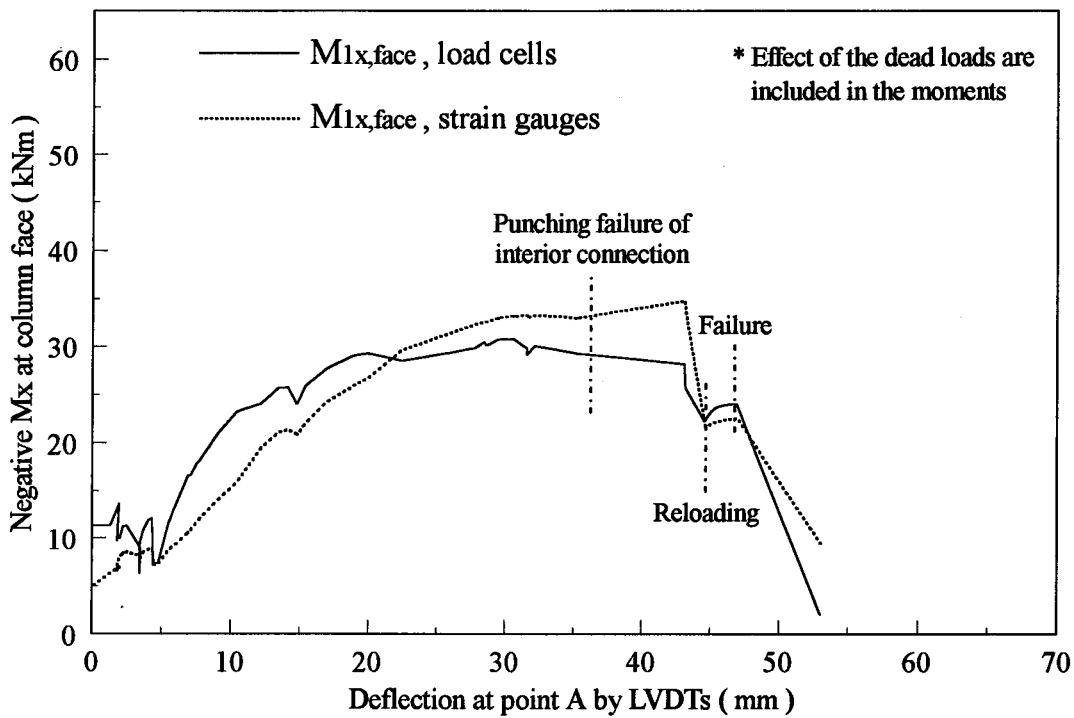


Figure 4.12 Negative moment in the x direction at the face of the north column versus the deflection of the specimen

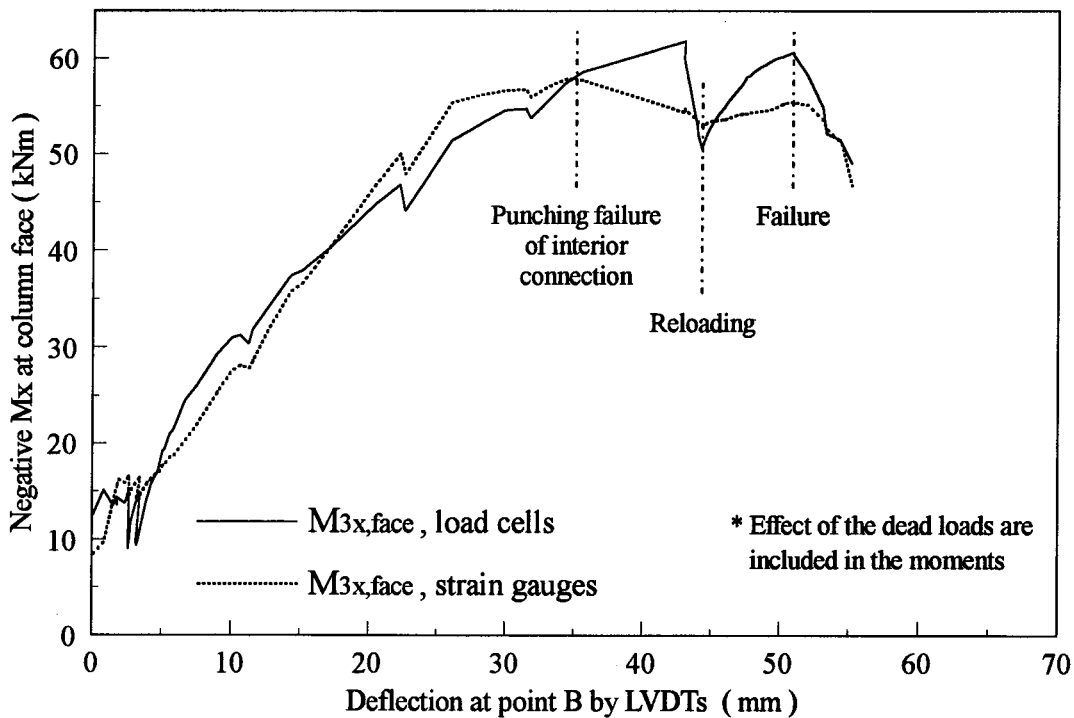


Figure 4.13 Negative moment in the x direction at the face of the south column versus the deflection of the specimen

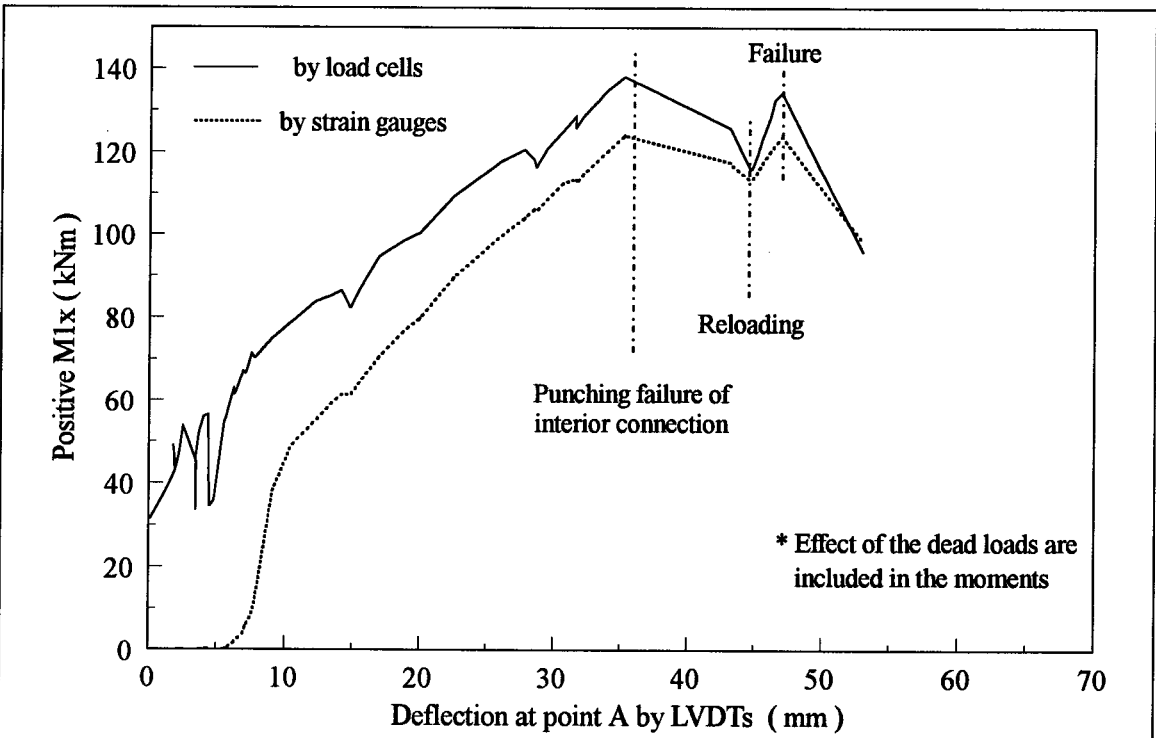


Figure 4.14 Positive moment in x direction, north panel

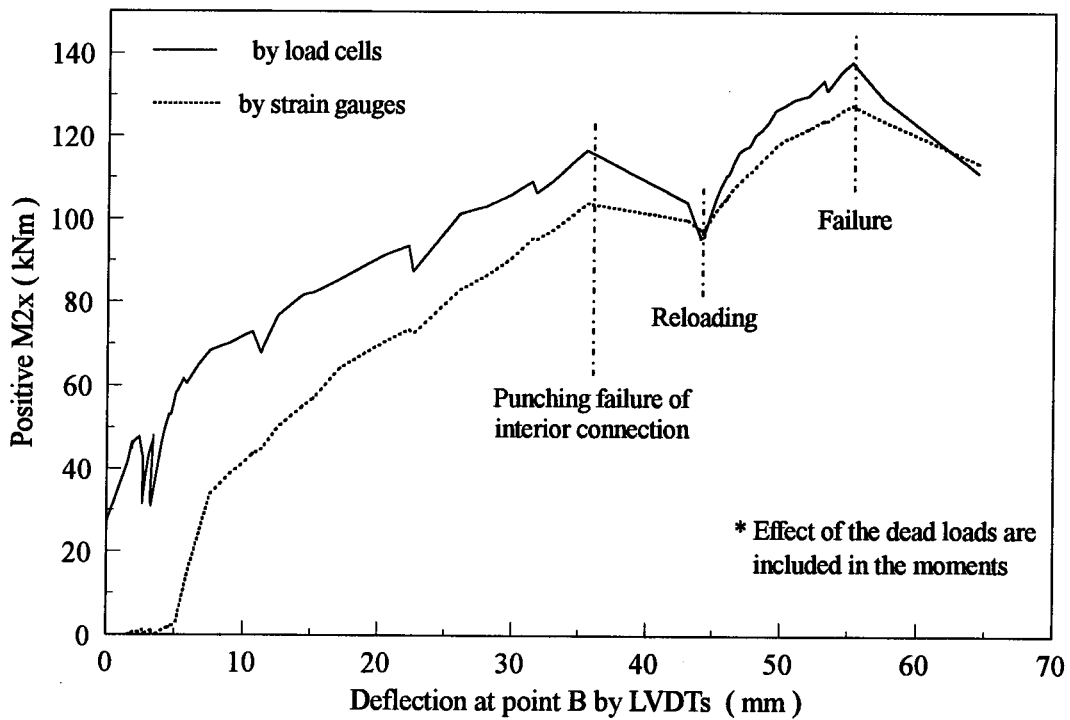


Figure 4.15 Positive moment in x direction, south panel

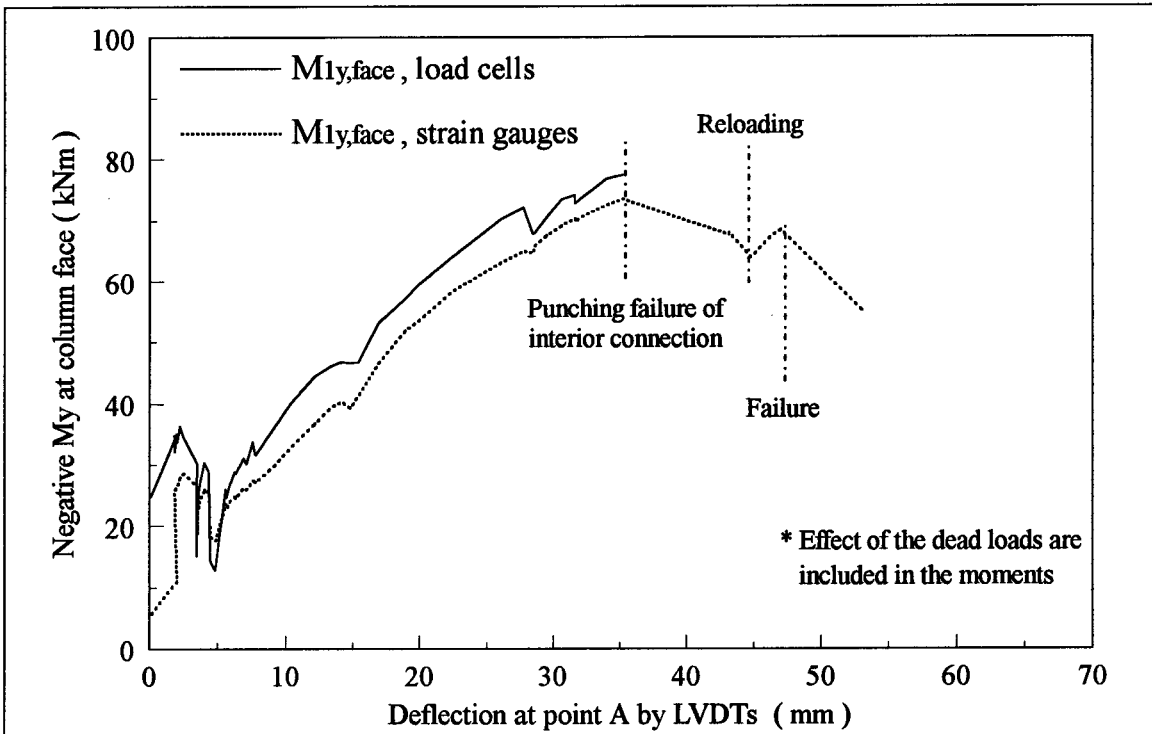


Figure 4.16 Negative moment in the y direction at the face of the north column versus the deflection of the specimen

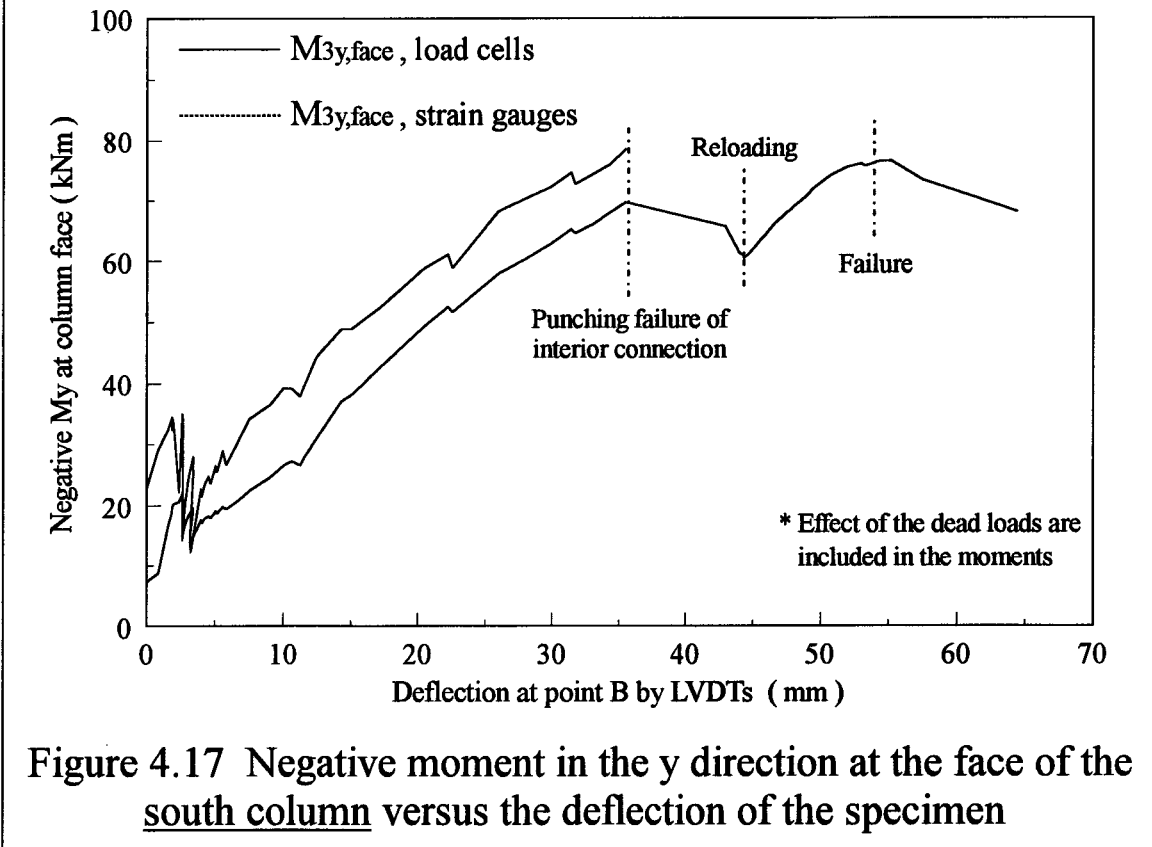


Figure 4.17 Negative moment in the y direction at the face of the south column versus the deflection of the specimen

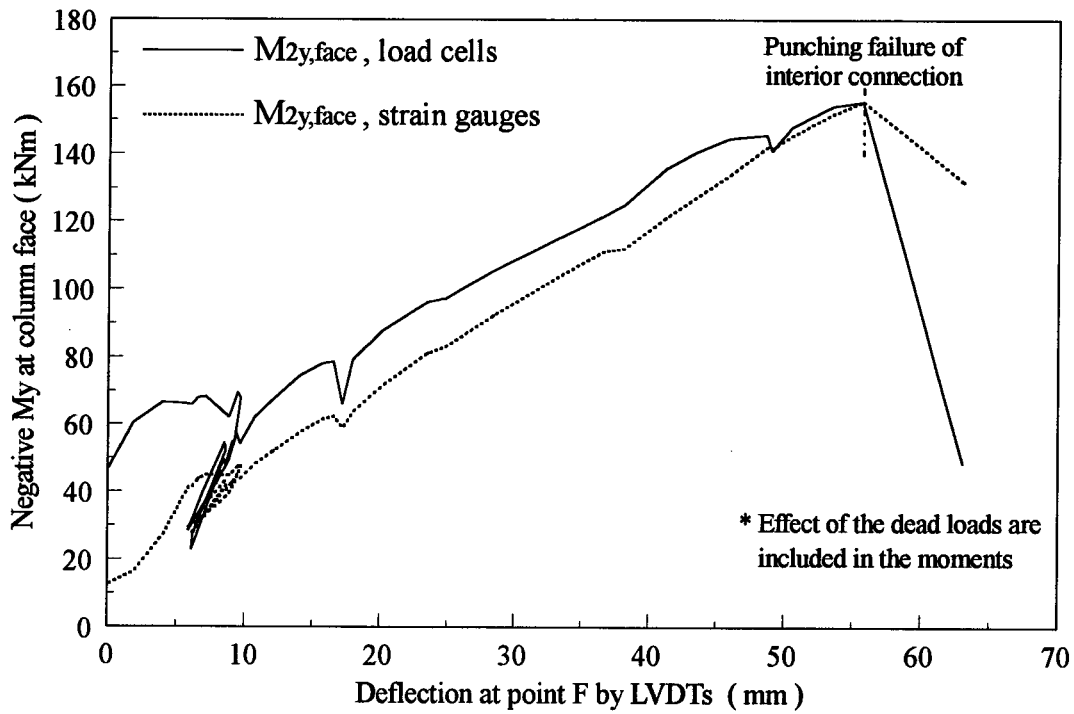


Figure 4.18 Negative moment in the y direction at the face of the interior column versus the deflection of the specimen

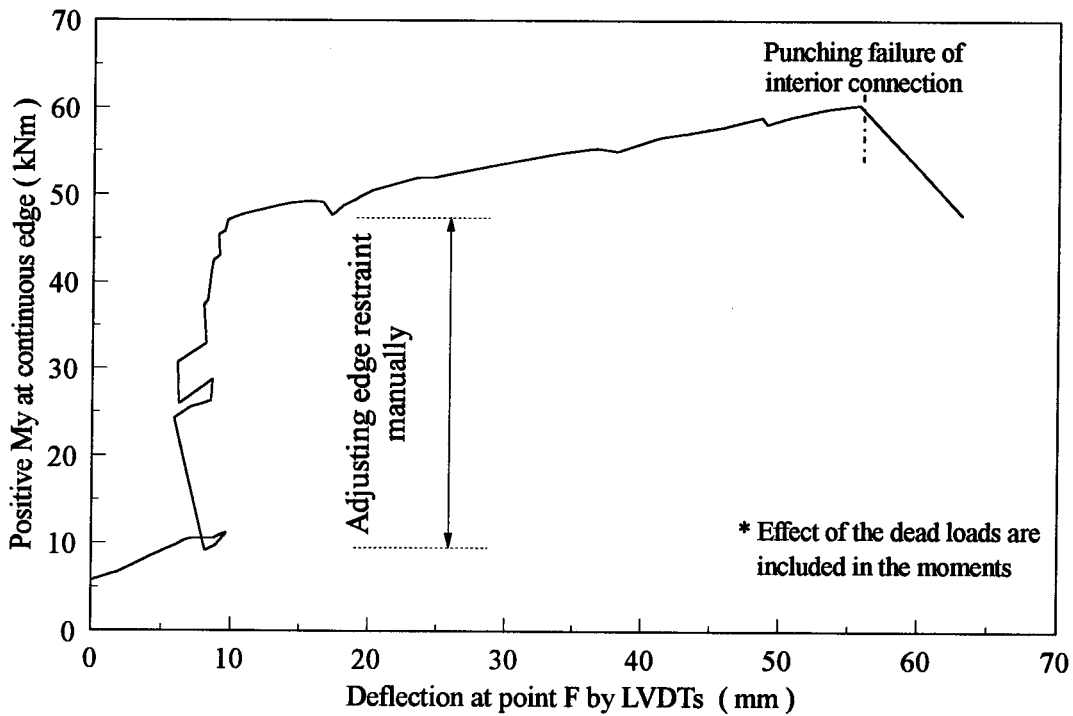


Figure 4.19 Positive moment in the y direction at the continuous edges versus the deflection of the specimen

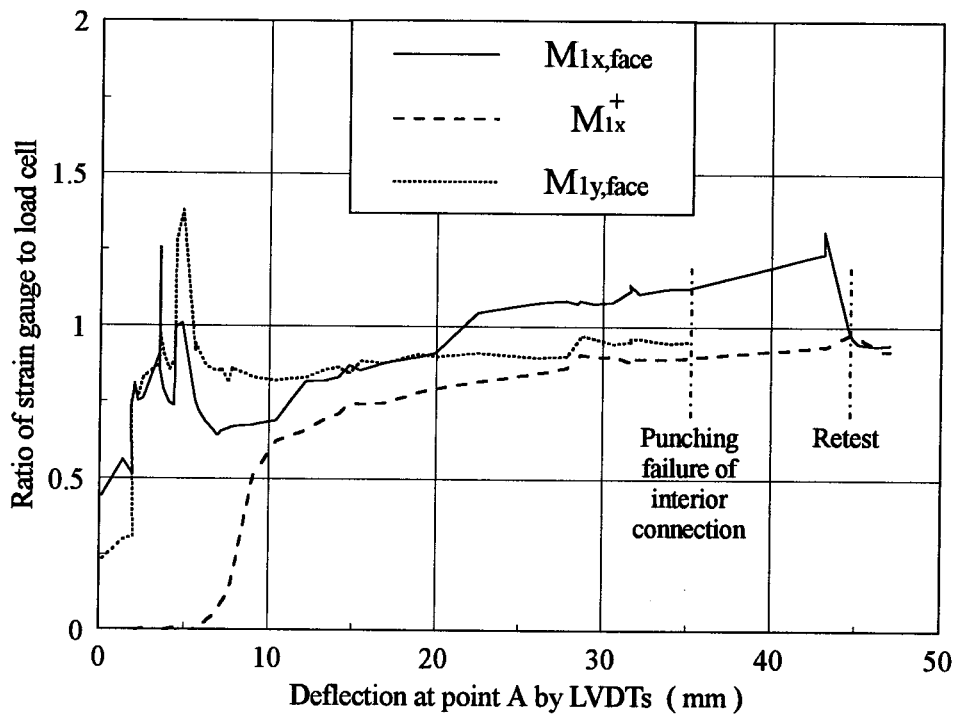


Figure 4.20 Comparison of the external measurements with the internal measurements in the north connection

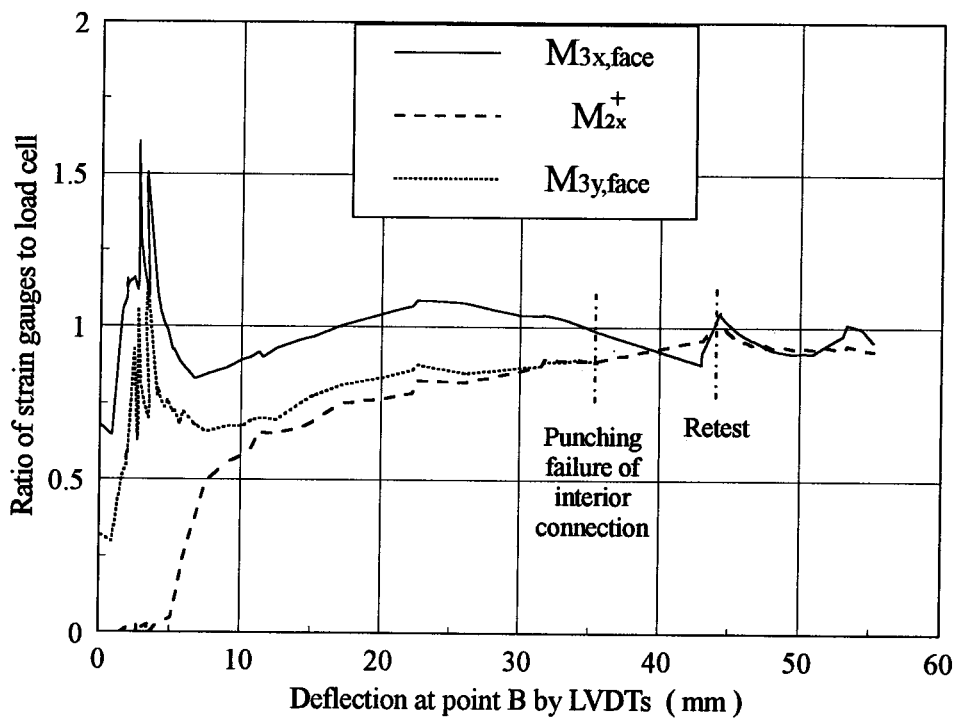


Figure 4.21 Comparison of the external measurements with the internal measurements in the south connection

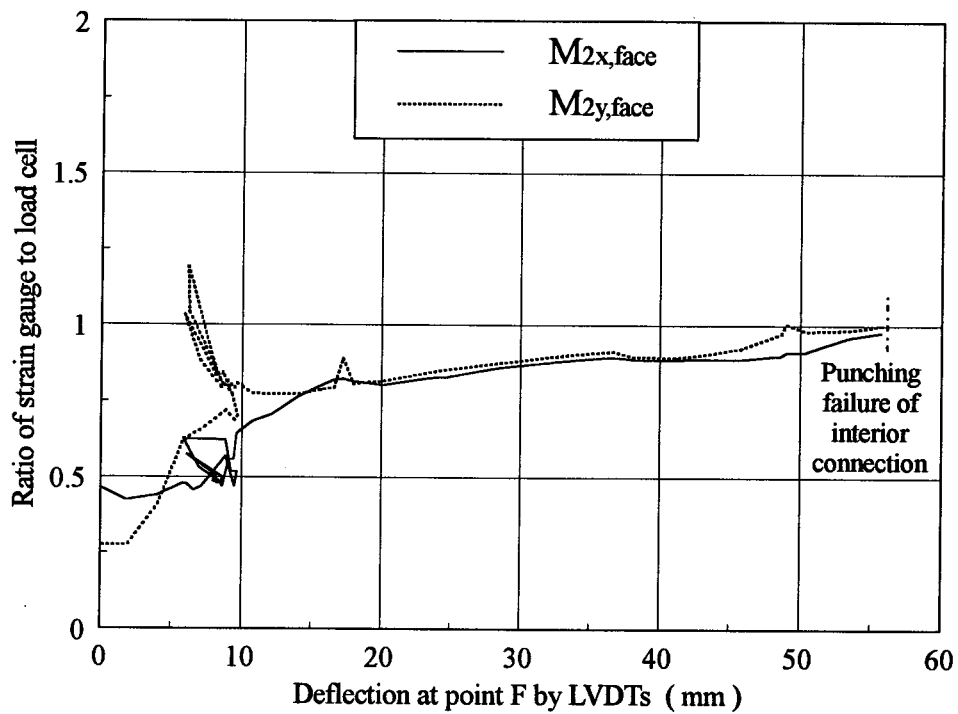


Figure 4.22 Comparison of the external measurements with the internal measurements in the interior connection

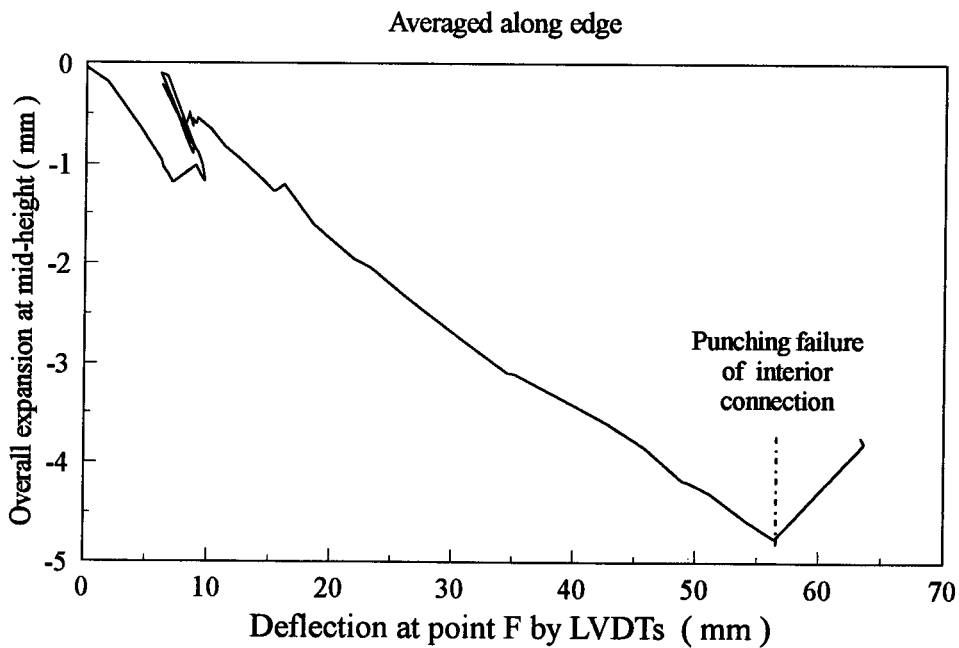


Figure 4.23 Overall expansion at mid-height of the continuous edge

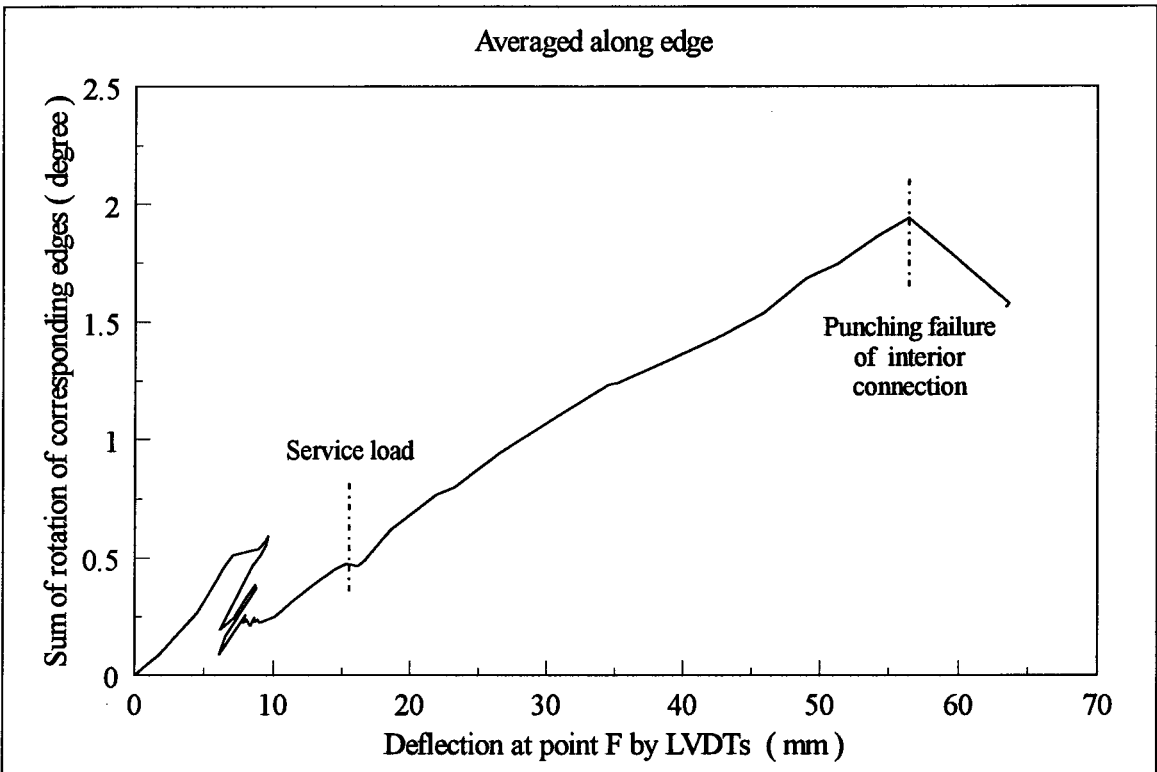


Figure 4.24 Sum of rotation of corresponding continuous edges

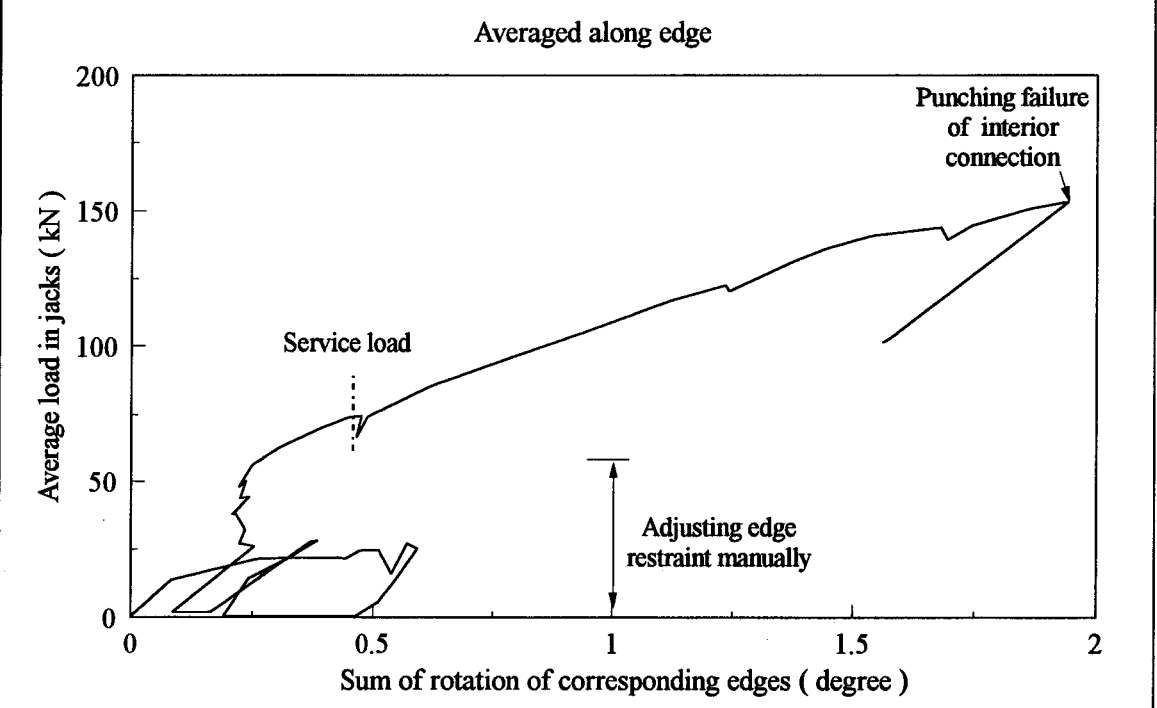
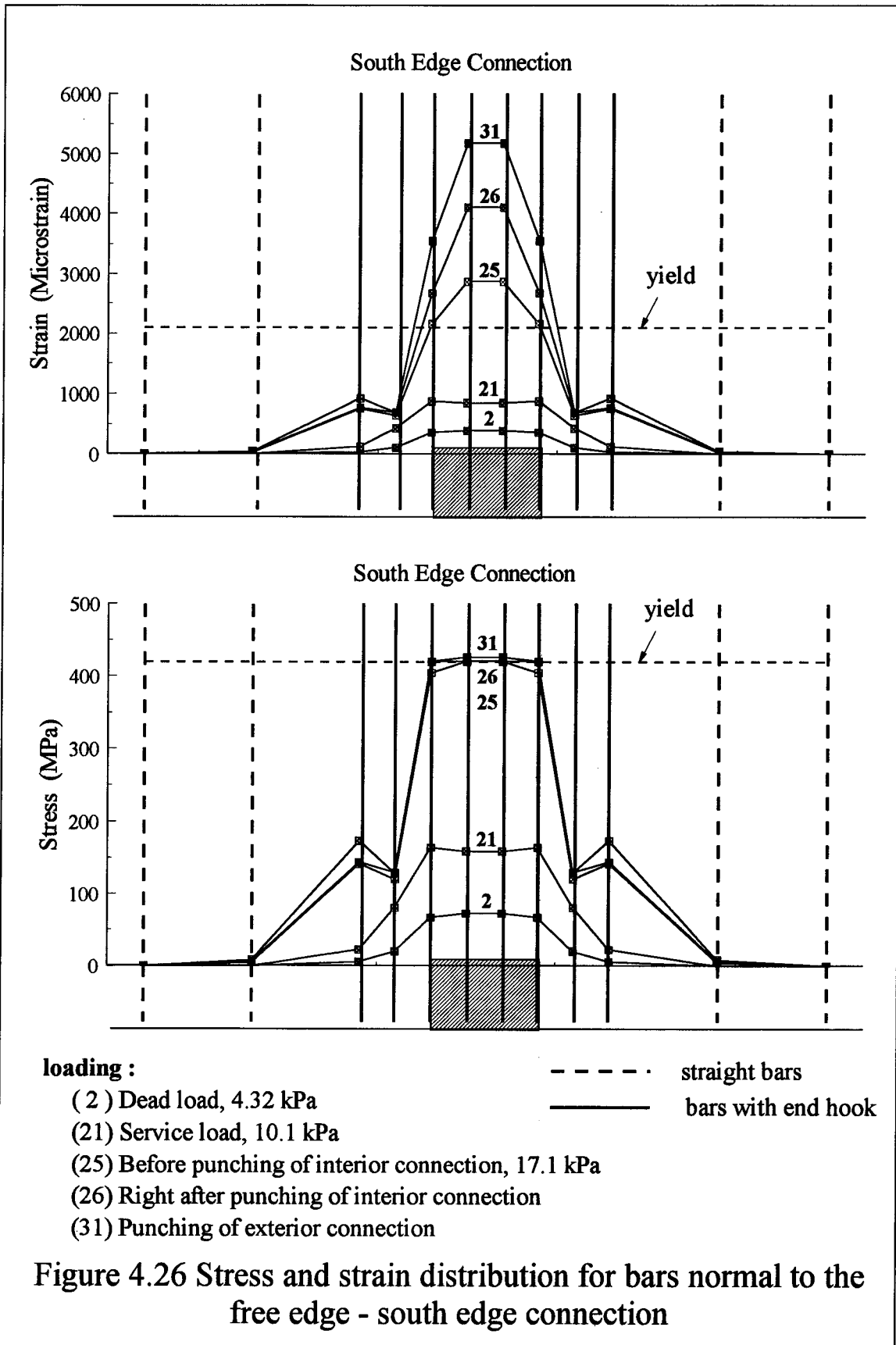
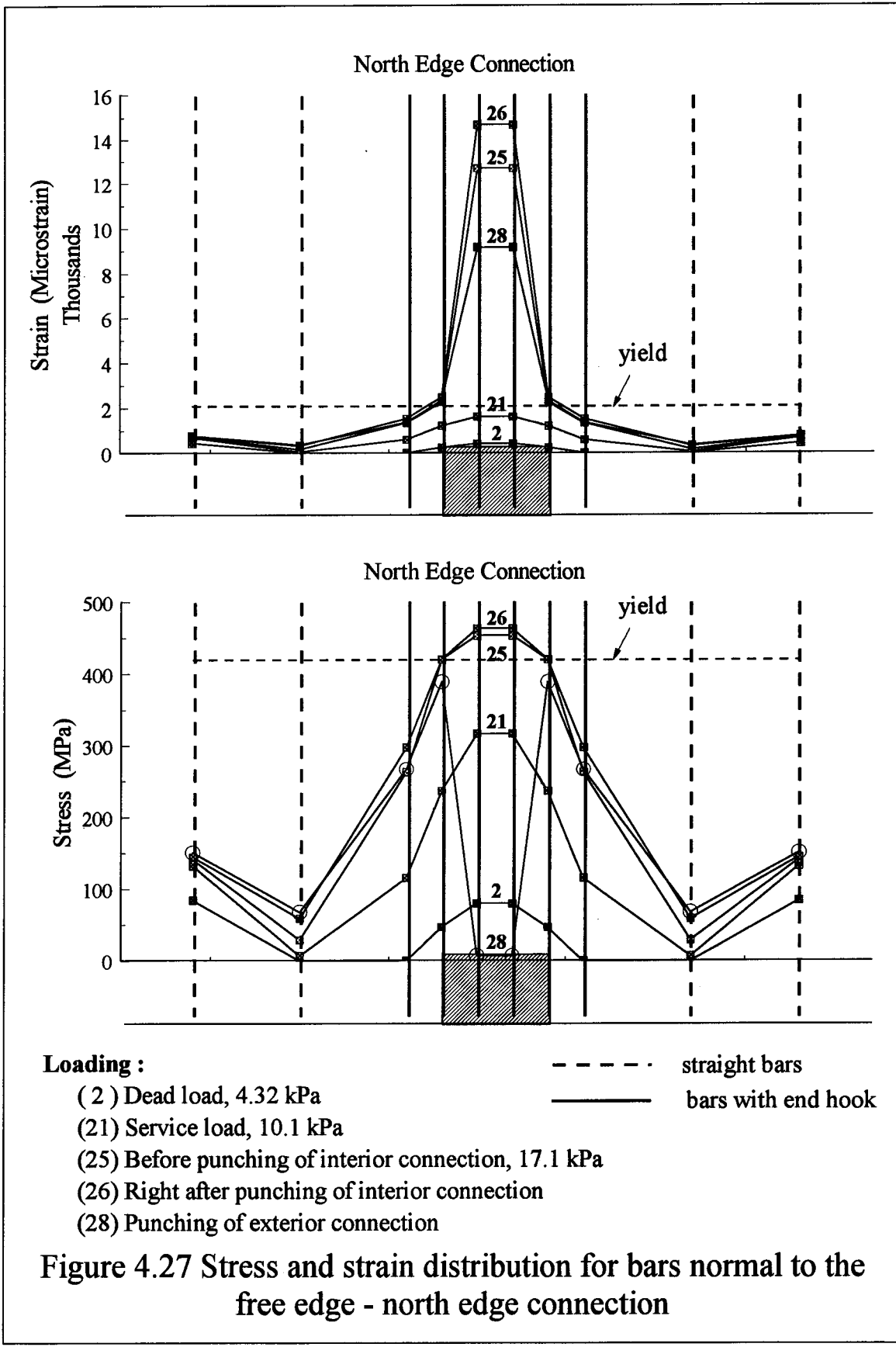


Figure 4.25 Average load in jacks versus the rotation of the continuous edge





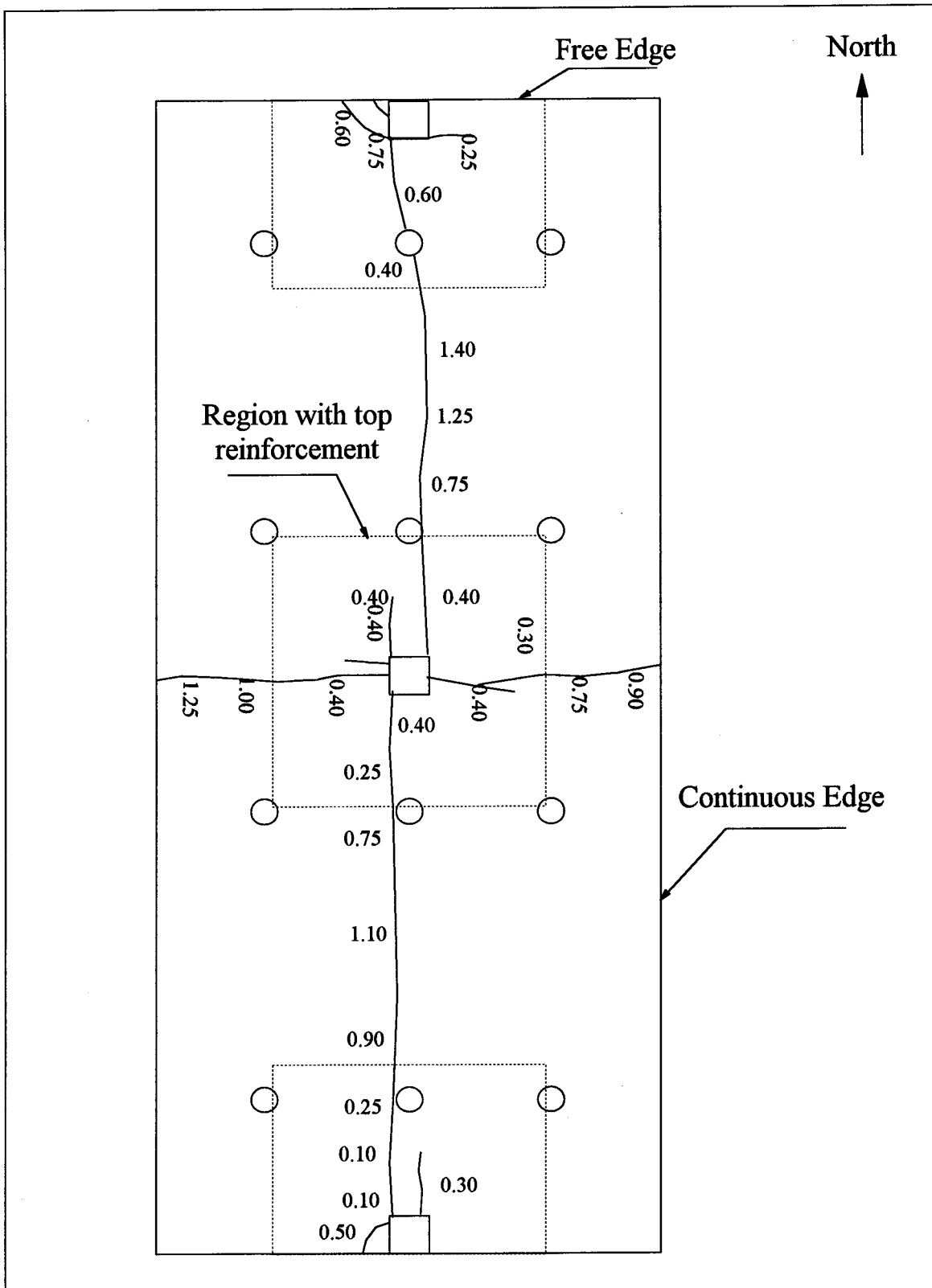


Figure 4.29 Crack widths in mm at the load of 13.06 kPa, top surface

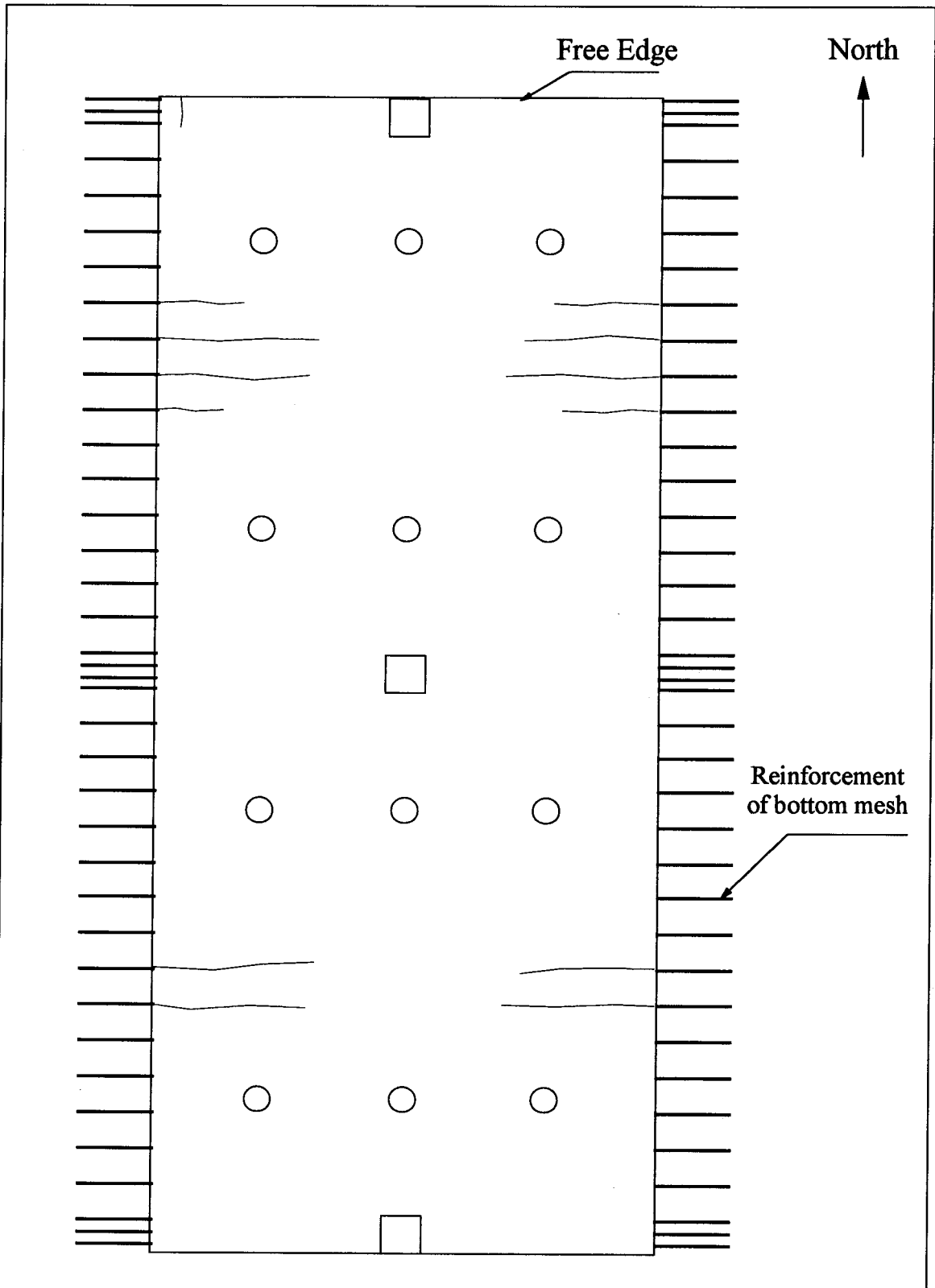


Figure 4.30 Crack pattern underneath the slab at service load, $q = 10.1 \text{ kPa}$

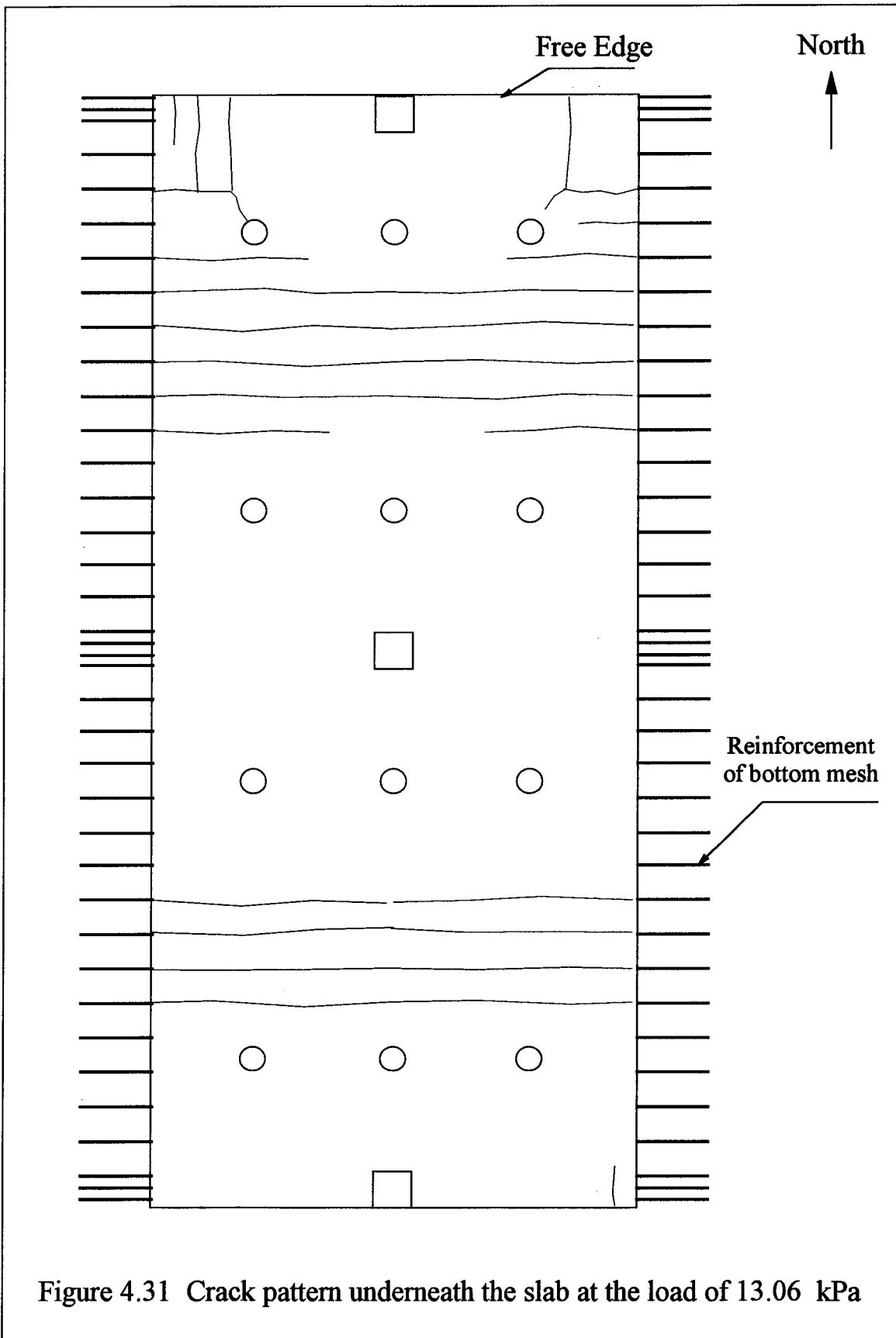


Figure 4.31 Crack pattern underneath the slab at the load of 13.06 kPa

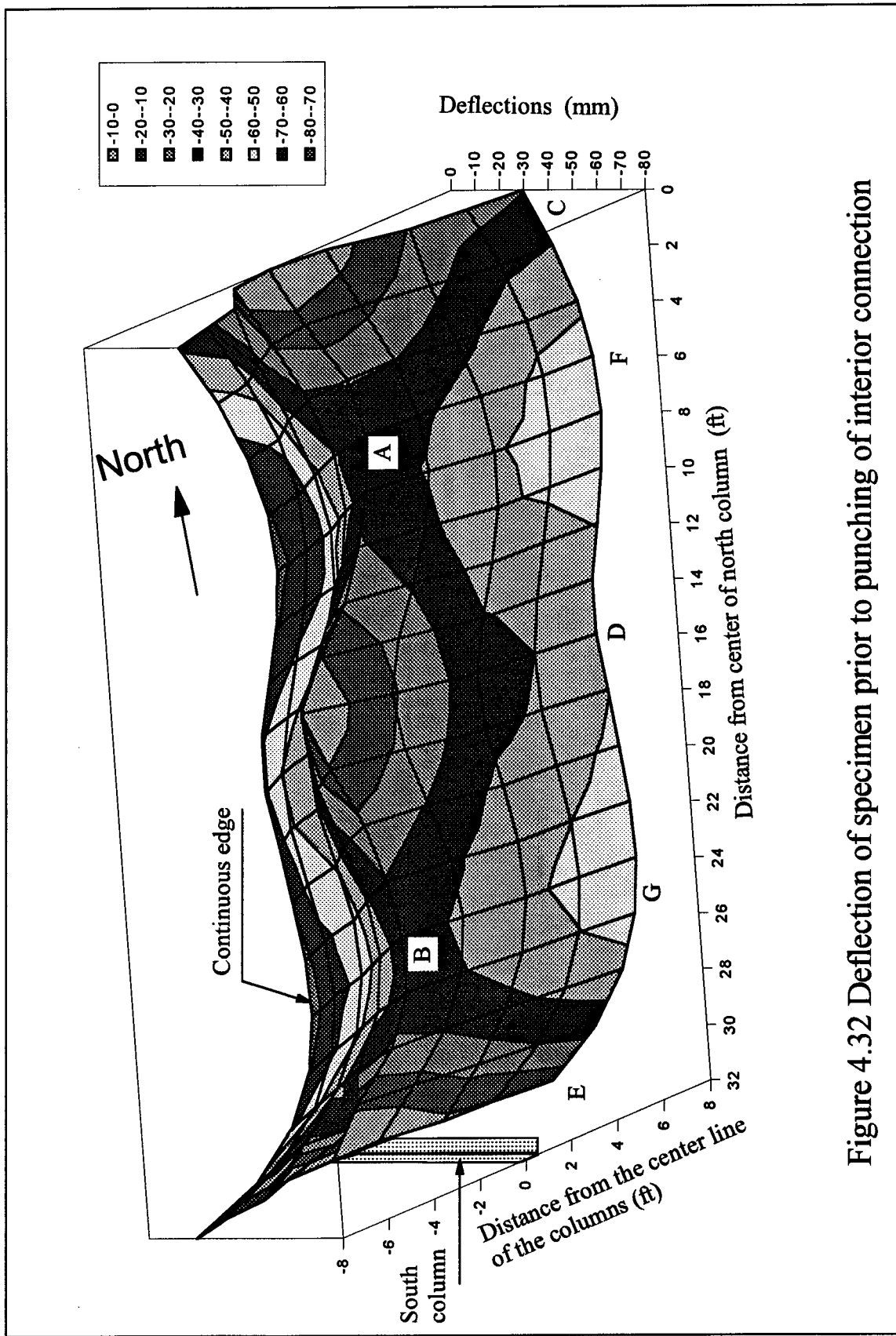
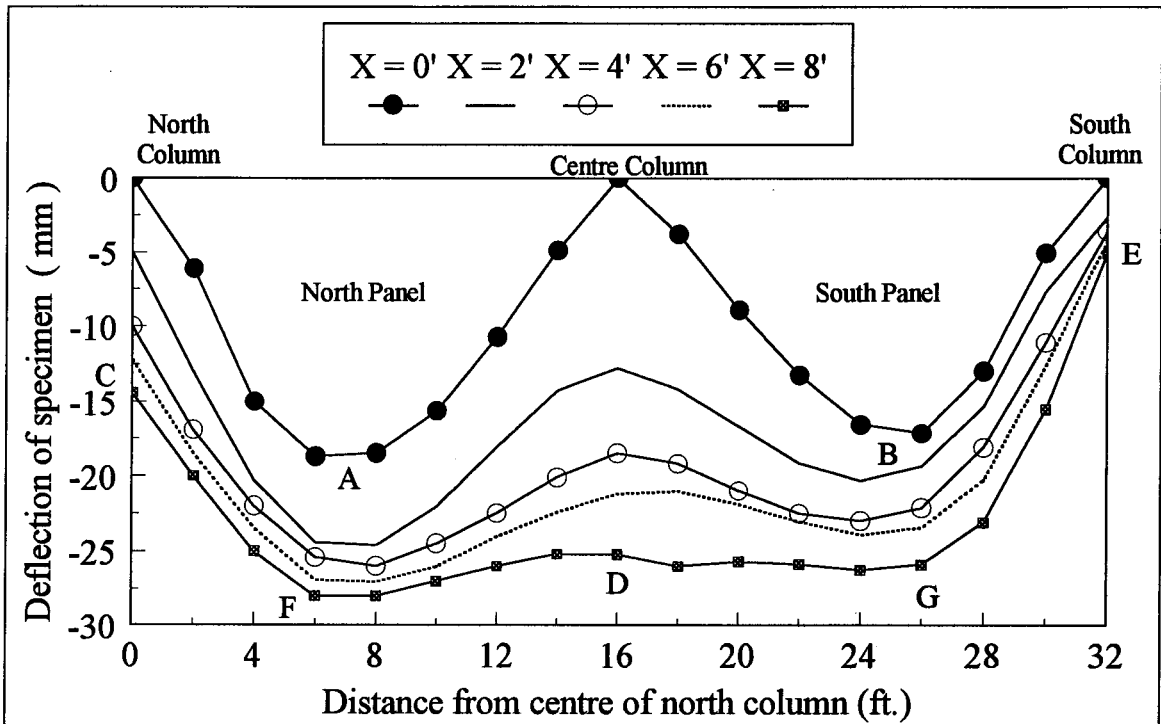
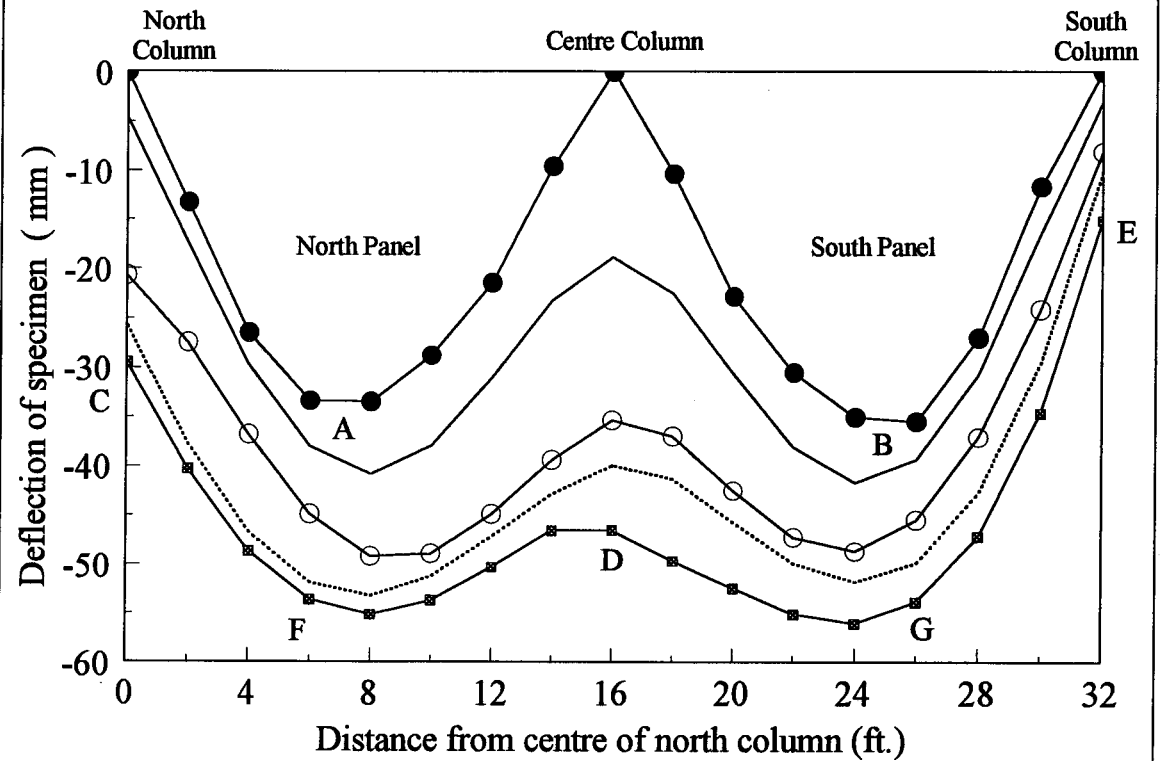


Figure 4.32 Deflection of specimen prior to punching of interior connection



(a) At the load of $q = 13.06$ kPa



(b) Right before punching of interior connection, $q = 17.1$ kPa

Figure 4.33 Deflection of specimen

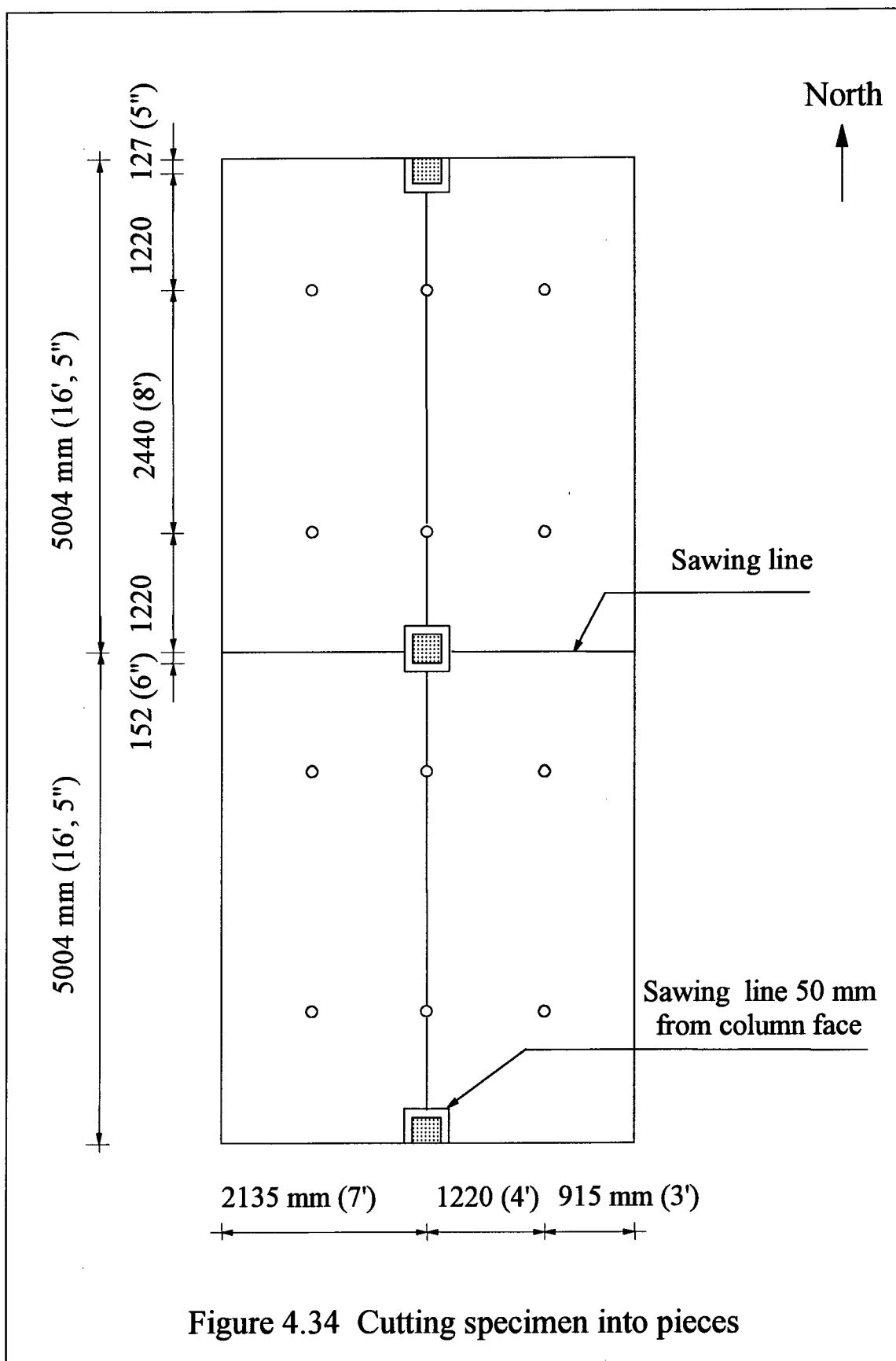


Figure 4.34 Cutting specimen into pieces

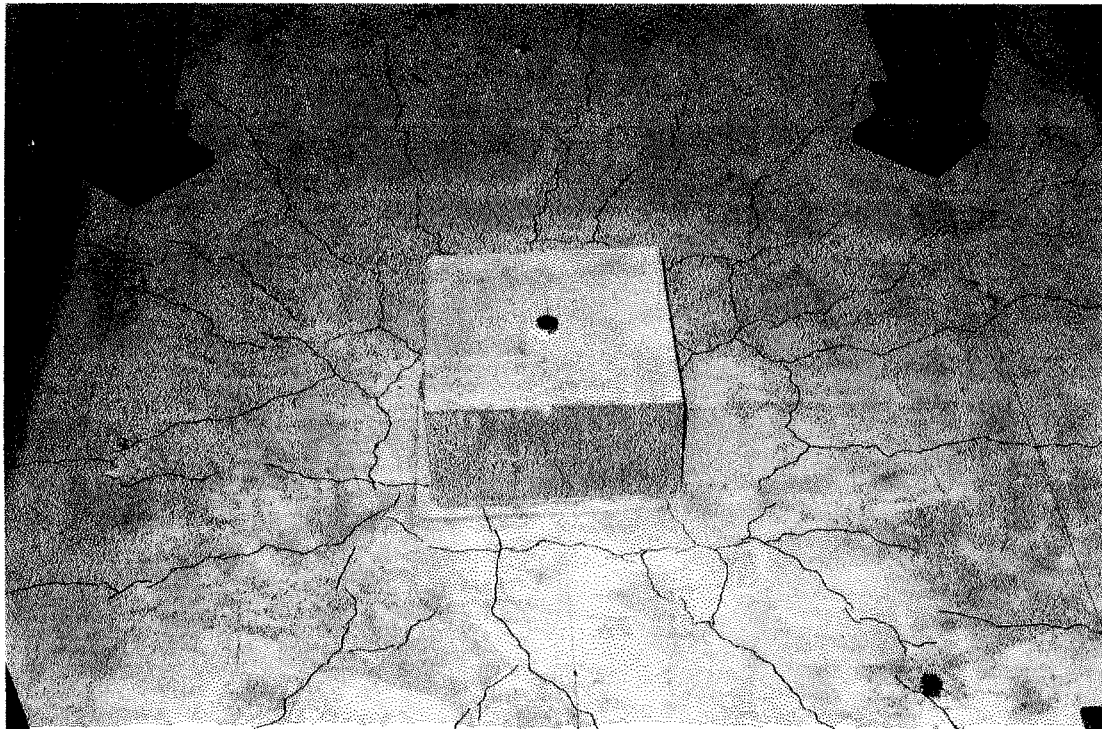


Figure 4.35 Crack pattern around interior column, load stage 2 in table 4.1 (crack widths less than 0.1 mm)



Figure 4.36 Punching of interior connection

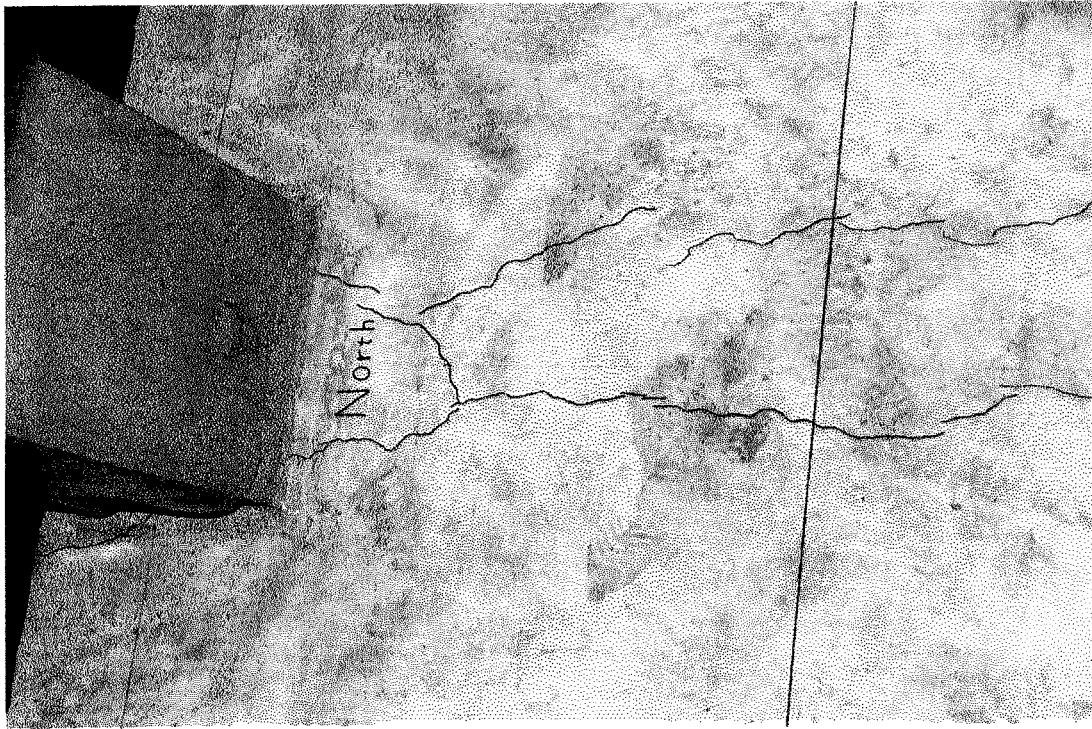


Figure 4.37 Crack pattern around north edge column, load stage 2 in table 4.1 (crack widths less than 0.1 mm)

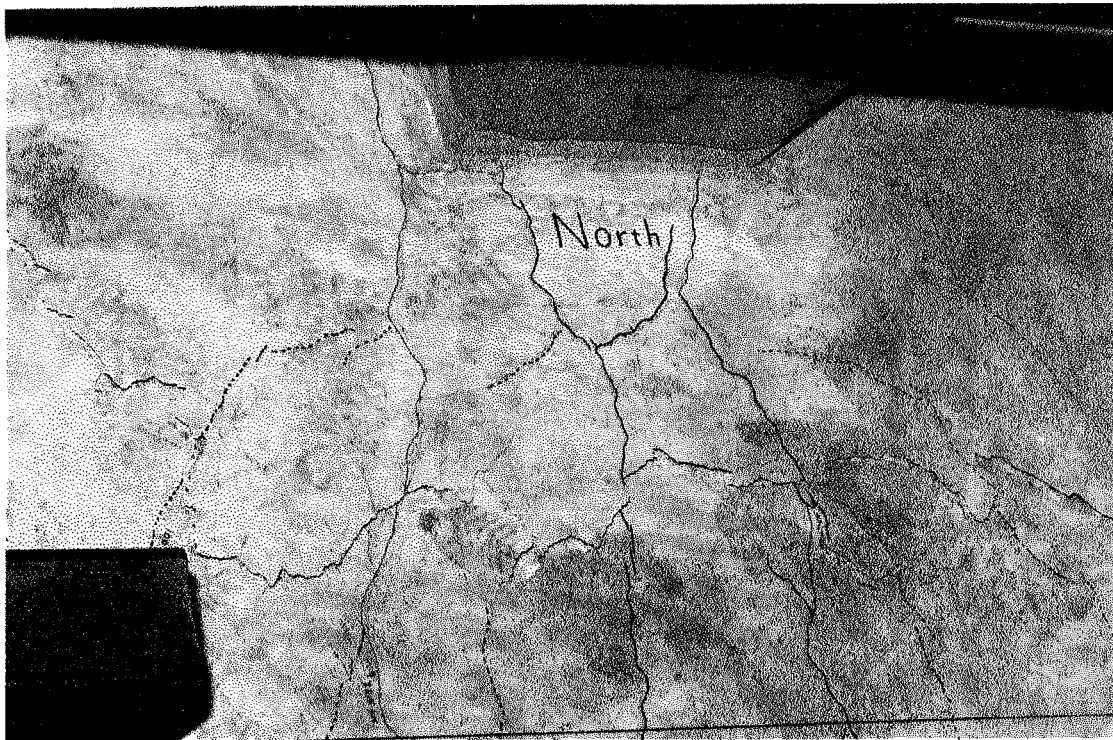


Figure 4.38 Punching of north connection

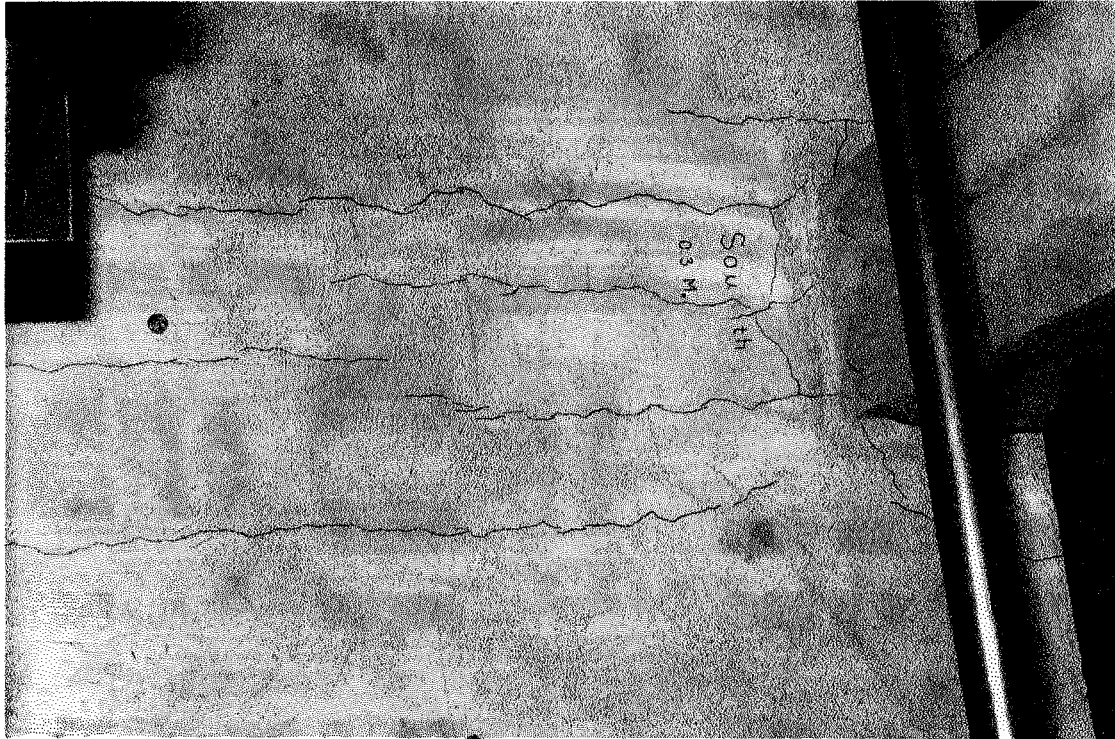


Figure 4.39 Crack pattern around south edge column, load stage 2 in table 4.1 (crack widths less than 0.1 mm)

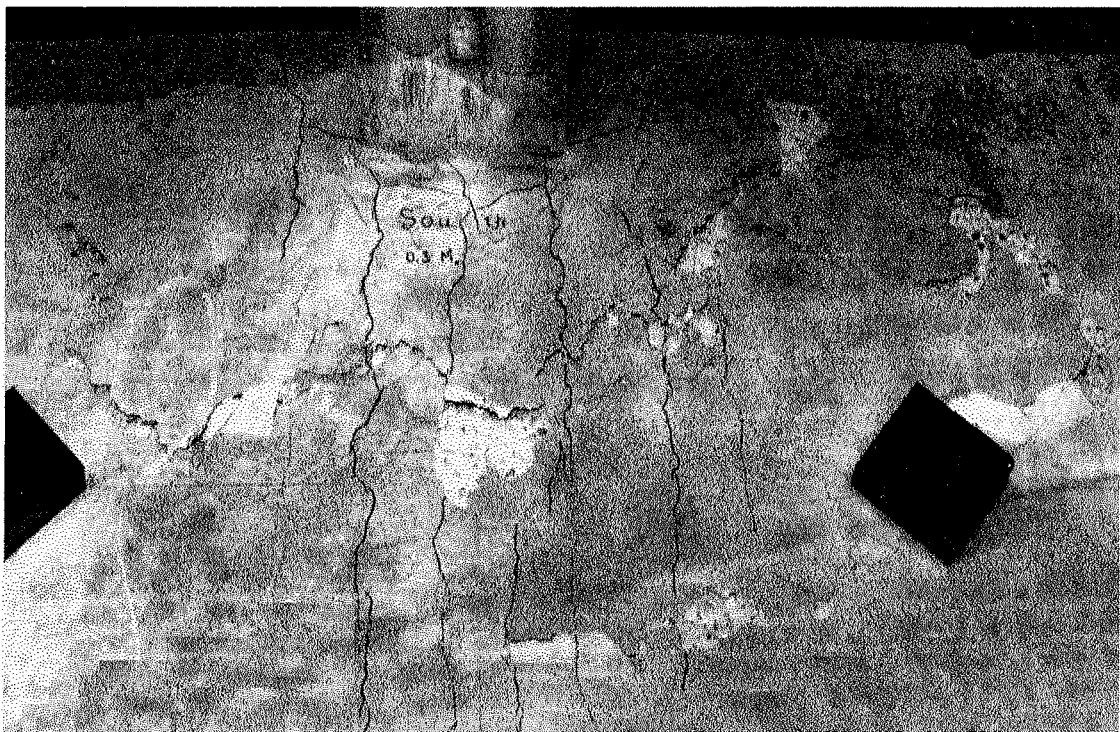


Figure 4.40 Punching of south connection

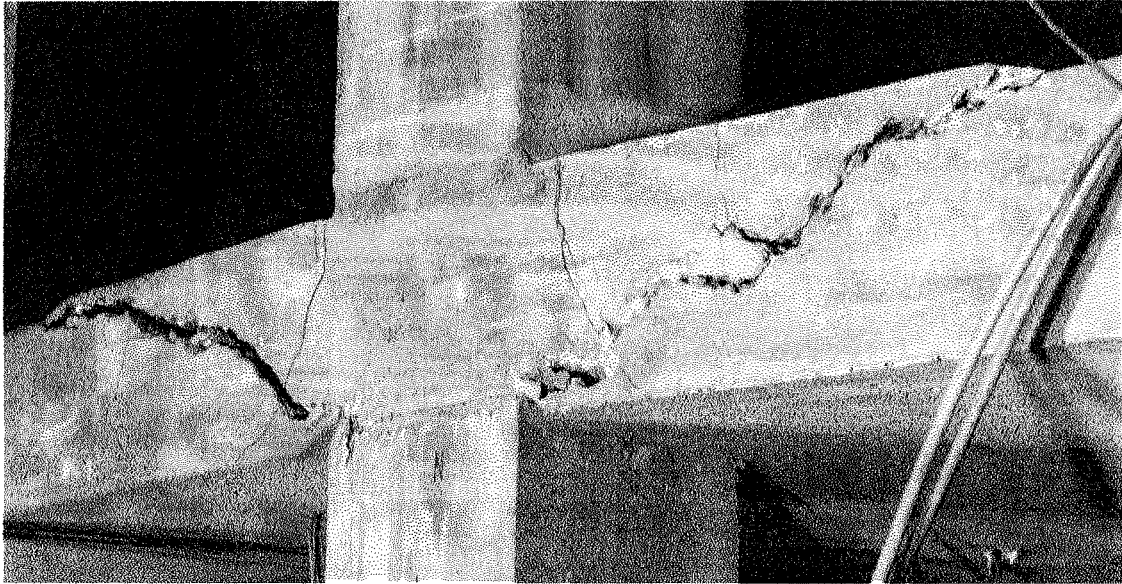


Figure 4.41 Side view of punching of north connection



Figure 4.42 Side view of punching of south connection

5. Internal Shear Forces and Torsional Moments

In this chapter, strain gauge measurements are used to calculate internal shears and torsional moments. Results of tension tests on reinforcement given in Section 3.7.1 are used to calculate the force gradient in the reinforcement. Results of the reinforced concrete beam tests given in Section 3.7.3 are used to determine the bending shear associated with each reinforcing bar, called bar shears, and to provide a detailed analysis of the mechanisms of load transfer in the interior and the south column-plate connections.

Internal shears so obtained are compared with the shears measured by the load cells and reported in chapter 4. Test results are then discussed, and the shear transfer in the test specimen is explained. In this regard, an important distinction between different types of testing is addressed.

5.1 Test Results

5.1.1 Force Gradient in Reinforcement

Force gradients are used to assess the average bond between the reinforcement and its surrounding concrete. According to clause 12.2.2 of A23.3-94, the minimum development length for 15M deformed bars in tension are 468 mm and 328 mm, respectively for bars in the outer (N-S) and inner (E-W) layers where the clear cover was 20 mm, $f_y = 420$ MPa, and $f'_c = 34.8$ MPa. These correspond to average force gradients of 180 and 256 N/mm², respectively. In the negative moment region, top bars in both directions are in tension. As a result of this biaxial tension, the critical average bond (or force gradient) of plates is expected to be smaller than the above values.

The average force gradient based on the first and the third row of gauges, $\frac{T_1 - T_3}{2 \times s}$, was calculated for reinforcing bars at the interior and at the south column-plate connections. T is the tensile force in the reinforcing bar, and its subscript refers to the position of the gauges as shown in Figures 3.18 and 3.19. The results are plotted in Figures 5.1 through 5.4 versus the deflection of the specimen (refer to Section 3.3.3.5 for the bar designations).

At the interior connection, comparing Figures 5.1 and 5.2, the force gradient of bars running in the N-S direction were greater than those of the bars running in the E-W direction, and were near their critical values as given by A23.3-94. At the south connection, the force gradient of bars running E-W were greater than those of the bars in the N-S direction.

Force gradients over the first and second intervals are plotted in Appendix B. These Figures are not used in this investigation. However, they might be useful in future studies, and are presented for completeness.

5.1.2 Internal Shear Forces, and Torsional Moments - General

5.1.2.1 Equations to Calculate Bar Shears

Bar shear can be calculated using Equations 2.16 through 2.18. These equations require an estimate of the internal moment arm, jd. As an alternative these equations are rewritten in terms of moment as Equations 5.1 through 5.3. Values of moments are estimated using strain gauge readings and the strain-moment relationships developed from the beam tests (Section 3.7.3).

$$V_{bar} = \frac{M_1 - M_2}{s} \quad [5.1]$$

$$V_{bar} = \frac{M_1}{s} \times \frac{M_2 - M_3}{2 \times M_2 - M_3} \quad [5.2]$$

$$V_{bar} = \frac{M_1 - M_3}{2 \times s} \quad [5.3]$$

Equations 5.1, 5.2, and 5.3 are each valid over a limited range. Equations 5.1 and 5.3 are correct if beam action dominates. Equation 5.2, however, accounts for some additional shear carried by arching action between sections 1 and 2 or by gradient in torsional moments.

To be valid, all equations require that the slab be cracked. These equations will underestimate the bar shears prior to cracking at section 1. Equations 5.1 and 5.3 require cracking at sections 2 and 3, respectively, and will overestimate bar shears if this is not satisfied.

For example, compare these equations for a given $M_3 = 0.5 M_1$. The values of $(V_{bar} \times s) / M_1$ are plotted versus the ratio of M_2 over M_1 in Figure 5.5. With the yielding of a bar at section 1, M_1 becomes almost constant, and the x and y axes in Figure 5.5 become non-dimensional indicators of M_2 and V_{bar} , respectively.

It can be seen that the three equations coincide at point B, where gauge readings are consistent with shear transfer by beam action [$M_2 = 0.5 (M_1 + M_3)$]. Where M_2 is greater than the average of M_1 and M_3 , Equation 5.2 (BC) accounts for the extra shear carried either by arching action or by the gradient in torsion.

In cases where gauge 2 does not lie at a fully cracked section, values of M_2 are underestimated and Equation 5.1 overestimates the shear (segment FB in Figure 5.5). In this range, Equation 5.2 also results in an unrealistic estimate of shear (segments FG and HB in Figure 5.5). Hence, where M_2 is smaller than the average of M_1 and M_3 , Equation 5.3 is used. The following equations describe the governing segment ABC that is used to process the test results in this thesis.

$$V_{bar} = \frac{M_1}{s} \times \frac{M_2 - M_3}{2M_2 - M_3} \quad \text{If } M_2 \geq \frac{M_1 + M_3}{2} \quad [5.4]$$

$$V_{bar} = \frac{M_1 - M_3}{2 \times s} \quad \text{Otherwise} \quad [5.5]$$

For different values of M_3 / M_1 , Figure 5.6 graphically describes the Equations 5.4 and 5.5. In cases where gauge 3 does not lie at a fully cracked section, M_3 is underestimated, and hence V_{bar} is overestimated. This overestimation is not a problem at the ultimate as the strains become large enough to crack section 3.

5.1.2.2 Equations for Internal Shears and torsions

The shear transferred through a radial strip is calculated by adding the shears associated with all the bars perpendicular to this strip. An internal measurement of the shear transferred by a connection is obtained by summing shears of all of its associated

radial strips. This sum is compared to the shear measured by the load cells, an external measurement of the shear.

The net torsion along side faces of a radial strip is calculated using rotational equation of equilibrium of the radial strip. Rewriting Equations 2.14 and 2.15 in terms of individual bar shears, total shear of each radial strip and the torsional moment on each side face of the radial strip can be calculated using Equations 5.6 through 5.8. In these equations, $r_{(i)}$ is the distance of bar i from the column face.

$$P_s = 2 \sum_{i=1}^n V_{bar(i)} \quad [5.6]$$

$$M_t = \frac{1}{4} \left[2 \sum_{i=1}^n V_{bar(i)} \times r_{(i)} - M_s \right] \quad \text{for interior radial strips} \quad [5.7]$$

$$M_t = \frac{1}{2} \left[2 \sum_{i=1}^n V_{bar(i)} \times r_{(i)} - M_s \right] \quad \text{for spandrel strips} \quad [5.8]$$

5.1.3 Internal Shear Forces, and Torsional Moments - Interior Connection

In Figures 5.7 and 5.8, calculated bar shears (V_{bar}) of the interior connection are plotted versus the deflection of the slab at point F, illustrated in Figure 3.22. This deflection is due to jack loads only and does not include the deflection under self-weight and super imposed loads. The strain gauge data, however, do include the effect of the dead loads.

The top mat at the center column, as shown in Figure 3.18, consists of sixteen 15M bars in the outer layer running N-S, and eighteen 15M bars in the inner layer running E-W. Bar 1, the first bar from the column center in each direction, passes through the column, and is assumed to contribute only to the flexural capacity, M_s , of the radial strip. It is assumed that the remaining bars in each direction transfer all the load from the quadrant to the radial strips. Of these, the outermost bars, 8 and 9, were not expected to contribute significantly to the shear transfer and were therefore not gauged.

Shear transferred through the N-S radial strips is calculated by adding the shear attributed to bars running E-W. Similarly, shear transferred through the E-W radial strips is calculated by adding the shears of bars running N-S. Assuming that the contribution of bars 8 and 9 is negligible, the sum of these shears should be equal to the total load transferred through the connection. The internal shear so obtained together with the external shear are plotted in Figure 5.9 versus the deflection of the plate.

It is observed in Figure 5.9 that at a deflection of about 9 mm, the external measurement of shear was in excellent agreement with the internal measurement of shear. The ratio of the internal to the external shear varies between 0.875 and 1.11, having an average of 1.013. This ratio is plotted versus the deflection in Figure 5.15.

Figure 5.9 shows that the N-S radial strips transferred a smaller load than did the E-W radial strips, although their shear capacity according to the Bond Model was essentially equal. At a deflection of about 9 mm, the N-S radial strip carried only about 35 percent of the total load. Towards the end of the test, this ratio dropped to about 25

percent. This means that E-W radial strip transferred three times more load than did the N-S radial strip.

Based on the calculated bar shears, the total torsional moment, M_t , on the side faces of the radial strips was determined using Equation 5.7. Defining positive torsion as that which adds to the bending capacity of the radial strip, M_t is plotted in Figure 5.10 versus the deflection at point F. It can be seen that while torsional moment on the side faces of the E-W radial strip increases the shear capacity of the strip, the torsional moment on the side faces of the N-S radial strip decreases the shear capacity of this strip (Approximately, three quarters of one 15M bar capacity within the N-S radial strip was used to carry negative torsion on the two side faces of this strip).

5.1.4 Internal Shear Forces, and Torsional Moments -South Edge Connection

As shown in Figure 3.19, the south connection was reinforced with four 15M bars perpendicular to the free edge on either side of the column center line. These bars were in the outer layer (running N-S) and were spaced 100 mm apart. Bar number 1 passes through the column and was totally used in providing flexural support to the interior radial strip. Bar 2 was placed exactly on the boundary of column and slab. It is assumed that half of this bar participated in transferring shear to the radial strip and the other half added to the bending capacity, M_s , of the interior radial strip. Bars three and four were responsible for transferring part of the shear to the spandrel strip.

Referring to the E-W reinforcing bars, four 15M bars participated in equilibrium of spandrel strip: two as main reinforcement; and two anchorage bars as illustrated in Figure 3.7. The next six bars (bars 3/9 through 8/9) were gauged so that bar shears could be calculated. It is assumed that the shear contribution of the last bar, 9/9, was negligible. In Figures 5.11 and 5.12, shears for individual bars, V_{bar} , are plotted against the deflection of the slab at point B in Figure 3.22.

In Figure 5.13, the amount of shear transferred through each spandrel strip is compared to the shear passing through the interior radial strip. The total internal shear (two spandrel strips plus the interior radial strip) can be compared with the external shear measured by the vertical load cell located under the south column. The shear transferred by each spandrel strip was only about 10 percent of the total shear throughout the test.

The ratio of the internal shear to the external shear is plotted in Figure 5.16. It can be seen that after a deflection of only 1.7 mm, corresponding to a distributed load of 5.5 kPa (including self weight of slab), the two measurements are in excellent agreement. For deflections in excess of 1.7 mm, the ratio of internal to external measurement of shear varies between 0.882 and 1.219 and has an average of 1.00.

Net torsion along the side faces of the radial strips are calculated using Equation 5.7 for the interior radial strip and Equation 5.8 for the spandrel strip. The fact that spandrel strips were transferring a small portion of the load suggests that, as shown in Figure 5.14, very high negative torsional moments are applied to their interior side face, and implies that a considerable part of the bending capacity of the spandrel strip is used up by these torsional moments.

5.2 Discussion

It is shown in Sections 5.1.3 and 5.1.4 that the shear estimate entirely based on strain gauge readings consistently and accurately matches the total load measured by load cells. Agreement of internal measurements with the external measurements strongly suggests that the assumed mechanism of shear transfer is fundamentally correct in both the interior and the edge connections. However, the fact that one strip carried more shear than the other one, especially in the edge connection, indicates that the capacity of the connection can not be determined simply by adding the independently calculated shear capacity of each strip. Torsional moments become very important in estimating the shear capacity of each strip, and may reduce the bending capacity of the radial strip, even in an interior connection. This has implications for different testing techniques which will be discussed in the next section.

5.2.1 General

5.2.1.1 Comparison of Different Test Methods

The fact that, at ultimate, the radial strips might not necessarily be loaded to their nominal capacities (Equations 2.5 or 2.7) is closely related to the nature of the test. In the current test, the load distributing system maintained nearly equal loads at eight load points per jack. More importantly, the deflected shape of the slab was not constrained by the loading system. Therefore, more possible mechanisms of failure could form in the specimen.

In enforced deformation tests, however, the loading system dictates a certain pattern for the deformation of the specimen. As a result, the loads at different load points are not necessarily equal, and provided that the load carrying mechanisms are sufficiently ductile, all radial strips meet their maximum capacity.

For example, consider the interior connection shown in Figure 5.17a. If equal deformations are imposed at the load points, the only kinematically admissible yield line mechanisms are those shown in Figures 5.17b and 5.17c (or their combination). In these mechanisms, each radial strip may be considered as a separate test, and will be loaded to its maximum capacity. However, in a test with equal applied loads, in addition to the mechanisms 1 and 2, the yield line mechanism shown in Figure 5.17d may form. In this case, a single negative yield line, in the direction with smaller capacity, forms the mechanism. Note that the first two mechanisms are the upper bound solutions of the latter, and therefore, similar to the prototype plate, the third mechanism is the governing one.

In the particular case where conditions in both directions are identical, the loads in an enforced deformation test might be relatively equal in all load points, and the test realistically models the prototype. However, it is difficult to ensure equal strength and stiffness in both directions, and inevitably, slab is stiffer in one direction than in the other. As a result, mechanism 3 is more typical of a structure with uniformly applied loads.

5.2.1.2 Shear Transfer in Plates with Different Stiffness in the Two Directions

Figure 5.18 examines mechanism 3 in more detail. Both the loading and the gross geometry of the specimen are symmetric about a diagonal axis. However, if the slab is stiffer in the N-S direction, the deflections will not be symmetric about a diagonal axis. In particular, the deflection at D will be greater than that at A. Since the slab must satisfy

equilibrium in both the N-S and the E-W directions, lack of symmetry about a diagonal axis implies that the shear transfer mechanisms in the N-S direction are not the same as in the E-W direction. Within each quadrant, more shear is transferred by beam action in the stiffer N-S direction than in the E-W direction. As a result, load in strip 1 exceeds its nominal capacity while strip 2 is not loaded to its nominal capacity.

The flexural strength of the strip 1 is augmented by reinforcement outside this strip because they have not been fully used for shear transfer to strip 2. This contribution of bars outside the column, as shown in Figure 5.18b, may be interpreted in two ways: (a) by assuming a larger width for the strip 1, and hence increasing the flexural capacity, M_s , of the radial strip, or (b) by considering the torsional moments along the side faces of the radial strips in the rotational equilibrium. While the second method leads to a more convenient way of describing the behavior, the first method results in a practical approach for estimating the shear capacity of the connection. The magnitude of the torsional moment is equal to the flexural capacity of the contributing bars outside the column.

In summary, beam action is a stiffer mechanism of shear transfer than arching action. In a stiff direction, that is, one in which curvatures are relatively small, the dominant mechanism of shear transfer is beam action. In a flexible direction, the dominant mechanism of shear transfer is arching action.

5.2.2 Interior Connection

5.2.2.1 Different Behavior of the Radial Strips

Internal measurement of shear revealed that the N-S radial strip behaved differently from the E-W radial strip and from what was expected. It was loaded less by its adjacent quadrant, and the overall torsional moment on the side faces of the radial strips was in the opposite direction of the bending moments.

From Figures 4.32 and 4.33, it can be seen that the midspan deflections along the column lines were not the same in the two directions. The experimental evidence suggests that the zero rotation requirement at the edge was not enforced. Larger deflection at point D, non-zero rotation at the continuous edge, and also the early formation of the N-S crack suggests that the plate was much stiffer in the N-S direction. As a result, as described in Section 5.2.1.2, a large portion of the load was transferred in the N-S direction to the E-W radial strips.

Different behavior of the radial strips in the two directions, was a direct result of the inadequate stiffness of the edge restraining system. In practice, the behavior of the radial strips may be different as the structure may have: (1) unequal spans, (2) large openings, (3) rectangular column, (4) unequal capacity of the radial strips, (5) difference in the arrangement of the reinforcement in the two directions, (6) concentrated loads, and (7) line loads (e.g. walls or partitions).

Specimens with any of these features should not be subjected to enforced deformation tests because the capacity of the connection in these tests might be larger than that of the prototype building.

The Bond Model solution, with its assumption of adding the capacity of the individual radial strips, is a lower bound solution for enforced deformation tests only. Another solution using bond model will be introduced in chapter 7. This method will

provide a lower bound solution for a real structure, even where the behavior of the radial strips are different in the two directions.

5.2.2.2 Interaction of a Radial Strip and its Adjacent Quadrant

The direction of the torsional moments along the side face of the radial strips is consistent with the explained shear transfer in the specimen. Assume that the radial strips are isolated from their adjacent quadrant, and consider the E-W direction first. The radial strips in this direction were heavily loaded, and hence their associated curvature should be very large. On the other hand, inside the quadrant, a small portion of the load was carried in the flexible E-W direction. Therefore, the curvature of the quadrant in the E-W direction should not be very large. Since the deformation of the radial strip and its adjacent quadrant must be compatible, relatively high torsional moments are required along the side faces of the E-W radial strips. The net effect of these torsional moments augments both the bending and the shear capacities of the E-W radial strips. The stiffer quadrant helped the radial strip to carry more load, through the torsion along the side faces.

In contrast, the quadrant deforms more than the radial strip in the N-S direction, and negative torsion on the side face of the N-S radial strips is required to satisfy the compatibility of deformations. This torsion decreases the bending capacity and hence the shear capacity of the N-S radial strip.

5.2.2.3 Ductility of the Interior Connection

In the Bond Model procedure, two basic assumptions are made which require some ductility at the connection. First, it is assumed that the distribution of shear on the side faces of the radial strips is uniform. Since the E-W radial strip transferred 175 kN, about 45 percent more than the predicted capacity, it is believed that the connection was ductile enough to allow the uniform distribution of shears. Second, it is assumed that all radial strips reach their shear capacity at the time of failure of the connection. If strips are not loaded in proportion to their nominal capacities, the second assumption requires two conditions to be satisfied; (a) quadrant should have the ability to load its adjacent radial strips independently; and (b) the strip that reaches its maximum capacity first, should have enough ductility to deform without substantial loss of capacity while the other strip carries the additional load.

At the time of failure of the interior connection, the N-S radial strips could still transfer more load, and the positive moments in both directions were less than the yield moments. As a result, the specimen neither reached the full yield line load, nor the capacity of all of its radial strips. It is believed that the connection was not able to satisfy the first condition and that part of the additional load increment had to be transferred by the E-W radial strip, which was at its maximum capacity. The connection failed due to the failure of this radial strip as exemplified by Figure 5.9.

5.2.3 Edge Connection

For reinforcement parallel to the free edge, the behavior at an edge connection is basically the same as at an interior connection. This is not the case for reinforcement perpendicular to the free edge. Perpendicular to the free edge, the bending capacity of the edge connection depends on the stiffness of the edge column and is limited to its bending

capacity. For a concentrically loaded interior connection, the bending capacity of the slab is neither related to the column stiffness nor to its bending capacity.

Yielding of bars perpendicular to the free edge and passing outside the column is affected by rotation of the spandrel strip and, hence, their proximity to the column. The corresponding moment is limited to the torsional capacity of the spandrel strip. In concentrically loaded interior connections, yielding of bars are neither effectively related to the distance of the bars from the column nor to the torsional capacity of the radial strip.

Since the shear force applied to each radial strip is actually the gradient in bending moment, and the flexural behavior of an edge connection itself is different in the two directions, it is not surprising that the spandrel strip should behave differently in shear than the interior strip. As illustrated in Figure 5.13, each spandrel strip only transferred about 10 percent of the total load. Therefore, the intensity of the shear at the column end of the spandrel strip was not large, and was approximately equal to the intensity of shear on the side faces of the interior radial strip. This means that all the load in the edge quadrant was carried in the direction parallel to the free edge by beam action into the interior radial strip and side faces of the column. The load inside the interior radial strip was then transferred to the column by arching action.

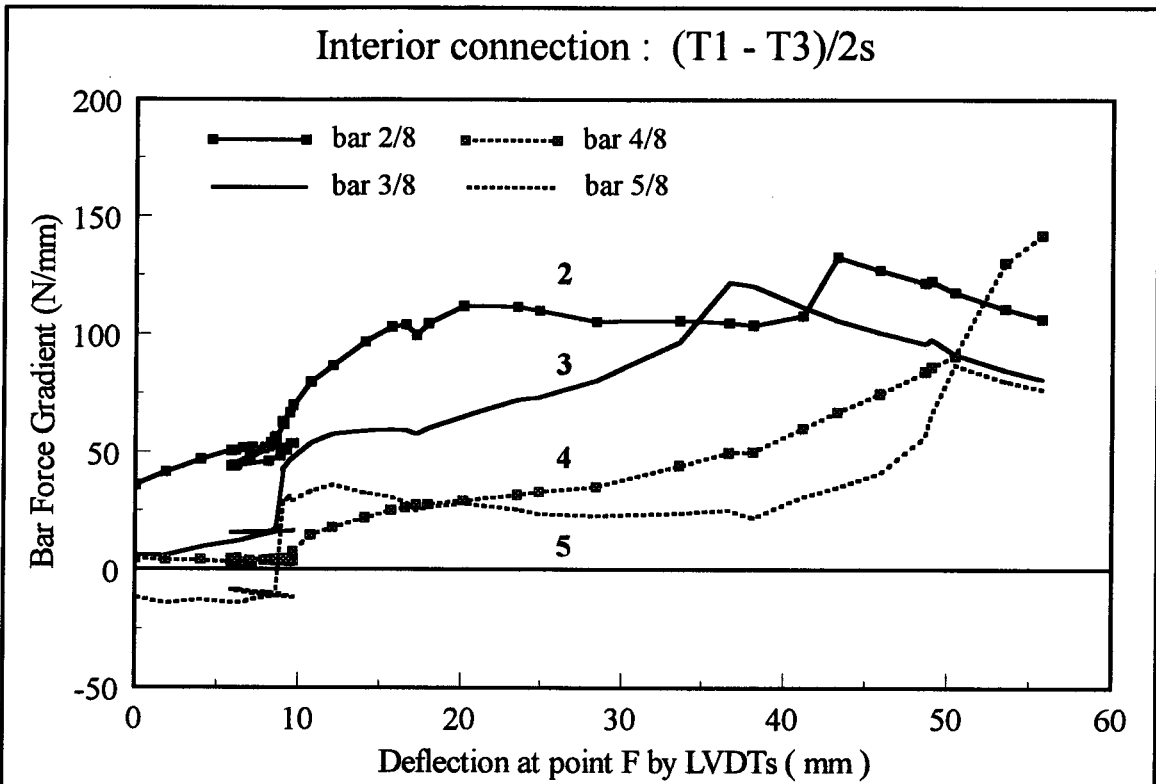


Figure 5.1 Force gradient in bars running N-S, interior connection, (T1 - T3)/2s

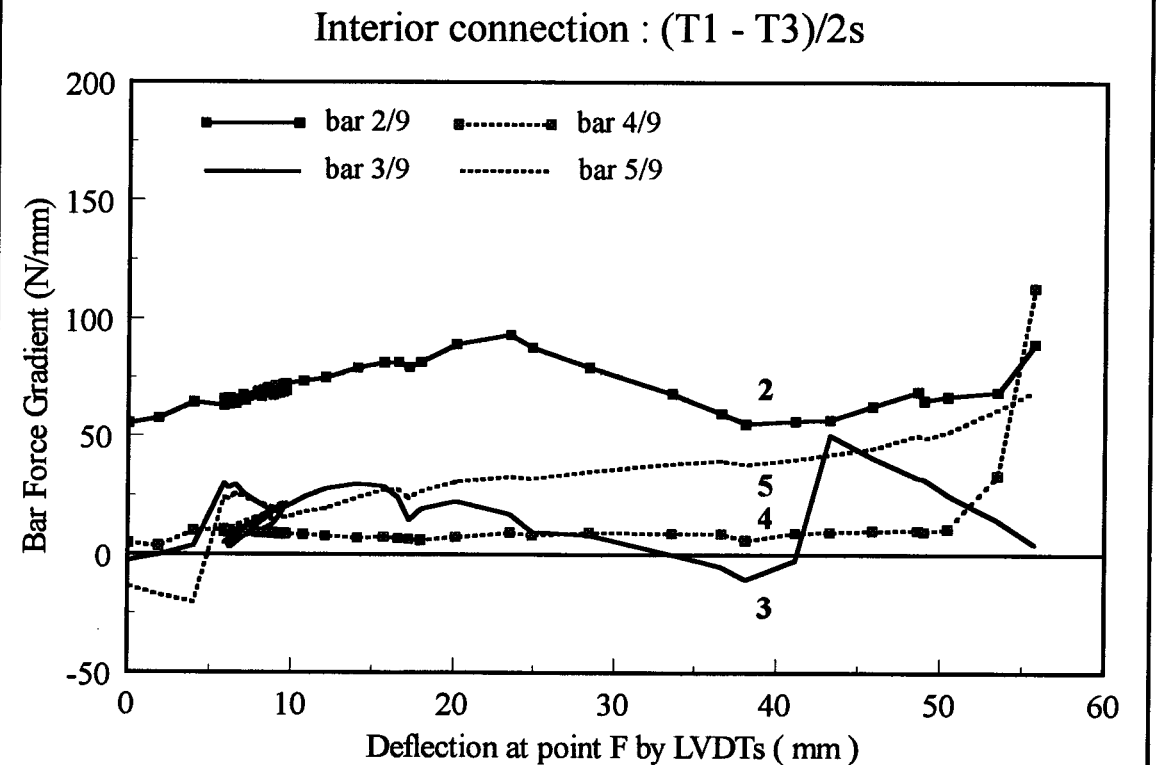


Figure 5.2 Force gradient in bars running E-W, interior connection, (T1 - T3)/2s

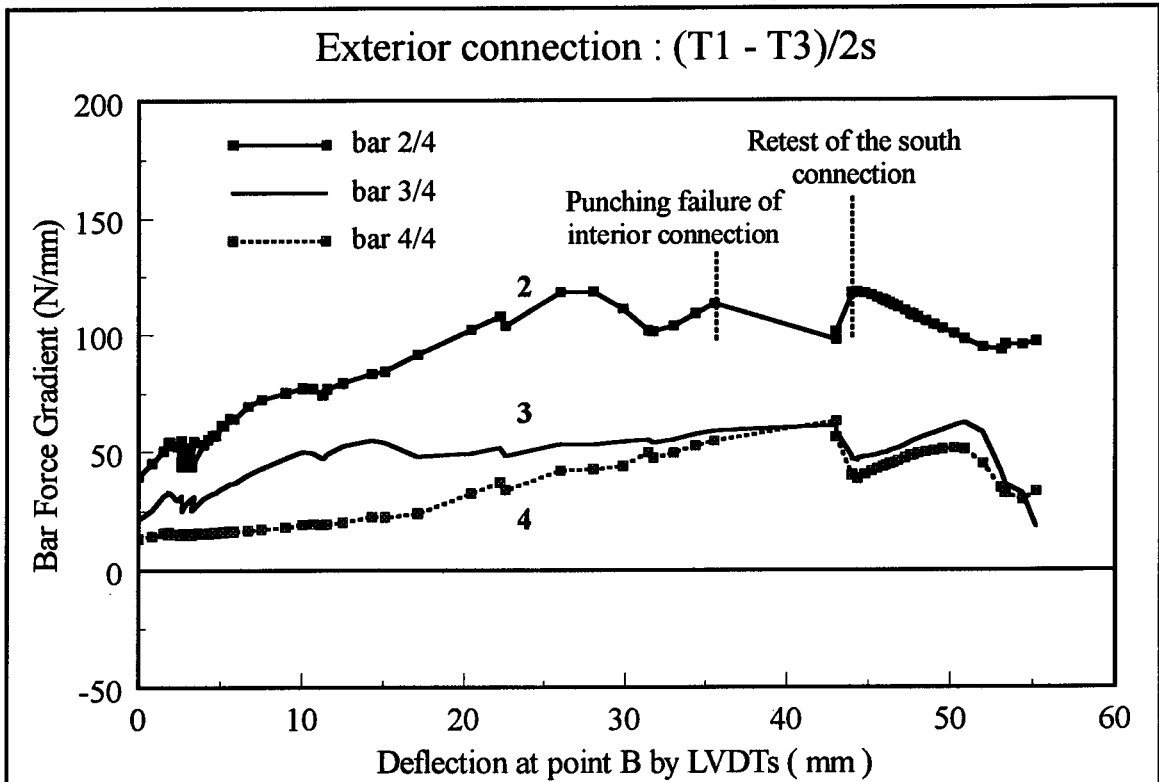


Figure 5.3 Force gradient in bars running N-S, south connection, (T1 - T3)/2s

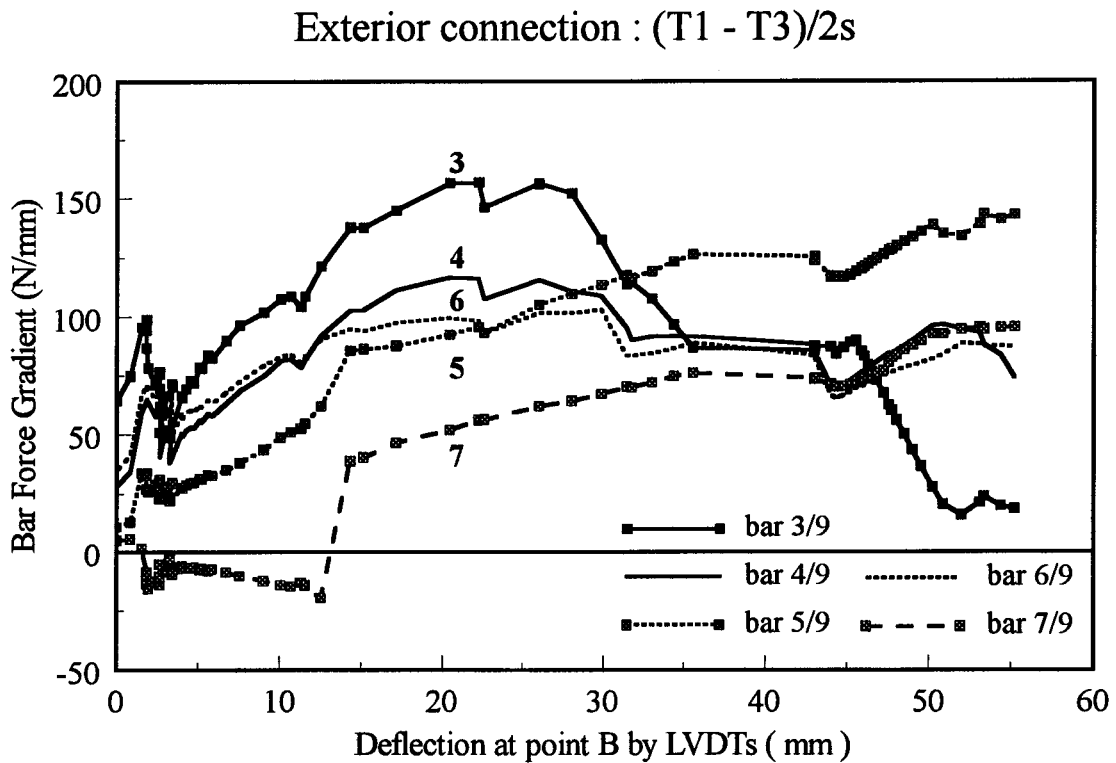


Figure 5.4 Force gradient in bars running E-W, south connection, (T1 - T3)/2s

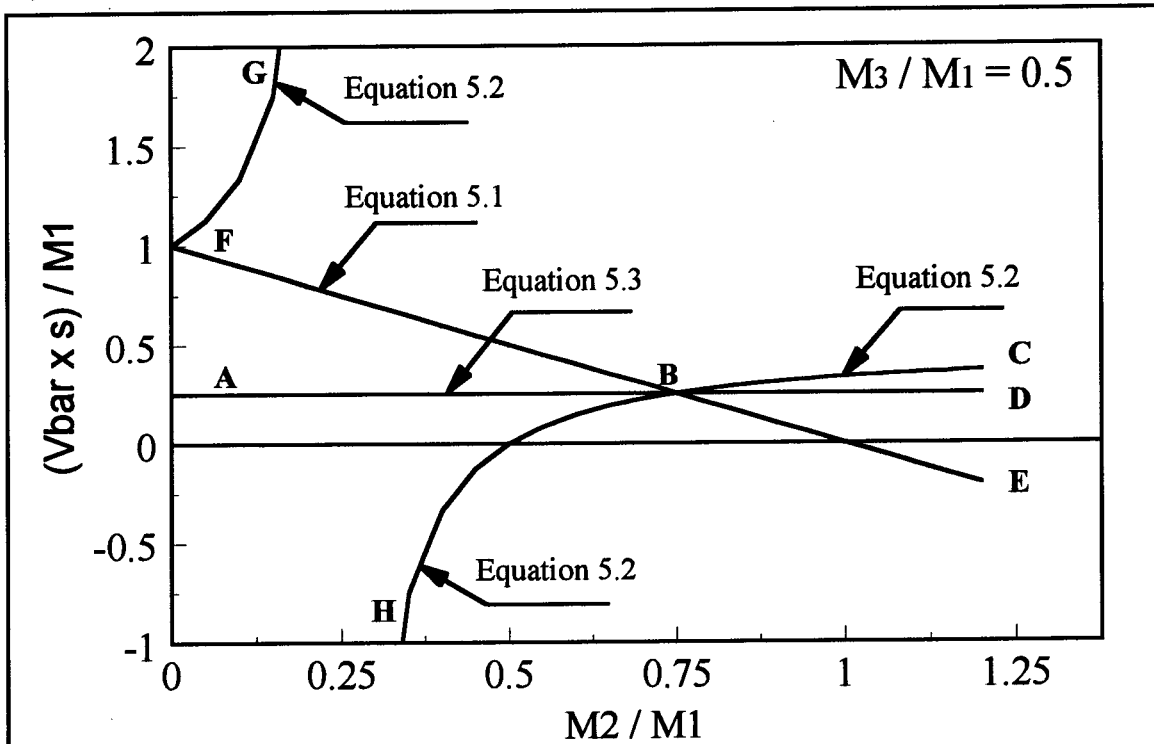


Figure 5.5 Mathematical comparison of equations 5.1, 5.2, and 5.3

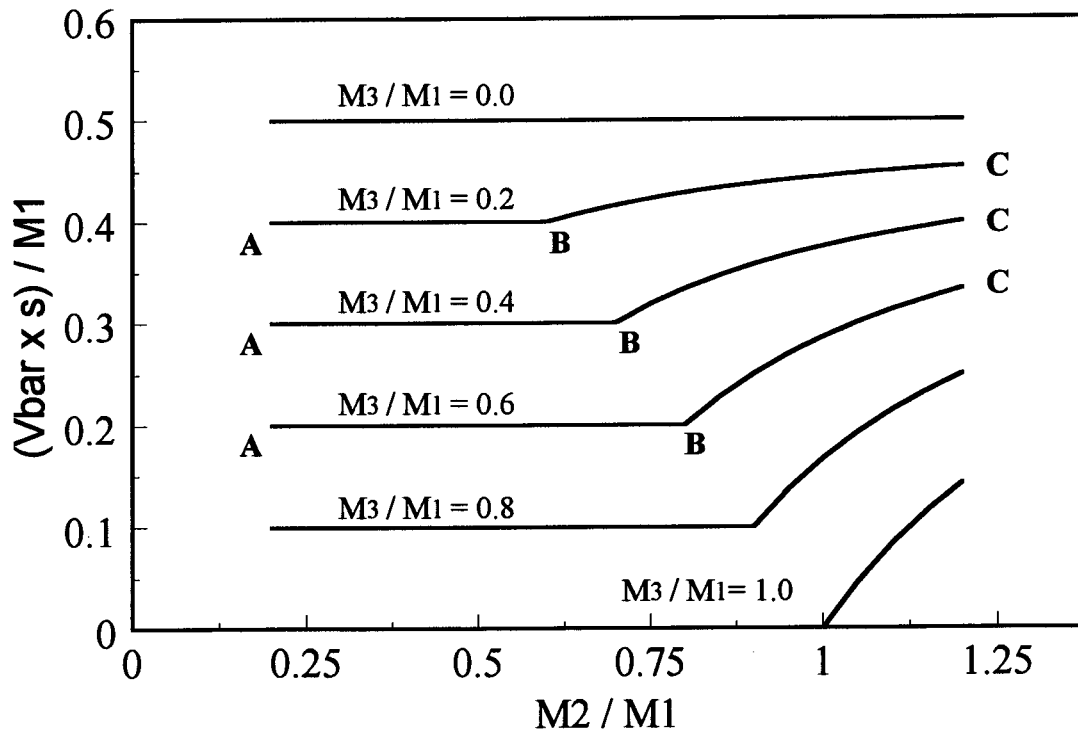


Figure 5.6 Suggested equations (5.4 and 5.5) for V_{bar}

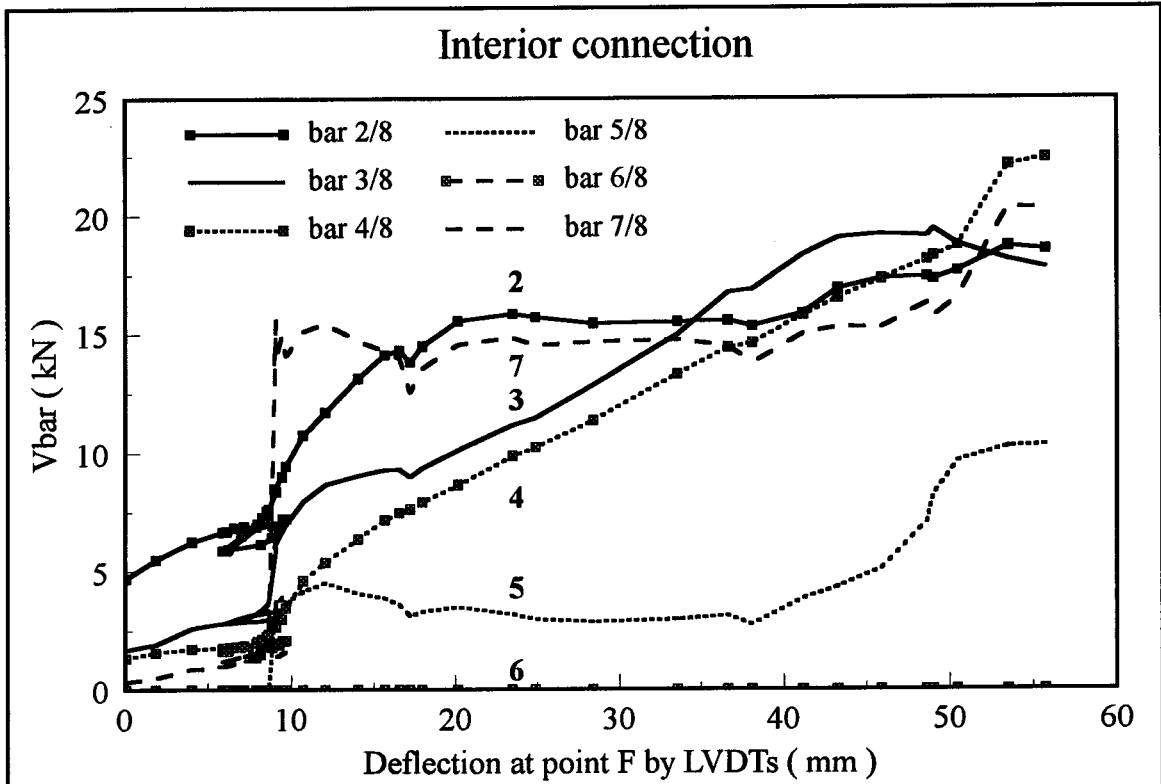


Figure 5.7 Shear attributed to individual bars running N-S, interior connection

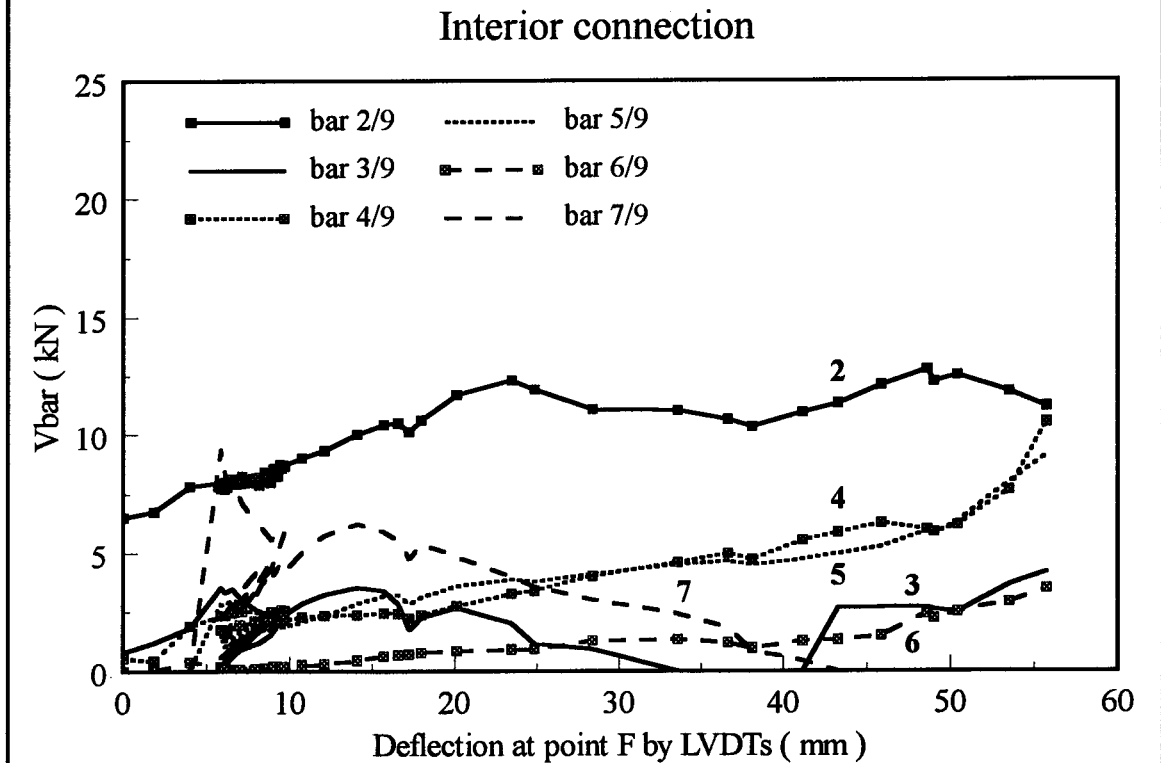


Figure 5.8 Shear attributed to individual bars running E-W, interior connection

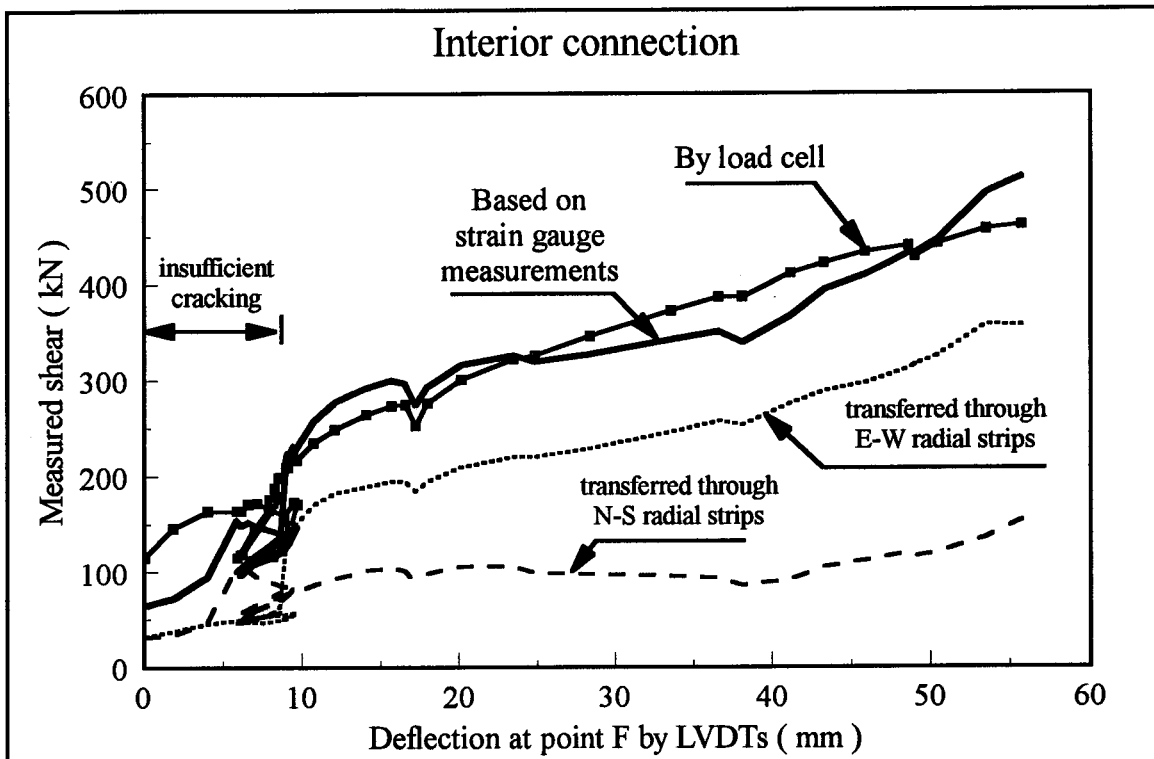


Figure 5.9 Measured shear at interior connection by load cell and strain gauges

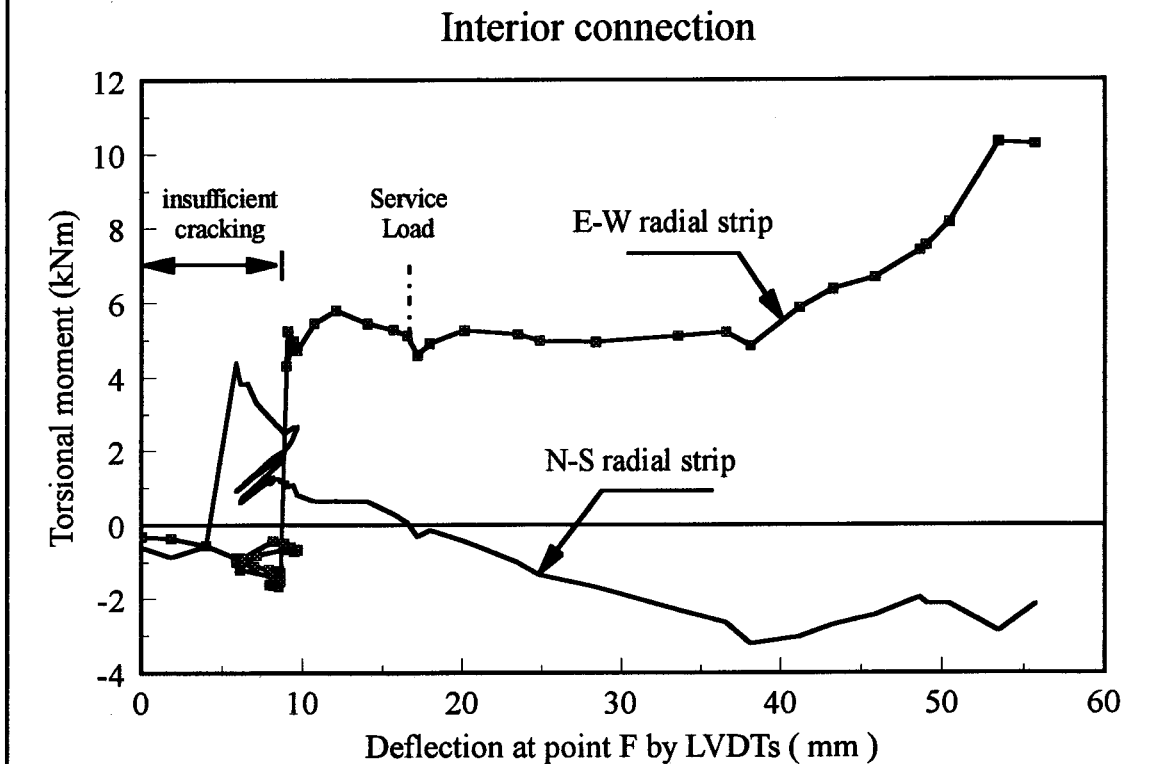


Figure 5.10 Torsion along each side face of radial strips of interior connection

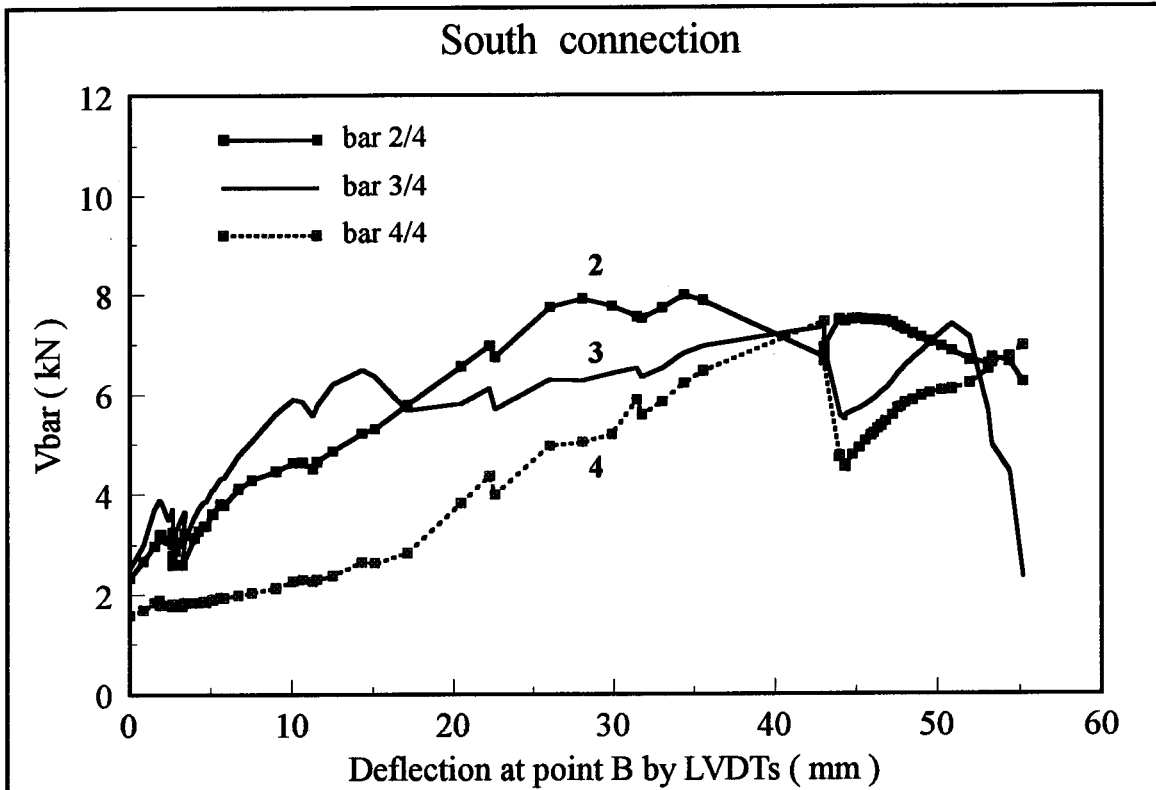


Figure 5.11 Shear attributed to individual bars running N-S, south connection

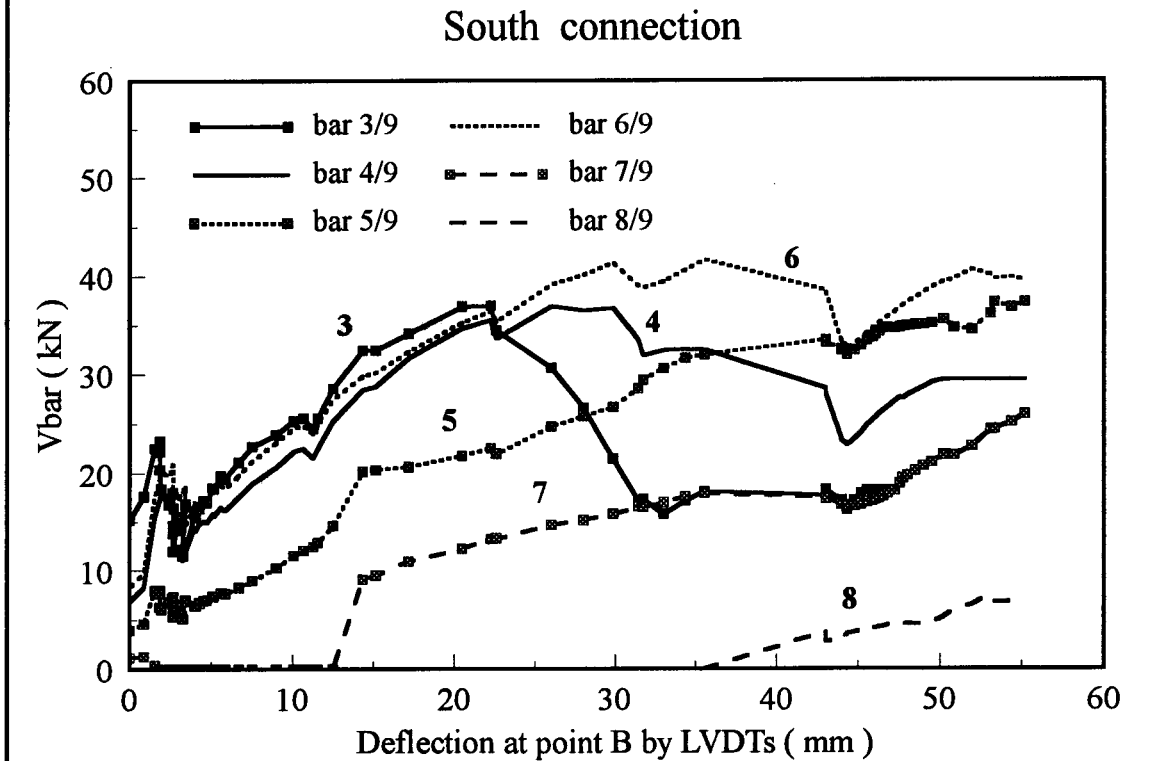


Figure 5.12 Shear attributed to individual bars running E-W, south connection

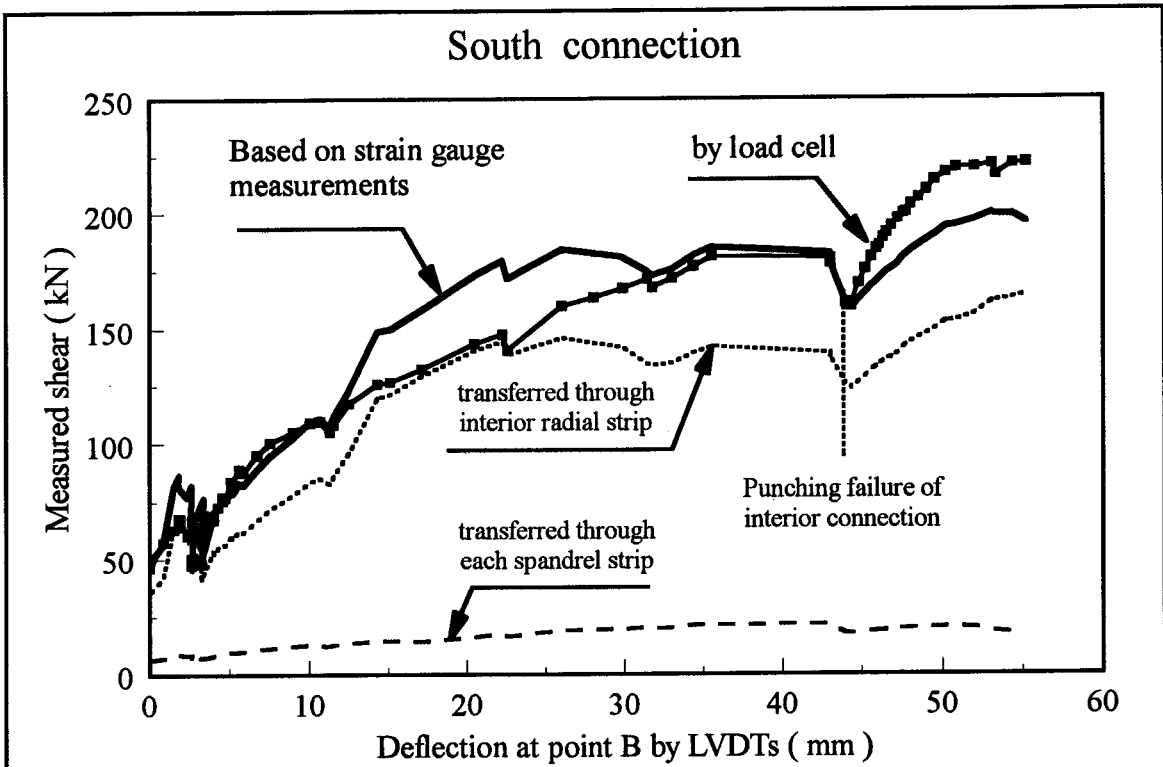


Figure 5.13 Measured shear at south connection by load cell and strain gauges

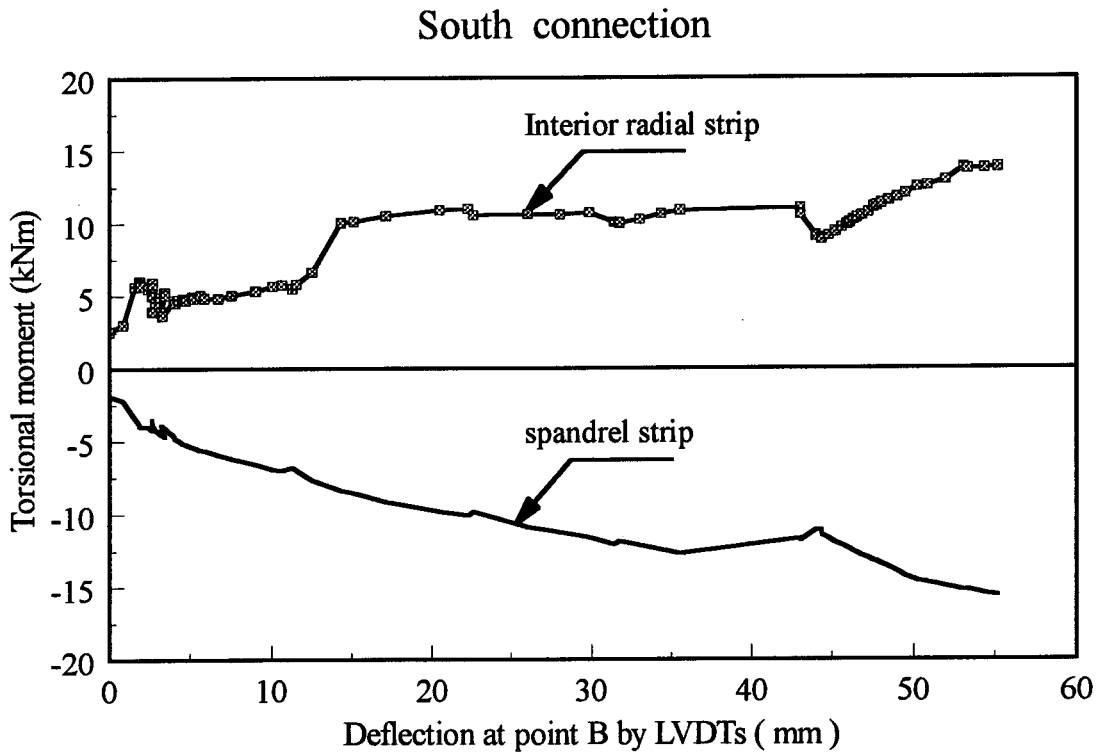


Figure 5.14 Torsion along each side face of radial strips of south connection

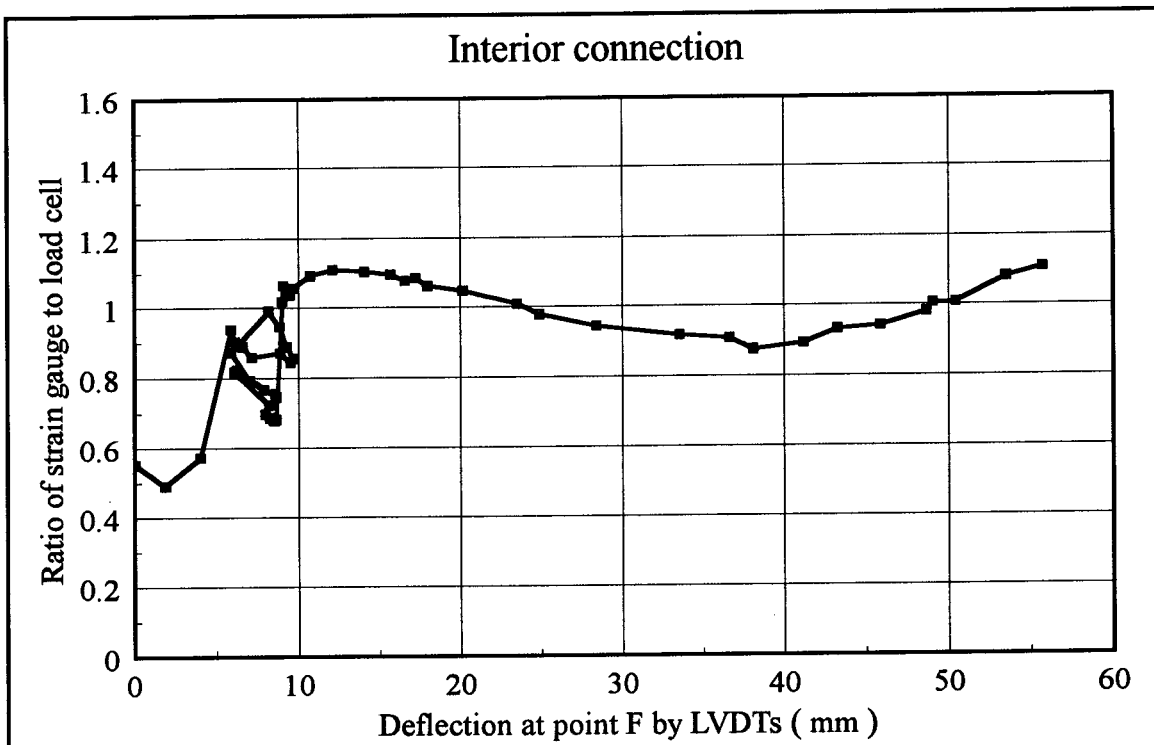


Figure 5.15 Ratio of measured shear by strain gauges to measured shear by load cell in interior connection

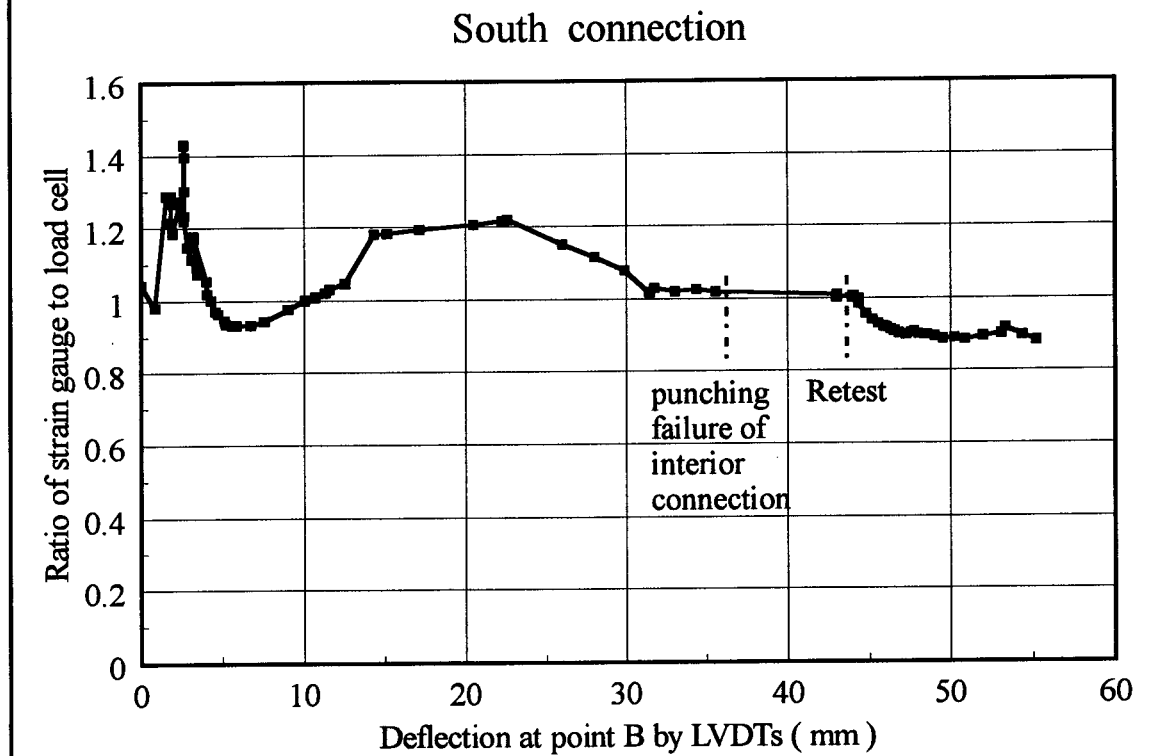


Figure 5.16 Ratio of measured shear by strain gauges to measured shear by load cell in south connection

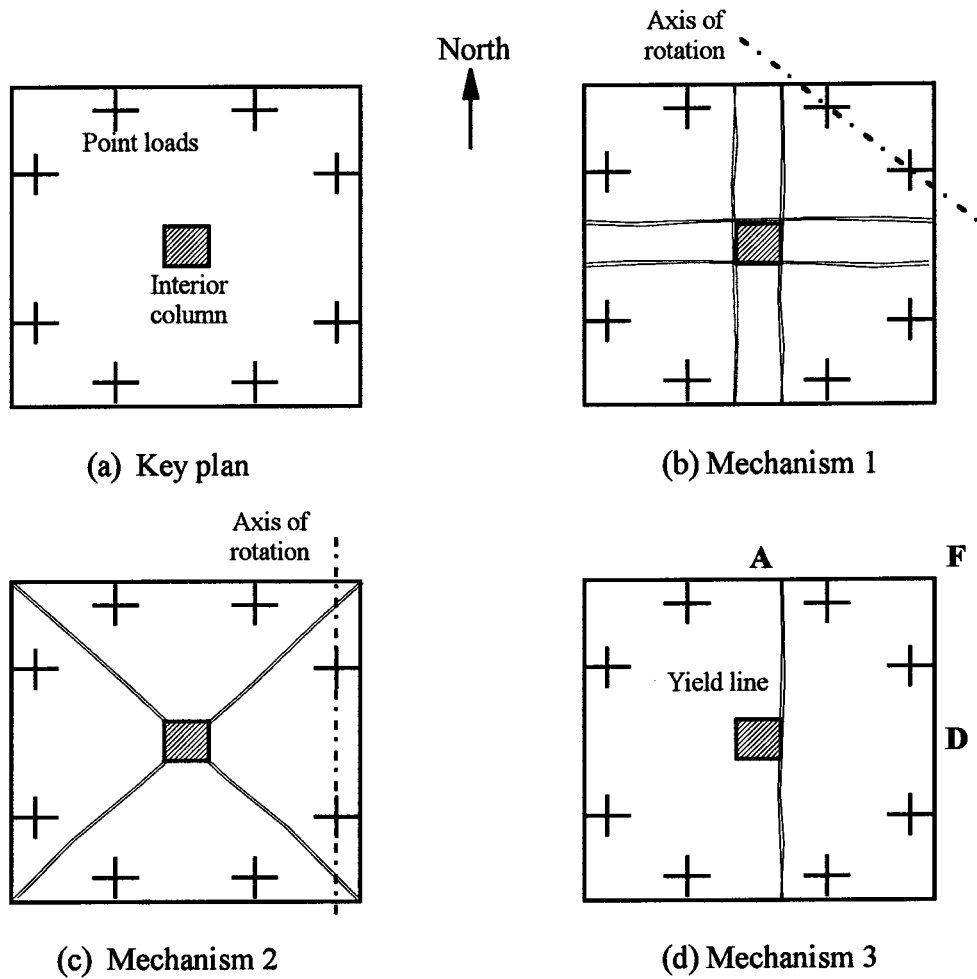


Figure 5.17 An example of possible mechanisms of failure

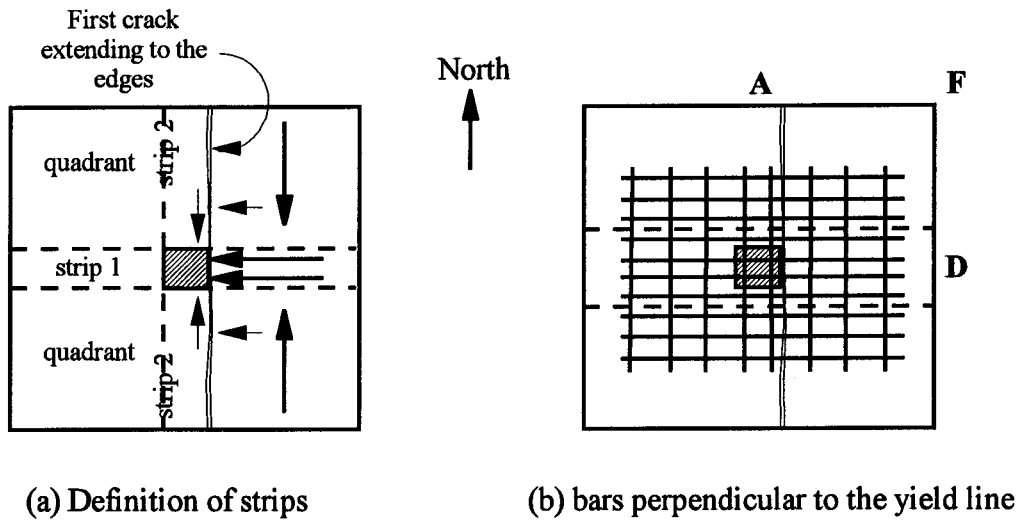


Figure 5.18 Description of the third mechanism

6. Behavior of Radial Strips in Flat Plate Structures

The Bond Model is based on certain assumptions regarding the distribution of shear forces as well as torsional moments along side faces of the radial strips. Although test results support the mechanics of this model, analytical analysis would be useful to verify these assumptions.

The available finite element programs can, to some extent, account for the flexural cracking and are therefore able to predict the overall behavior of reinforced concrete plates. However, when it comes to dealing with shear or torsional cracks in flat plates, the accuracy of the results in areas close to columns becomes doubtful. Moreover, the interaction between cracked concrete and single bars is not accurately modeled. As a result, these analyses can not reliably predict bond failure and/or punching failure. Nevertheless, far from the column and prior to the formation of the inclined cracks, these programs can be expected to provide a reasonable description of the behavior.

This study focuses on the distribution of shear and torsion along the side faces of the radial strips in interior and exterior connections. Also, of interest are the factors that may induce different behavior of the radial strips in the two directions.

In this chapter, the finite element program NISA 90, with a Paramono and Willam's concrete material model modified by Xie et al. (1994), will be used to qualitatively study the behavior of the flat plate structures. Difficulties and concerns regarding finite element modeling of three dimensional reinforced concrete structures are briefly discussed to give an overview of the range of appropriate application of this technique.

The results of the test and finite element studies will be combined to explain the behavior of the radial strips in flat plate structures. The distribution of shear, torsional moment, and shear resulting from these torsional moments along the side faces of different types of radial strips are discussed for both concentrically loaded interior and edge connections.

6.1 Finite Elements, Background

6.1.1 General

Behavior of a flat plate structure is fundamentally three dimensional. In addition to bending moments in two perpendicular directions, torsional moments are generated. Out of plane forces are more significant than membrane forces. Concrete cracks in the early stages of loading, especially near columns, as a result of shrinkage and the self-weight of the slab. These cracks will propagate as the load increases. Moreover, in the vicinity of the columns, where transverse shear and torsion are high, inclined cracks develop and usually dominate the response of the reinforced concrete in this region. A perfect finite element program should include the effects of all these cracks.

Two different approaches exist for modeling a crack, namely a "discrete crack" or a "smeared crack". In the discrete crack approach, each single crack introduces discontinuity in the continuum and causes a change in geometry of the structure. Modeling each potential crack as an individual discrete crack is very difficult and in most cases not practical, especially for large structures in which the number of cracks is large. The nature of the inclined cracks in zones of high shear also adds tremendously to the complexity involved in the change of geometry of the structure.

In the smeared crack approximation, the geometry is left unchanged and cracks are modeled by a distributed softening effect. This approach is suitable until the development of a localized failure zone in the structure. The use of the smeared crack method seems to be the only practical approach for analysis of large concrete structures.

In addition to a crack formulation, the material model in an ideal finite element analysis must represent the reinforcement and include the effect of tension stiffening of concrete, as well as bond degradation between concrete and single bars. However, interaction between concrete and reinforcement in the region of cracked concrete is highly non-linear, and makes the modeling of reinforced concrete very complex. One approximation is to represent reinforcement as sheets of uniform thickness, located at certain relative depths and having only unidirectional properties. In this approach, the strains of reinforcement and its surrounding concrete are assumed to be compatible.

Among the existing major groups of concrete material models are the elastic models and the plastic models. In general, elasticity based models are suitable for the range of elastic to moderately non-linear behavior, before anisotropic behavior becomes significant. Beyond this, plasticity based models are preferred because they are thought to render more accuracy, generality and also convenience in formulation (Ziyaeifar, 1996).

6.1.2 Finite Element Program NISA 90

The program NISA was originally written by the Institut für Baustatik, universität Stuttgart, Germany. The program performs static incremental nonlinear analysis of structures, and includes three dimensional degenerated plate shell element (Ramm, 1976) with five degrees of freedom per node; three translations and two rotations. Among the options is the sixteen node bicubic element. Gaussian integration is carried out parallel to the surface of the element, while Simpson's integration rule is adopted across the thickness.

The program NISA 90 is a modified version of NISA 80 by A.E. Elwi (1993). A number of concrete material models have been implemented, including Massicotte's model (1990) and a modified Paramono and Willam's model by Xie (1994). Since the latter requires an asymmetric equation solver, the program has been equipped with one written by D. Chan at the university of Alberta. Reinforcement is still modeled as sheets of uniform thickness. For solution strategy, the program permits use of one of (a) the Modified Constant Arc Length Method (CALM) introduced by Ramm (1981), (b) a displacement control procedure, or (c) the standard or a Modified Newton-Raphson iteration procedure. It is also possible to switch from one procedure to another.

6.2 Finite Element Study

6.2.1 Scope

Because of the following major limitations, replicating the results of the test specimen using finite elements is not intended, nor is it practical with the available techniques.

1. Modeling a specimen of this size and with so many variations in reinforcement would require a great number of elements and nodes. Because the reinforcement of the north panel was different from the south panel, only one axis of symmetry can be used to

reduce the number of elements. Even this would introduce some approximation since the crack pattern in the specimen was actually asymmetric.

2. Modeling the interaction between bars and their adjacent concrete is very complicated, especially in the zone of cracked concrete.

3. There were relatively wide and discrete cracks in both directions during the test. Also, discrete inclined shear or torsional cracks initiated at early stages of loading in the zone of high shear forces near columns. Modeling the discontinuity in the continuum, especially that caused by the inclined cracks, is very complicated and is out of the scope of this study.

The objective of current finite element study is a qualitative description of certain aspects of slab column connection behavior. In particular, the following questions are to be examined: (1) Is the assumption of the uniformly distributed one-way shear over a certain length along the side faces of the radial strips appropriate? (2) Is the torsion calculated on the basis of strain gauge measurements realistic? (3) Can the net torsion along the side faces of the radial strips be in the opposite direction to its flexural capacity? (4) What are the important parameters that lead to the different behavior in the two directions? (5) Does the steel perpendicular to the free edge and passing outside the edge column yield?

Three interior and two edge connections are examined. INT01, INT02, and INT03, respectively, address the aspects of the reinforcement layout, panel rectangularity, and loading sequence in interior connections. EXT01 and EXT02 examine the shear transfer in edge connections, as well as yielding of reinforcement perpendicular to the free edge and placed outside the column width.

6.2.2 Plates under Study, General

Using symmetry to reduce the number of elements, each mesh consists of sixteen plate elements with uniform thickness of 150 mm. The total number of nodes is 169. Each node has five degrees of freedom; two rotational and three translational. Newton-Raphson iteration with 1 kPa constant incremental load was selected as the solution strategy because it converged faster. The maximum load obtained this way was improved only by a fraction of one kPa when the strategy was changed to the constant arc length method.

Geometry and material properties for the finite element plates were very close to those of the test specimen. Figures 6.1 to 6.4 show the geometry of the slab and layout of the elements, as well as the boundary conditions. Reinforcement ratios and the arrangement of steel are presented in Tables 6.1 to 6.4. Material properties are as follows;

Compressive strength of concrete	$f'_c = 34.8$ MPa
Tensile strength of concrete	$f_{ct} = 2.36$ MPa
Modulus of elasticity of concrete	$E_c = 26500$ MPa
Yield stress of steel	$f_y = 420$ MPa
Modulus of elasticity of steel	$E = 200\ 000$ MPa
Slope of strain hardening of steel	$E_s = 466$ MPa
Maximum strain for reinforcements	$\epsilon_{max} = 0.125$

To model the interaction between column and plate, element #1 was assigned different material properties. The tensile strength and the compressive strength were both set to 35000 MPa to avoid material failure inside column, and modulus of elasticity was increased by a factor of 10 000 so that the deflection of element #1 would be almost zero.

Graphical presentation of the study is based on the data at the integration points. At each load increment, and for each direction, shear forces along sections $x = 17.5$ mm or $y = 17.5$ mm (right at the integration points) were integrated and the results were compared with the shear due to the applied loads. Due to the numerical problems near the column faces, the vertical equilibrium was satisfied within 10 percent tolerance. Alternatively, shear on the side faces of the two radial strips were integrated and compared to the loads on the quadrant. With this check, vertical equilibrium was satisfied within a 5 percent tolerance. As a result, a more accurate estimate of the average shear along a column face is obtained by adding the load on the side faces of the corresponding strip and the load directly applied to this strip. The finite element results in tables are based on the average shear so obtained.

Around the column of a prototype building, diagonal cracks form due to very high shear intensities. Since these cracks do not prevent shear transfer by arching action, the plate is able to carry additional load. In the finite element analysis, however, high shear intensities near the column is associated with numerical instability. As a result, it is expected that the load in the simulated plates will not reach the design load.

6.2.3 Interior Connections

6.2.3.1 Interior Connection INT01

This simulation examines the effect of a difference in the effective depth of the steel layers, inevitable in flat plates. Figure 6.1 and Table 6.1 show the geometry and the reinforcement of simulation INT01. A square panel with a square column was selected. The ratio of positive design moment to the total panel moment in both directions is 0.385. Since negative moments are equal in the two directions, the required area of top steel in the inner layer is slightly greater. Assuming the same bar size in the two layers, the steel in the inner layer is over a wider band. Hence, element 11 is rectangular.

The maximum load program reached was 15 kPa, or about 80 percent of the yield line mechanism load. At this load, distribution of shear intensity along two perpendicular sections is plotted versus the distance from column corner in Figure 6.5. It can be seen that 48 percent of the total load was transferred to the column through E-W radial strip, or through east face of the column (element #2).

Distribution of torsional moment intensity is plotted in Figure 6.6 at the last load step. Also in Figure 6.7, torsional moment along side face of radial strips is plotted versus the load. A positive value means that this moment was in the same direction as bending moments in the rotational equations of equilibrium of the radial strips.

6.2.3.2 Interior Connection INT02

Simulation INT02 examines the effect of panel rectangularity. As shown in Figure 6.2, N-S span is 200 mm larger than E-W span. This reflects the effect of shifting of zero shear line toward the exterior column in an edge panel. The yield line mechanism load of

this slab is equal to that of the INT01. Negative moments in two directions are equal. However, since span length are different, positive moments are not the same. Details of reinforcement are presented in Table 6.2.

Maximum load program reached was 14 kPa, about 75 percent of the yield line mechanism load. At this load, distribution of shear and torsion are plotted in Figures 6.8 and 6.9. The behavior of the slab in the two directions is almost the same. According to Table 6.6 and Figure 6.20, about 48 percent of the load was transferred through the east face of the column and 52 percent through the north face. As shown in Figure 6.7, torsion along the side faces of all radial strips augments the bending capacity and hence the shear capacity of these strips.

6.2.3.3 Interior Connection INT03

Slab INT03 was designed to see if loading sequence would induce different behavior in the two directions. The layout of elements and details of reinforcement of slab INT03 are the same as those of INT02, except for the east edge which is assumed to be a free edge with positive moment applied uniformly on it. Up to a uniform load of 9 kPa, the applied moment was set to 10 percent of the panel moment at each load step. For loads of 10 kPa or more, 40 percent of the panel moment was applied to this edge. The sudden increase in the positive moment between 9 and 10 kPa load steps caused a sudden upward movement of slab and a sudden decrease in the corresponding negative moment.

A direct comparison between the specimen and slab INT03 is not appropriate, because their loading history is different. The specimen was unloaded before applying the first adjustment. Moreover, adding positive moments to the edges of the specimen was done early in testing and caused an increase in jack loads, since they prevented the plate from deflecting upward. In slab INT03, however, the sudden increase of the positive moment was associate with an upward deflection of the plate and a sudden decrease in the negative moments.

The maximum load for slab INT03 was 13 kPa. It can be seen from Table 6.8 that at a load of 9 kPa, 50 percent of the load was transferred through the east face of the column. This means that as long as flexural condition near column remains the same in the two directions, according to the finite element analysis, each strip carries its own share of the load, regardless of the condition of the mid-span. However, as presented in Table 6.7, at a load of 13 kPa, only 38 percent of load was transferred through the east face of the column. Further investigation showed that after redistribution of the moments, or in other words, after unloading the negative moment about y axis, limited load was carried by the E-W strip and most of the additional load was transferred through the N-S strip (Figure 6.20).

Distribution of shear and torsion at the last load step are plotted in Figures 6.11 and 6.12. Torsional moments along the side face of the radial strips are plotted versus the load in Figure 6.13. This torsion always added to the bending capacity of the radial strips, and therefore increased the shear capacity of the strips.

6.2.4 Exterior Connections

6.2.4.1 Edge Connection EXT01

Reinforcement for this slab is designed for a load of 18 kPa, and is shown in Table 6.3. Negative moment at the column face and about an axis parallel to the free edge is assumed to be 30 percent of the panel moment. In the other direction, the ratio of the negative design moment to the panel moment is 0.62.

The maximum load reached in the finite element analysis was only 10 kPa. At this load, distribution of shear intensity is plotted in Figure 6.14. Shear behavior was different in the two directions. Upward shear acted on east side face of the column, close to the edge. This shear was the result of high torsional moments on the side faces of the column. Figure 6.21 shows that the shear transferred by the spandrel strip was much less than the shear transferred by the interior radial strip. According to Table 6.9, only 20 percent of the load was transferred through the spandrel strip; about 10 percent was directly applied to the spandrel strip, and 10 percent comes from the load on the quadrant.

Distribution of the torsion along the side face of the interior radial strip is shown in Figure 6.15. Total torsion on the side face of the spandrel strip, as shown in Figure 6.16, was in the opposite direction of the bending moments. Therefore, by using up part of the flexural capacity of the strip, this torsion reduced the shear capacity of the spandrel strip.

6.2.4.2 Edge Connection EXT02

Case EXT02 was analyzed to further examine the yielding of the reinforcement perpendicular to the free edge. Therefore, dimensions, layout of elements, and total area of the reinforcement were chosen exactly the same as the case EXT01, except that the top reinforcement perpendicular to the free edge is uniformly distributed in a 1.15 m wide band, rather than 0.4 m as in EXT01.

Top steel perpendicular to the free edge and far from the column did not contribute significantly to the bending moments. That is why at the load of 9 kPa, or 50 percent of the design load, negative moment at the column face was only about 27.8 percent of its design moment.

According to Table 6.10, at the load step of 9 kPa (Maximum load program reached), about 72 percent of the total load is transferred through the interior radial strip. In Figures 6.17 and 6.18, distribution of shear and torsion are shown. Total torsion along the side face of the radial strips is plotted in Figure 6.19.

6.2.5 Discussion

Shear intensity diagrams based on the finite element analysis (i.e. Figure 6.5) are pretty ragged because of the numerical problems at the integration points. However, the average shear on the elements are reliable results (i.e. Table 6.5), and to some extent, may be used to verify the Bond Model. According to the finite element results, shear on the side face of the radial strips can be approximated by a rectangle in a region near the column, and its maximum value is roughly 110 N/m, which is about the right value for the critical one way shear (element #6 in Tables 6.5 through 6.10).

Knowing from symmetry that the torsion is zero along the center line of the columns, it becomes very important to find out if the torsion calculated using the strain gauge measurements at a very small distance from the center line of the columns are realistic. In finite element study of the INT03, a positive torsion of 4.5 kNm was obtained

at the load of 13 kPa. At this load, the maximum torsion at the interior connection of the specimen was about 5 kNm, which is consistent with the test results.

The results of the finite element study on the edge connections strongly support the test results, and confirm that a negative torsion along the side face of a spandrel strip is usual. At the load of 10 kPa, the maximum negative torsion (consuming rather than augmenting the flexural capacity) was about 2.5 and 6.5 kNm, respectively in the finite element analysis and the test specimen.

With finite element analysis, different behavior of the radial strips in the two directions was observed for both interior and edge connections (see Figures 6.20 and 6.21). However, at the interior connection, this kind of behavior required a non-symmetric loading history, while at the edge connections, it started right at the beginning of the loading.

Finally, consistent with the test results, steel perpendicular to the free edge and out side the column width did not contribute significantly to the flexural capacity of the edge connections. This steel was not yielded and its contribution became smaller as it was spread out in a wider band.

6.3 Distribution of Shear and Torsion along Side Faces of Radial Strips

For most tests on interior connections reported in the literature, the ratio of the test load to that calculated according to the Bond Model is greater than one. These tests are mostly enforced deformation tests, in which all radial strips are loaded to their maximum capacity, torsional moments along side faces of the radial strips are in the same direction as the flexural moments, and the behavior in the two directions is basically the same. Such connections are referred to as **case (a)**.

The current test, however, revealed that under certain conditions (Section 5.2.2.1), the radial strips of an interior connection might not be loaded in proportion to their nominal capacities. Such connections (**case b**) punch when the radial strips in one direction reach their maximum capacity. Along side faces of these radial strips, the torsional moments are in the same direction as the flexural moments. However, along side faces of radial strips not loaded to their nominal capacity, the resultant of the torsional moments is in the opposite direction of the flexural moments.

In an edge connection (**case c**), a large portion of the load is transferred through the interior radial strip, and torsional moments along side faces of this strip are in the same direction as the flexural moments. Also, high torsional moments are generated along the side faces of the column. Spandrel strips of flat plates transfer a small portion of the load compared to the interior radial strips. The resultant of the torsional moments is in the opposite direction of the bending moments.

For these three cases, based on the results of the finite element analysis, mechanics of the bond model, and the test results, typical shear intensity diagrams, typical torsional moment intensity diagrams, and typical torsional shear diagrams are plotted along the critical section (sections ABF and A'BF' in Figure 4.22; side face of column, AB or A'B, and side face of radial strips 1 or 2, BF or BF'). The diagrams are described in Figures 6.23 through 6.26, and are presented in Figures 6.27 to 6.30 for case (a), Figures 6.31 to 6.34 for case (b), and Figures 6.35 to 6.38 for case (c). Note that the

values shown on these diagrams are given as examples and do not represent any test or analytical data.

6.3.1 General

6.3.1.1 Shear Intensity

Figure 6.23 shows a typical shear intensity diagram along side face of strip 1. The area under shear intensity diagram between any two points equals to the total load transferred in that region.

The shear intensity on the column face is very high because the column provides a vertical support and allows for significant arching action in this region. Shear intensity suddenly drops to a value controlled by the critical one way shear within a small distance from column corner, since along the side faces of the radial strips, the dominant mechanism of shear transfer is beam action.

This sudden change in the shear intensity is the main reason for the results of the finite element analysis being rather ragged in this region. In other words, some kind of numerical problem occurs in the integration points of the elements close to the column, because of the so called discontinuity. However, the average shear intensity in these elements are acceptable, especially since the size of these elements are relatively small.

6.3.1.2 Torsional Moments

Figure 6.24 shows a typical torsional moment intensity along the side face of the radial strip 1. In concentrically loaded interior connections, the torsional moment must be zero at the center line of the column (point A) and also at the remote end of the strip (point F), because of symmetry. Along the side face of the interior radial strip of an edge connection, the torsional moment must be zero at the remote end because of symmetry, and is also zero at the corner of the column on the free edge. The results of finite element analyses show that in all cases, torsional moment is also zero at another point (D) located on the side face of the radial strip. This means that torsional moment is negative in one part of the diagram (i.e. part AD), and positive in the other part (DF). Consistent with the sign convention used in the finite element analyses, positive torsional moment on the side face of the radial strip is in the same direction as the bending moments of the strip, and helps increasing both shear and flexural capacity of the strip.

It is worth mentioning that the total torsion along the side face of the radial strip (between column corner B and remote end F) equals the net area under the torsional moment intensity diagram, and directly enters the rotational equations of equilibrium of the radial strip 1.

6.3.1.3 Torsional Shear

Torsional shear on the side face of the radial strip is the result of the gradient in the torsional moment in a direction parallel to the radial strip. Therefore, the value of the

torsional shear at any point equals the slope of the torsional moment diagram. As a result, torsional shear diagram can be constructed based on the torsional moments.

In regions AC and EF of Figures 6.24 and 6.25, the slope of the torsional moment diagram is negative, and so is the torsional shear. Note that with the chosen sign convention for the torsional moments, negative shear represents an upward shear on the face of the radial strips. At points C and E, slope of the torsional moment diagram equals zero, and so does the torsional shear. At point F, the value of shear intensity is relatively small and is assumed to be zero.

The area under the torsional shear intensity diagram between any two points represents the amount of shear transferred by torsional moment gradient between these points. This area is also equal to the difference between the torsional moments at these points. Therefore, between any two points with zero torsional moment (for example, D and F), the net shear transferred by the torsional moment becomes zero ($V_1 + V_3 = 0$, or V_3 equals V_1 but in opposite direction), and the torsional shear only cause a change in the distribution of the vertical shear. Note that the net torsion between D and F equals $V_1 \times d_1$ and between A and D equals $V_2 \times d_2$.

6.3.1.4 Torsional Moment at the Corner of the Column

At failure, torsional moment at the corner of the column can not be determined by the available analytical methods, nor can it be measured by the existing instrumentation. However, in the early stages of loading, a finite element analysis may provide an estimate of these moments. The purpose of this section is to describe, based on the equilibrium and the mechanics of the shear transfer inside a radial strip, how these torsional moments change with the increase of the applied loads.

Figure 6.26a shows the position of a small segment of the radial strip adjacent to the column. A free body diagram of this element is shown in Figure 6.26b. Due to symmetry, the torsional moment, M_{t1} , at the center line of the column is zero. Torsional moment, M_{t2} , on the side face of the radial strip is determined using rotational equation of equilibrium as follows;

$$M_{t2} = (T_2 jd_2 + V_2 \Delta s) + w_1 \Delta s^2 / 2 - T_1 jd_1 \quad [6.1]$$

Term $(w_1 \Delta s^2 / 2)$ is negligible compared to other terms if Δs is small enough. Throughout a large range of loading, $M_{t1} = T_1 jd_1$ equals the yield moment and has a large constant positive value. Internal moment arm jd_2 , as shown in Figure 6.26c and 6.26d, depends on the geometry of the compression arch, and increases with the increase in the loaded length, l_w (compare Figures 6.26b and 6.26c).

In early stages of loading, in all of the finite element simulations, M_{t2} had a negative value. In cases where the load in the strip does not change significantly, such as spandrel strips, all terms in Equation 6.1 remain almost unchanged. As a result, M_{t2} is expected to remain negative until failure.

In cases where radial strips reach or exceed their nominal capacity, such as those in an enforced deformation test, or the interior radial strip of an edge connection, the magnitude of $(T_2 jd_2 + V_2 \Delta s)$ increases with increasing load, while $(T_1 \times jd_1)$ remains

almost constant. As a result, torsional moment at the column corner, initially negative, increases towards zero. This means that with the increasing load, point D in Figure 6.24 moves towards the point B. For these strips, the torsional moment at the column corner is assumed to be zero at the time of failure (points D and B become one point).

6.3.2 Interior Radial Strips Reaching or Exceeding Their Nominal Capacity

For radial strips that reach or exceed their nominal capacity, a typical shear intensity diagram is plotted in Figure 6.27. According to the finite element analysis, at about 75 percent of the failure load, shear intensity at the center line of the column is smaller than the shear intensity at the corner of the column due to the torsional moments and their related shears. The difference becomes smaller as the load is increased to the failure load since due to the extensive yielding, torsional moments reduce to about zero.

Consistent with the test results, the finite element analysis (e.g. Figure 6.5) suggests that the distribution of shear, as shown in Figure 6.27, can be approximated by a rectangle. In Figure 6.28, based on the results of the finite element analyses, idealized torsional moment intensity is plotted along the critical section 1. As discussed in Section 6.3.1.4, the torsional moment at the column corner is assumed to be zero. Torsional shear intensity is plotted in Figure 6.29. Net torsion along the side face of the strip between B and F (3.79 kNm) and also the couple due to its associated shear ($4.59 \times d_1$) augments the flexural capacity, and hence the shear capacity of the radial strip.

6.3.3 Radial Strips Not Reaching Their Nominal Capacity

Figures 6.30a and 6.30b show typical shear intensity diagrams along the critical sections A'BF' and ABF in a connection with behavior in the two directions. In Figure 6.30a, the dotted area (load transferred through radial strip 1) is considerably more than the dashed area (load transferred through radial strip 2).

Shear intensity at ultimate is plotted so that the load transferred through radial strip 2 remains more or less constant, while the load in the radial strip 1 increases considerably. Also, from Figure 6.31 it can be seen that the total torsional moment along the side face of the radial strip (between B and F') is in a direction that reduces the flexural capacity of the strip (i.e. $M_t = 5.36 - 3.14 = 2.22$ kNm must be deducted from M_s).

Bending shear is the difference between the total shear and the torsional shear. Torsional shear intensity is plotted in Figure 6.36. This figure shows that a considerable amount of load is removed from column region (A'B) and even part of the radial strip (BC') and is added to the radial strip in region C'D'. High values of torsional shear in region C'D' suggest that the bending shears in this region are small, and might explain why bar 3/9 of the test specimen transferred a considerably smaller shear than bar 2/9 and even bars 4/9 and 5/9 (Figure 5.16).

6.3.4 Interior Radial Strips in an Edge Connection

Test results and finite element analysis agree that in the south edge connection, spandrel strips carry a much smaller portion of the load than does the interior radial strip. In Section 5.3.2, some of the similarities and differences between the behavior of the edge connections and the behavior of the interior connections were briefly discussed. In

chapter seven, another aspect which is the basis for constructing moment-shear interaction diagram of an edge connection, will be discussed in detail. This aspect is introduced here, and perhaps is the most important difference in the behavior of the radial strips between concentrically loaded interior connections and the edge connections.

In a concentrically loaded interior connection, no matter which portion of the load is transferred through each radial strip, the equations of equilibrium are satisfied because of symmetry. In edge connections (and also interior connections with unbalanced loading), the magnitude of the vertical load and the bending moment are known and therefore the eccentricity of the vertical load can be specified. This introduces a relation between the maximum load transferred through the interior radial strip and the maximum load that can be transferred through the spandrel strip, since the resultant force must have the same eccentricity as the applied loads. In practice, the majority of edge connections are designed so that they have relatively large eccentricity. This means that a much larger portion of the load must be transferred through the interior radial strip to satisfy the equations of equilibrium. This is a situation similar to the test specimen and therefore the shear intensity, torsional moment intensity, and torsional shear intensity diagrams presented here represent the behavior of the radial strips in the majority of edge connections.

Figure 6.33 illustrates a likely shear intensity diagram along the side face of a spandrel strip. The amount of shear transferred through spandrel strip (shaded area) is much smaller than the load transferred through the interior radial strip. In the spandrel strip, unlike other radial strips, in the region where beam action dominates, the shear intensity can not be approximated by a rectangle, simply because either no top reinforcement is provided or the top reinforcement does not reach the yield stress. Note that because of the large eccentricity of the forces, the curvature of the plate is such that shear can not be transferred effectively by the force gradient in the bottom bars.

Figure 6.34 illustrates a typical shear intensity along the side face of an interior radial strip of an edge connection. It can be seen that a large portion of the total load is transferred by beam action to this strip. The shear intensity shown on the side face of the column is only based on the results of the finite element analysis (note that program stopped at a load considerably smaller than the failure load). According to this analysis high torsional moments on the column face result in upward and downward shears along the column face. Also, in a narrow band (dotted area), the load in the spandrel strip is being transferred by arching action to the column.

In Figures 6.35 and 6.36 torsional moment and torsional shear intensities are plotted along the side face of the spandrel strip. These diagrams are basically similar to the diagrams for case b (Figures 6.29 and 6.30), except that the amount of torsion that diminishes the flexural capacity of the spandrel strip is more ($M_t = 6.0 - 2.23 = 3.72$ kNm).

Table 6.1 Reinforcement of Simulation INT01

Position	Effective Depth (mm)	Total Area (mm ²)	Element Number				
			Reinforcement Ratio (percent)				
Top (E-W)	106	1800	Element #	2,3	5,6,7	9,10,11	
			ρ (%)	1.31	1.31	1.31	
Top (N-S)	122	1600	Element #	5,9	2,6,10	3,7,11	
			ρ (%)	1.14	1.14	1.14	
Bottom (E-W)	113	1000	Element #	2,3,4	5,6,7,8	9,10,11,12	13,14,15,16
			ρ (%)	1.47	0.289	0.289	0.289
Bottom (N-S)	125	900	Element #	5,9,13	2,6,10,14	3,7,11,15	4,8,12,16
			ρ (%)	1.33	0.226	0.226	0.226

Table 6.2 Reinforcement of Simulations INT02 and INT03

Position	Effective Depth (mm)	Total Area (mm ²)	Element Number				
			Reinforcement Ratio (percent)				
Top (E-W)	106	1800	Element #	2,3	5,6,7	9,10,11	
			ρ (%)	1.31	1.31	1.31	
Top (N-S)	122	1600	Element #	5,9	2,6,10	3,7,11	
			ρ (%)	1.14	1.14	1.14	
Bottom (E-W)	113	1230	Element #	2,3,4	5,6,7,8	9,10,11,12	13,14,15,16
			ρ (%)	1.47	0.347	0.347	0.347
Bottom (N-S)	125	1350	Element #	5,9,13	2,6,10,14	3,7,11,15	4,8,12,16
			ρ (%)	1.33	1.33	0.267	0.267

Table 6.3 Reinforcement of Simulation EXT01

Position	Effective Depth (mm)	Total Area (mm ²)	Element Number				
			----- Reinforcement Ratio (percent)				
Top (E-W)	106	1870	Element #	2,3	5,6,7	9,10,11	
			ρ (%)	1.26	1.26	1.26	
Top (N-S)	122	800	Element #	5,9	2,6,10	3,7,11	
			ρ (%)	1.64	1.64	-----	
Bottom (E-W)	113	1000	Element #	2,3,4	5,6,7,8	9,10,11,12	13,14,15,16
			ρ (%)	0.885	0.289	0.289	0.289
Bottom (N-S)	125	1600	Element #	5,9,13	2,6,10,14	3,7,11,15	4,8,12,16
			ρ (%)	0.66	0.66	0.66	0.4

Table 6.4 Reinforcement of Simulation EXT02

Position	Effective Depth (mm)	Total Area (mm ²)	Element Number				
			----- Reinforcement Ratio (percent)				
Top (E-W)	106	1870	Element #	2,3	5,6,7	9,10,11	
			ρ (%)	1.26	1.26	1.26	
Top (N-S)	122	800	Element #	5,9	2,6,10	3,7,11	
			ρ (%)	0.696	0.696	0.696	
Bottom (E-W)	113	1000	Element #	2,3,4	5,6,7,8	9,10,11,12	13,14,15,16
			ρ (%)	0.885	0.289	0.289	0.289
Bottom (N-S)	125	1600	Element #	5,9,13	2,6,10,14	3,7,11,15	4,8,12,16
			ρ (%)	0.66	0.66	0.66	0.4

Table 6.5 Average Out of Plane Shear Intensity in kN/m - INT01 at 15 kPa

Side face of N-S radial strip				
Element Number	2	6	10	14
Element Width (mm)	150	250	900	1150
Shear Intensity (kN/m)	289	101	13	4
Side face of E-W radial strip				
Element Number	5	6	7	8
Element Width (mm)	150	250	750	1300
Shear Intensity (kN/m)	312	102	15	1

Table 6.6 Average Out of Plane Shear Intensity in kN/m - INT02 at 14 kPa

Side face of N-S radial strip				
Element Number	2	6	10	14
Element Width (mm)	150	250	900	1350
Shear Intensity (kN/m)	287	109	17	0
Side face of E-W radial strip				
Element Number	5	6	7	8
Element Width (mm)	150	250	750	1300
Shear Intensity (kN/m)	316	108	16	-1

Table 6.7 Average Out of Plane Shear Intensity in kN/m - INT03 at 13 kPa

Side face of N-S radial strip				
Element Number	2	6	10	14
Element Width (mm)	150	250	900	1350
Shear Intensity (kN/m)	215	84	15	9
Side face of E-W radial strip				
Element Number	5	6	7	8
Element Width (mm)	150	250	750	1300
Shear Intensity (kN/m)	344	94	16	-6

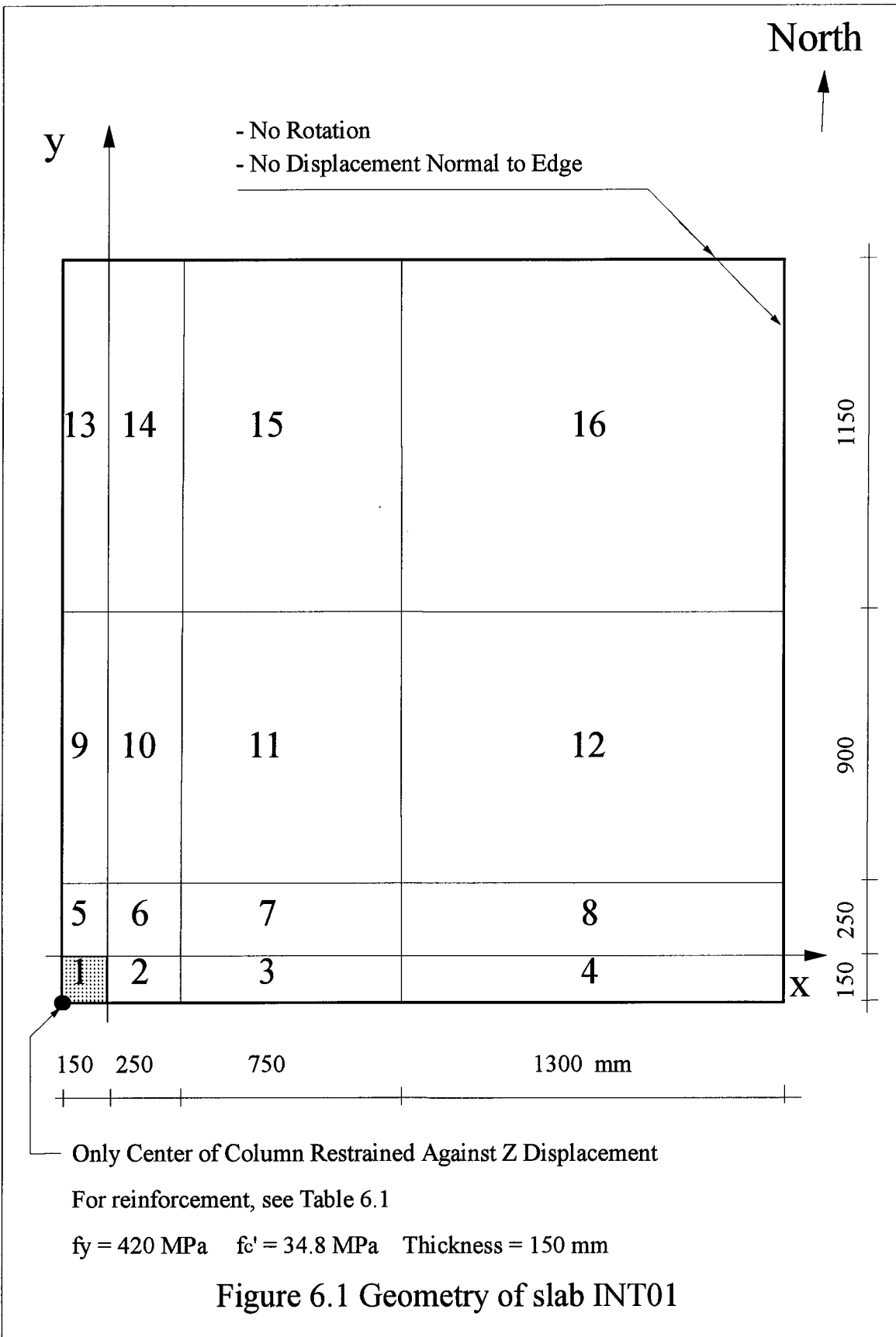
Side face of N-S radial strip				
Element Number	2	6	10	14
Element Width (mm)	150	250	900	1350
Shear Intensity (kN/m)	194	64	9	1
Side face of E-W radial strip				
Element Number	5	6	7	8
Element Width (mm)	150	250	750	1300
Shear Intensity (kN/m)	194	69	10	1

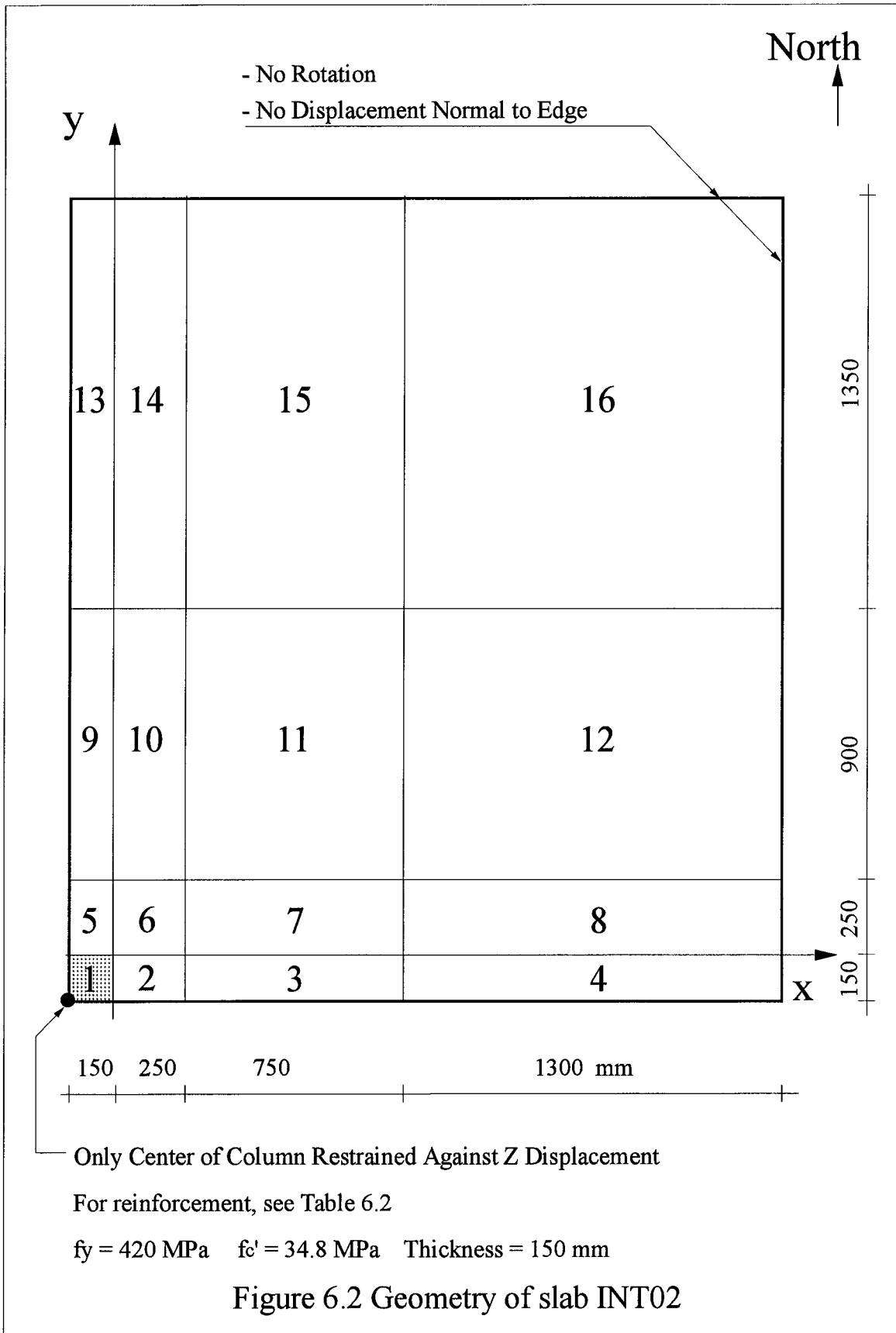
Table 6.9 Average Out of Plane Shear Intensity in kN/m - EXT01 at 10 kPa

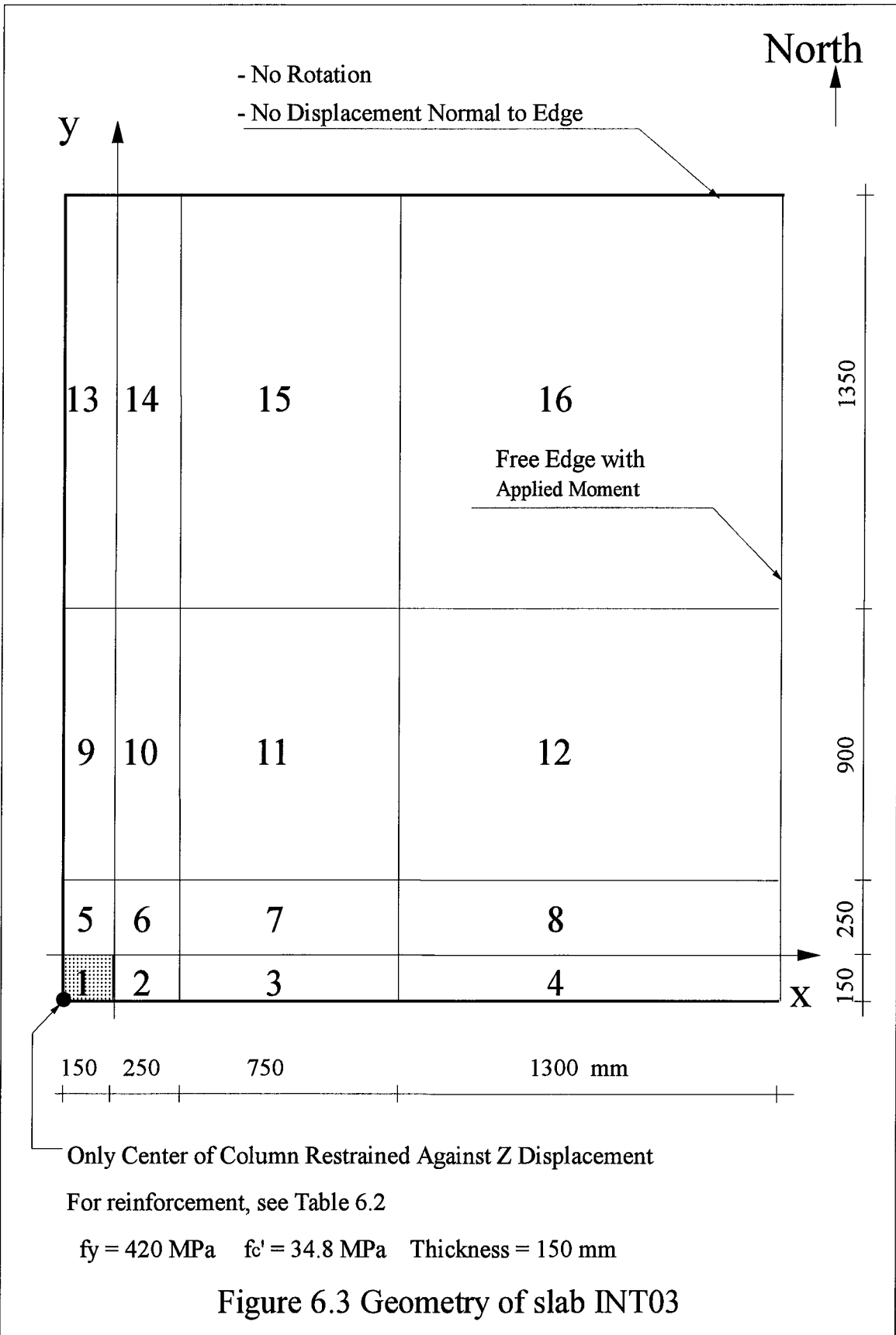
Side face of N-S radial strip				
Element Number	2	6	10	14
Element Width (mm)	250	250	900	1150
Shear Intensity (kN/m)	49	114	17	2
Side face of E-W radial strip				
Element Number	5	6	7	8
Element Width (mm)	150	250	750	1300
Shear Intensity (kN/m)	330	46	-10	2

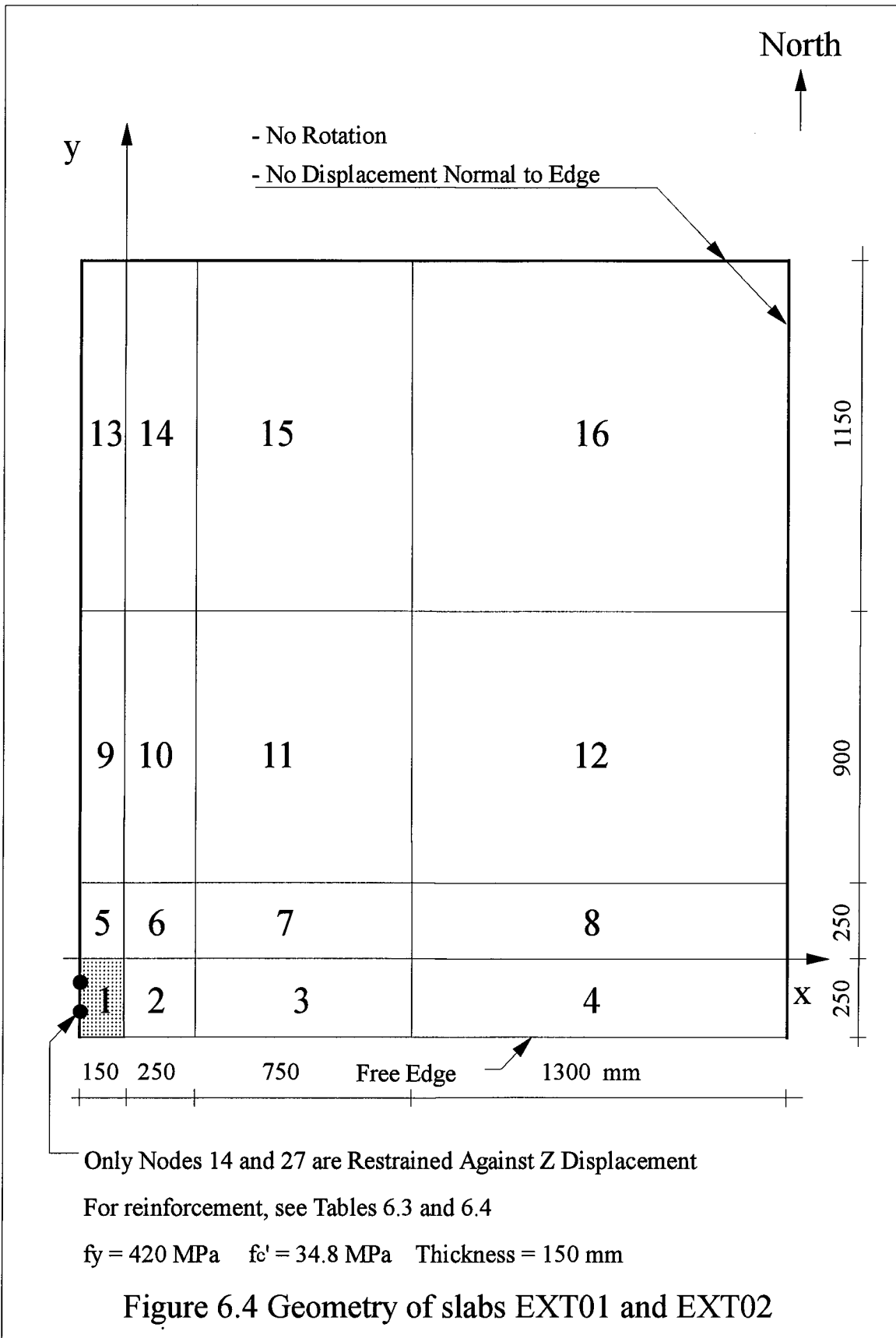
Table 6.10 Average Out of Plane Shear Intensity in kN/m - EXT02 at 9 kPa

Side face of N-S radial strip				
Element Number	2	6	10	14
Element Width (mm)	250	250	900	1150
Shear Intensity (kN/m)	63	100	11	2
Side face of E-W radial strip				
Element Number	5	6	7	8
Element Width (mm)	150	250	750	1300
Shear Intensity (kN/m)	269	48	-7	3









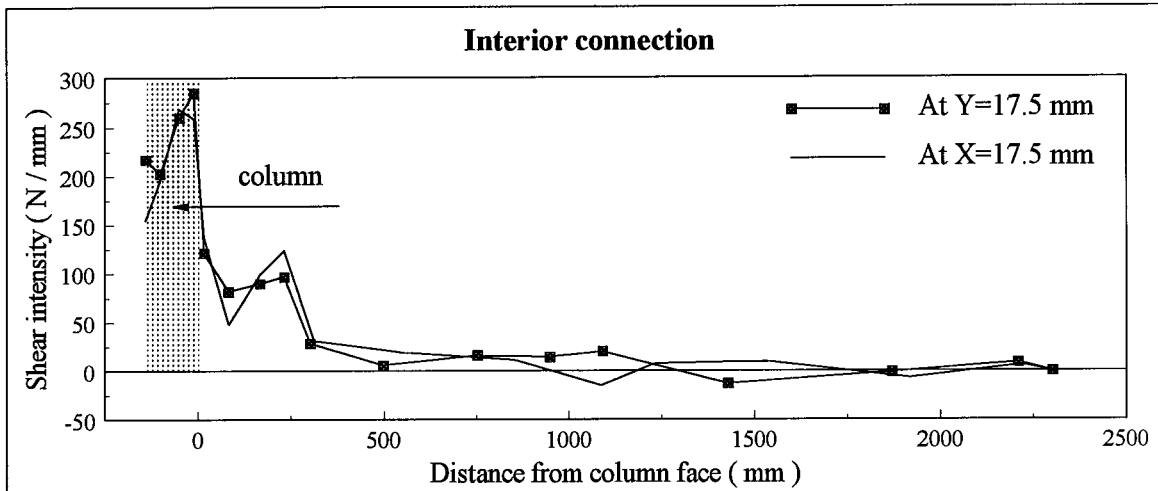


Figure 6.5 Shear intensity at a load of 15 kPa, slab INT01

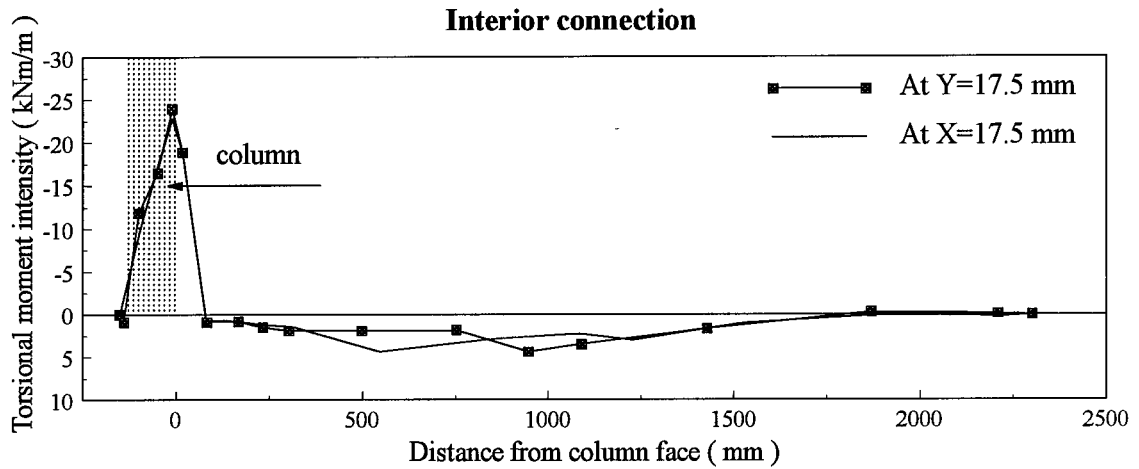


Figure 6.6 Torsional moment intensity at a load of 15 kPa, slab INT01

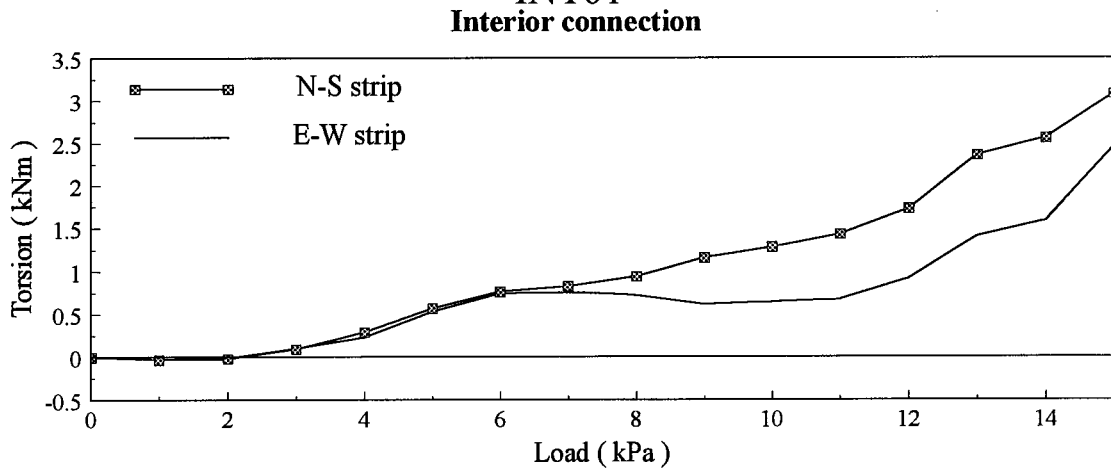


Figure 6.7 Torsional moment along each side face of radial strips, slab INT01

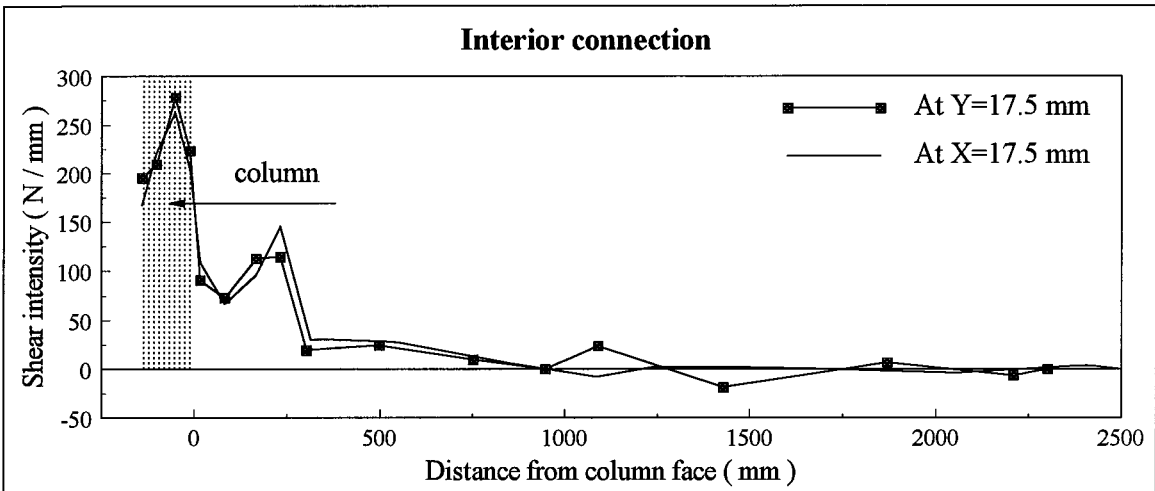


Figure 6.8 Shear intensity at a load of 14 kPa, slab INT02

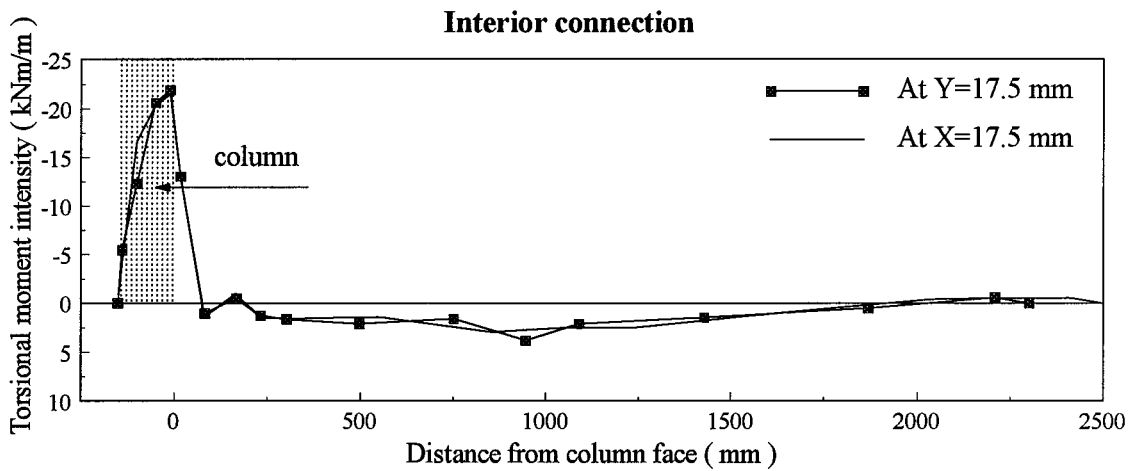


Figure 6.9 Torsional moment intensity at a load of 14 kPa, slab INT02

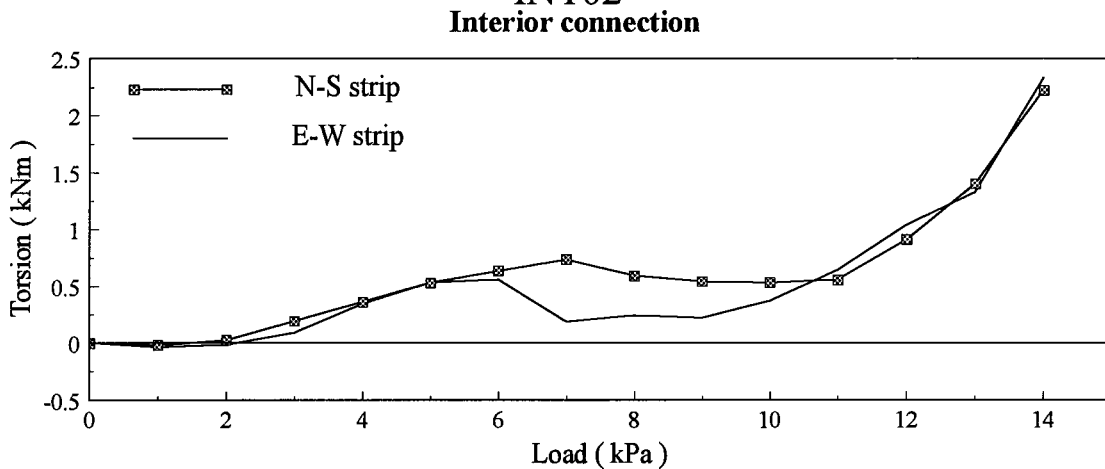


Figure 6.10 Torsional moment along each side face of radial strips, slab INT02

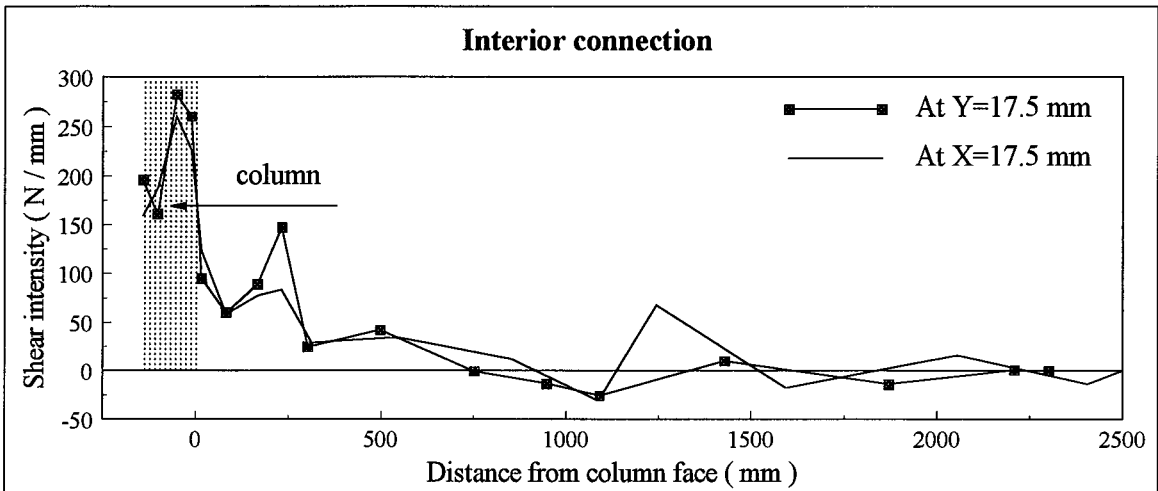


Figure 6.11 Shear intensity at a load of 13 kPa, slab INT03

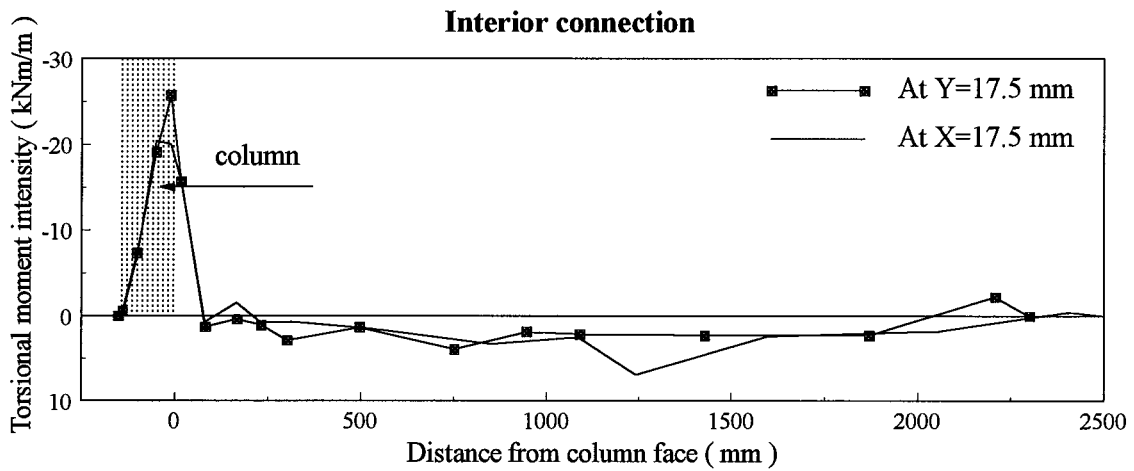


Figure 6.12 Torsional moment intensity at a load of 13 kPa, slab INT03

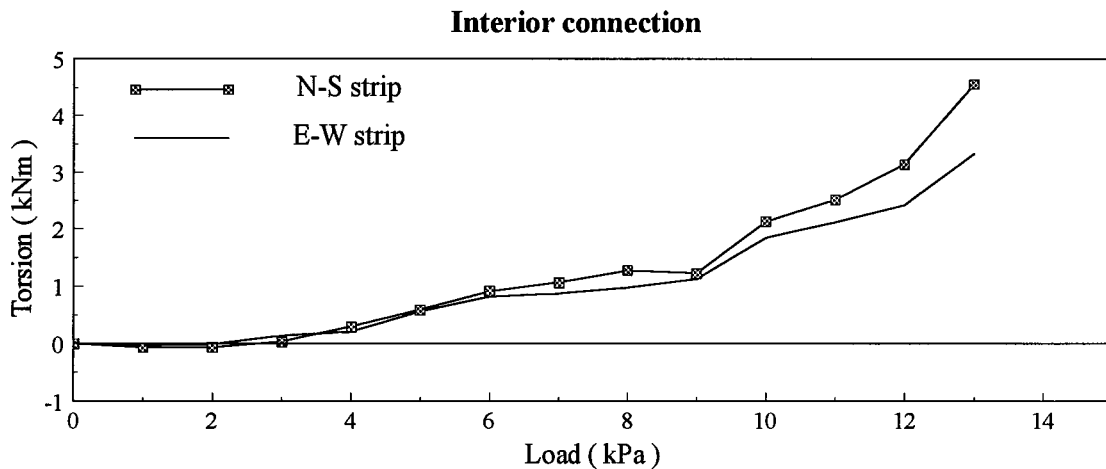


Figure 6.13 Torsional moment along each side face of radial strips, slab INT03

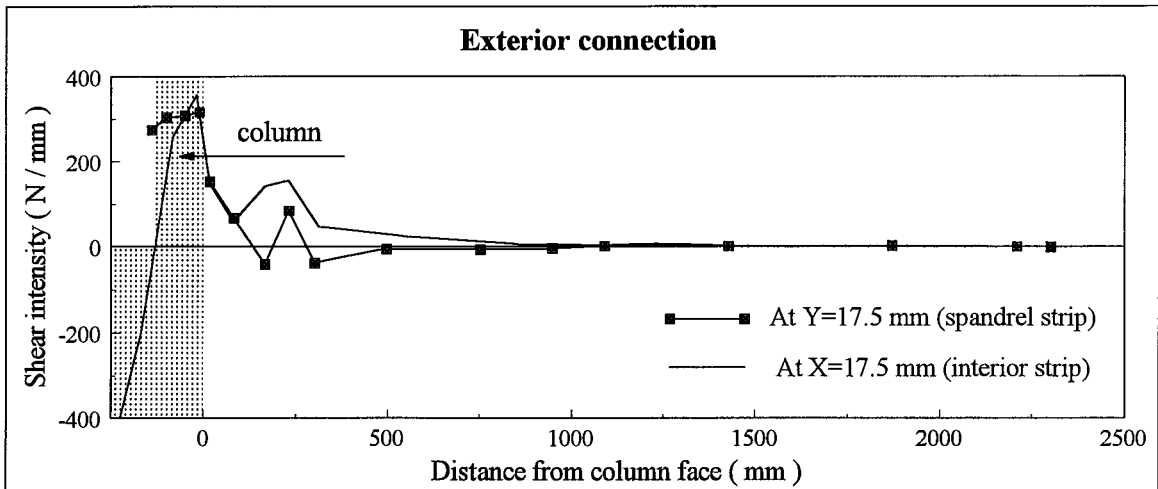


Figure 6.14 Shear intensity at a load of 10 kPa, slab EXT01

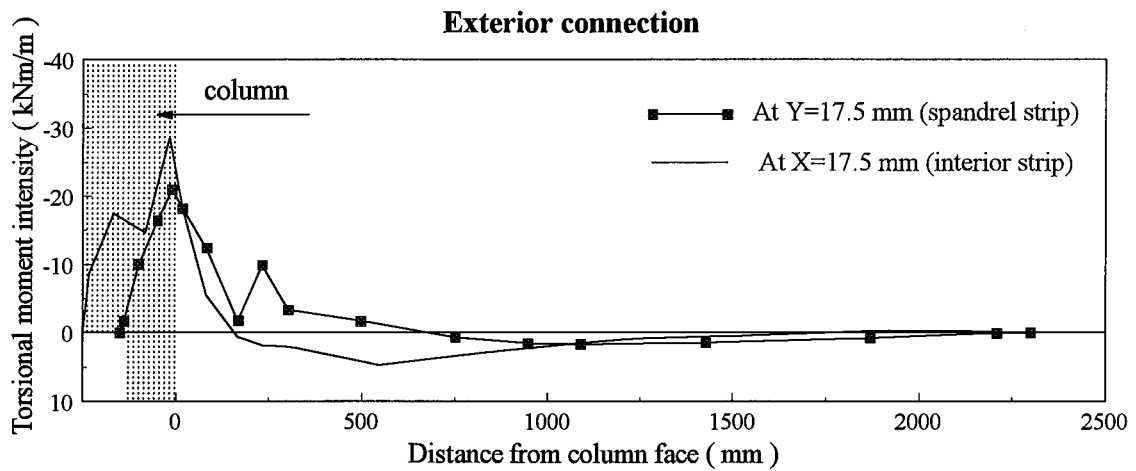


Figure 6.15 Torsional moment intensity at a load of 10 kPa, slab EXT01

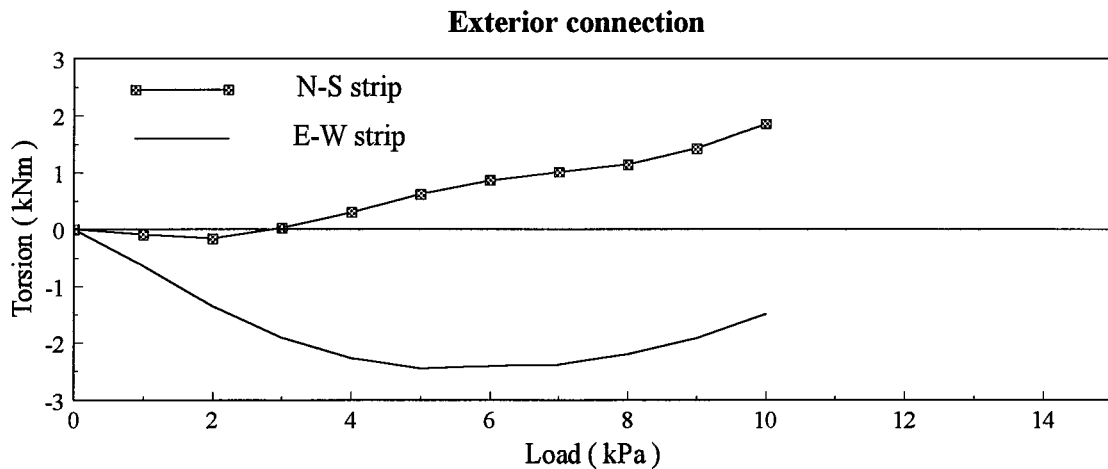


Figure 6.16 Torsional moment along each side face of radial strips, slab EXT01

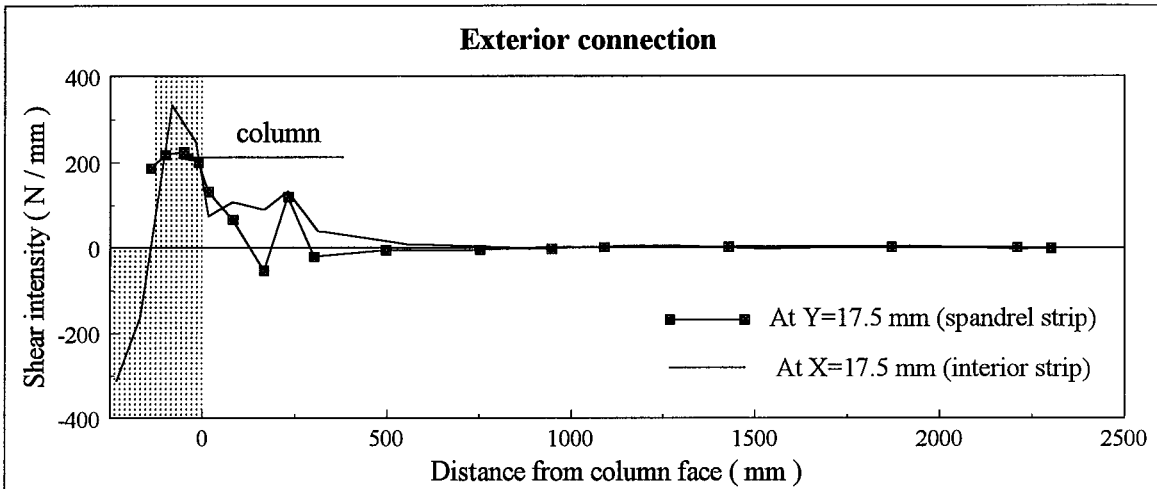


Figure 6.17 Shear intensity at a load of 9 kPa, slab EXT02

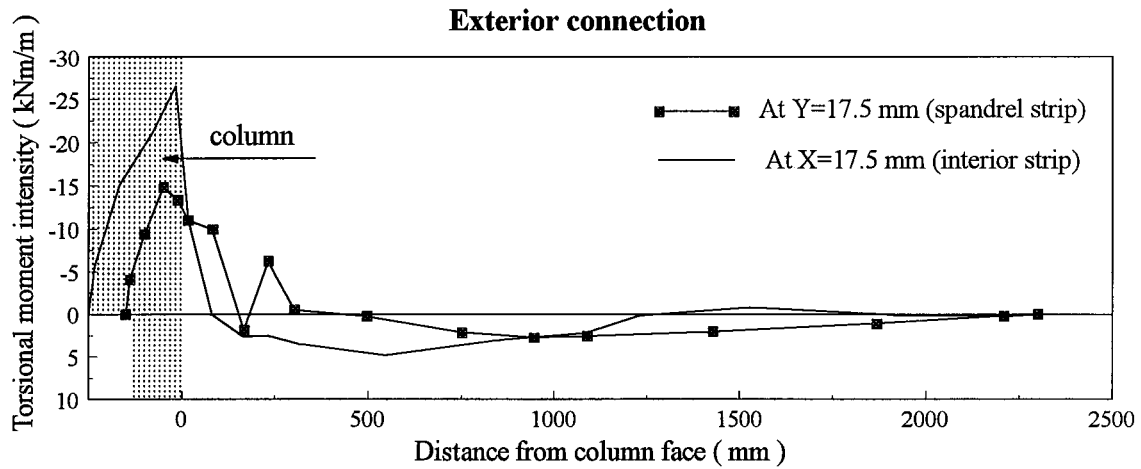


Figure 6.18 Torsional moment intensity at a load of 9 kPa, slab EXT02

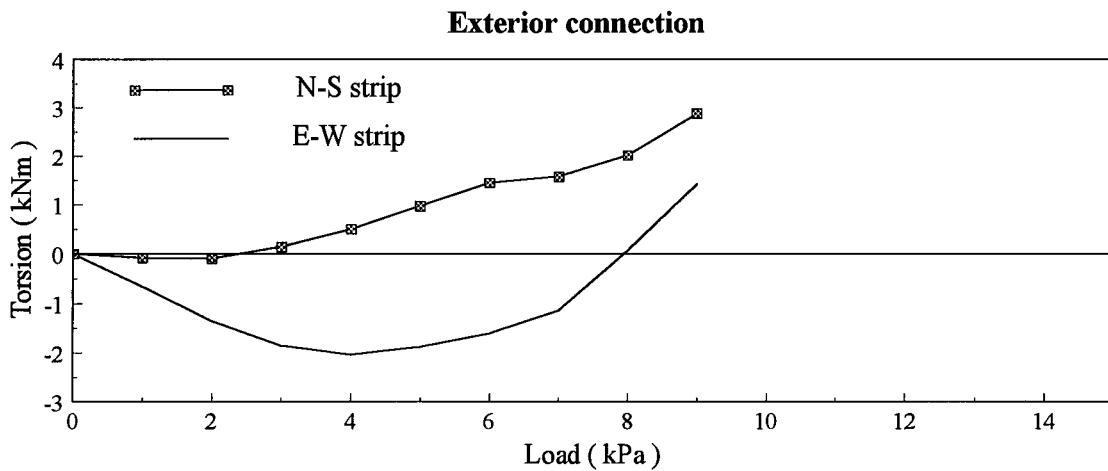


Figure 6.19 Torsional moment along each side face of radial strips, slab EXT02

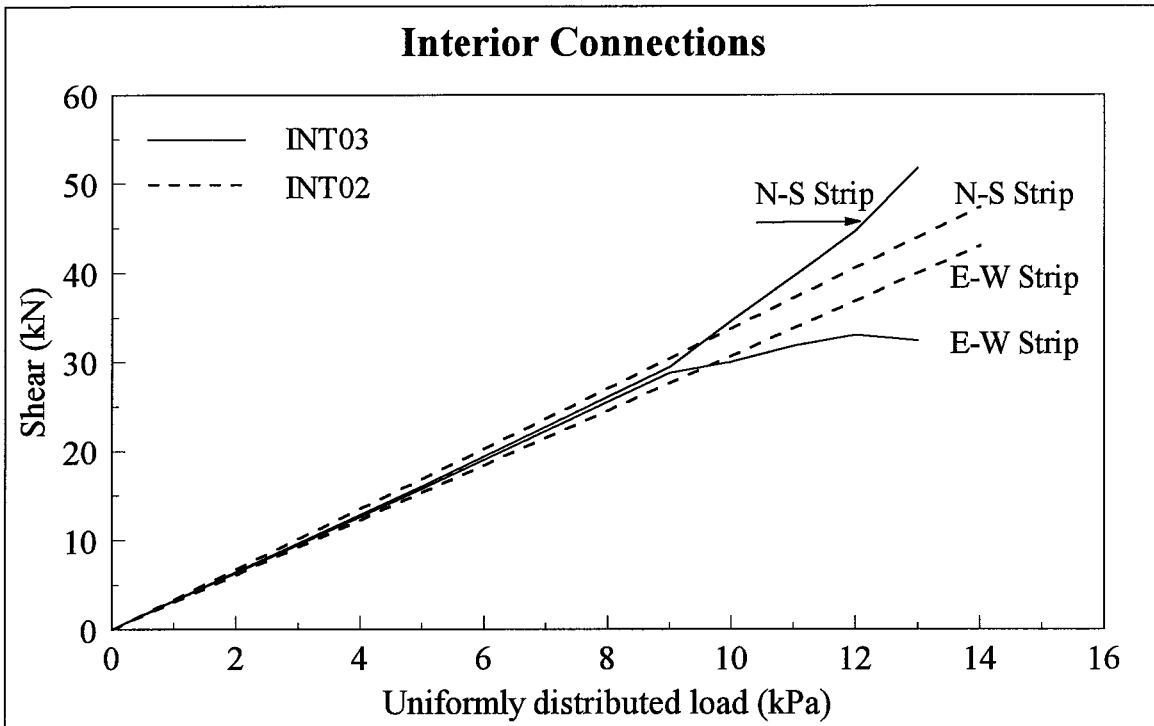


Figure 6.20 Load transferred through each radial strip, Interior connections

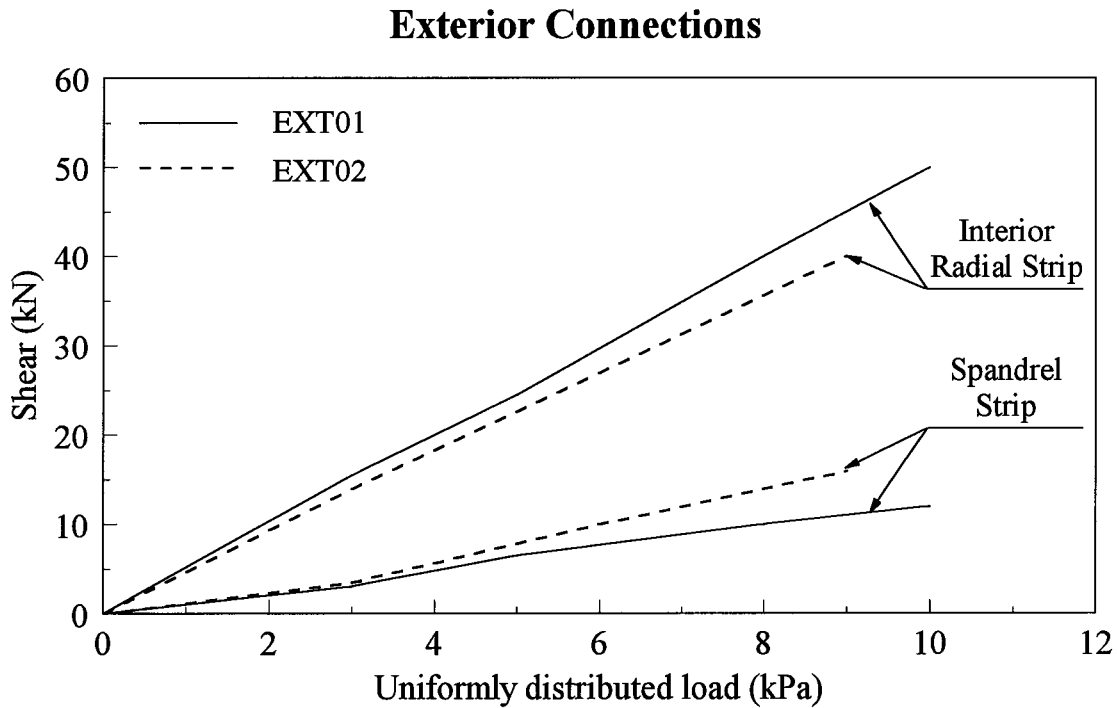


Figure 6.21 Load transferred through each radial strip, Exterior connections

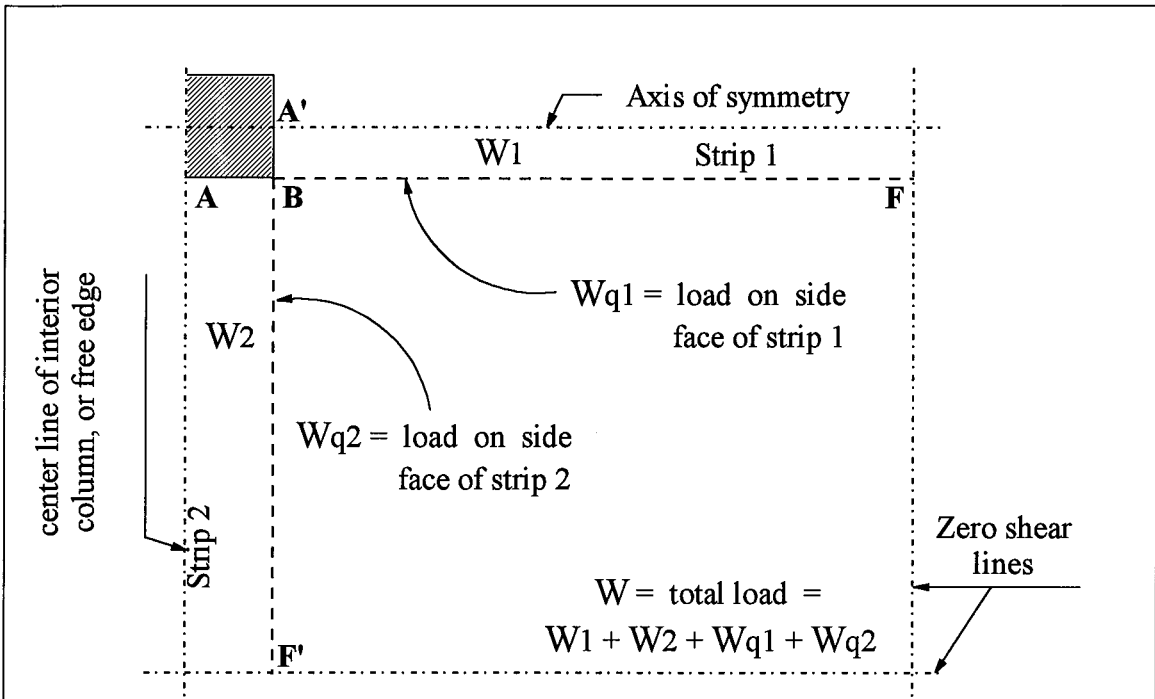


Figure 6.22 Key plan for figures 6.21 through 6.35

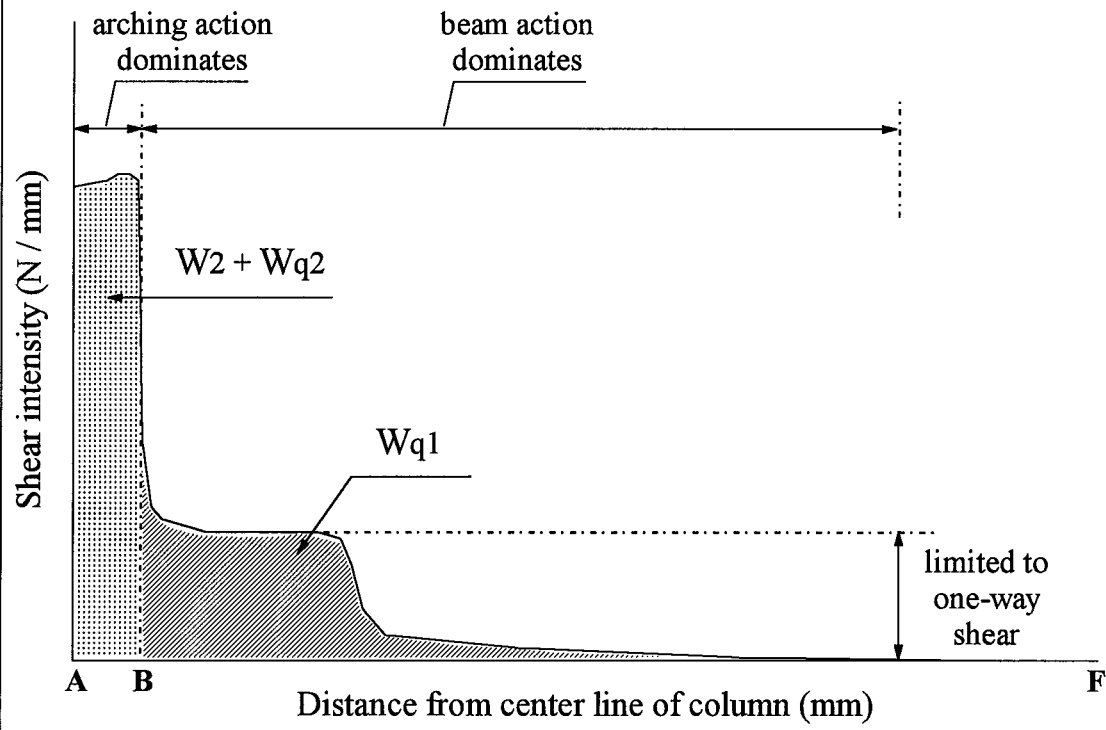


Figure 6.23 Typical shear intensity diagram along section ABF

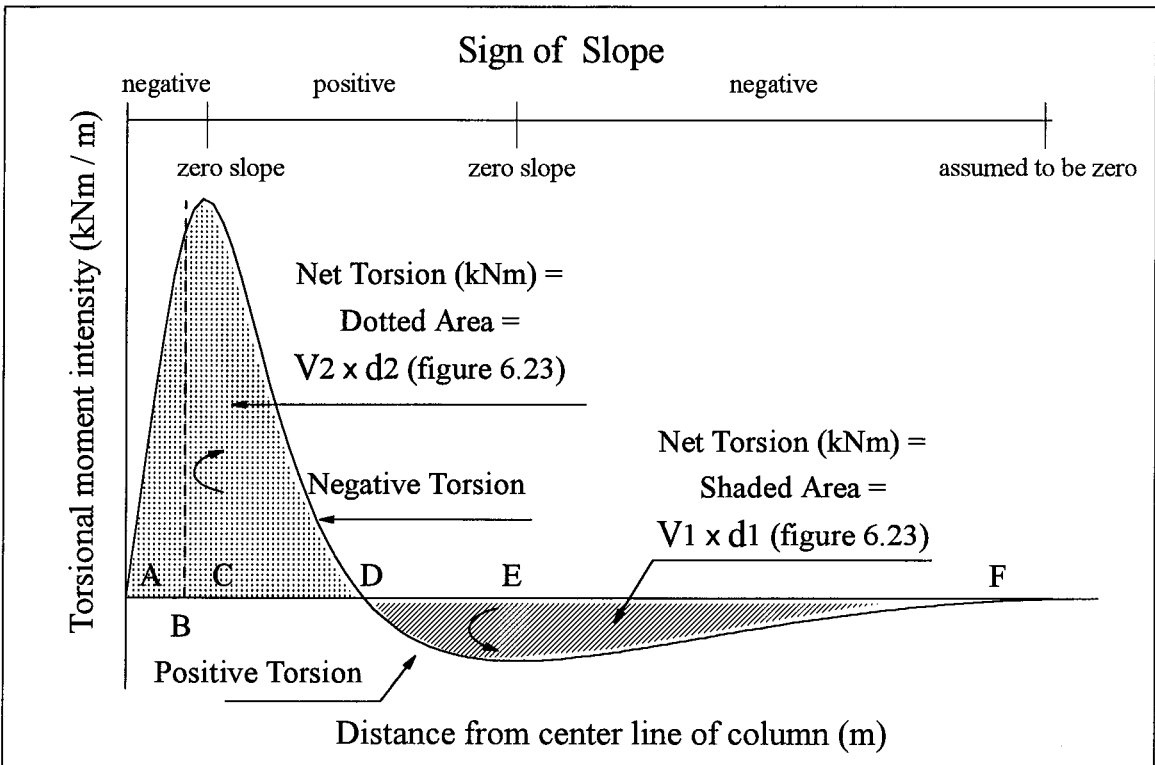


Figure 6.24 Typical torsional moment intensity diagram along side faces of strip 1

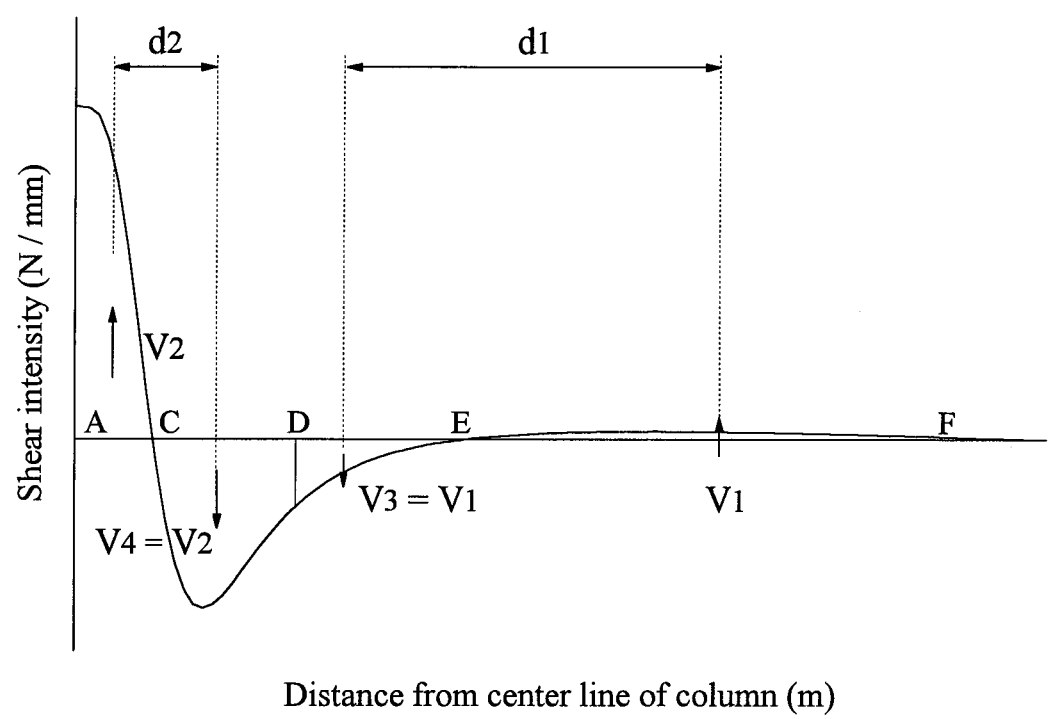
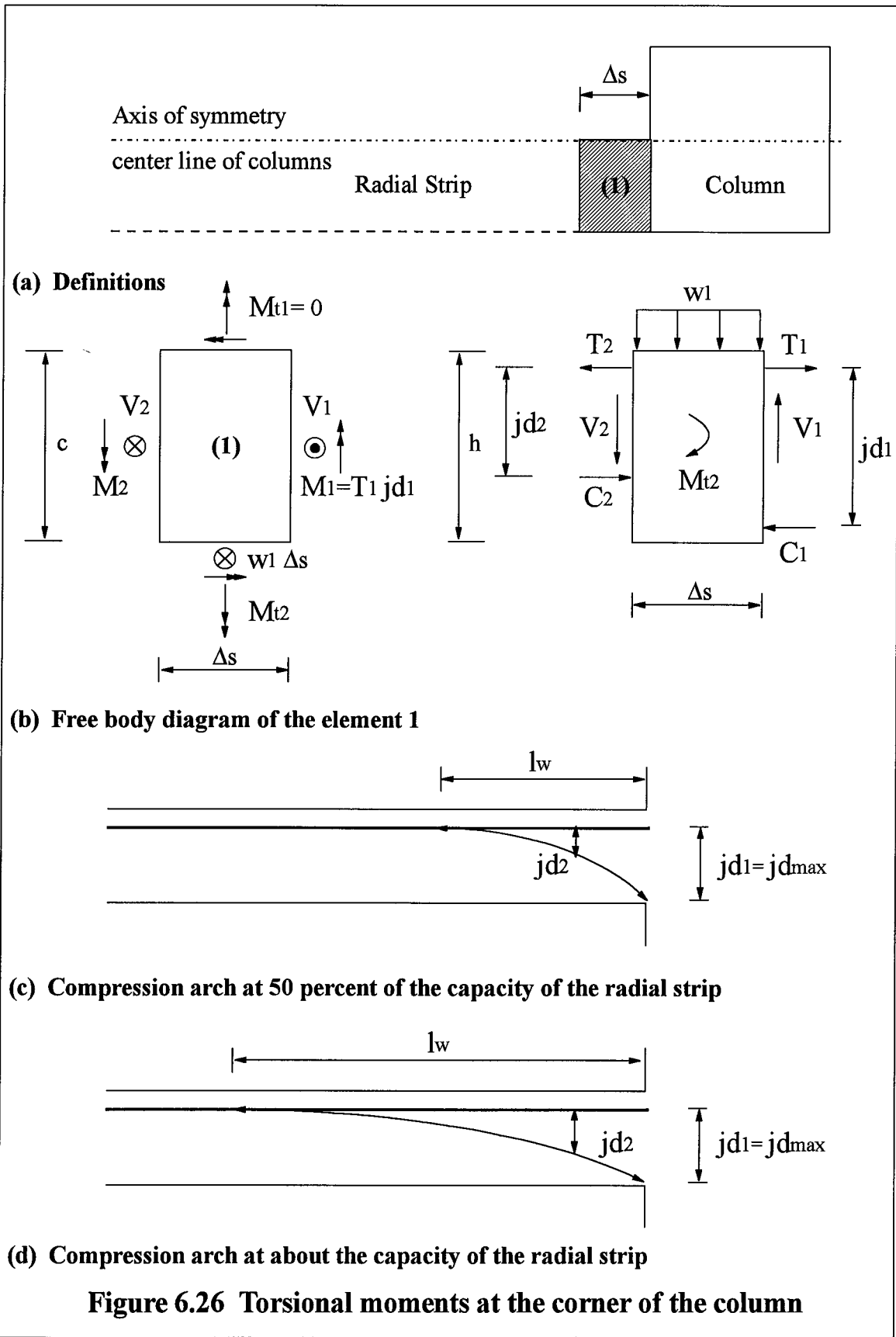


Figure 6.25 Typical torsional shear intensity diagram along side faces of strip 1



Interior Connections

Case a

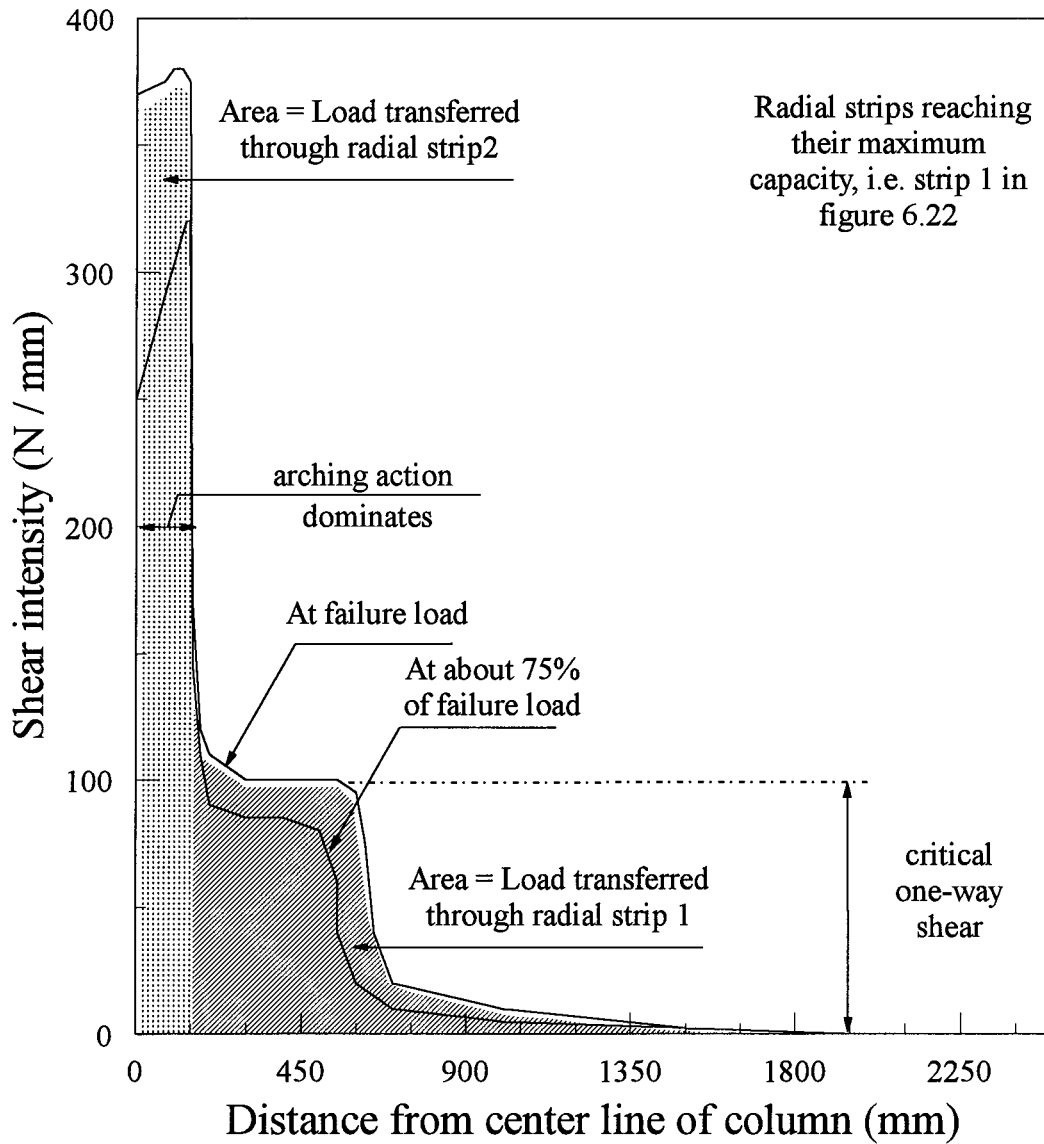


Figure 6.27 Typical shear intensity diagram along side faces of interior radial strips, case a

Interior radial Strips

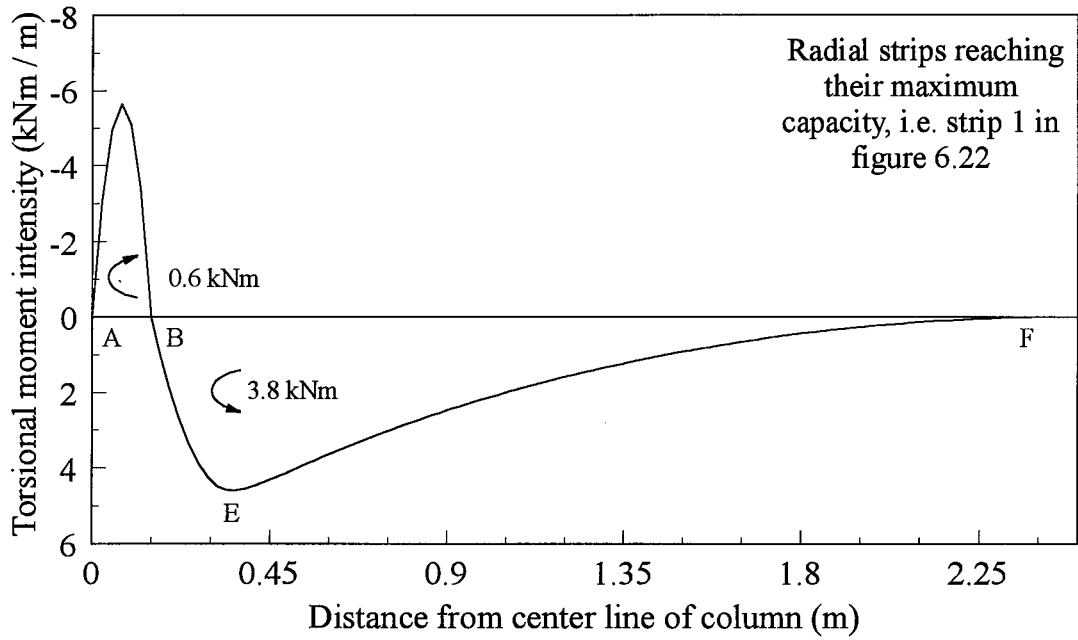


Figure 6.28 Idealized torsional moment intensity diagram along side faces of interior radial strips, case a

Interior radial Strips

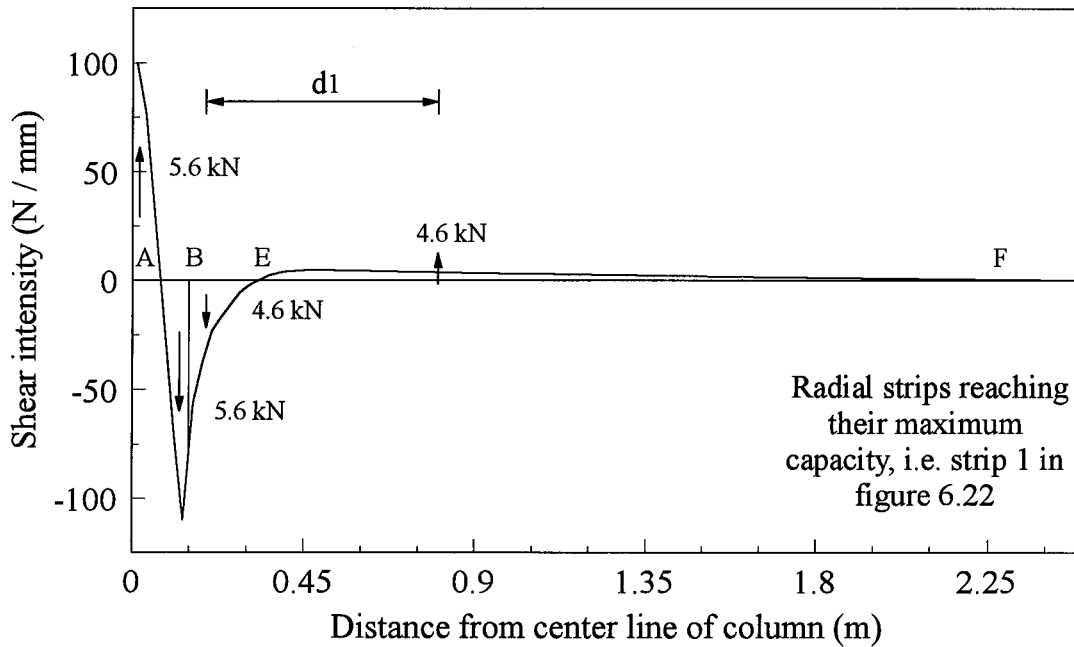
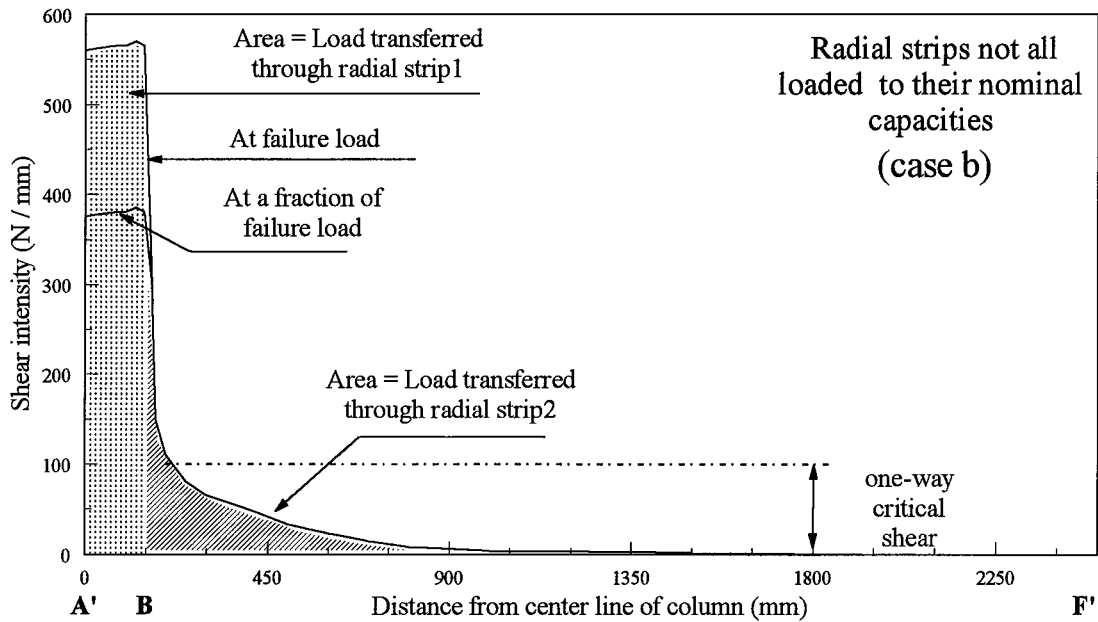


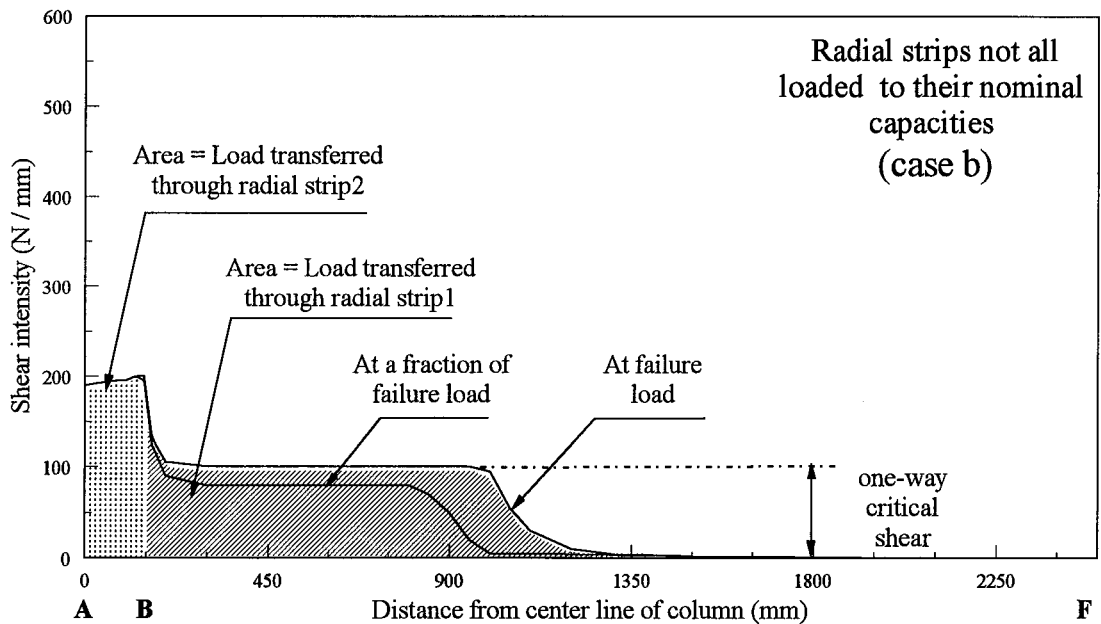
Figure 6.29 Idealized torsional shear intensity diagram along side faces of interior radial strips, case a

Interior Connections



(a) Section A'BF' in figure 6.22

Interior Connections



(b) Section ABF in figure 6.22

Figure 6.30 Typical shear intensity diagram along side faces of interior radial strips not loaded in portion to their capacity, case b

Interior radial Strips

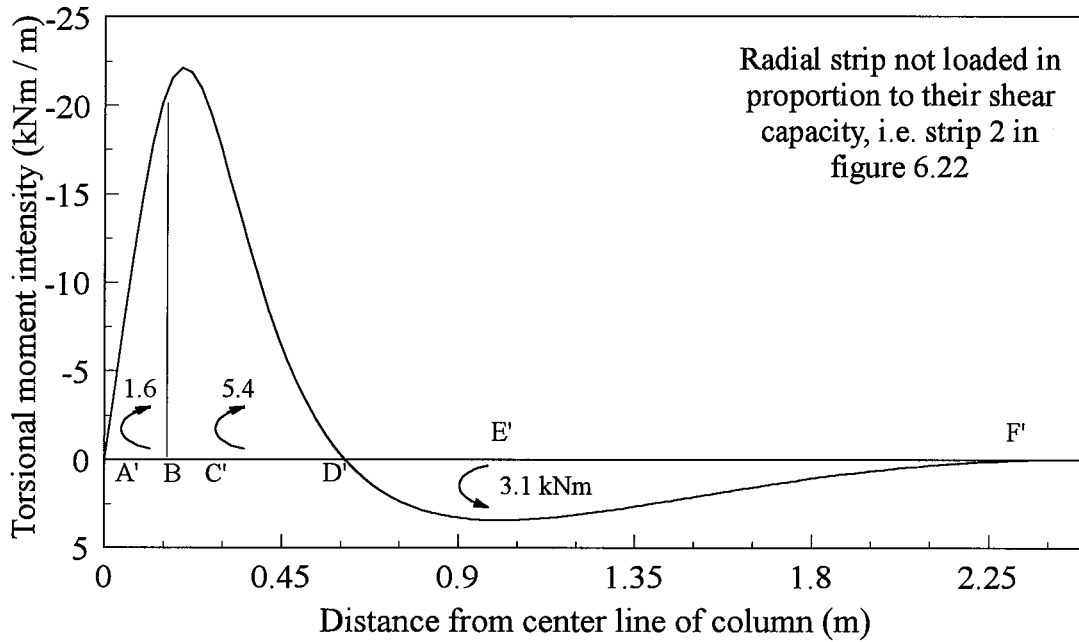


Figure 6.31 Idealized torsional moment intensity diagram along side faces of interior radial strips, case b

Interior radial Strips

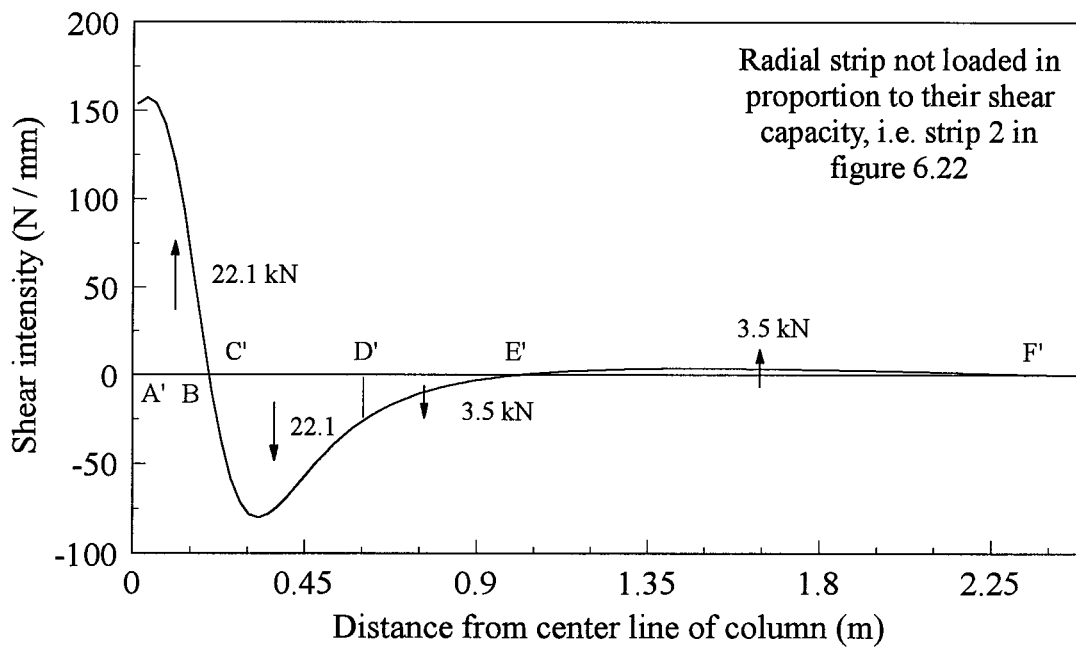


Figure 6.32 Idealized torsional shear intensity diagram along side faces of interior radial strips, case b

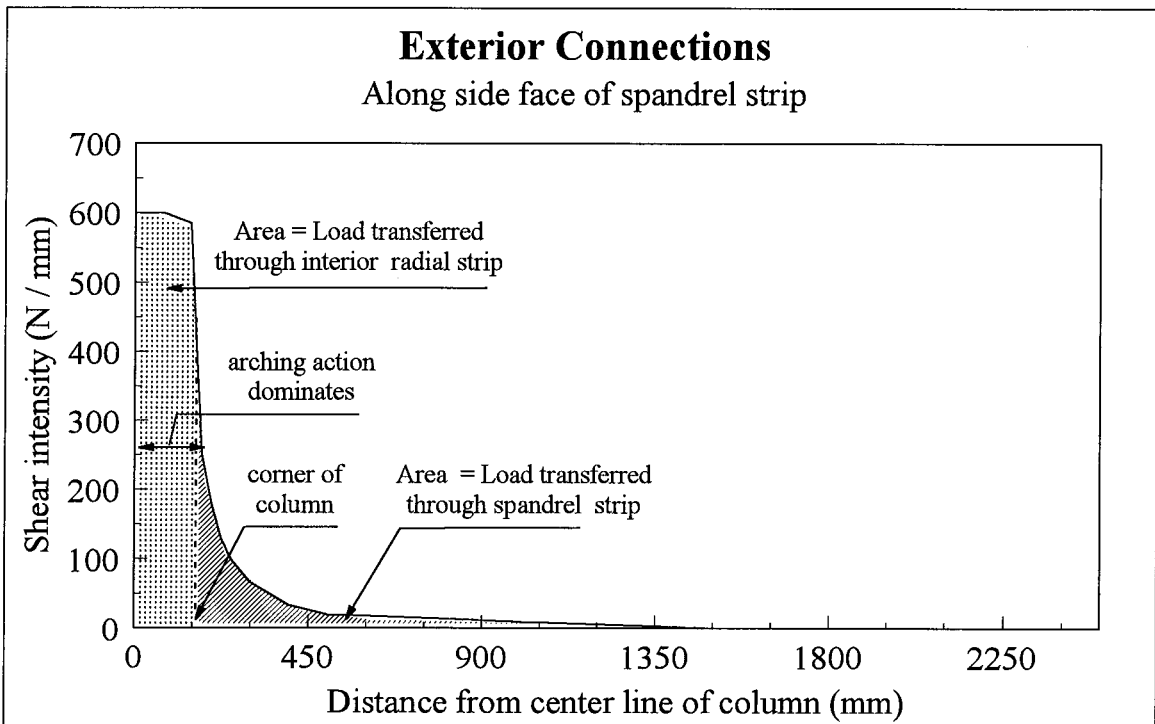


Figure 6.33 Typical shear intensity diagram along side face of a spandrel strip

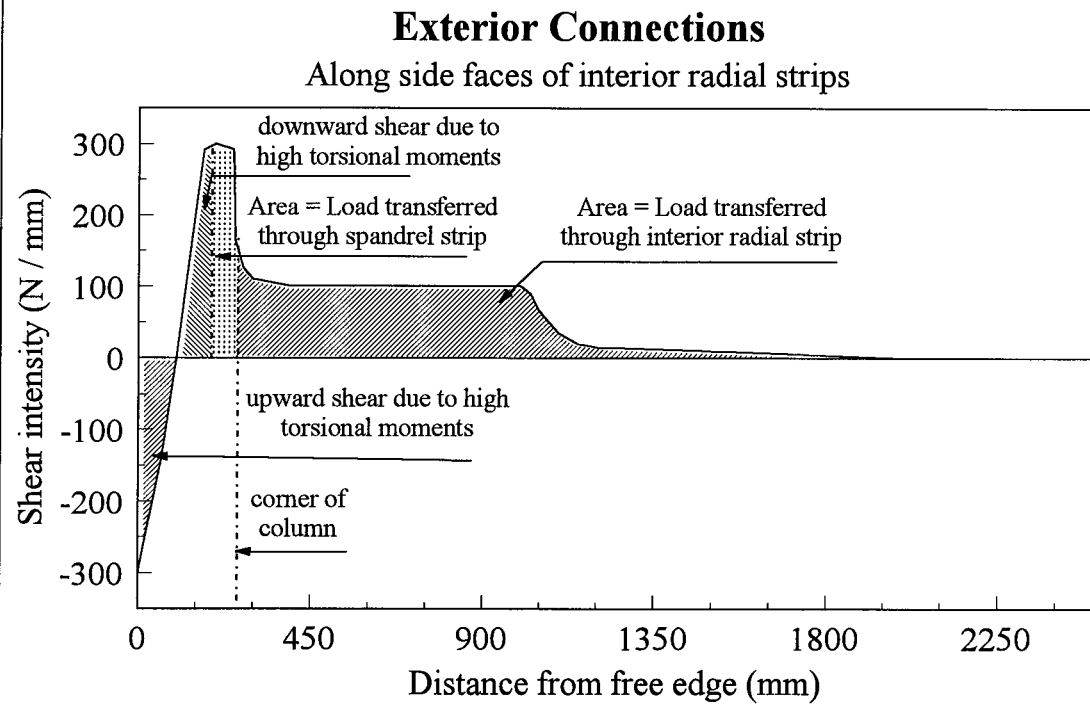


Figure 6.34 Typical shear intensity diagram along side faces of an interior radial strip of an edge connection

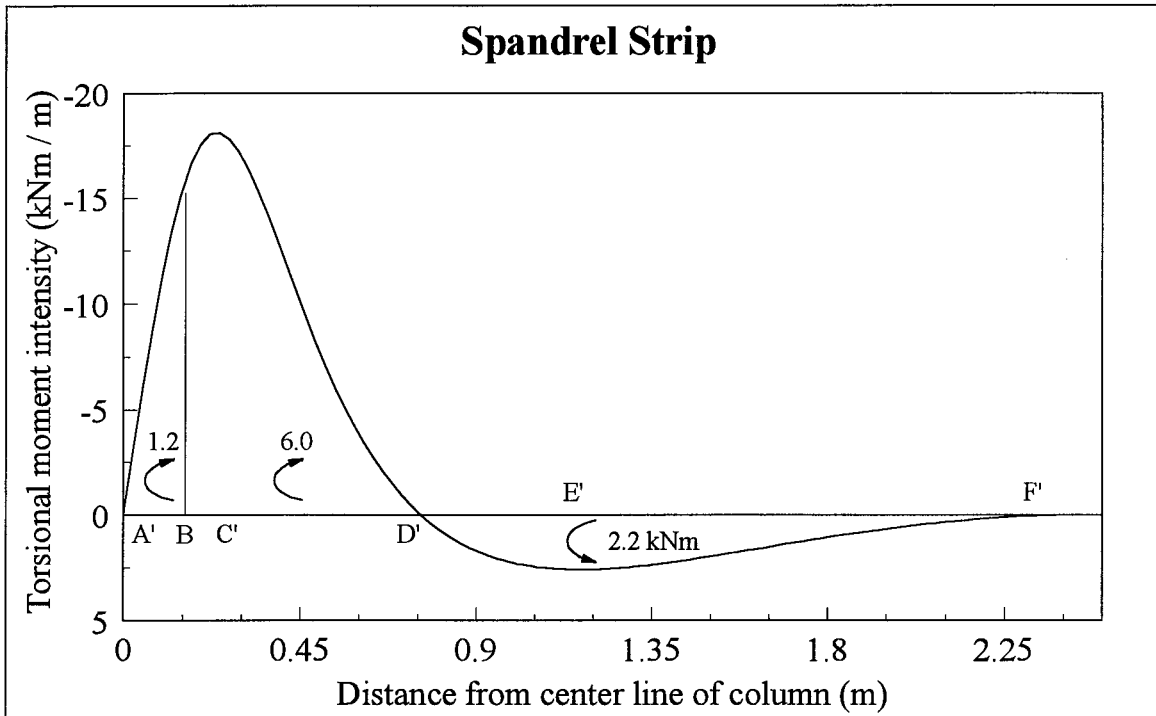


Figure 6.35 Idealized torsional moment intensity diagram along side faces of spandrel strips

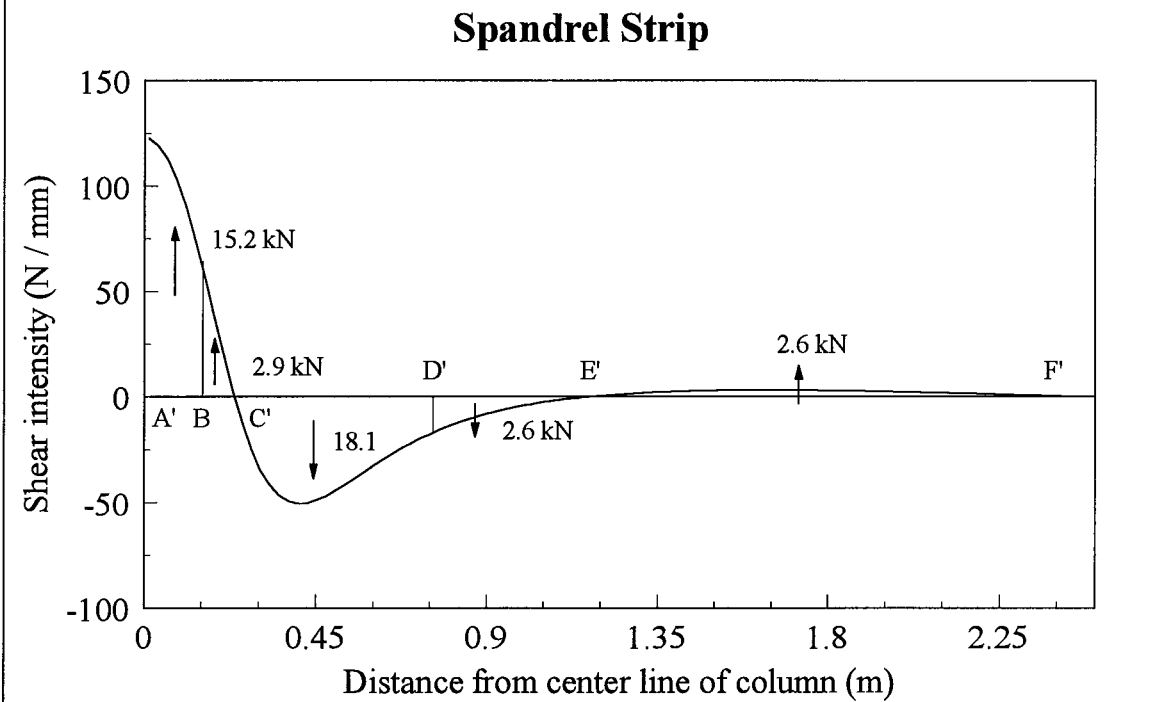


Figure 6.36 Idealized torsional shear intensity diagram along side faces of spandrel strips

7. Strip Model for the Capacity of Interior and Edge Connections

Lower bound estimates of the punching capacity of concentrically loaded interior column-plate connections are derived first. These estimates of the punching capacity are applicable to connections where the radial strips are not loaded in proportion to their nominal shear capacities. The results of the new model will be compared numerically to that of the existing Bond Model.

Shear-moment interaction diagrams are useful to evaluate the capacity of existing connections under unbalanced moment, and to assess the accuracy of a model by applying it to the tests in the literature. The interaction diagram would also be useful in evaluating a design procedure. Development of this design procedure is outside the scope of this work.

Based on the assumed mechanisms for transferring the load to the columns from the radial strips, moment shear interaction diagrams for the capacity of both the exterior connections and the interior connections under unbalanced moments can be constructed.

Finally, other considerations regarding the evaluation of the flexural capacity of the radial strips such as defining M_s^+ when punching occurs before a complete yield line mechanism, or how to estimate the flexural capacity of the radial strips in a plate with non-uniform mesh, are discussed.

7.1 Shear Capacity of Concentrically Loaded Interior Connections

7.1.1 General

The Bond Model provides a lower bound estimate of the shear capacity of a single radial strip, because the equilibrium and the boundary condition of the strip is satisfied, and both the flexural capacity of the strip and the shear capacity of the adjacent quadrants that load the strip are not exceeded at any point. However, it does not necessarily provide a lower bound estimate of the capacity of a connection.

In a concentrically loaded interior connection, when the radial strips are loaded in proportion to their shear capacities by their adjacent quadrants, as is the case in an enforced deformation test, the punching capacity of the connection equals the sum of the shear capacities of its radial strips. For this case, called proportional behavior, the shear distribution along one face of the column in Figure 6.27 can be simplified as illustrated in Figure 7.1a.

However, the results of the tested interior connection shows that it is possible to have cases in which strips are not all loaded to their nominal capacities. In such cases, called non-proportional behavior, the share of the load being applied to each strip can not be determined solely by the equations of equilibrium. Compatibility of deformations must also be considered. Radial strips in one direction, for example strip 1 in Figure 6.30b, reach their ultimate capacity while those in the other direction are loaded to only a fraction of their nominal capacity. The failure of the connection occurs when the load in strip 1 exceeds its ultimate capacity.

The minimum shear capacity of a connection occurs when the least loaded strips develop minimum shear capacity. As illustrated in Figure 7.1b, this occurs when the shear intensity along the side face of the column equals the maximum shear intensity along the radial strip 1. In this extreme case, bars parallel to the strip 1 and close to the column (but not passing through it) augment the flexural capacity of the strip. The effective width of

the strip 1 becomes greater than the column width, and the flexural capacity of the strip increases from M_s^- to M_{ss}^- . In this extreme case, the shear capacity of the load carrying strip is expected to be more than the shear capacity of the same strip were the behavior proportional.

7.1.2 Derivation of a Lower Bound Estimate for the Shear Capacity of a Concentrically Loaded Interior Connection

A free body diagram of one quarter of an interior connection in a simplified model is shown in Figure 7.2. Three independent equations of equilibrium are used (Equations 7.1 to 7.3, respectively); (a) vertical equilibrium of forces, (b) rotational equilibrium of half radial strip 1, and (c) rotational equilibrium of half radial strip 2.

$$P = 4 \times (P_1 + P_2) \quad [7.1]$$

$$\frac{M_{s1}}{2} + M_{t1} = \frac{w_1 \times l_1^2}{2} \quad [7.2]$$

$$\frac{M_{s2}}{2} + M_{t2} = \frac{w_2 \times l_2^2}{2} \quad [7.3]$$

In these equations, w is the total shear intensity (torsional shear plus primary shear) along the side face of the radial strip, P is the total load applied to the connection, and $P_1 = l_1 \times w_1$ and $P_2 = l_2 \times w_2$ are the loads transferred through half radial strips 1 and 2, respectively. $M_{s1} = M_{s1}^+ + M_{s1}^-$ and $M_{s2} = M_{s2}^+ + M_{s2}^-$ are the flexural capacities of the radial strips, and M_{t1} and M_{t2} are the integration of the torsional moment intensity along the side face of the radial strip. Rearranging Equations 7.2 and 7.3 produces Equations 7.4 and 7.5.

$$(M_{s1} + 2 \times M_{t1}) \times w_1 = (w_1 \times l_1)^2 = P_1 \quad [7.4]$$

$$(M_{s2} + 2 \times M_{t2}) \times w_2 = (w_2 \times l_2)^2 = P_2 \quad [7.5]$$

Note that with the assumption that the torsional moments on the side faces of the radial strips are zero ($M_{t1} = M_{t2} = 0$), as in the Bond Model, the two equations reduce to $P_1 = \sqrt{M_{s1} \times w_1}$ and $P_2 = \sqrt{M_{s2} \times w_2}$. From Equation 7.1 the shear capacity of the connection for a proportional behavior can be determined by Equation 7.6.

$$P = 4 \times (P_1 + P_2) = 4 \times \sqrt{M_{s1} \times w_1} + 4 \times \sqrt{M_{s2} \times w_2} \quad \text{the Bond Model} \quad [7.6]$$

In general, however, Equations 7.4 and 7.5 can not be solved independently as the torsional moments are not zero. In some cases, relatively large negative torsion occurs along the side faces of the radial strips, and Equation 7.6 will not result in a safe estimate of the capacity of the connection.

Adding Equations 7.4 and 7.5 results in a relationship between P_1 and P_2 .

$$P_1^2 + P_2^2 = M_{s1} \times w_1 + M_{s2} \times w_2 + 2 \times (M_{t1} \times w_1 + M_{t2} \times w_2) \quad [7.7]$$

As shown in Figure 7.3a, Equation 7.7 can be interpreted graphically as a right angle triangle with two sides equal to P_1 and P_2 and a hypotenuse equal to the square root of the right hand side of the Equation 7.7.

Since w_1 almost equals w_2 , the term $(M_{t1} \times w_1 + M_{t2} \times w_2)$ is simplified to $w_1 \times (M_{t1} + M_{t2})$. The overall effect of torsion is so that it always adds to the capacity of the connection, and neglecting it ($M_{t1} + M_{t2} = 0$), results in a conservative estimate of the capacity of the connection. Hence, Equation 7.7 is simplified as follows;

$$P_1^2 + P_2^2 = M_{s1} \times w_1 + M_{s2} \times w_2 \quad [7.8]$$

To calculate P_1 and P_2 from Equation 7.8, one must consider the compatibility of deformations throughout the slab to find out how load is distributed among the radial strips. The solution so obtained is always a lower bound estimate of the shear capacity of the connection.

For example, in enforced deformation tests, radial strips are loaded independently and, as shown in Figure 7.3b, will reach their nominal shear capacity ($P_1 = P_{s1}$ and $P_2 = P_{s2}$). This estimate is a lower bound solution in these tests, and is equal to the estimate by the Bond Model (Equation 7.6).

In general, however, ratio of P_1 to P_2 is not known. To avoid complicated analysis for finding this ratio, the maximum and the minimum capacities obtained by Equation 7.8 is calculated here and will be compared to the Bond Model solution in the next section.

The maximum capacity occurs when plate equally loads the radial strips, $P_1 = P_2$ (Figure 7.3c), and can be expressed as Equation 7.9. In this case, P_2 is greater than P_{s2} , which means that torsion is helping the strip with smaller nominal capacity. However, P_1 is smaller than P_{s1} suggesting that torsion along the side faces of the radial strip 1 is decreasing its shear capacity.

$$P_{\max} = 4\sqrt{2} \times \sqrt{M_{s1} \times w_1 + M_{s2} \times w_2} \quad [7.9]$$

The minimum of all the estimates of punching capacity is always a lower bound solution. The smallest estimate occurs when either P_1 or P_2 has its minimum value (Figure 7.3d). Note that the minimum shear transferred through each face of the column is equal to the one way shear times the width of the column (Figure 7.1b). Assuming that P_2 is equal to $(c_1 \times w_1 / 2)$, the magnitude of P_1 is determined by Equation 7.8 as expressed in 7.10. Substituting P_1 and P_2 into Equation 7.1, the smallest estimate of the punching capacity of the connection, P_{\min} , can be determined by Equation 7.11.

$$P_1 = \sqrt{M_{s1} \times w_1 + M_{s2} \times w_2 - \frac{c_1^2 \times w_1^2}{4}} \quad [7.10]$$

$$P_{\min} = 2 \times c_2 \times w_1 + 4 \sqrt{M_{s1} \times w_1 + M_{s2} \times w_2 - \frac{c_1^2 \times w_1^2}{4}} \quad [7.11]$$

7.1.3 Comparison of P_{bond} , P_{max} , and P_{min}

To facilitate a comparison of P_{bond} with P_{max} and P_{min} , it is convenient to reformulate the expression in a simple format using the non-dimensional constants K_1 and K_2 . Consider an interior connection in which strip 1 has a larger nominal capacity than strip 2 (i.e. $M_{s1} \times w_1 > M_{s2} \times w_2$), and define K_1 as Equation 7.12. A reasonable range for K_1 would be from 0.25 to 1.0 (ratio of P_1 to P_2 between 0.5 and 1.0). Equations 7.6 and 7.8 can be manipulated into Equations 7.13 and 7.14, respectively.

$$K_1 = \frac{M_{s2} \times w_2}{M_{s1} \times w_1} = \left(\frac{P_{s2}}{P_{s1}}\right)^2 \quad [7.12]$$

$$P_{\text{Bond}} = 4 \times (\sqrt{K_1} + 1) \times \sqrt{M_{s1} \times w_1} \quad \text{the Bond Model} \quad [7.13]$$

$$P_{\text{max}} = 4 \times \sqrt{2 \times (1 + K_1)} \times \sqrt{M_{s1} \times w_1} \quad \text{Strip Model} \quad [7.14]$$

Introducing K_2 (Equation 7.15) as the ratio of one way shear in strip 2 to the nominal shear capacity of strip 1, Equation 7.11 can be rearranged as Equation 7.16. A practical range for K_2 is between 1/5 and 1/2.

$$K_2 = \frac{c_1 \times w_1}{2 \times \sqrt{M_{s1} \times w_1}} = \frac{c_1 \times w_1}{2 \times P_{s1}} \quad [7.15]$$

$$P_{\text{min}} = 4 \times (K_2 + \sqrt{1 + K_1 - K_2^2}) \times \sqrt{M_{s1} \times w_1} \quad \text{Strip Model} \quad [7.16]$$

Equations 7.13, 7.14, and 7.16 are compared in Table 7.1. It can be seen that if the capacity of both strips is almost the same ($K_1 = 1$), the Bond Model and the maximum estimate in Strip Model are exactly equal. The difference between these two estimates can be practically ignored for other values of K_1 .

Most connections have a square column and uniformly spaced mesh ($K_1 = 1.0$). Shear intensity at the column face is usually 2 to 3 times the one-way shear ($K_2 = 1/2$ to $1/3$). Therefore, according to Table 7.1, P_{Bond} is about 10 to 17 percent larger than P_{min} .

When columns are extremely small, to maintain the same punching capacity, a high reinforcement ratio is required, and K_2 may be as small as 1/5. In such cases, when the behavior is non-proportional (e.g. due to the panel rectangularity), the capacity of the connection may be overestimated by the Bond Model by 25 percent.

When the strips in one direction are more heavily reinforced, or when rectangular columns are used, both K_1 and K_2 are small. For K_2 equal to 1/5 and $K_1 = 1/4$ (e.g. for column aspect ratio of 4), the maximum difference between P_{min} and P_{Bond} becomes about 15 percent.

7.2 Moment-Shear Interaction for the Capacity of the Edge Connections

7.2.1 General

Figure 7.4 shows the free body diagram of an edge connection. Subscripts x and y are associated with the interior radial strip and the spandrel strips, respectively. Based on the equations of equilibrium, the total load transferred through the connection, P, and the moment at the center line of the column, M, can be determined from Equations 7.17 and 7.18, respectively. In these equations, M_{tc} is the torsional moment on each side face of the column, P_x and P_y are the load transferred through the corresponding radial strips, and the eccentricity of the load P_x is $C_y/2$. M_{sx} and M_{sy} are rotational capacity of the radial strips, and each consists of three components: (1) negative moment at the column end of the strips, M_{sx}^- or M_{sy}^- ; (2) positive moment at the remote end of the strips, M_{sx}^+ or M_{sy}^+ ; and (3) torsion along side faces of the radial strips, M_{tx} or M_{ty} .

$$P = P_x + 2 \times P_y = 4 \times \sqrt{M_{sx}^- \times w_x} + 2 \times \sqrt{2 \times M_{sy}^- \times w_y} \quad [7.17]$$

$$M = M_{sx}^- + 2 \times M_{tc} + P_x \times \frac{C_y}{2} \quad [7.18]$$

Based on the Equations 7.17 and 7.18, shear-moment interaction diagram for the capacity of an edge connection is plotted in Figure 7.5. Five distinct points are recognized in this figure, which will be discussed in detail. The interaction diagram is constructed by simply linking these points by straight lines.

7.2.2 Point 4 on the Interaction Diagram

Point 4 represents cases like "twist off tests", for which $P_x = P_y = 0$. Therefore, P_4 equals zero, and Equation 7.18 simplifies to Equation 7.19, by which moment in the connection is calculated.

$$M_4 = M_{sx}^- + 2 \times M_{tc} \quad [7.19]$$

M_{tc} in Equation 7.19 is the lesser of two values: torsional moment capacity of the side faces of the column, M_{tr} ; and the flexural capacity associated with the top reinforcement placed perpendicular to the free edge outside the column. M_{tr} may be calculated according to any rational method. However, the amount of reinforcement required for this torsion must be added to the amount of the reinforcement provided to satisfy bending in the y direction. In this investigation, a method based on shear friction is used to determine M_{tr} .

In this method, torsion is assumed to be the result of two equal and opposite horizontal shearing forces. One of the forces, V_v , acts at the level of the top reinforcement and its magnitude depends on the area of the top steel as well as the width of the column, c_y . The equal and opposite force acts at the level of the center of the compression block. The distance between the two forces can be approximated by the flexural depth of the plate, jd . Therefore, the torsional moment along each side face of the column may be determined using Equation 7.20.

$$M_{tr} = j \times d \times V_t \quad [7.20]$$

The maximum value for the shearing forces, V_v , is governed by the force at the level of the top reinforcement. The width of the contributing area of the concrete is equal to the column width, c_y , and the depth of it is equal to $2d'$, where d' is the distance from centroid of bars to the top surface. Therefore, the area of concrete, A_v , resisting the shearing force equals $2d' \times c_y$. For this area, according to the Section 11.6.3 of the Canadian standard A23.3-94, the maximum shear, V_v , equals to $0.6 \times \sqrt{(A_s \times f_y) \times (A_v \times f'_c)}$, but should not exceed $0.25 A_v \times f'_c$ nor $7 \text{ (MPa)} \times A_v$.

7.2.3 Points 3a and 3b on the Interaction Diagram

Points 3a and 3b on the interaction diagram correspond to the maximum moment that an edge connection can transfer. At Point 3b zero shear is carried by the spandrel strips, while at point 3a some limited shear is transferred through the spandrel strips by beam action. To get the maximum moment, according to Equation 7.18, torsion along side faces of the column is at its maximum value, and the interior radial strip is loaded to its maximum capacity.

At these points, the interior radial strip behaves very similarly to the load carrying strip of an interior connection with non-proportional behavior (Section 7.1.1): bars normal to the free edge and outside the column (a) augment the flexural capacity of the interior radial strip and (b) do not transfer any shear by beam action to the spandrel strip. The first effect is taken into account by term the M_{tx} in Equation 7.21. A good estimate for M_{tx} would be the negative flexural capacity of a strip of slab adjacent to the interior radial strip. Consistent with A23.3-94, the width of this strip is chosen equal to $1.5 h$. M_{tx} should not be more than M_{tr} , since the negative moment in this strip is limited to the torsional moment capacity on the side face of the column, M_{tr} . The maximum moment this connection is able to transfer, can be determined using Equation 7.22.

The second effect dictates that shear transfer inside the spandrel strips, if any, must be by beam action, thereby limiting P_y to $w_x \times c_y$. Torsion in the spandrel strip has its maximum value at the column face and usually yields all the top bars. Unless additional top steel is provided, M_{sy}^- equals zero. For most tests in the literature, M_{sy}^+ is also zero. With no gradient in bending moments, no shear can be transferred through the spandrel strip ($P_y = 0$). In these cases, points 3a and 3b coincide. In Equation 7.23, coefficient β (ranging from zero to one) accounts for this effect.

$$P_{3b} = P_x = 2 \times \sqrt{(M_{sx}^- + M_{sx}^+ + 2 \times M_{tx}) \times w_x} \quad [7.21]$$

$$M_{3a} = M_{3b} = M_4 + P_{3b} \times \frac{c_y}{2} \quad [7.22]$$

$$P_{3a} = P_{3b} + 2 \times \beta \times c_y \times w \quad [7.23]$$

7.2.4 Point 2 on the Interaction Diagram

The maximum shear that can be transferred through the connection occurs when all strips reach their nominal capacities. The Bond Model gives this load by Equation 7.24. The associated bending moment, M_2 , can be determined using Equation 7.15, and by setting $M_{tc} = 0$, since the top reinforcement is used for flexural equilibrium. This results in Equation 7.25.

$$P_2 = 2 \times \sqrt{2 \times (M_{sy}^- + M_{sy}^+) \times w_y} + 2 \times \sqrt{(M_{sx}^- + M_{sx}^+) \times w_x} \quad [7.24]$$

$$M_2 = M_{sx}^- + c_y \times \sqrt{(M_{sx}^- + M_{sx}^+) \times w_x} \quad [7.25]$$

7.2.5 Point 1 on the Interaction Diagram

Point 1 on the interaction diagram represents the case where moment is equal to zero ($M_1 = 0$). Shear transfer in this case is similar to that of a simply supported beam. Shear is transferred by beam action (gradient in positive bending moment) to the side faces of spandrel strips, and from there by arching action to the column. The shear capacity of the connection with zero eccentricity of load can be determined by the Bond Model using Equation 7.26. In this equation a good estimate for M_{ly} is the flexural capacity associated with the top reinforcement of a strip adjacent to the spandrel strips. Consistent with A23.3, the width of this strip is chosen equal to 1.5 h .

$$P_1 = c_x \times w_y + 2 \times \sqrt{2 \times (M_{sy}^- + M_{sy}^+ + M_{ly}) \times w_y} \quad [7.26]$$

7.3 Moment-Shear Interaction Diagram for the Capacity of the Eccentrically Loaded Interior Connections

Figure 7.6 describes the moment-shear interaction diagram for the capacity of an interior column-plate connection in a flat plate structure. Point 1 in this figure corresponds to cases under balanced loading. At failure, all strips are loaded to their maximum shear capacity, and according to the Bond Model, the shear capacity of the connection can be determined from Equation 7.27.

$$P_1 = 4 \times \sqrt{(M_{sy}^- + M_{sy}^+) \times w_y} + 4 \times \sqrt{(M_{sx}^- + M_{sx}^+) \times w_x} \quad [7.27]$$

At point 2, both strips in the y direction and only one of the strips in the x direction are loaded to their ultimate capacity. The other strip in the x direction is carrying no load. The eccentric load P_x , therefore, causes an unbalanced moment of $P_x \times c_y / 2$. This moment is added to the negative moment of the loaded radial strip, M_{sx}^- and the positive moment at the column face of unloaded radial strip, M_{sx}^+ . The unbalanced moment and the shear force at point 2 can be determined using Equations 7.28 and 7.29, respectively.

$$M_2 = M_{sx}^- + M_{sx}^+ + c_y \times \sqrt{(M_{sx}^- + M_{sx}^+) \times w_x} \quad [7.28]$$

$$P_2 = 4 \times \sqrt{(M_{sy}^- + M_{sy}^+) \times w_y} + 2 \times \sqrt{(M_{sx}^- + M_{sx}^+) \times w_x} \quad [7.29]$$

Moving from point 2 to point 3 on the interaction diagram, the torsional moments become significant. Torsion along side faces of the loaded radial strip in the x direction, M_{tx} , augments the flexural capacity of this strip. Also, torsional moment on the side faces of the column (common with the strips in the y direction), M_{tc} , adds to the unbalanced moment. Similar to the edge connections, shear transfer through strip y is limited by one-way critical shear ($P_y = \beta \times c_y \times w_x$). If additional top reinforcement is provided to resist M_{tc} , β is equal to one. However, when all top reinforcement is used up by M_{tc} and M_{sy}^+ can not be generated (as is the case for most tests in the literature), β equals zero. Equations 7.31 and 7.30 are therefore used to predict the shear capacity of the connection and the unbalanced moment at point 3.

$$M_3 = M_{sx}^- + M_{sup}^+ + 2 \times M_{tc} + c_y \times \sqrt{(M_{sx}^- + M_{sx}^+ + 2 \times M_{tx}) \times w_x} \quad [7.30]$$

$$P_3 = 2 \times \beta \times c_y \times w_x + 2 \times \sqrt{(M_{sx}^- + M_{sx}^+ + 2 \times M_{tx}) \times w_x} \quad [7.31]$$

Point 4 on the interaction diagram represents a case with small or no net shear force, but a large bending moment. The bending moment at this point is the maximum unbalanced moment that can be applied to the connection. In this case, upward forces are generated in one span and downward forces in the other one. In the radial strip in the x direction, what counteracts the moment due to the upward forces are the flexural capacity of the bottom bars at the column face, M_{sup}^+ , and the torsional moment on the side faces of the radial strip, M_{tx} . Based on the bond model procedure, the maximum upward force, P_{xu} , is equal to $2 \times \sqrt{(M_{sup}^+ + 2 \times M_{tx}) \times w_x}$. At point 4b, where net shear is equal to zero, this upward force must be equal to the downward force in the other strip, P_{xd} . The moment associated with this couple equals to $P_{xu} \times c_y$. The maximum unbalanced moment, therefore, can be estimated by Equation 7.32. Its associated load varies between zero (point 4b) and the shear that can be transferred by beam action in the y direction (point 4a). The latter can be determined by Equation 7.33.

$$M_{4a} = M_{4b} = M_{sx}^- + M_{sup}^+ + 2 \times M_{tc} + 2 \times c_y \times \sqrt{(M_{sup}^+ + 2 \times M_{tx}) \times w_x} \quad [7.32]$$

$$P_{4a} = 2 \times \beta \times c_y \times w \quad [7.33]$$

The boundary condition of all available tests on eccentrically loaded interior connections reported in the literature are such that a positive moment can not be generated. This means that the positive flexural capacities of the radial strips, M_{sx}^+ and M_{sy}^+ , are zero for these tests. Hence, according to the Strip Model (Equations 7.27 to 7.33), the moment-shear interaction diagram of these tests becomes similar to diagram B in Figure 7.6. The accuracy of this diagram will be verified in the next chapter. However, except for point 1 (balanced loading), there are no tests in the literature to evaluate the accuracy of the Strip Model when considering the effect of the positive reinforcement on the capacity of an eccentrically loaded interior connection (diagram A).

7.4 Non-Proportional Behavior in the Presence of Unbalanced Moments

7.4.1 Edge Connections

Figure 7.7 illustrates shear transfer in an edge connection at different eccentricities of load. Point 1 on the interaction diagram refers to zero eccentricity, and as shown in Figure 7.7b, is the case of non-proportional behavior in which all the shear is transferred by beam action in the direction normal to the free edge and by arching action parallel to the free edge.

As illustrated in Figure 7.7c, point 2 associates with proportional behavior in an edge connection where all radial strips are loaded to their nominal capacity.

At points 3a and 3b, torsional moments become significant, and as illustrated in Figure 7.7d, shear transfer is solely by beam action parallel to the free edge and by arching action normal to the free edge. This case of non-proportional behavior is the common case in actual buildings. At point 4, no shear is transferred through the connection.

7.4.2 Interior Connections

Points 3 and 4a in Figure 7.6 are associated with large torsional moments and are consistent with pure beam action in one direction and pure arching action in the other direction. Hence, these points are extreme cases of non-proportional behavior.

Point 1 in Figure 7.6 refers to concentrically loaded interior connections, and is based on the assumption that all radial strips are loaded to their nominal capacities. Concentrically loaded interior connections, however, are subject to non-proportional behavior, and as discussed in Section 7.1, their capacity varies between P_{\max} and P_{\min} (Equations 7.9 and 7.11).

To account for the non-proportional behavior, moment-shear interaction diagram for the capacity of interior connections is modified as in Figure 7.8. Since the effect of non-proportional behavior at point 2 is not clear, the interaction diagram is constructed by joining points 1, 3, 4a, and 4b.

7.5 Other Considerations Regarding Capacity of Plate-Column Connections

7.5.1 Non-uniform Distribution of Reinforcement

There are many cases both in practice and in the literature tests in which the top or bottom reinforcement is not uniformly distributed around the column. For example, in the test reported in this investigation, integrity steel passing through the columns causes a concentration of steel in the column width. Also if the connection does not satisfy shear requirements, according to the Bond Model, one way to improve the shear capacity is to increase the area of steel passing through the column. In such cases, the designer must consider two issues. The first issue is that if the ratio of steel is too high, failure might occur locally due to the crushing of the compression block of the concrete, before yielding of the tensile reinforcement.

The other issue is how to define the flexural capacity of the radial strip. All the reinforcement inside the column width contribute to the tensile component of the bending moment, however, their associated compression force is not necessarily confined to the column width. Both flexural capacity of the radial strip and the arching action shear depend on the compression force inside the radial strip.

In these cases, assume that the compression block within $c+3h$ (column width plus 1.5 time the thickness of the plate from each side of the column) is of uniform depth. Then the average spacing of the bars, s_{avg} , and the area of steel, A_s , given by Equations 7.34a and 7.34b can be used to calculate the flexural capacity of the radial strips. In these equations, A_b is the area of a single bar, and $A_{s,c+3h}$ is the area of steel placed within $c+3h$.

$$s_{avg} = \frac{A_b}{A_{s,c+3h}} \times (c + 3h) \quad [7.34a]$$

$$A_s = \frac{c}{c + 3h} \times A_{s,c+3h} \quad [7.34b]$$

7.5.2 Considerations Regarding M_s^+

Top bars passing through the column yield first, and therefore their yield moment can always be used as the negative flexural capacity of the radial strip, M_s^- . Bottom bars within the radial strip do not always reach their yield stress. For example in cases where the designer decides to add a few bars to the top or bottom mat in just one direction, it is most likely that in this direction all top bars yield, and that the bottom bars will not yield. It is essential that the actual moment, M^+ , rather than the yield moment, M_y^+ , at the positive critical section be used as the M_s^+ in the bond model formulation. This is achieved using Equation 7.35, in which A_s^+ is the area of the bottom steel within the radial strip, that is calculated from Equation 7.34. $A_{s,total}^+$ is the total area of the positive reinforcement, and M^+ is calculated based on equations of equilibrium with the assumption that all top reinforcement yields.

$$M_s^+ = M^+ \times \frac{A_s^+}{A_{s,total}^+} \quad [7.35]$$

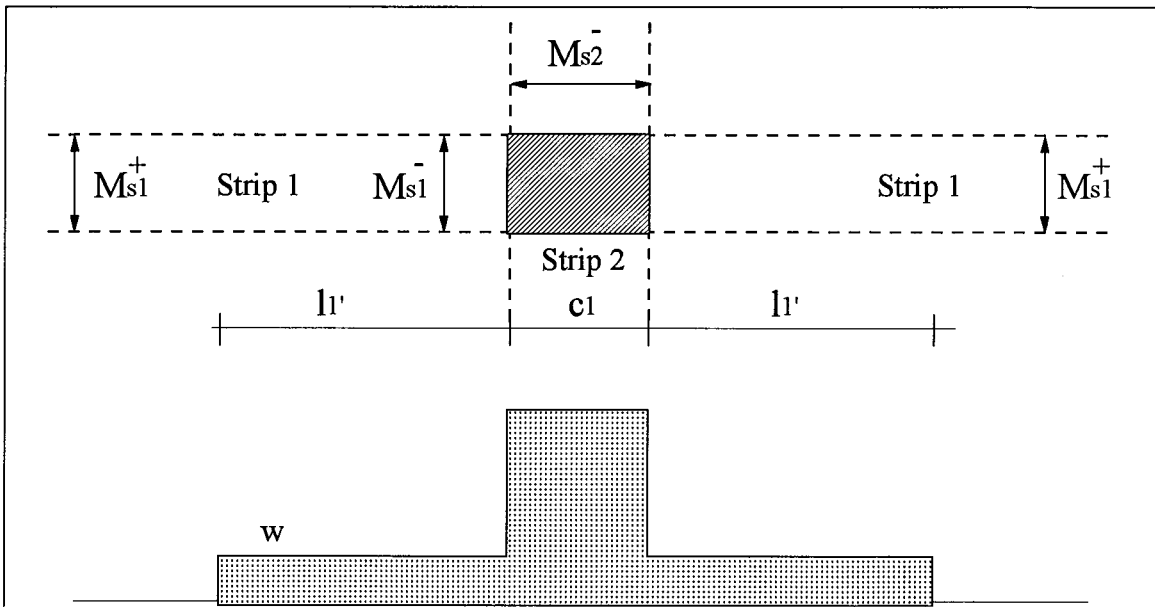
7.5.3 Cases Where Shear Capacity of the Connection is Smaller Than the Yield Line Mechanism Load

The bond model procedures predict the punching capacity of a flat plate-column connection as the lesser of the two capacities; shear capacity of the connection, and the yield line mechanism load. The shear capacity of the connection is determined based on the assumption that both top and bottom reinforcement within radial strips are yielded. If the load obtained based on this assumption, q_0 , is smaller than the yield line mechanism load, q_y , the punching failure occurs prior to the formation of the positive yield line, and the positive moment in the radial strip, M_s^+ , will be smaller than the assumed yield moment. Determination of the positive moment, and hence the shear capacity of the connection requires an iterative procedure. The distributed load obtained from Equation 7.36 is recommended for the first iteration, since it is very close to the actual punching load.

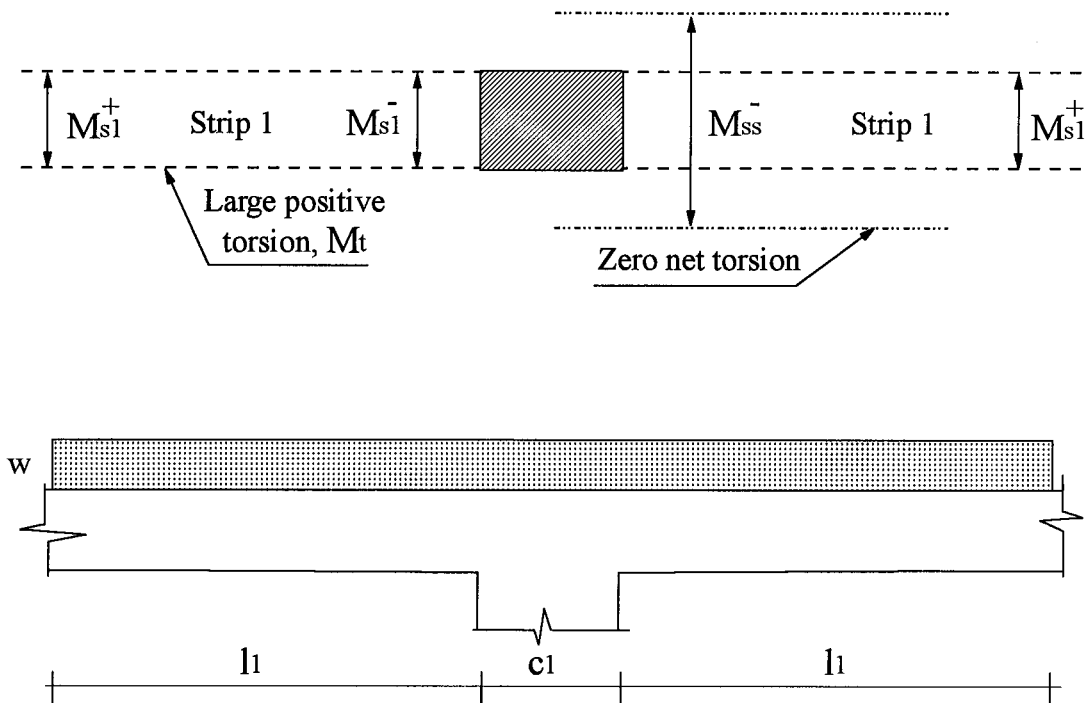
$$q = \frac{q_0^2}{q_y} \quad [7.36]$$

Table 7.1 Comparison of P_{Bond} , P_{max} , and P_{min} (Equations 7.13, 7.14 and 7.16)

Ratio	K_2	$K_1 = 1$	$K_1 = 1/2$	$K_1 = 1/3$	$K_1 = 1/4$
$P_{\text{max}} / P_{\text{Bond}}$	any value	1	1.02	1.04	1.05
$P_{\text{Bond}} / P_{\text{min}}$	1/2	1.1	1.05	1.02	1
	1/3	1.17	1.13	1.1	1.07
	1/4	1.22	1.18	1.15	1.12
	1/5	1.25	1.21	1.18	1.15



(a) Simplified model for proportional behavior



(b) Simplified model for non-proportional behavior - extreme case

Figure 7.1 Distribution of shear in simplified models

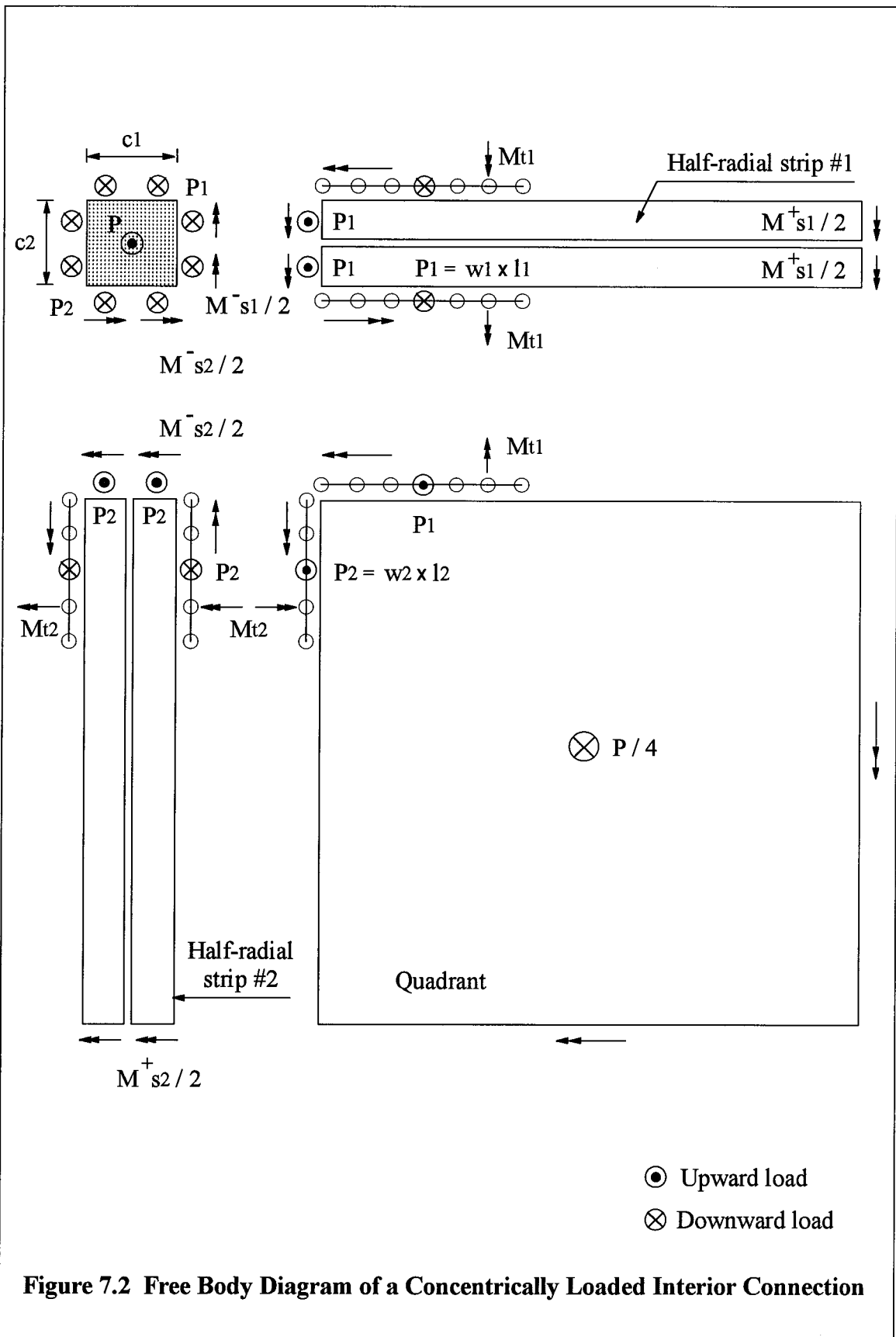
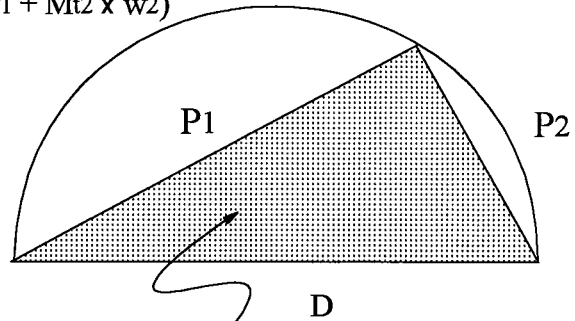


Figure 7.2 Free Body Diagram of a Concentrically Loaded Interior Connection

$$D = \sqrt{M_{s1} \times w_1 + M_{s2} \times w_2 + 2(M_{t1} \times w_1 + M_{t2} \times w_2)}$$

In a simplified model:

$$D = \sqrt{M_{s1} \times w_1 + M_{s2} \times w_2}$$



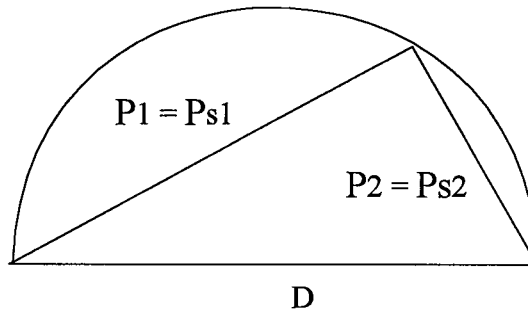
Right angle triangle

(a) General

Radial strips all loaded to their nominal capacities;

$$P_{s1} = \sqrt{M_{s1} \times w_1}$$

$$P_{s2} = \sqrt{M_{s2} \times w_2}$$

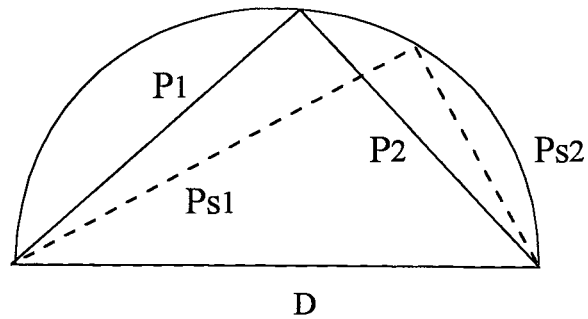


(b) The Bond Model

Non-proportional behavior

$$P_1 = P_2$$

(c) Maximum estimate



Non-proportional behavior

Always a lower bound solution

$$P_2 = c_1 \times w_1 / 2$$

(d) Minimum estimate

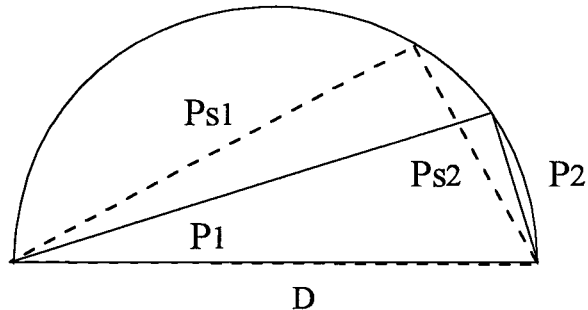


Figure 7.3 Relation between loads transferred through each half radial strip

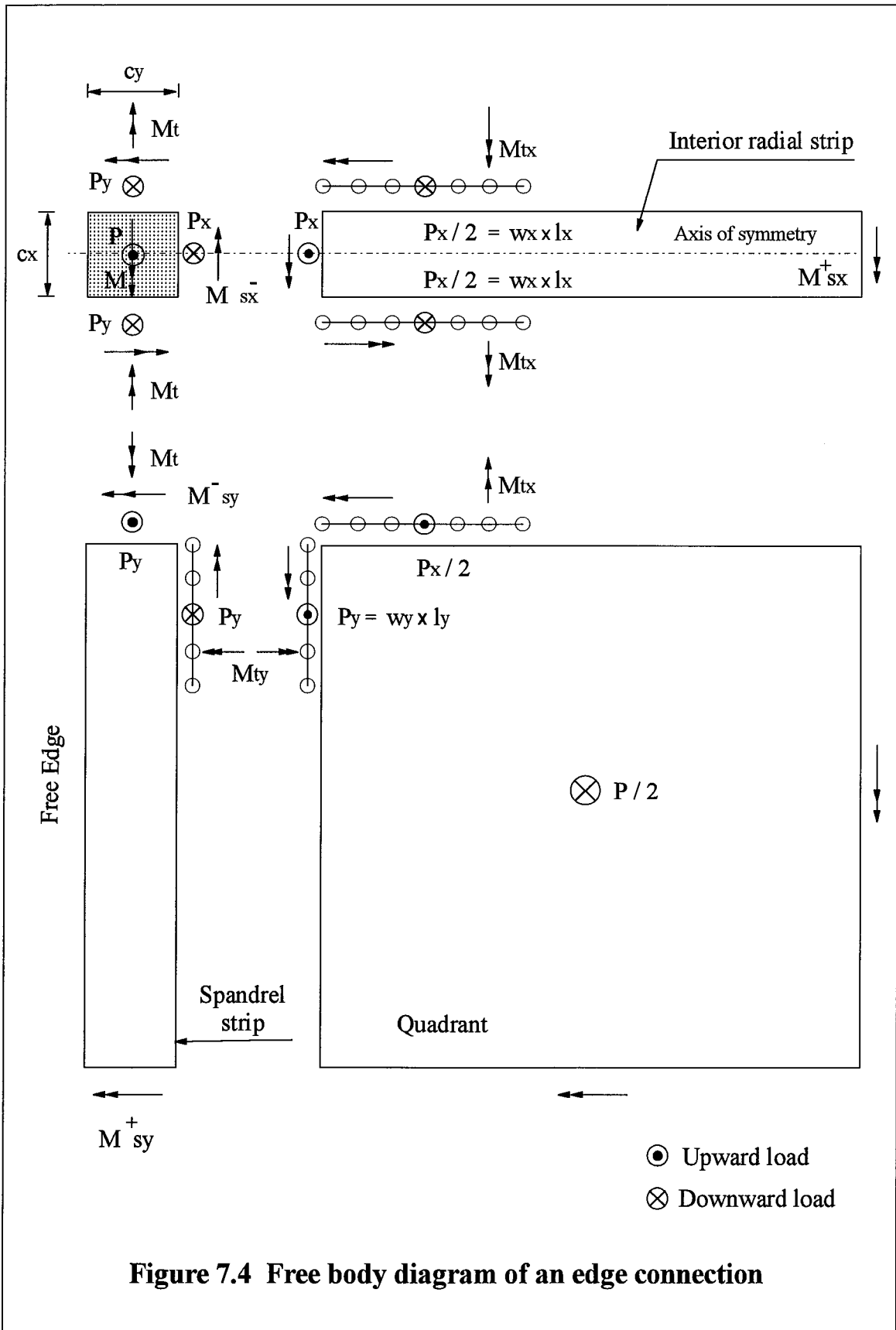
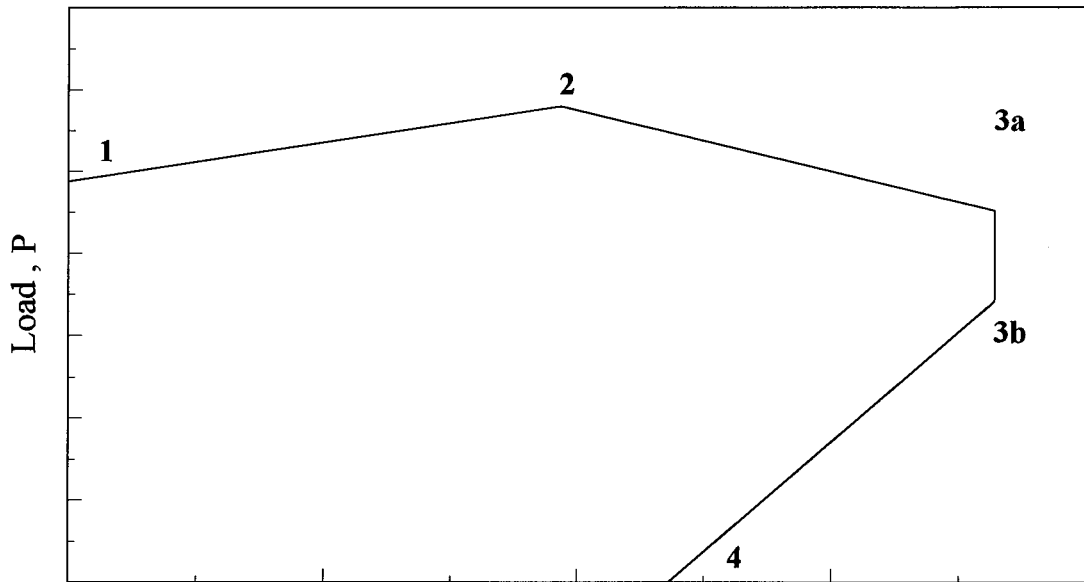
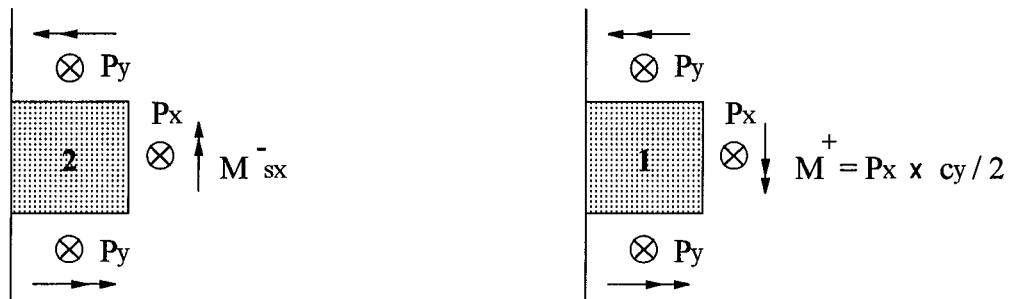
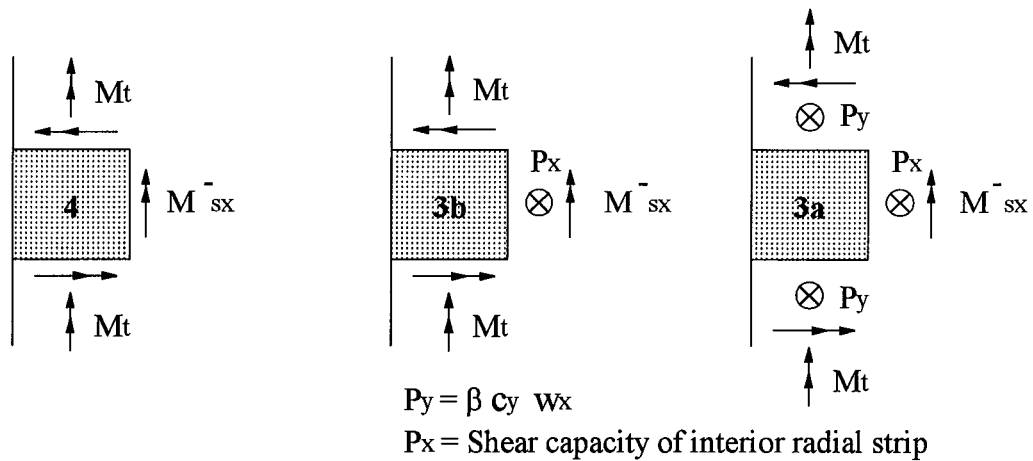


Figure 7.4 Free body diagram of an edge connection

Exterior Connections



Moment at center line of column, M



$P_y = \text{Shear capacity of spandrel strip}$

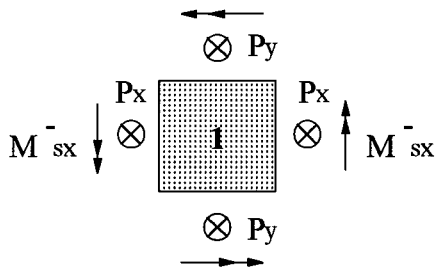
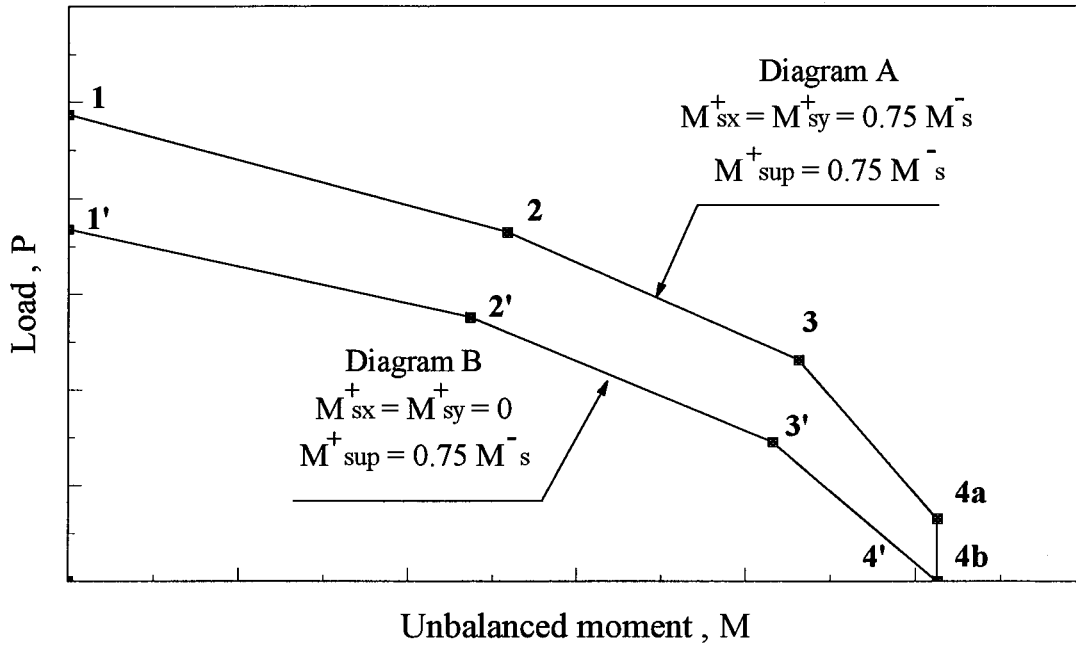
$P_y = \text{Shear capacity of spandrel strip}$

$P_x = \text{Shear capacity of interior radial strip}$

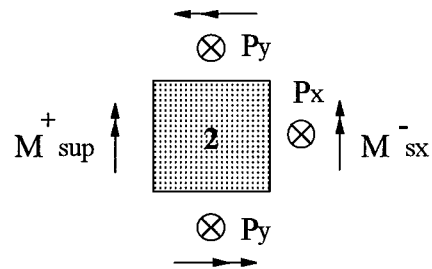
$P_x = c_x \times w_y$

Figure 7.5 Moment-shear diagram for the capacity of edge connections

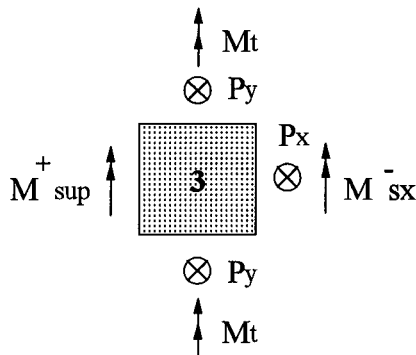
Interior Connections



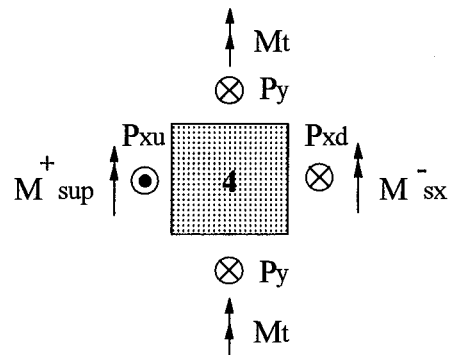
P_y = Shear capacity of radial strip y
 P_x = Shear capacity of radial strip x



P_y = Shear capacity of radial strip y
 P_x = Shear capacity of radial strip x



$P_y = \beta c_y w_x$
 P_x = Shear capacity of radial strip x



$P_y = \beta c_y w_x$ at point 4a
 $P_y = 0$ at point 4b

Figure 7.6 Moment-shear diagram for the capacity of interior connections

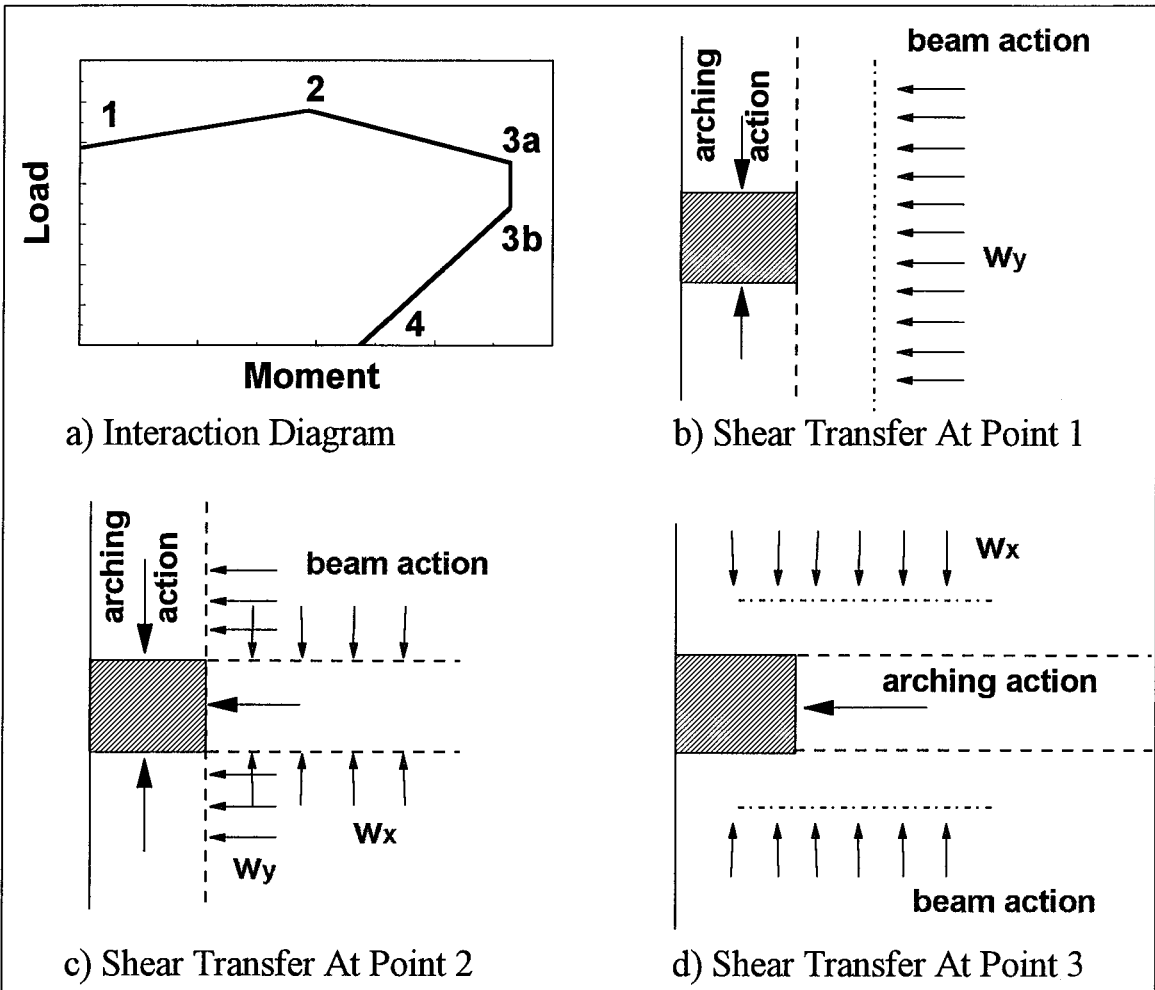


Figure 7.7 Shear Transfer in Edge Connections

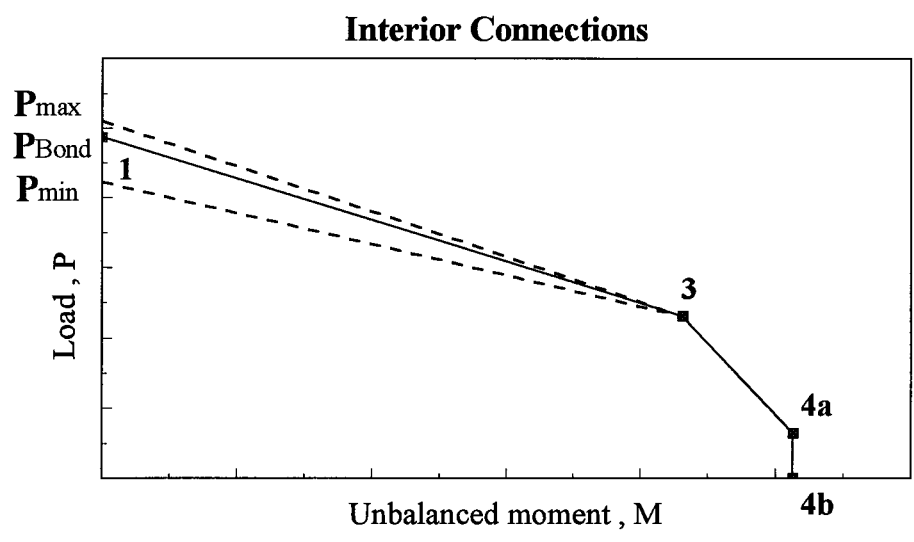


Figure 7.8 Moment-Shear Diagram for the Capacity of Interior Connections - Non-Proportional Behavior

8. Strip Model, North American Standards, and Tests in Literature

8.1 General

The Bond Model has been applied to 145 tests on the concentrically loaded interior connections by Alexander (1996). All test specimens had either square or circular columns and uniformly spaced flexural reinforcement. An average test to predicted ratio of 1.3 with a coefficient of variation of 12.2 percent is reported. Also, the average test to predicted ratio, using the ACI code method, is reported as 1.56 with a coefficient of variation of 26.2 percent.

Eighty-three individual slab-column connections are considered here (Section 8.2) to evaluate the moment-shear interaction diagrams suggested by the Strip Model. These include forty edge connections from nine separate investigators and forty-three eccentrically loaded interior connections from four separate researchers. A brief description of each test, geometry, and analytical results are provided in appendices C and D for the edge and interior connections, respectively.

In Section 8.3, shear-moment interaction diagrams based on the North American building codes are briefly explained. These diagrams are applied to the edge and interior connections reported in the literature. The results of the study are then compared to the results based on the Strip Model in Section 8.4, with the focus on the two edge connections tested and reported in this thesis.

8.2 Applying the Strip Model to Tests in the Literature

8.2.1 Strip Model and Tests on Edge Connections

Test to calculated ratio of forty edge connections reported in the literature are presented in Figure 8.1. The geometry and boundary conditions of the test specimens were variable. The moment to shear ratio, e , ranged from 0 to ∞ . The column size varied from 75 to 355 mm and the thickness of the plate ranged from 48 to 152 mm. The sampling, therefore, provides a diverse set of data with which to test the proposed model.

The test to calculated ratio varies between 1.08 and 1.60, and has an average of 1.32. The related coefficient of variation is only 12.3 percent. These data indicate that the Strip Model provides an accurate lower bound estimate of the capacity of the edge connections.

In Figure 8.1, a perfect correlation between tested and predicted capacities would produce a quarter of a circle with a radius of one. In this figure, any radial line corresponds to a constant value of h/e . In practice, design assumption for most edge connections results in a value of e of about 2.0 to 2.5 times the thickness of the plate. The corresponding lines are also presented in Figure 8.1. Any point on the horizontal axis represents a test in which no shear is transferred through the connection. Points on the vertical axis, however, correspond to tests in which no bending moment is transferred.

The test to calculated ratios are also plotted in Figures 8.2 and 8.3 as functions of, respectively, the reinforcement ratio of the top bars in the interior radial strip, and the compressive strength of the concrete, f'_c .

8.2.2 Strip Model and eccentrically loaded interior connections

Test to calculated ratio of forty three interior connections reported in the literature are presented in Figure 8.4. The average ratio of test to calculated load is 1.39. Test to calculated ratios vary between 0.97 and 1.83 with the coefficient of variation of 16.2 percent.

Except for the two tests of Regan et. al., all tests were isolated single column tests. The moment to shear ratio ranged from 0 to ∞ . Plate thickness varied from 65 to 152 mm. Column dimension ranged from 76 to 305 mm. The sampling provides a diverse set of data with which to test the proposed model. Since in all tests, value of M_{sy}^+ is zero, only diagram B in Figure 7.5 is being examined.

In most interior connections in practice, the ratio of the unbalanced moment to the shear, e , varies between 0 and a value of about 2.5 times the thickness of the slab. This corresponds to a region between the vertical axis ($e=0$) and the line $e=2.5 h$. Tests falling in this region realistically model the condition in flat plate structures.

The test to calculated ratios are also plotted in Figure 8.5 versus the reinforcement ratio, and in Figure 8.6 versus the compressive strength of the concrete, f_c .

8.3 North American Standards in the Presence of the Unbalanced Moments

8.3.1 Strength of a Connection

In the presence of unbalanced moments, North American Standards use design moments at three different sections of a flat plate-column connection; (a) moment at the face of the column, used in determining the overall flexural capacity (or yield line mechanism load), P_y , (b) moment about the centroid of the column, M , obtained from analysis of the whole structure and used to design the column, and (c) unbalanced moment about the centroid of the critical section for shear, M_u .

A fraction of the unbalanced moment, $\gamma_v \times M_u$, is assumed to be transferred by eccentric shear stresses. The distribution of the vertical shear stresses around the critical section is assumed to be linear (Equation 8.1). This provides a relation between shear and unbalanced moment, by which the shear capacity of the connection at a certain eccentricity, P_s , can be determined. It is worth mentioning that the critical section property, J , includes terms that accounts for horizontal shear stress, although the contribution of this term is minor.

$$v_{\max} = \frac{V_u}{p \times d} \pm \frac{\gamma_v \times M_u \times c}{J} \quad (\text{same as Equation 2.11}) \quad [8.1]$$

The fraction of unbalanced moment not transferred by the shear, $(1 - \gamma_v) \times M_u$, is assumed to be transferred by flexure over an effective slab width of $c_x + 3 h$. This introduces a completely independent limitation on the connection strength, P_f .

The capacity of the flat plate structure is therefore equal to the smallest value of the yield line mechanism load, P_y , shear capacity of the connection, P_v , and the flexural limitation of the connection, P_f .

8.3.2 Moment-Shear Interaction Diagrams

Moment-shear interaction diagram for an interior connection is plotted in Figure 8.7. In the interior connections, the centroid of the critical section in shear coincides with the centroid of the column ($M_u = M$). The shear due to the applied load and the shear due to the unbalanced moment are always additive. As a result, Equation 8.1 predicts a simple linear interaction (line ab). Shear at point a, V_a , and moment at point b, M_b , are determined by Equations 8.2 and 8.3, respectively.

$$V_a = p \times d \times v_{\max} \quad (\text{Interior Connections}) \quad [8.2]$$

$$M_b = \frac{2 \times v_{\max} \times J}{\gamma_v \times (c_y + d)} \quad (\text{Interior Connections}) \quad [8.3]$$

Figure 8.8 shows the shear-moment interaction diagram for an edge connection. The different shape of the interaction diagram for the edge column-plate connection is due to the asymmetry of the critical section. Figure 8.9 describes the shear distribution along the critical section for points a through d on the interaction diagram, as well as the relation between the moment about the centroid of the critical section and the moment about the centroid of the column (Equation 8.4).

$$M = M_u + V_u \times c_3 \quad [8.4]$$

Along segment ab of the interaction diagram, failure is governed by the stress condition near the free edge. Along segment bc, the critically stressed region is the interior side of the critical section. Along segment cd, failure is again governed by the stress condition at the free edge. However, unlike other segments, the shear component due to the applied load is of opposite sign to the shear component due to the unbalanced moment. For convenience, Equation 8.1 is manipulated to Equations 8.5 through 8.8, by which shears and moments related to points a through d can be directly determined.

$$V_a = \frac{v_{\max}}{\frac{1}{p \times d} + \frac{\gamma_v \times c_2 \times c_3}{J}} \quad (\text{Edge Connections}) \quad [8.5]$$

$$V_b = v_{\max} \times p \times \quad (\text{Edge Connections}) \quad [8.6a]$$

$$M_b = V_b \times c_3 \quad (\text{Edge Connections}) \quad [8.6b]$$

$$V_c = v_{\max} \times p \times d \times \left(1 - \frac{2 \times c_1}{c_y + \frac{d}{2}}\right) \quad (\text{Edge Connections}) \quad [8.7a]$$

$$M_c = \frac{2 \times J \times v_{\max}}{\gamma_v \times (c_y + \frac{d}{2})} + c_3 \times V_c \quad (\text{Edge Connections}) \quad [8.7b]$$

$$M_d = \frac{v_{\max} \times J}{\gamma_v \times c_2} \quad (\text{Edge Connections}) \quad [8.8]$$

8.3.3 Comparison with the Tests in the Literature

Test to calculated ratios, based on the North American Standards, are presented in Tables C5 and D5, respectively for the edge and interior connections reported in the literature.

For the edge connections, the test to calculated ratios range between 1.08 and 2.52, and have an average of 1.59 with the coefficient of variation of 23.7 percent. These ratios are presented graphically in Figure 8.10 based on the eccentricity of the load, non-dimensionalized by the thickness of the specimens. Also, in Figures 8.11 and 8.12, test to calculated ratios are plotted versus the reinforcement ratio and the concrete compressive strength.

For interior connections under unbalanced loading, the test to calculated ratios vary from 1.03 to 2.7, having an average of 1.61 and a coefficient of variation of 24.3 percent. These test to calculated ratios are presented graphically in Figures 8.13 to 8.15.

8.4 Comparison of Strip Model, North American Standards, the Test Results

Any analytical model should be able to predict the behavior of a specimen under a wide range of conditions, provide an understanding of the load carrying mechanisms, and result in a safe prediction of the ultimate capacity of the specimen without significant loss of accuracy. A usual measure to evaluate an analytical model is the ratio of test to predicted result. Table 8.1 summarizes the statistics on the test to calculated predictions based on the Strip Model and the North American Standards.

Both models result in a safe prediction of the capacity of the plate-column connections, when the reinforcement ratio is within a reasonable range. However, for extremely lightly reinforced interior connections under balanced loading, the code predictions might be unsafe.

The coefficients of variation of the test to calculated predictions by the Bond Model the Strip Model are considerably smaller than those by the North American Standards. This indicates that the bond model approach is more reliable than the North American codes in predicting the punching capacity of the column-plate connections.

The two edge connections reported in this thesis provide a good opportunity to examine which model predicts the behavior of the plate-column connections more accurately. In these tests, the geometry of the connections are identical and the same concrete is used. Also, the capacity of the connections is not governed by the yield line mechanism load, and the reinforcement provided satisfies the flexural limitations of the code (with the exemption that one connection is designed for less moment). The only variable is the area of the reinforcement normal to the free edge.

In Figures 8.16 and 8.17 the test results are plotted against the moment-shear interaction diagrams based on the Strip Model and on the North American codes for the north and the south edge connections, respectively. Since the interaction diagram of the code is independent of the reinforcement ratio, this diagram is the same for both connections. For both connections, the governing region on the code interaction diagram is line bc, which has a negative slope. The eccentricity of load in the south connection is more, since this connection is more heavily reinforced. Therefore, according to the code, it should transfer less load.

The effect of increasing the area of the top reinforcement normal to the free edge, however, is considered by the Strip Model. Comparing Figures 8.16 and 8.17, the moment-shear interaction diagram is stretched to the right side and slightly to the top, as the reinforcement ratio increases. Therefore, the model predicts that the south connection should transfer more load and larger moment, compared to the north connection.

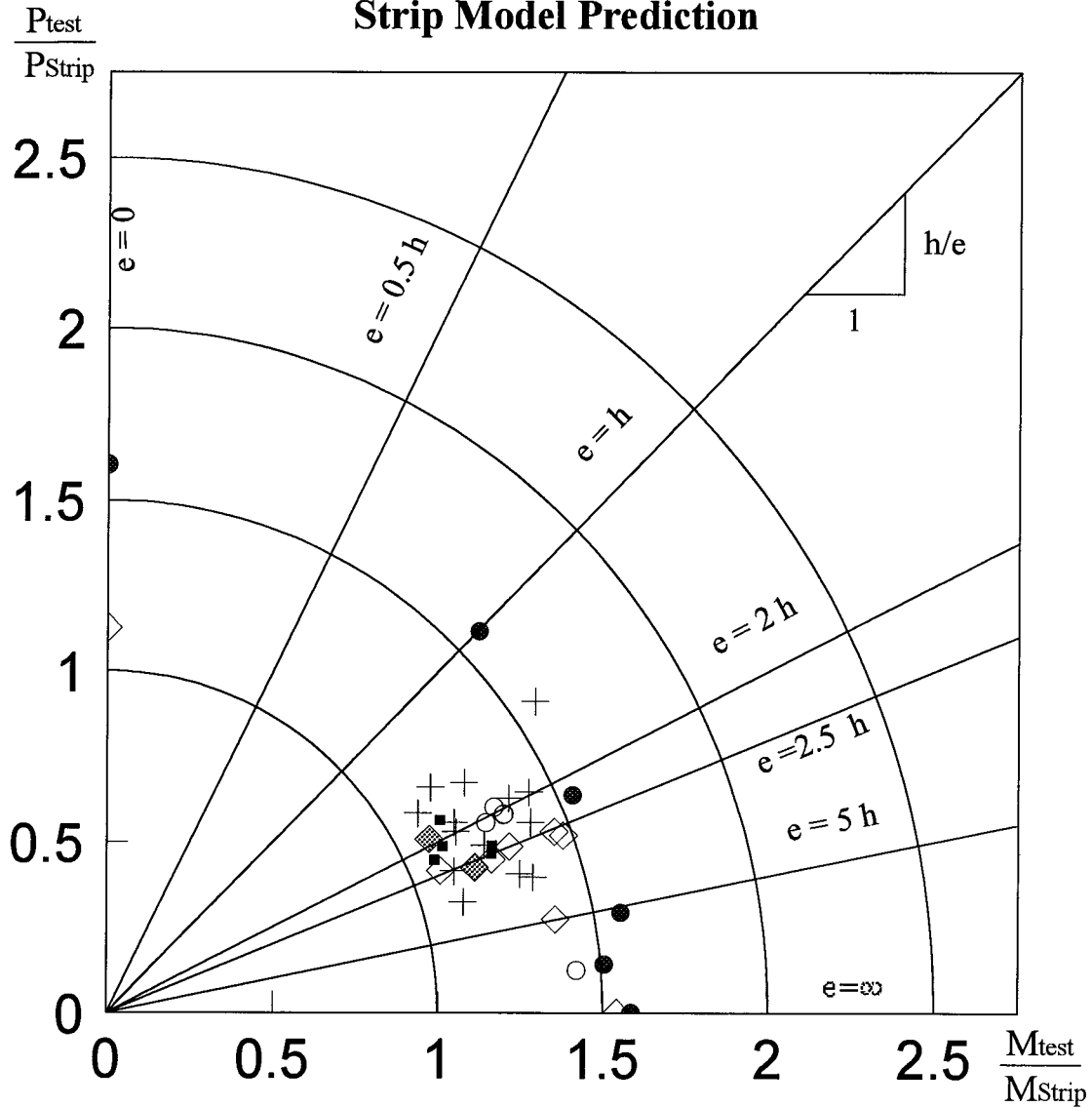
Test results show that the south connection has carried more shear while transferring a considerably larger moment. This observation is consistent with the Strip Model prediction of the behavior and not with the code interpretation of the behavior. The capacities predicted by the Strip Model are more reliable but still conservative.

Table 8.1 Comparison of the Strip Model, North American Standards, and Test Results

Test to calculated ratio	Interior connections *		Interior connections unbalanced moment		Edge connections	
	Bond Model	Codes	Strip Model	Codes	Strip Model	Codes
No. of tests	145	145	43	43	40	39
Average	1.3	1.56	1.39	1.61	1.32	1.59
coefficient of variation (%)	12.2	26.2	16.2	24.3	12.3	23.7
Minimum	0.86	0.7	0.97	1.03	1.08	1.08
Maximum	1.66	2.77	1.83	2.7	1.6	2.52

* After Alexander (1996)

Edge Connections Strip Model Prediction



Stamenkovic and Chapman	Kane / Hanson and Hanson	Scavuzo / Gosselin / Lamb
●	○	■
Zaghlool	Regan	Afhami
◇	+	◈

Figure 8.1 Test to calculated ratio for the edge connections reported in the literature - Strip Model

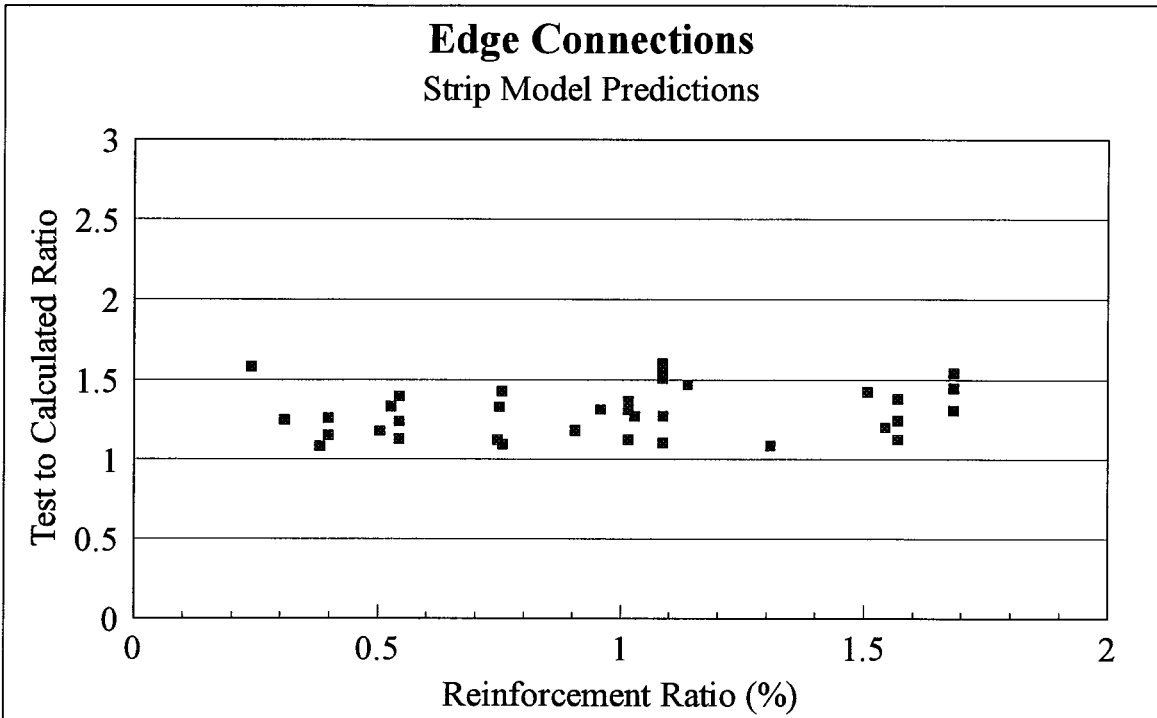


Figure 8.2 Test to calculated ratios of edge connections reported in the literature versus the reinforcement ratio of the top bars in the interior radial strip

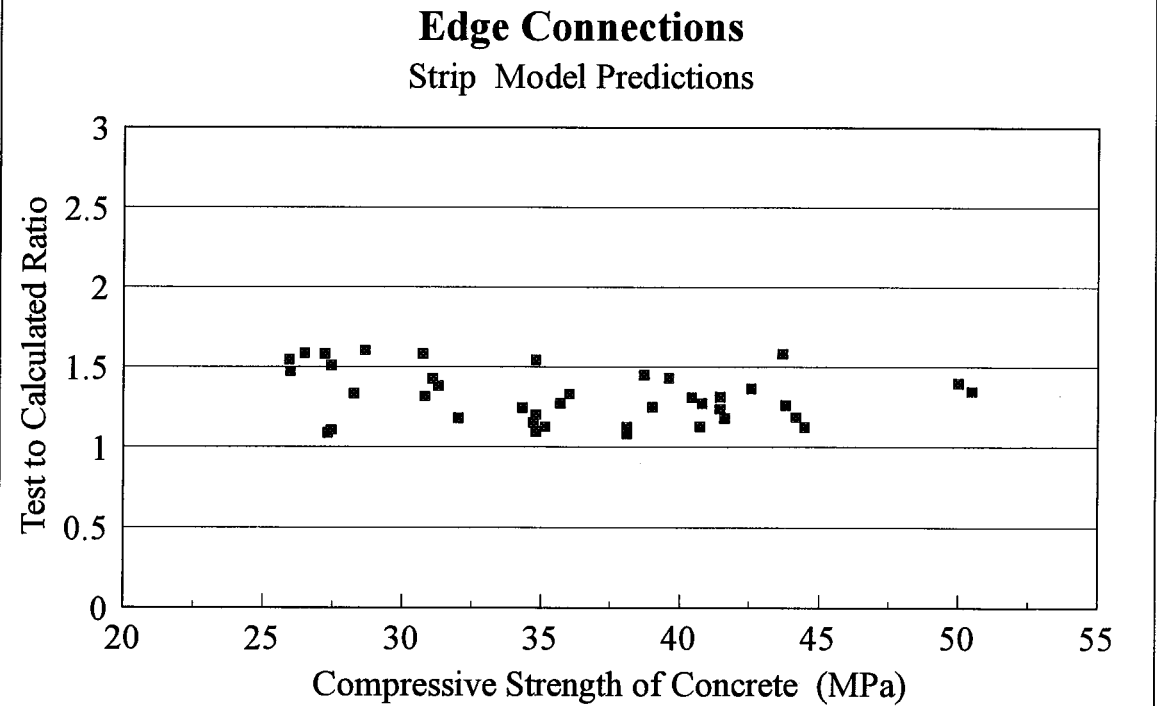


Figure 8.3 Test to calculated ratios of edge connections reported in the literature versus the compressive strength of the concrete, f_c

Interior Connections Strip Model Prediction

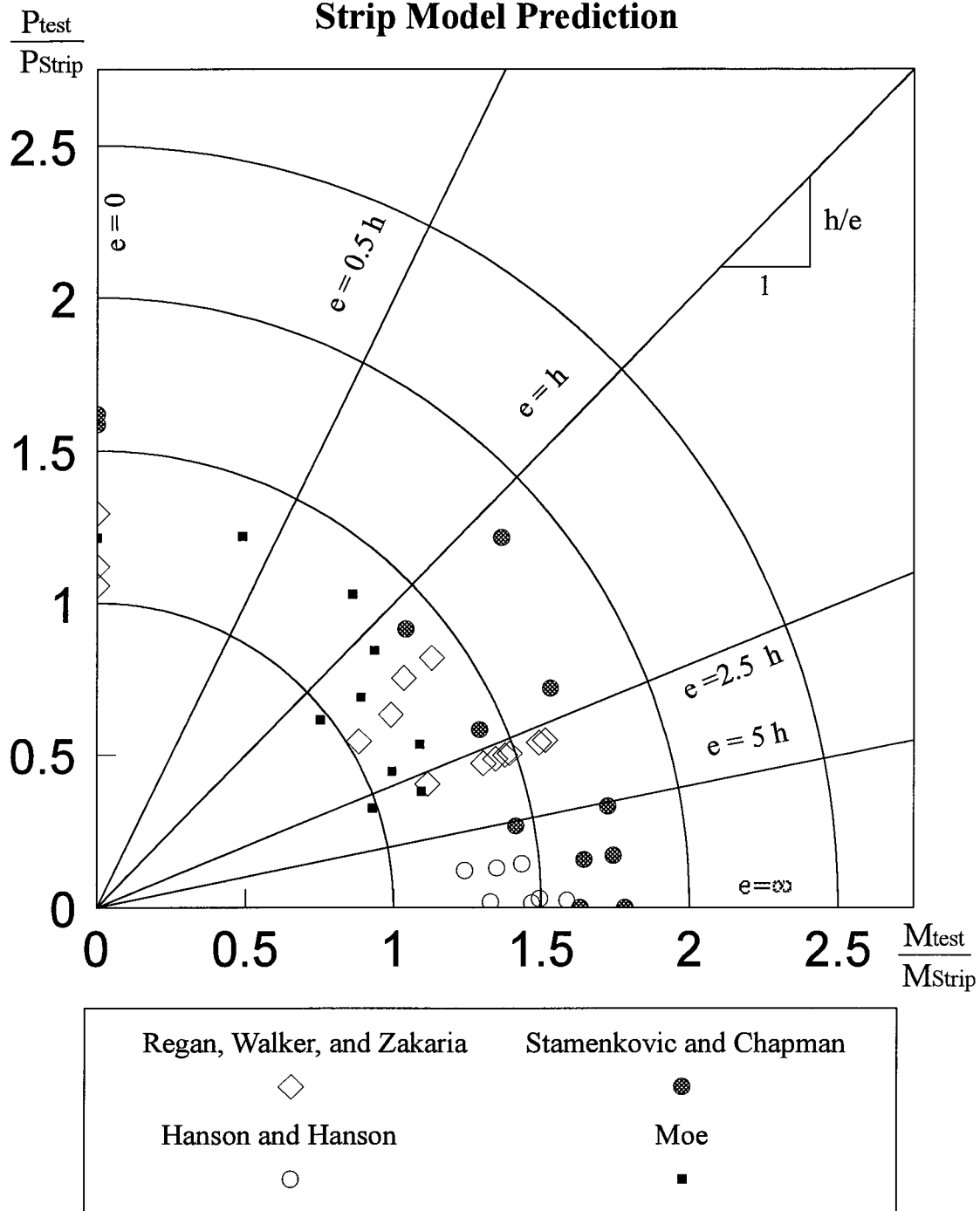


Figure 8.4 Test to calculated ratio for the interior connections reported in the literature - Strip Model

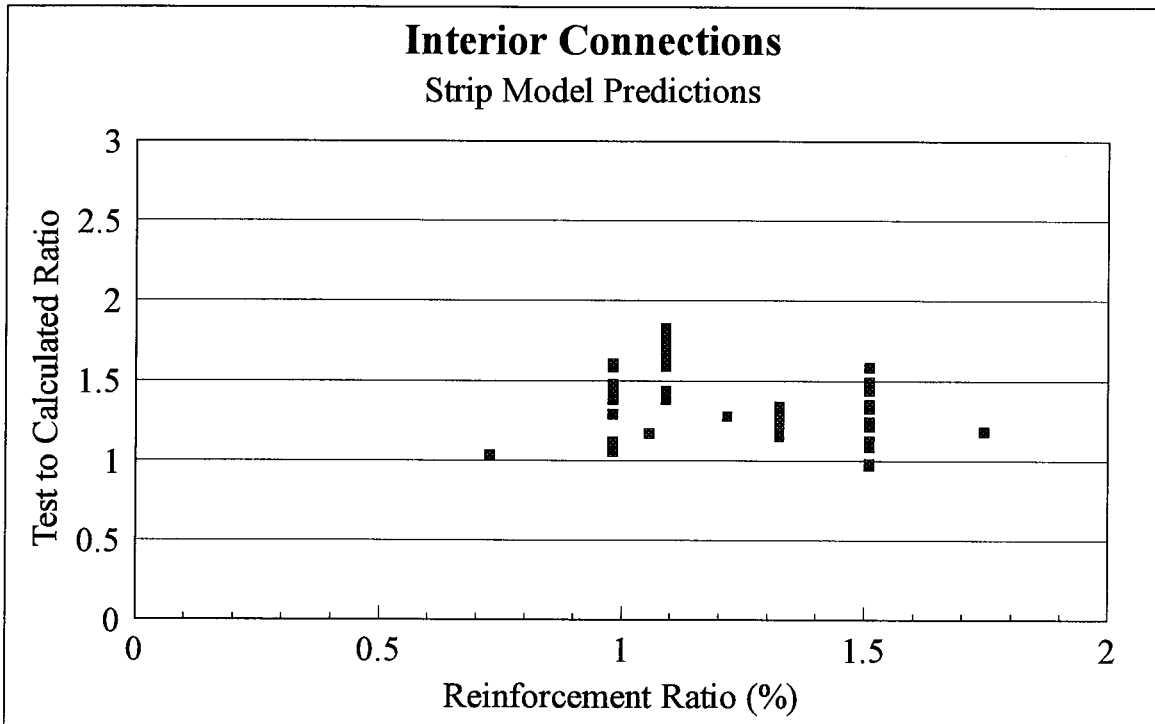


Figure 8.5 Test to calculated ratios of eccentrically loaded interior connections reported in the literature versus the reinforcement ratio

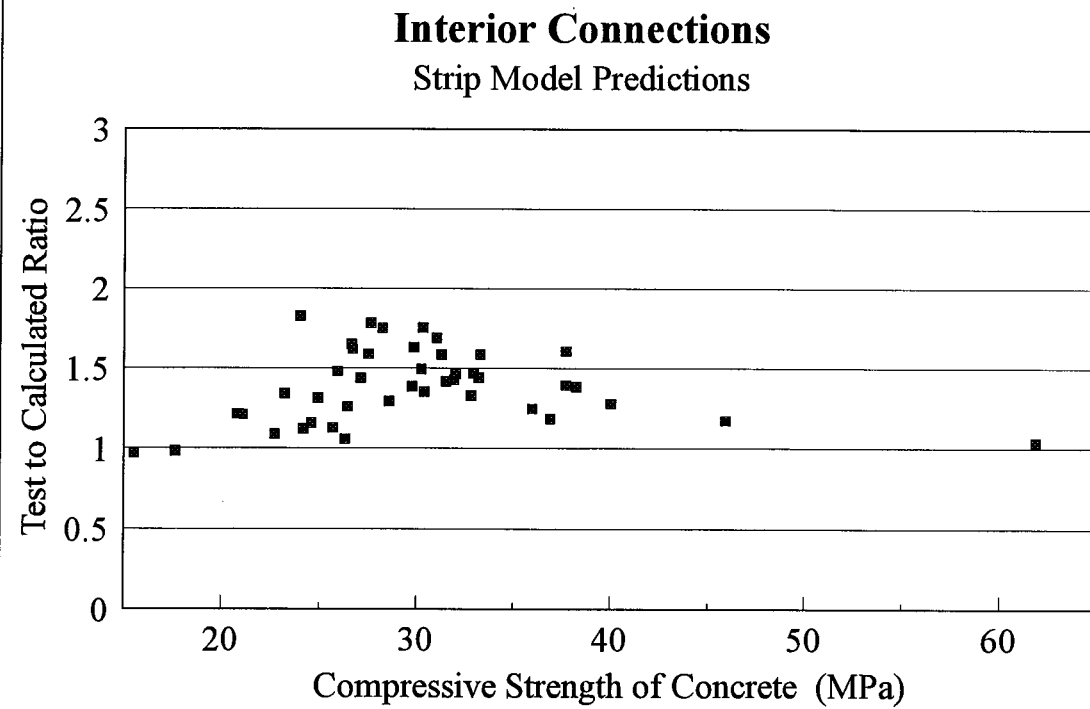


Figure 8.6 Test to calculated ratios of eccentrically loaded interior connections reported in the literature versus the compressive strength of the concrete, f_c

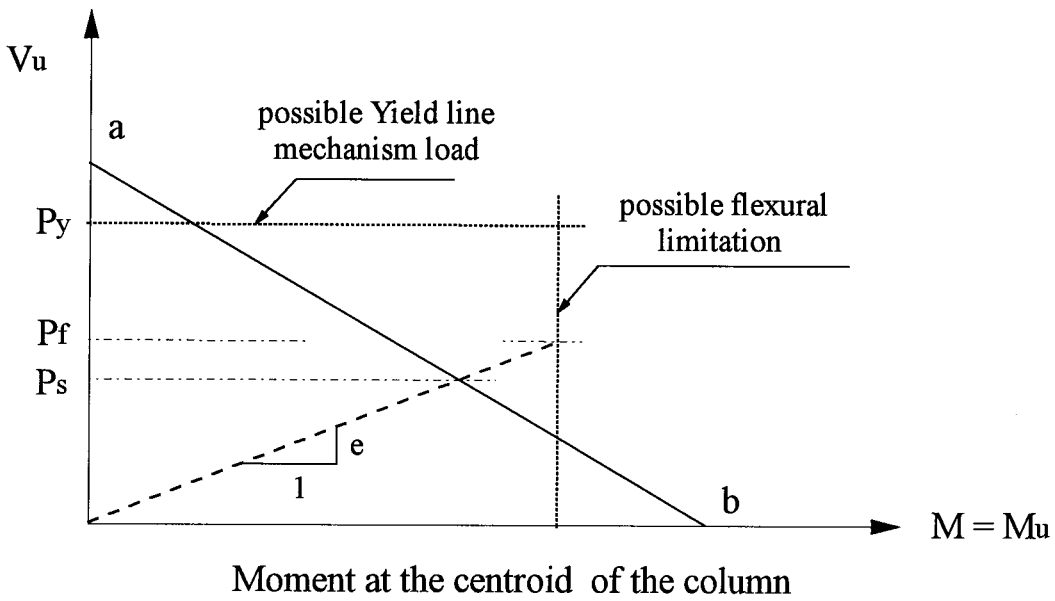


Figure 8.7 Moment-shear interaction diagrams for the interior connections - North American building codes

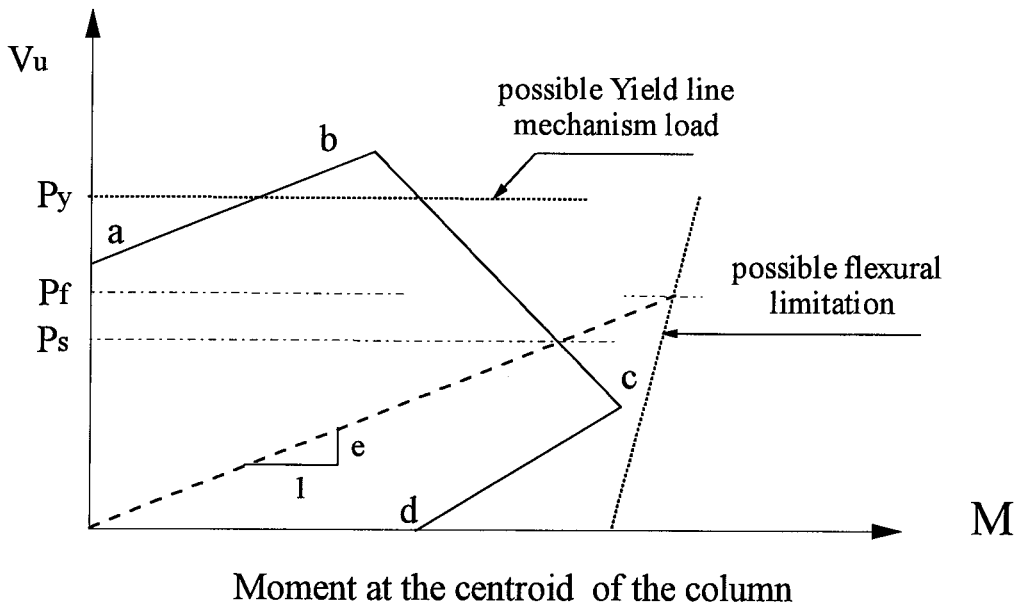
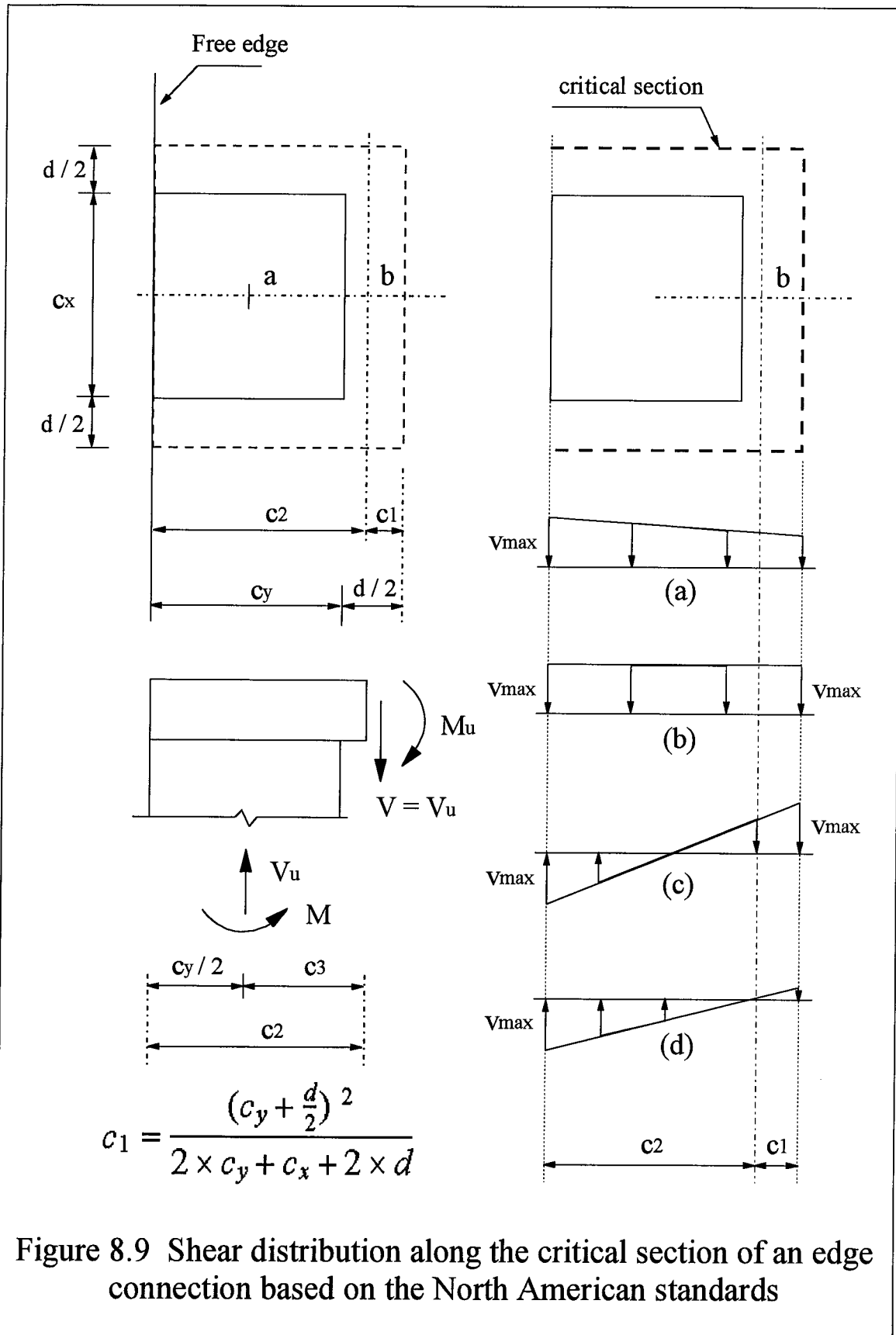
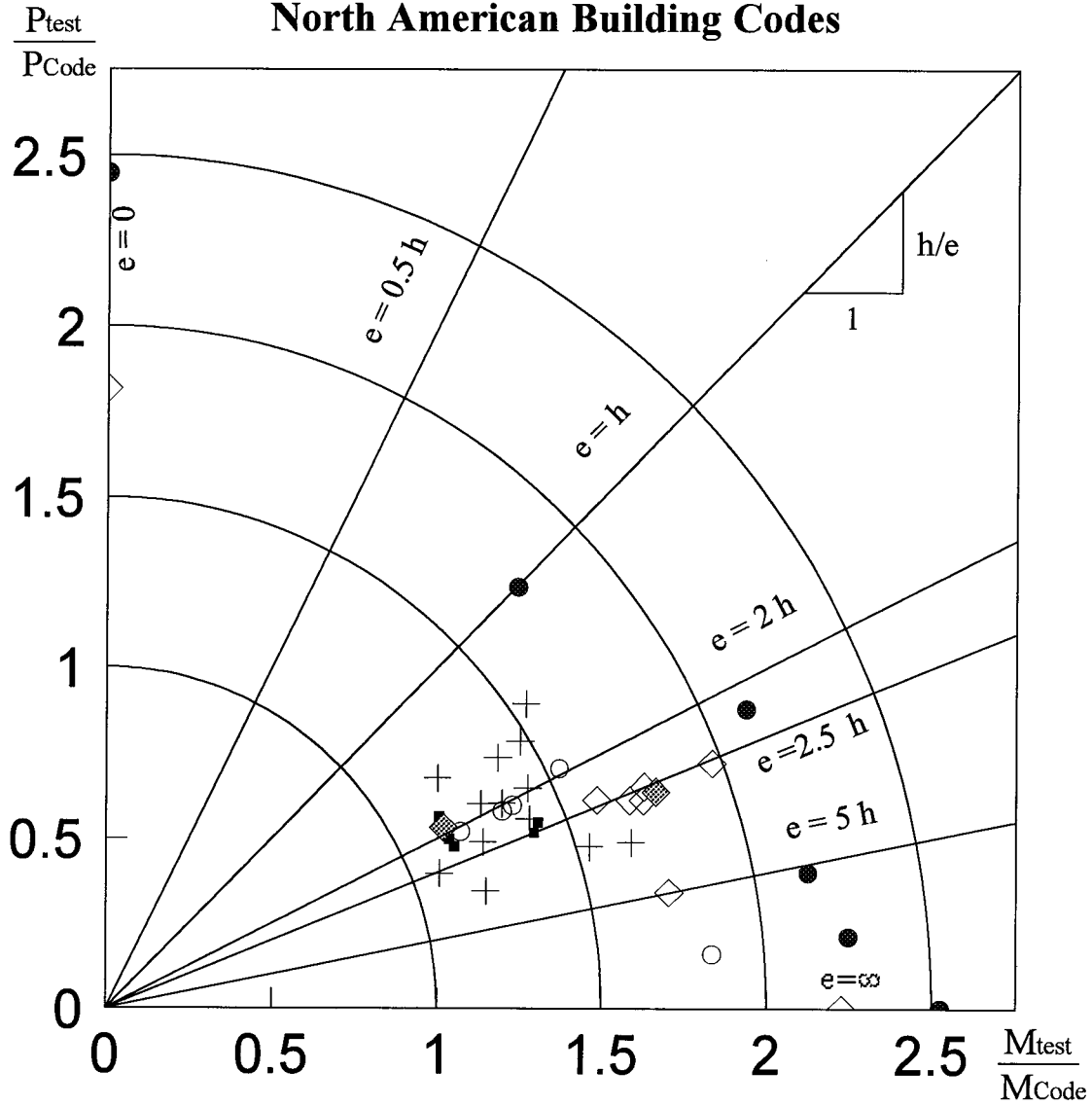


Figure 8.8 Moment-shear interaction diagrams for the edge connections - North American building codes



Edge Connections North American Building Codes



Stamenkovic and Chapman	Kane / Hanson and Hanson	Scavuzo / Gosselin / Lamb
●	○	■
Zaghlool	Regan	Afhami
◇	+	◩

Figure 8.10 Test to calculated ratio for the edge connections reported in the literature - North American standards

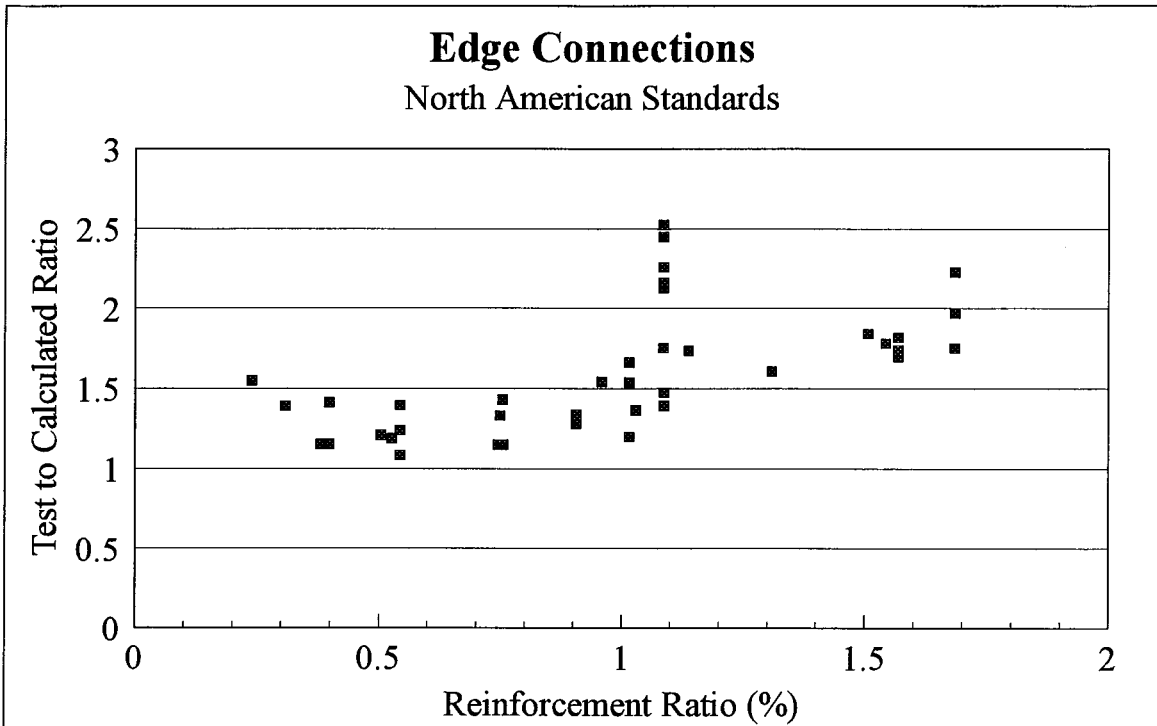


Figure 8.11 Test to calculated ratios of the edge connections reported in the literature versus the reinforcement ratio of the top bars in the interior radial strip

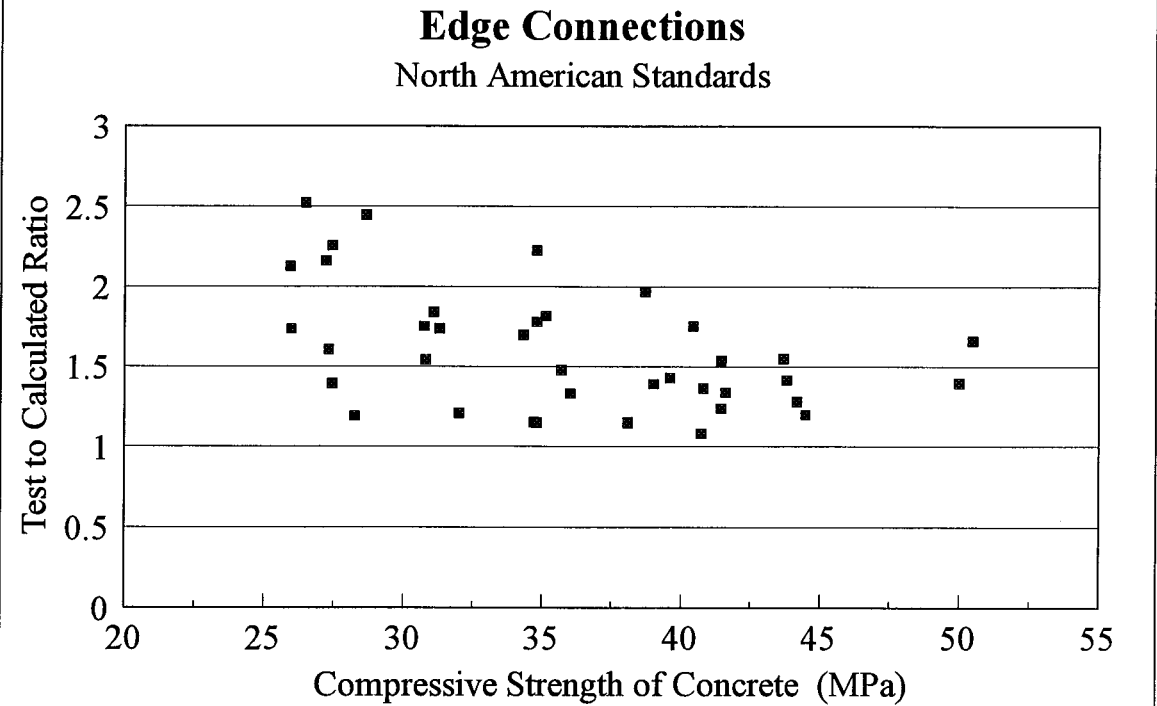


Figure 8.12 Test to calculated ratios of the edge connections reported in the literature versus the compressive strength of the concrete, f_c

Interior Connections North American Building Codes

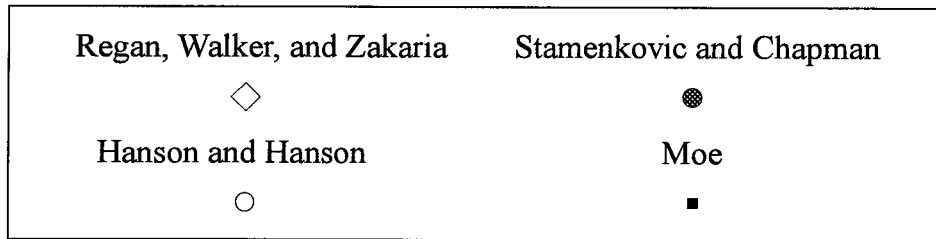
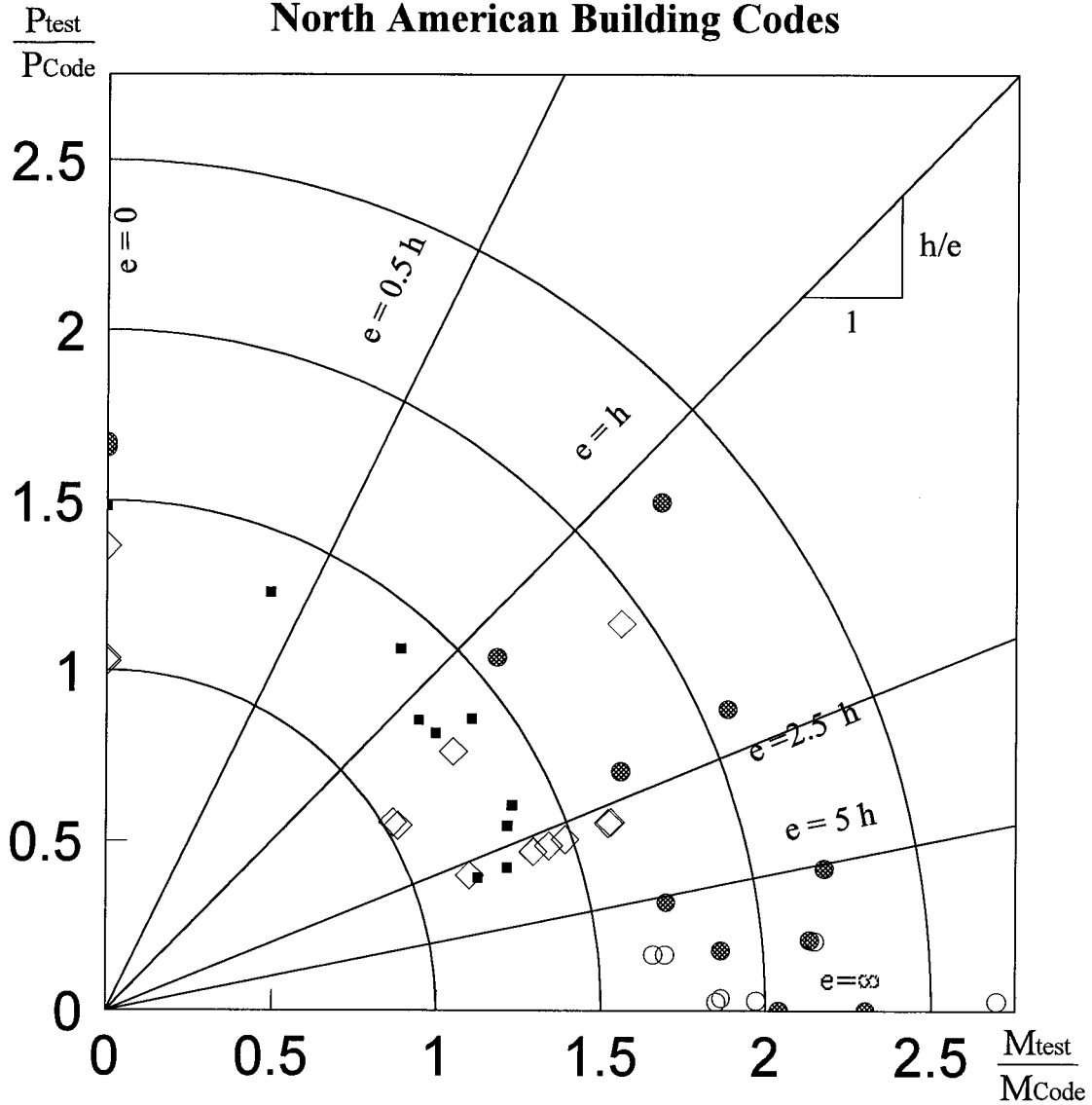


Figure 8.13 Test to calculated ratio for the interior connections reported in the literature - North American standards

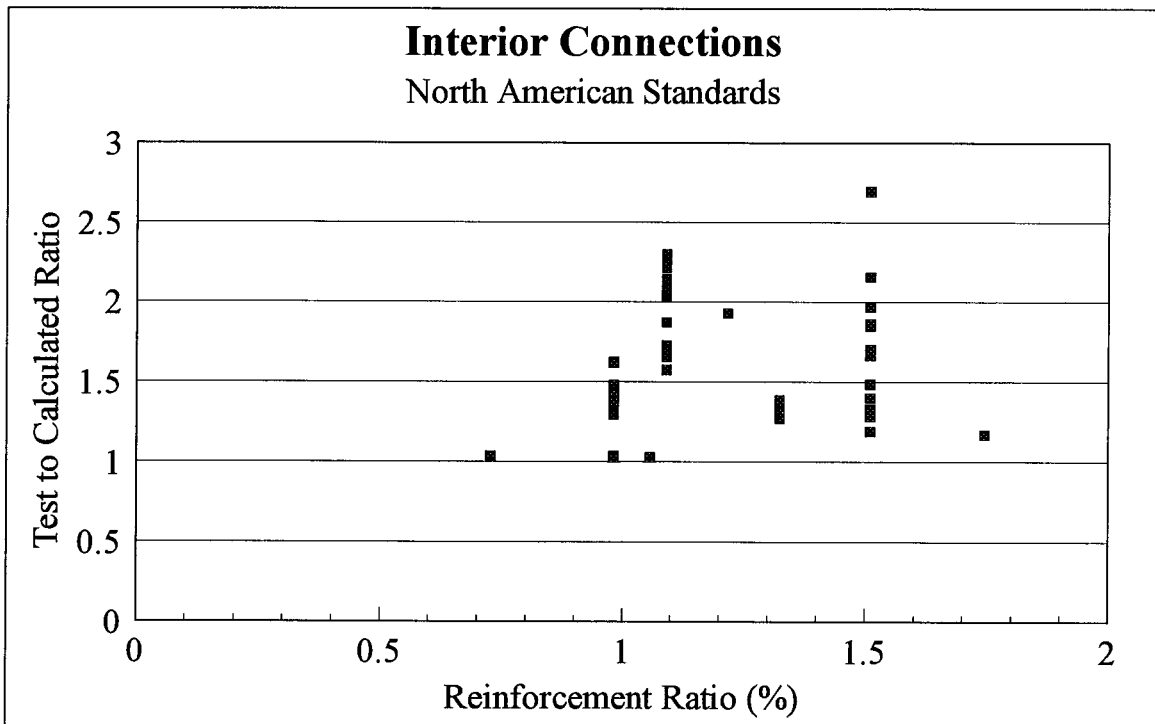


Figure 8.14 Test to calculated ratios of eccentrically loaded interior connections reported in the literature versus the reinforcement ratio

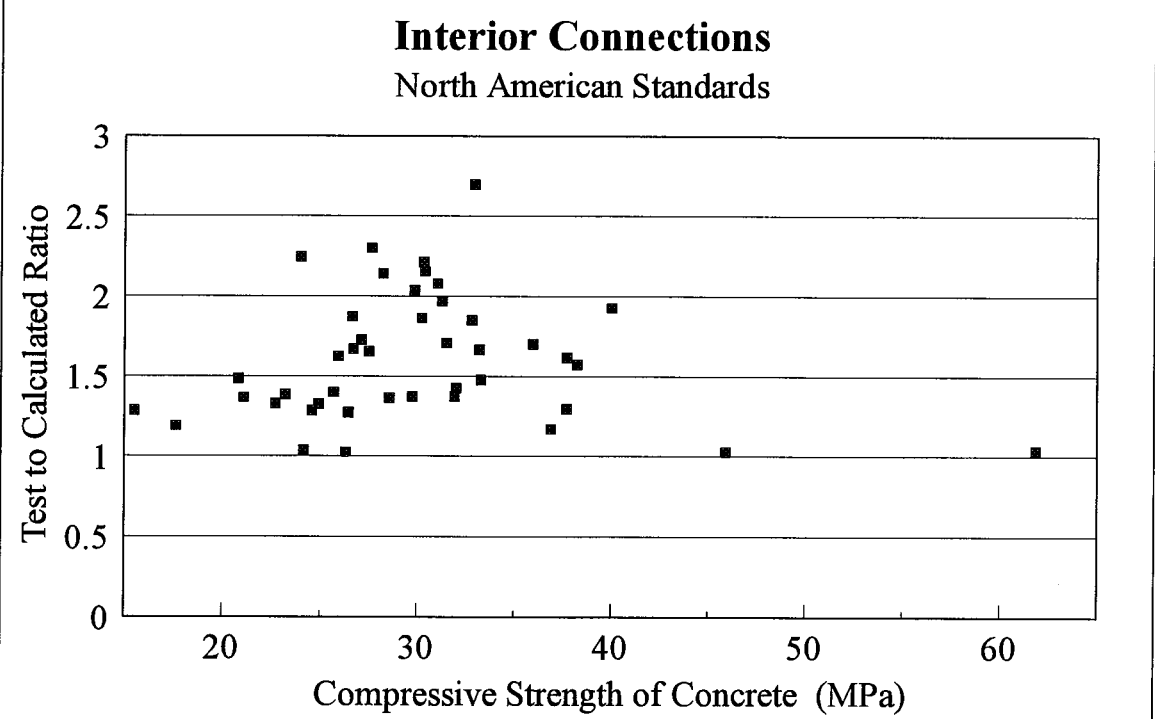


Figure 8.15 Test to calculated ratios of eccentrically loaded interior connections reported in the literature versus the compressive strength of the concrete, f_c

North Edge Connection

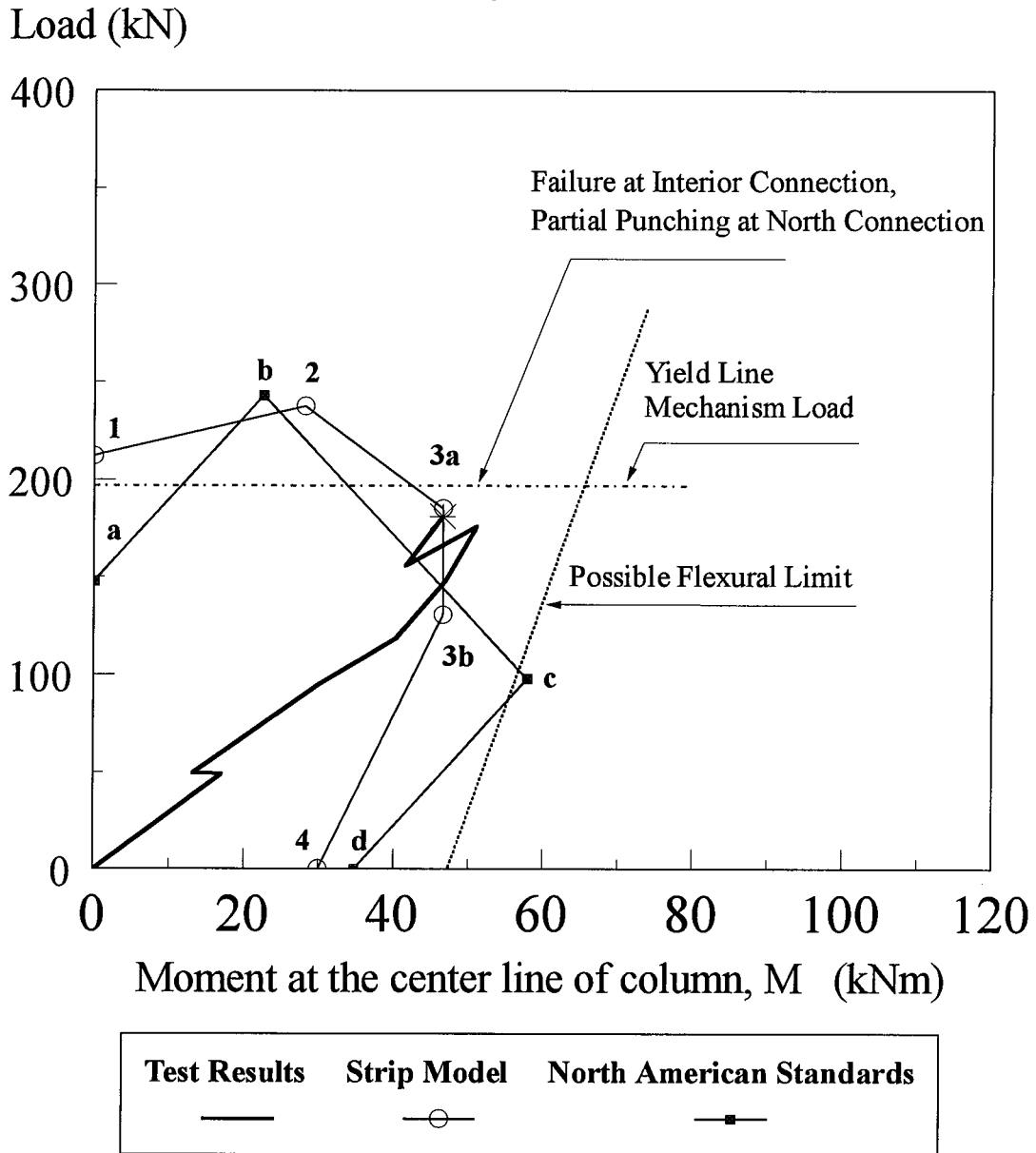


Figure 8.16 Comparison of North American standards, Strip Model, and the test results of the north edge connection in the current study

South Edge Connection

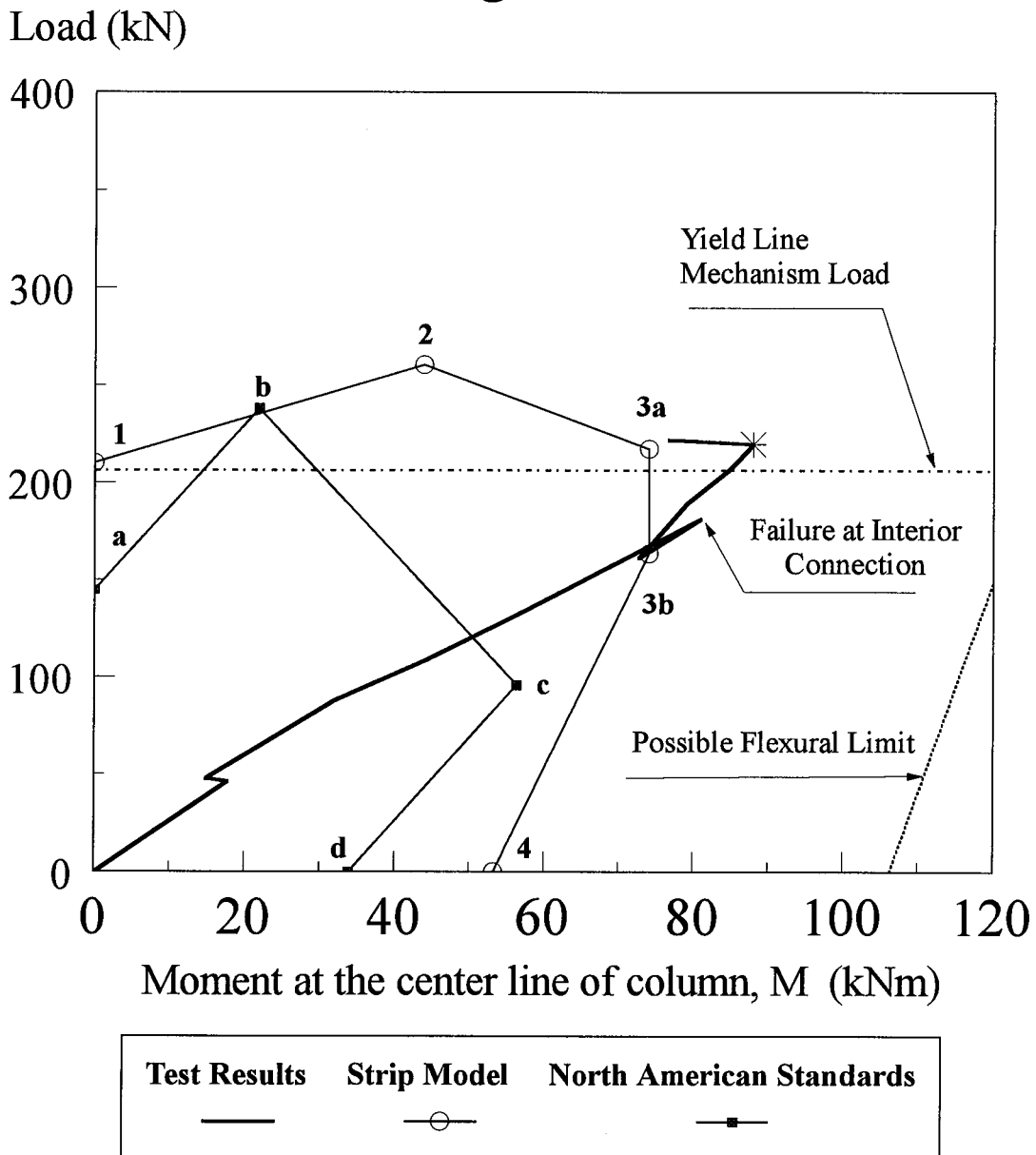


Figure 8.17 Comparison of North American standards, Strip Model, and the test results of the south edge connection in the current study

9. Summary and Conclusions

9.1 Summary

An analytical model, referred to as the Strip Model, is proposed that explains the physical mechanisms of transfer of vertical shear and bending moment from orthogonally reinforced concrete slabs to columns. The Strip Model is a generalization of the Bond Model which is limited to the behavior of interior slab-column connections under concentric load, that is, where only vertical shear is transferred to the columns.

The Strip Model uses the same vertical load transfer mechanism of arching action and beam action as the Bond Model. Hence, both models describe the transfer of the vertical shear between the plate and the column in terms of the available mechanisms of moment gradient. The connection is modeled with strips of slab, called radial strips, that are parallel to the reinforcement and cantilever from the column. Load is transferred to a radial strip from adjacent quadrants of the two-way slab by slender flexural behavior. A radial strip then transfers this load to the column primarily by arching action. The interaction of the flexural strength of the radial strip and the shear strength of the slender two-way slab defines the capacity of a radial strip. An important advantage of this model of shear transfer is that it provides a basis for calculating internal distribution of shear from measured strains in the flexural reinforcement of the slab.

Since the Bond Model was developed to predict the capacity of concentrically loaded interior slab-column connections, the width of a radial strip was selected to encompass those bars passing either through or immediately adjacent to the column. The resulting capacity is referred to as the nominal capacity of that strip. The capacity of the connection was taken to be the sum of the nominal capacities of the four radial strips. The Bond Model successfully predicted the results of 144 tests of concentrically loaded interior slab-column connections reported in the literature. However, most of the test specimens were of the enforced deformation type, that is, the specimens were supported and loaded so that each radial strip would undergo the same deformation. The reaction around the support need not be uniform and the connection can not fail until all radial strips fail. In practice, slabs are generally designed for a uniformly distributed load and the share of the load on each radial strip depends on the geometry of the slab. The possibility therefore exists in a 'real life' slab that all strips may not reach their nominal capacity.

For an edge connection, where some unbalanced moment is transferred to the column, the described mechanism of shear transfer results in a contradiction between the Bond Model and the North American design codes. Consider two edge connections with identical gross concrete dimensions but different design moments resulting in different flexural reinforcement. Based on the concepts of the Bond Model, the connection with the larger moment and correspondingly greater flexural reinforcement can be designed to carry more vertical shear. This is in direct contrast with the North American design codes which consider the connection with larger moment to have smaller shear capacity.

To resolve this contradiction and to determine whether at an interior column all radial strips reach their nominal capacity, a full scale slab specimen was tested. The test slab consisted of two equal spans to provide one interior and two edge columns and was rotationally restrained along two opposite edges to simulate an interior strip in a continuous slab. The test specimen was realistically reinforced for a uniformly distributed load which was simulated using 32 equal point loads. The slab design followed North American design procedures except that the column dimensions were selected to be critical in shear by these codes but not by the Bond Model. The two edge connections had the same concrete geometry. However, one connection was reinforced for 30 percent of the panel static moment and the other one for 10 percent with appropriate modifications to the positive reinforcement in the span. Strain gauges were installed on the flexural reinforcement to permit calculation of the internal vertical shears. Deflections and crack patterns were recorded until failure and crack widths were measured at service load.

The specimen was loaded monolithically to failure. Provision was made so that as the first connection failed, the load could be increased to fail the remaining connections. Evaluation of the internal shears from the strain gauge measurements matched closely with the reaction load cell measurements, and indicated that not all radial strips were at their nominal shear capacity at the failure of the connection. Observations and data analysis of this test led to the development of the Strip Model. The test findings were supported with a series of non-linear finite element analyses.

The condition where radial strips do not transfer shear in proportion to their nominal capacities is referred to as non-proportional behavior. Such behavior occurs in a connection transferring unbalanced moments since the effect of the moment is to load one radial strip more than the others. Non-proportional behavior may also occur in concentrically loaded interior connections as a result of, for example, column or panel rectangularity. Torsional moments increase the capacity of radial strips in one direction and reduce the capacity of the radial strips in the other direction. This leads to the concept of super radial strips where the shear capacity is greater than the nominal capacity assumed by the Bond Model as the effective width of the super radial strip is greater. The Strip Model permits computing a lower bound estimate of the vertical shear capacity of an interior or edge connection based on the column dimensions and the flexural capacity of the orthogonal radial strips.

The Strip Model can be used to construct the interaction diagrams for the capacity of edge and interior connections. The failure capacity of 40 tests on edge connections and 43 tests on eccentrically loaded interior connections reported in the literature were predicted by the Strip Model and the North American codes using resistance factors of one. While both models result in a safe prediction of the capacity, the predictions by the Strip Model were closer and had considerably less scatter, making the Strip Model a more reliable predictor of the connection capacity.

9.2 Conclusion

(1) The mechanism of shear transfer used as the basis of the Strip Model is essentially correct. Internal shears calculated from strain gauge measurements were in excellent agreement with external measurements of shear using load cells. The distribution of the torsional moments assumed in the derivation of the Strip Model are consistent with those obtained with non-linear finite element analysis.

(2) In the general case (non-proportional behavior) connection failure may be initiated by the failure of one radial strip while the remaining radial strips are loaded to less than their nominal capacities. For an interior connection under concentric load, the consequence of the non-proportional behavior is that there is not a unique failure capacity. The Strip Model gives a lower bound prediction of the capacity of a concentrically loaded interior connection.

(3) The Strip Model is a reliable predictor of the strength of edge and interior column connections under combined shear and moment.

(4) The Strip Model closely predicted the capacity of the two edge connections with different amounts of flexural reinforcement reported in this investigation whereas the North American codes were unable to distinguish between the connections even though their behavior was significantly different.

(5) At an edge connection, bars perpendicular to the free edge and not passing through the column may not yield even if placed within 1.5 times the thickness of the slab from the column. The moment that may be transferred to the column from the slab by bars outside the column width is limited by the torsional capacity at the side face of the column.

References

ACI Committee 318-89: 1989. Building code requirements for reinforced concrete. American Concrete Institute, Detroit, MI.

Alexander, S.D.B., and Simmonds, S.H. 1986. Shear-Moment Transfer in Slab-Column Connections. Structural Engineering Report No. 141, Department of Civil Engineering, University of Alberta, Edmonton, Alberta.

Alexander, S.D.B., and Simmonds, S.H. 1991. Bond Model for Strength of slab-column joints. Structural Engineering Report No. 174, Department of Civil Engineering, University of Alberta, Edmonton, Canada.

Alexander, S.D.B., and Simmonds, S.H. 1992. Tests of column-flat plate connections. ACI Structural Journal, Vol. 89, No. 5, pp. 492-502.

Alexander, S.D.B., Xilin Lu, and Simmonds, S.H. 1995. Mechanism of shear transfer in a column-slab connection. Canadian Society for Civil Engineering, Ottawa, Ontario, pp. 207-216.

Alexander, S.D.B. 1996. Plastic Design of Column-Slab Connections. Invited paper, presented at ACI Annual Conference in New Orleans.

British Standards Institution, 1985. The structural use of concrete: Part 1, Code of practice for design and construction (BS 8110: Part 1). British Standards Institution, London.

Broms, C.E. 1990. Punching of flat plates - a question of concrete properties in biaxial compression and size effect. American Concrete Institute Structural Journal, Vol. 87, No. 3, pp. 292-304.

CSA Standard A23.3-94: 1994. Design of concrete structures. Canadian Standards Association, Rexdale, Ontario, Canada.

CSA Standards CAN3-A23.3-M84: 1984. Design of concrete structures for buildings. Canadian Standards Association, Rexdale, Ontario, Canada.

Clyde, D.H., and Carmichael, D. 1974. Lower bound flexural fields and slab shear. Shear in Reinforced Concrete, SP-42, American Concrete Institute, Detroit, MI, pp. 769-783.

Criswell, M.E. 1974. Static and dynamic response of reinforced concrete slab-column connections. Shear in Reinforced Concrete, SP-42, American Concrete Institute, Detroit, MI, pp. 721-746.

- Elwi, A.E. 1993. NISA90, User's Manual; Department of Civil Engineering, University of Alberta, Edmonton, Canada.
- Gesund, H. 1975. Punching strength design criteria for flat slabs. Meeting Preprint, ASCE National Structural Engineering Convention, New Orleans, 28 pp.
- Gosselin, D. 1984. The behavior of reinforced concrete slab-column structures with drop panels subjected to gravity and lateral loading. The Royal Military College, Kingston, Ontario, 1984.
- Hanson, N.M., and Hanson, J.M. 1968. Shear and moment transfer between concrete slabs and columns. Journal of the Portland Cement Association Research and Development Laboratories, Skoike, Illinois.
- Kane, K.A. 1978. Some model tests on the punching action of reinforced concrete slabs at edge columns. Honours Project, The Queen's University of Belfast.
- Kinnunen, S., and Nylander, H. 1960. Punching of concrete slabs without shear reinforcement. Transactions of the Royal Institute of Technology (Sweden), No. 153, Stockholm, pp. 1- 110.
- Lamb, J.W. 1984. Moment transfer and joint stiffness in reinforced concrete flat plate-column connections. The Royal Military College, Kingston, Ontario.
- Long, A.E. 1975. A two-phase approach to the prediction of the prediction of the punching strength of slabs. Journal of the American Concrete Institute, Proceedings, Vol. 72, No. 2, pp. 37-45.
- Massicotte, B., MacGregor, J.G., and Elwi, A.E. 1990. Behavior of concrete panels subjected to axial and lateral loads. Journal of Structural Engineering, ASCE, Vol.116, No. 9, pp. 2324-2343.
- Masterson, D. M., and Long, A.E. 1974. The punching strength of slabs, a flexural approach using finite elements. Shear in Reinforced Concrete, SP- 42, American Concrete Institute, Detroit, MI, pp. 747-768.
- Moe, J. 1961. Shearing strength of reinforced concrete slabs and footing under concentrated loads. Development Department Bulletin No. D47, Portland Cement Association, Skokie.
- Mulenga, M.N., and Simmonds, S.H. 1993. Frame methods for analysis of two-way slabs. Structural Engineering Report No. 183, Department of Civil Engineering, University of Alberta, Edmonton, Canada.

- Ramm, E. 1976. Geometrisch nichtlineare elastostatik und finite elemente. Habilitation, Bericht Nr. 76-2, Institut für Baustatik, Universität Stuttgart, Germany.
- Regan, P.E., Walker, P.R., and Zakaria, K.A.A. 1979. Tests of reinforced concrete flat slabs. CIRIA Project No. RP 220, Polytechnic of Central London.
- Regan P.E. 1984. Punching shear in reinforced concrete; a state of the art report. Polytechnic of Central London, United Kingdom.
- Regan, P.E., and Braestrup, M.W. 1985. Punching Shear in Reinforced Concrete: a State of the art report. Bulletin d'Information No. 168, Comité Euro-International du Béton, Lausanne, Switzerland.
- Scavuzzo, L. 1978. Shear reinforcement at slab-column connections in a reinforced concrete flat plate structure. The Royal Military College, Kingston, Ontario.
- Stamenkovic A. and Chapman J.C. 1974. Local strength at column heads at flat slabs subjected to a combined vertical and horizontal loading. Proceedings of Institution of Civil Engineers, Part 2 Research and Theory, London.
- Xie, J., Elwi, A.E. , and MacGregor, J.G. 1994. Numerical investigation of eccentrically loaded tied high strength concrete columns. Structural Engineering Report, University of Alberta, Edmonton, Alberta, Canada.
- Zaghlool, E.R.F. 1971. Strength and behavior of corner and edge column-slab connections in reinforced concrete flat plates. Ph.D Thesis, Department of Civil Engineering, University of Calgary, Calgary, Alberta.
- Ziyaeifar, M. 1996. Refined Transverse Shear Strains in Thick Plate-Shell Elements. PhD Thesis, Department of Civil Engineering, University of Alberta, Edmonton, Canada.

Appendix A - Pictures of the Test Specimen

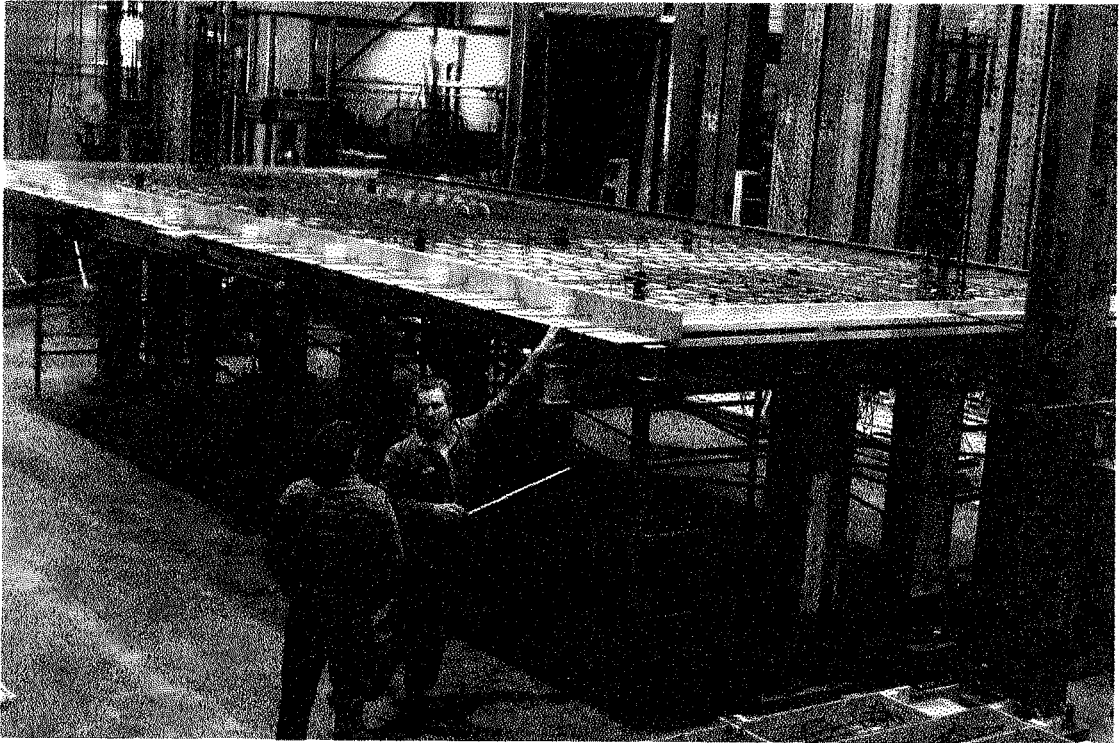


Figure A1 - Scaffolding and Form work

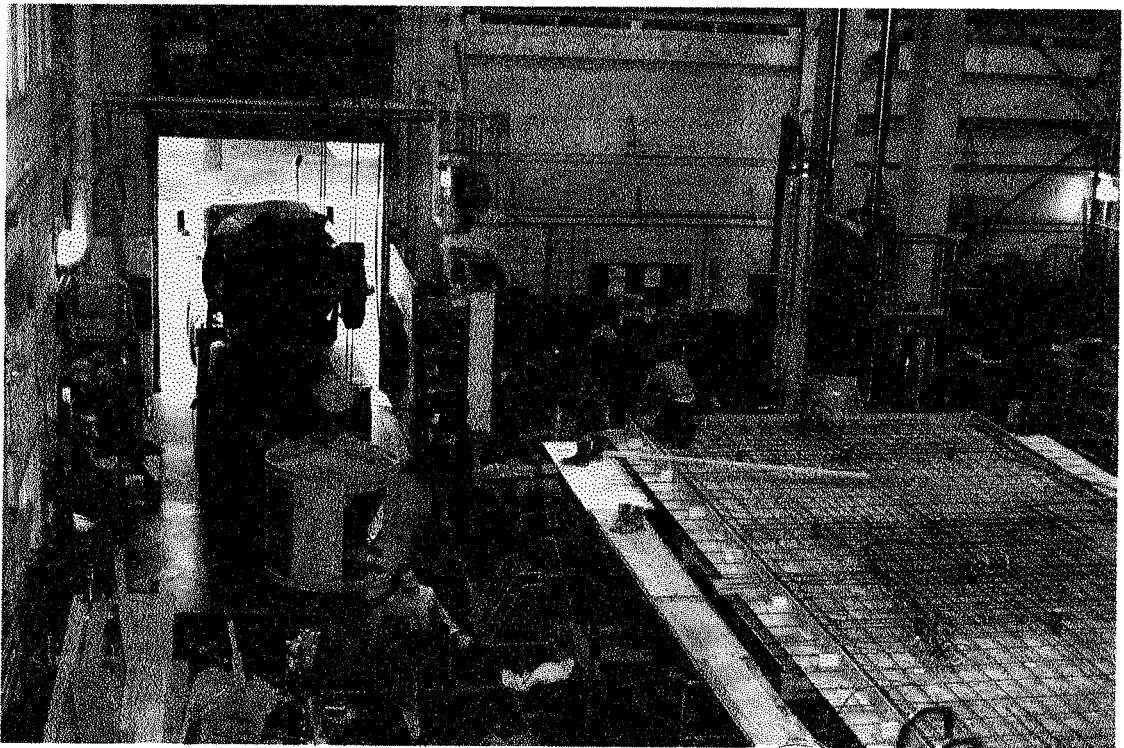


Figure A2 - Casting

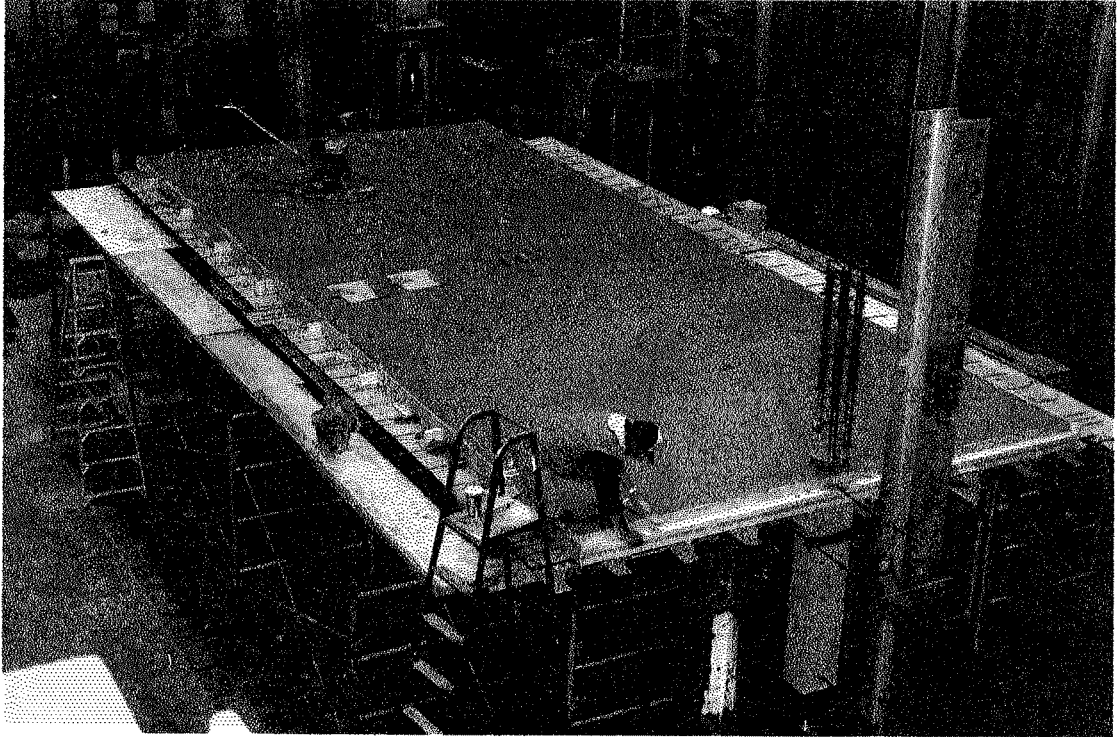


Figure A3 - Finishing the Surface

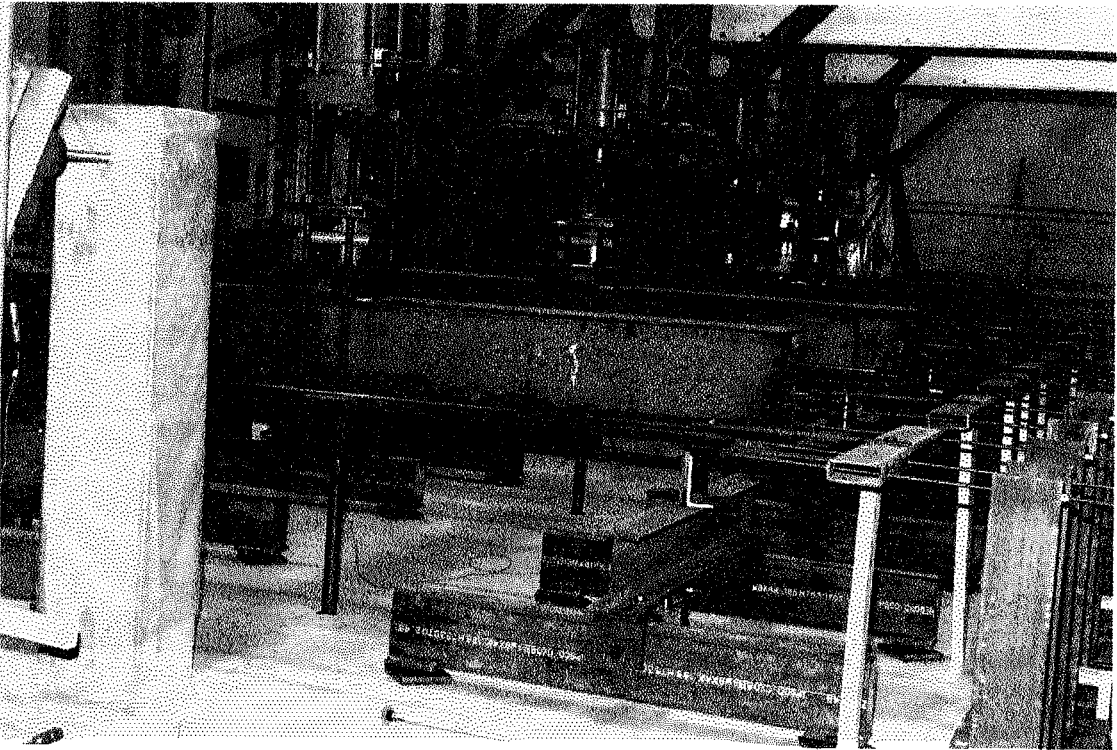


Figure A4 - Loading System

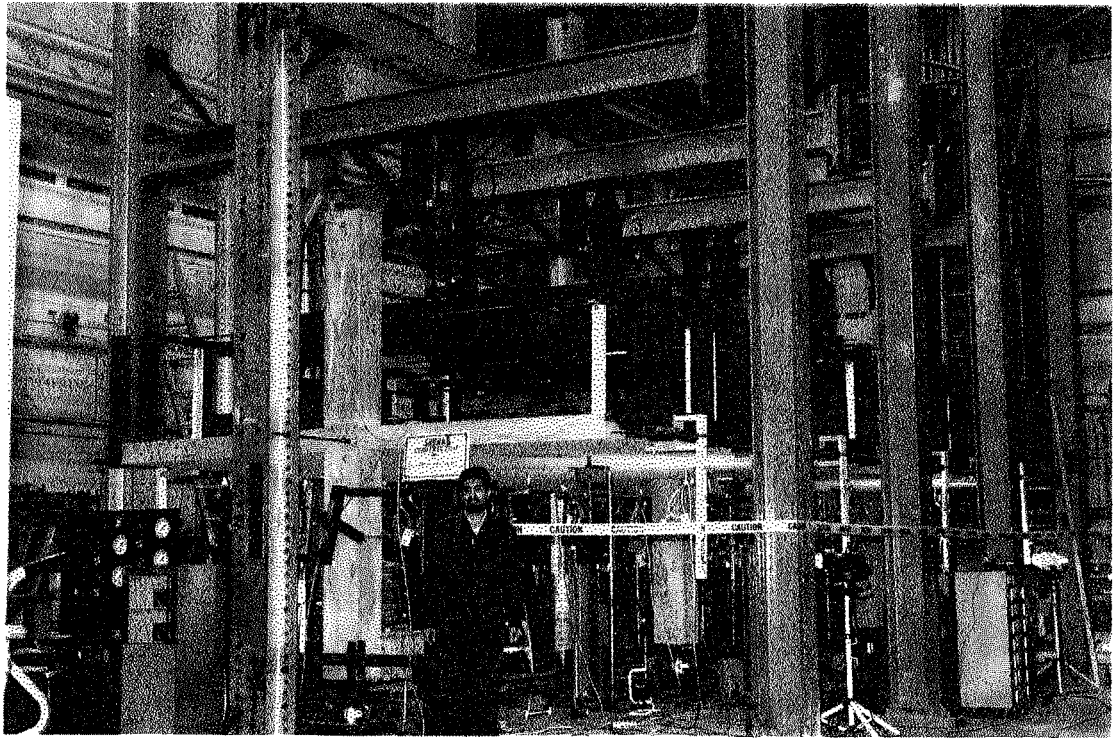


Figure A5 - Overall View

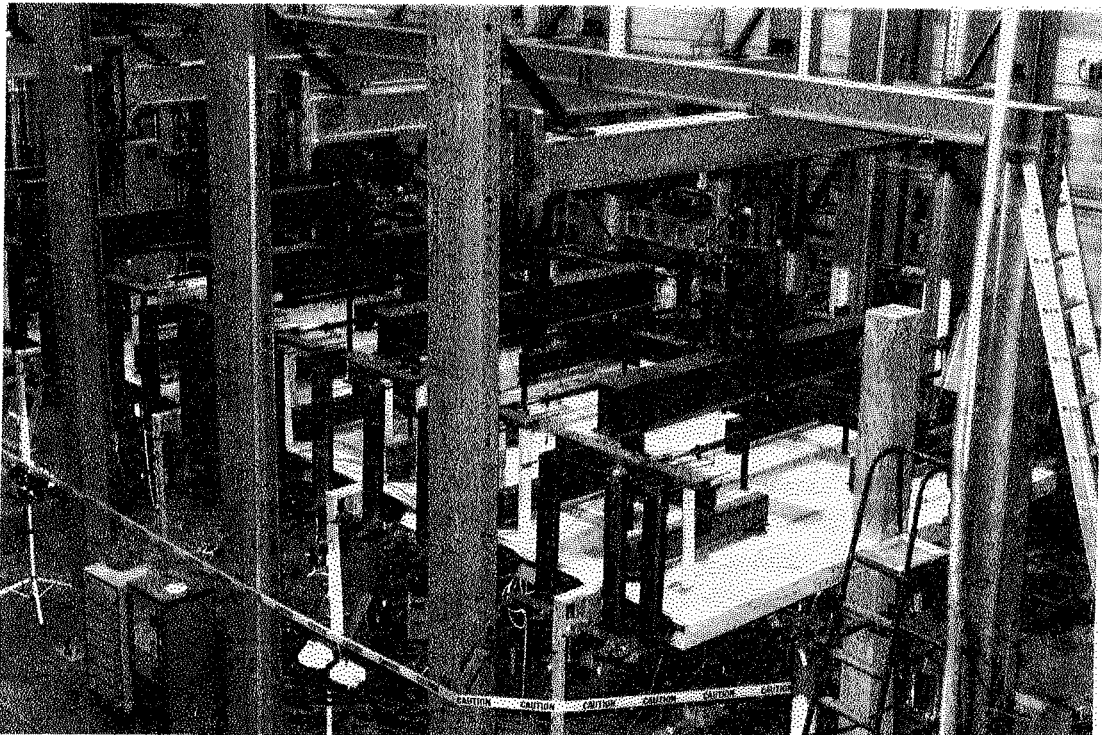


Figure A6 - Overall View

Appendix B - Force Gradient in Bars

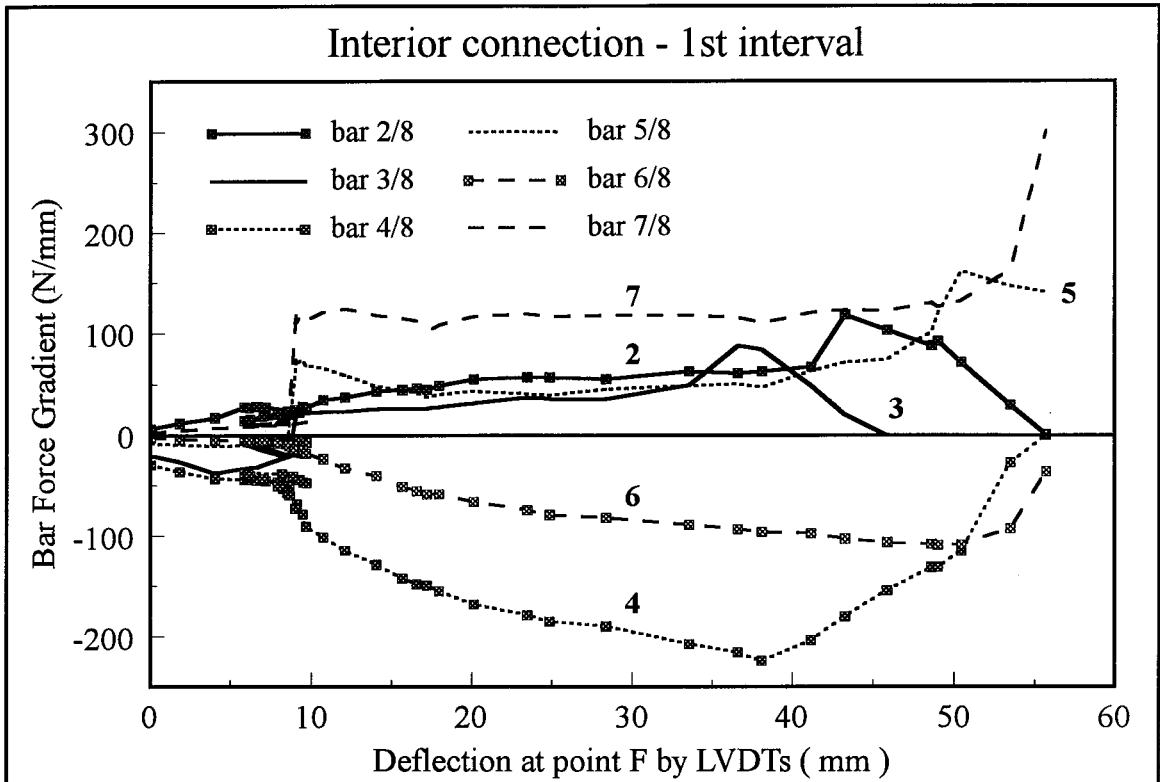


Figure B1 - Force gradient in bars running N-S, interior connection, 1st interval

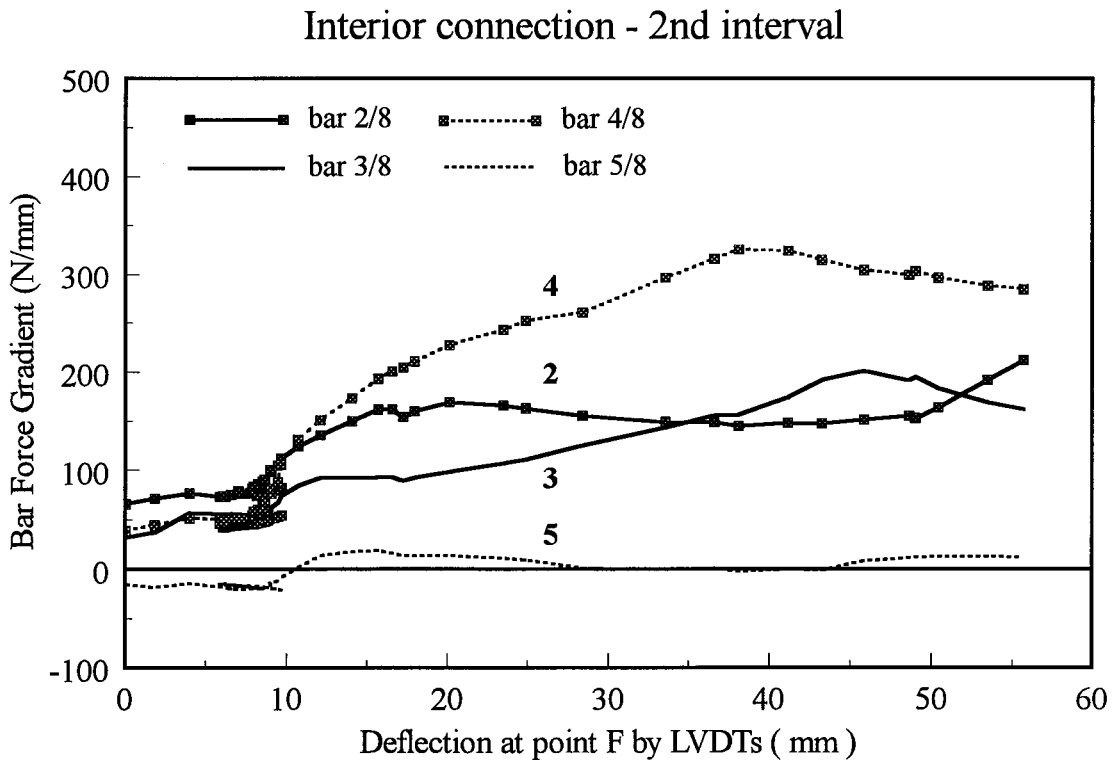


Figure B2 - Force gradient in bars running N-S, interior connection, 2nd interval

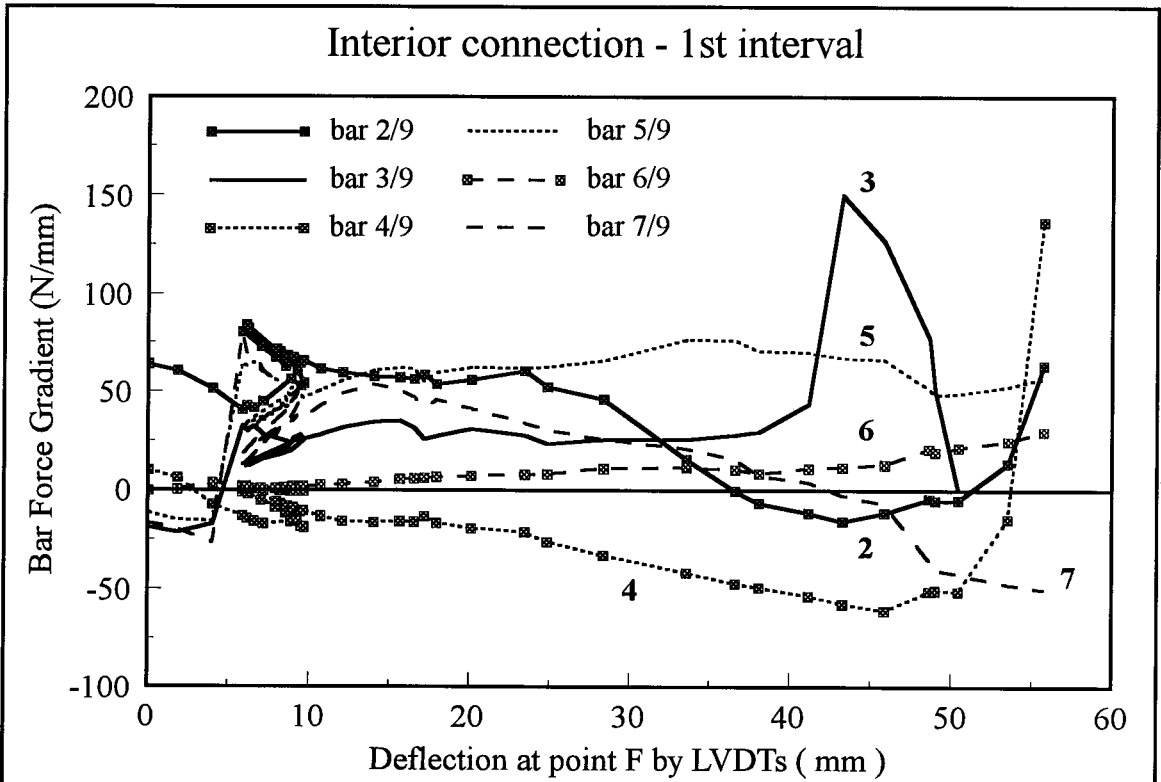


Figure B3 - Force gradient in bars running E-W, interior connection, 1st interval

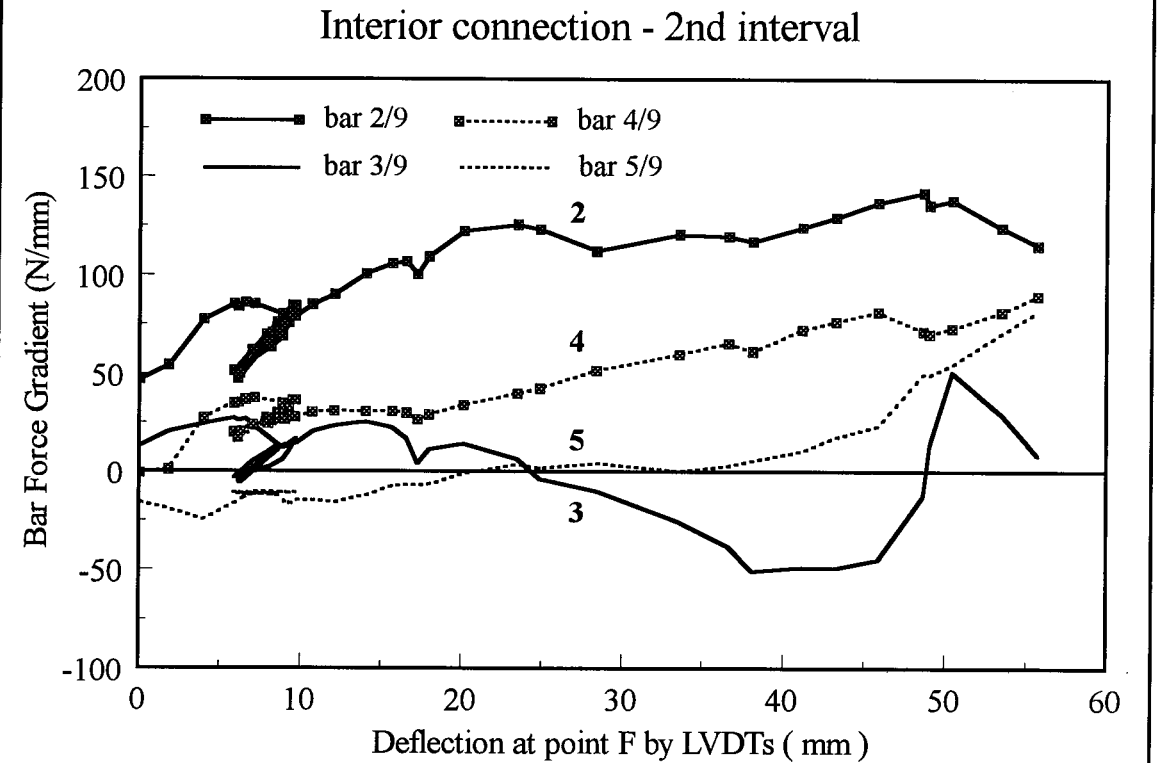


Figure B4 - Force gradient in bars running E-W, interior connection, 2nd interval

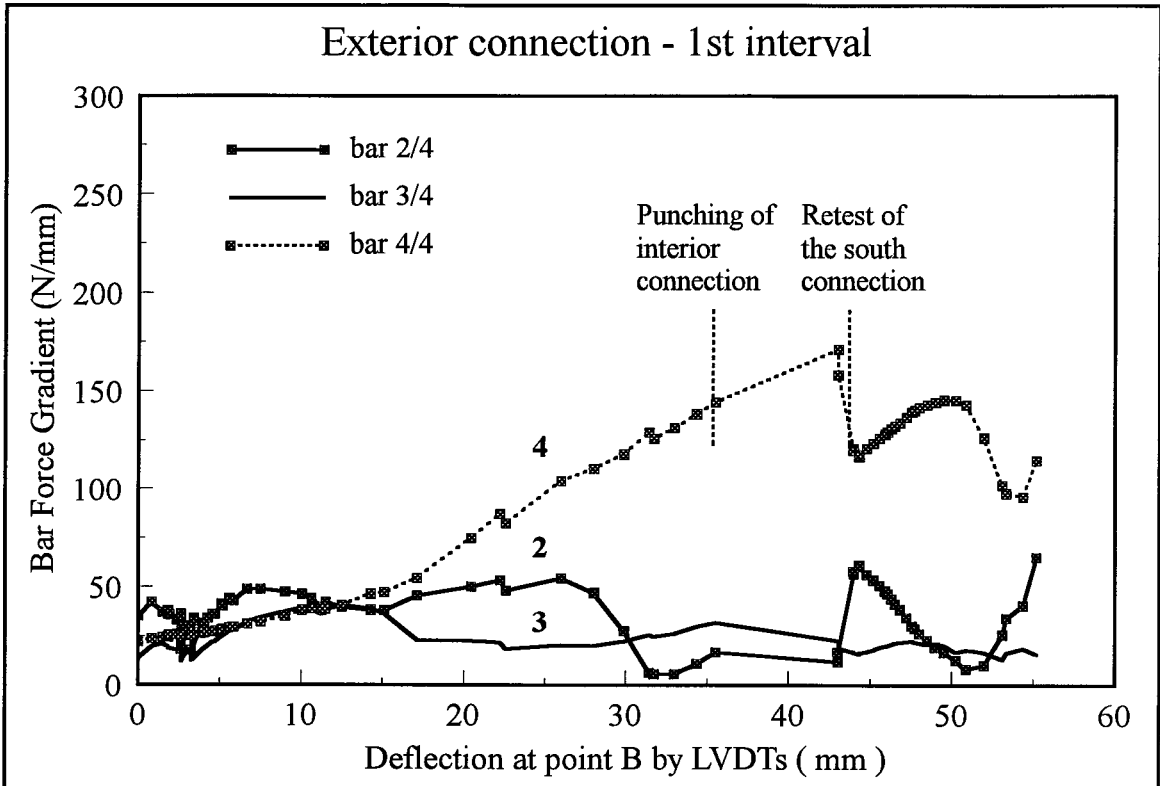


Figure B5 - Force gradient in bars running N-S, south connection, 1st interval

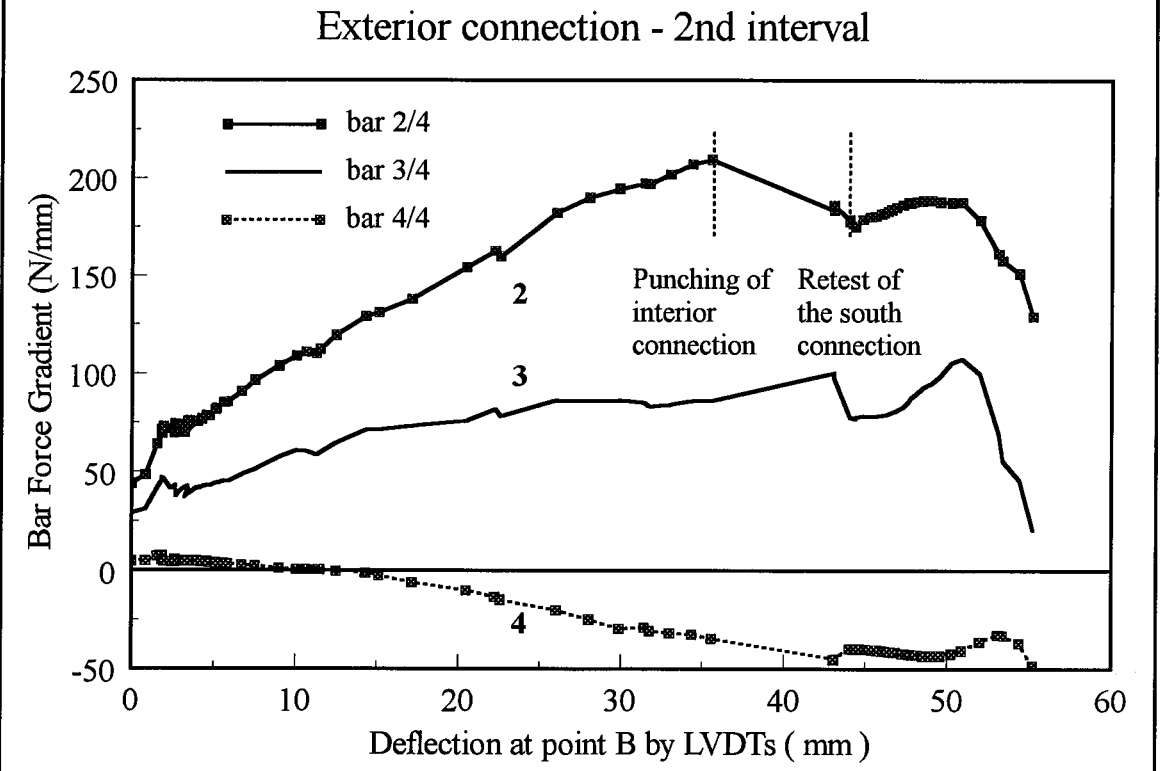


Figure B6 - Force gradient in bars running N-S, south connection, 2nd interval

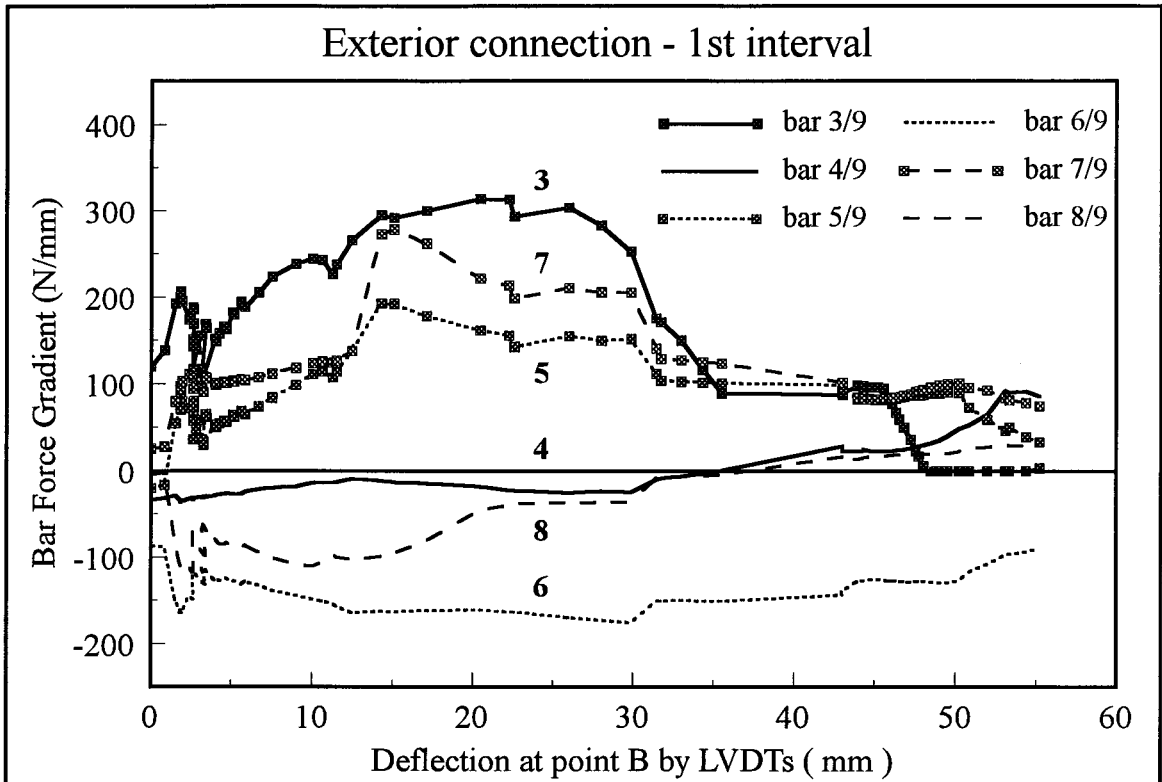


Figure B7 - Force gradient in bars running E-W, south connection, 1st interval

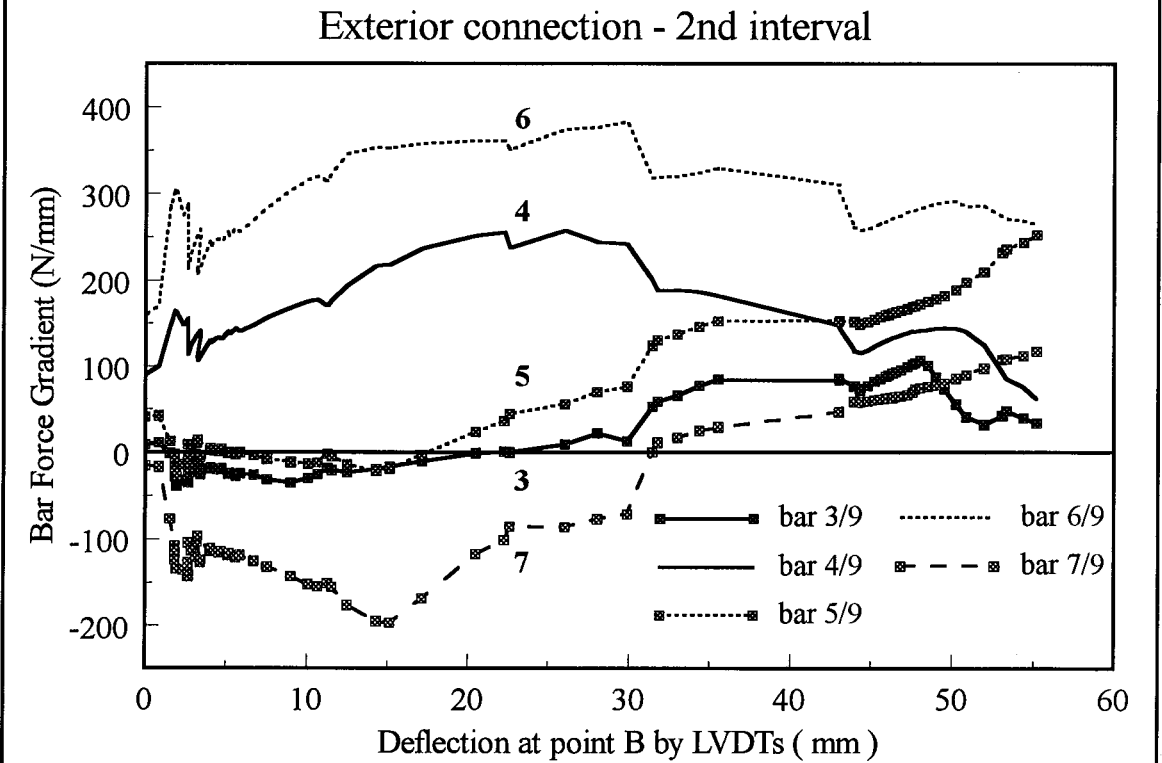


Figure B8 - Force gradient in bars running E-W, south connection, 2nd interval

Appendix C Tests in Literature - Edge Connections

Information regarding tests used in this appendix is summarized in five tables. Table C1 provides a summary of test results, geometry of the connections, and the material properties. In many tests, cube strength of concrete, f_{cu} , is measured and reported. The equivalent cylinder strength of concrete, f'_c , is assumed to be 80 percent of the cube strength.

In Table C2, the required information regarding the reinforcement of the specimens are summarized. Where bars are not uniformly spaced, the average spacing of bars is calculated based on the method suggested in Section 7.4.1 from Equation 7.34a. For uniformly spaced bars, the average spacing of bars equals the actual spacing.

Table C3 shows the calculated parameters required for constructing the moment shear interaction diagrams based on the Strip Model. The flexural capacity of the radial strips are calculated based on the average spacing of the bars reported in Table C2. Zero values for positive moments, M^+_{sx} and M^+_{sy} , indicate that either no bottom reinforcement has been provided, or no means has been provided to generate such moments.

In Table C4, analytical results required to construct the moment-shear interaction diagrams according to the Strip Model are presented, as well as the region in which the test specimen failed. The Strip Model estimates the punching capacity of the plate-column connection as the lesser of the shear capacity, P_v , and the bending capacity, P_y , of the connection. These values are also reported in Table C4, together with the test to calculated ratio and the governing mode of failure. The bending capacity reported in this table is the lesser of the flexural capacities in the two directions.

Finally, in Table C5, analytical results required to construct the interaction diagrams using the North American codes are presented, as well as the test to calculated ratios and the predicted governing mode of failure.

C1 - Stamenkovic and Chapman

Stamenkovic and Chapman (1974) conducted six tests of edge connections under a variety of loading condition. The moment to shear ratio varied from 0 to ∞ in these tests. The geometric similarity of the specimens allows some assessment of how well the Strip Model predicts the shape of the shear-moment interaction diagram. In Figure 8.1, it can be seen that how well the results lie on a circle with a radius of about 1.57 (average test to calculated ratio of these tests is reported in Table C4). The coefficient of variation of these six tests was as low as 2 percent.

In all tests, the slab was 76 mm thick and 914 mm square, attached to a single 127 mm square column. The load was applied to the column and was distributed by the slab to its boundaries. The boundary condition was not well defined. The slab was clamped by sixteen 38.1 mm rods by means of nuts. These rods were 914 mm long. It is not clear how much rotational and lateral restraint they provided. Also, the magnitude of the load in the individual rods is not known. Therefore, the flexural failure load of these tests, P_y in Table C4, can not be calculated.

These tests had the highest test to calculated ratio among those tests considered here. The supporting rods provided line supports allowing the slab to generate very high torsional moments. Also, since rods were clamped to the slab, they could generate a

limited positive moment along the edges of the specimens, which is very difficult to assess. These factors would increase the capacity of the connection.

C2 - Zaghlool

Zaghlool (1971) conducted eight tests on edge connections. Four of them were geometrically similar specimens with different moment to shear ratios [Z-V (1,4,5, and 6)]. In the remaining specimens, slab reinforcement and column size were the varying parameters. All slabs were 965 x 1830 x 152 mm with the larger size parallel to the free edge. All tests were single column tests with the load applied to the column. The boundaries were simply supported, and unlike the tests of Stamenkovic and Chapman, uplift was permitted. The average test to calculated ratio for these tests is 1.33 with a coefficient of variation of 11.6 percent.

C3 - Kane, Hanson and Hanson

Kane (1978) conducted four tests and Hanson and Hanson (1968) conducted one test on edge connections. These tests were single column tests with loads applied directly to the plate at a certain eccentricity to the center line of the column. Edges of the plate were all free.

Kane's slabs were approximately 700 x 400 x 50 mm with the larger side parallel to the spandrel strip. Forty percent of the load was directly applied on the center line of the spandrel strip and the remaining was applied at a fix distance from column center line. The principal variable was the distribution of the reinforcement. The shear capacity of the connections are close to the bending capacity of the specimens, and in all tests, the applied loads exceeded both of these calculated values. The average test to calculated value is 1.31 with a coefficient of variation of 1.8 percent.

Hansons' slab was 1220 x 1140 x 76 mm. A single line load was applied to the specimen by means of a steel beam bearing on the slab. The effect of the stiffness of the steel section is not clear.

C4 - Current Study

Two edge connections with the same geometry and the same material properties has been tested and documented in this study. The design moment, and therefore the detail of the reinforcement, were different for the two connections. Details of the specimen has been completely described in chapter 3.

In Table C4, P_y is the shear associated with the yield line mechanism. The value of P_y for each connection has been calculated in Section 3.3.7.1, and is presented in Table 3.6 as well. It can be seen that the specimen has punched before a complete yield line mechanism. In such cases, as described in Section 7.4.3, the positive moment in the radial strips is less than the yield moment. To estimate the value of these moments, an iterative procedure is required. However, the magnitude of these moments at failure has been measured. The values presented in Table C3 for M_{sy}^+ and M_{sx}^+ are the measured values at failure, and therefore there is no need for such iteration.

C5 - Scavuzzo / Gosselin / Lamb

Scavuzzo (1978), Gosselin (1984), and Lamb (1984) each tested four specimen with essentially identical loading and support condition. Each specimen consisted of one edge connection and one interior connection. The edges representing the mid span of the prototype were rotationally restrained by means of HSS profiles clamped to the slab, and compression struts connecting the corresponding HSS profiles. Specimens were subjected to cycles of both gravity and lateral loads prior to being failed under gravity load only. The gravity load was modeled by uniformly distributed load points applied to the slab. All slabs were 63 mm thick, however, Gosselin's specimen had drop panels.

The main objective of these three investigations was to examine the frame behavior of a slab-column system. Ultimate capacities were of secondary importance. As a result, the actual failure loads of some specimens were not recorded. For these cases (Gosselin and Lamb tests), the last reported shear and moment values are presented in Table C1 as P_{test} and M_{test}^- . The shear due to dead load is assumed to be 3.5 kN, and is accounted for, in the P_{test} .

In this table, the value of the maximum positive moment, M_{test}^+ , is also reported for these tests. This value is calculated based on equations of equilibrium, knowing the shear, the moment at the center line of the column, and the applied loads. The value of M_{test}^+ , if smaller than the positive yield moment, is used to calculate the positive moment in the radial strip at failure, M_{sx}^+ . The positive moment in the spandrel strip, M_{sy}^+ , is estimated in a similar way. Values of M_{sx}^+ and M_{sy}^+ are presented in Table C3.

C5.1 Scavuzzo; Three of the tests by Scavuzzo had some type of shear reinforcement. Only test S-1 which was described as having a punching failure is studied in this research.

C5.2 Gosselin; Two of the specimens of Gosselin failed by punching at the interior column. Since there was no indication that edge connections were near ultimate, these two tests have been excluded from this investigation.

Specimen G-1 had a punching failure at the edge column, accompanied by considerable cracking of concrete and yielding of steel. Specimen G-2 was described as having a rotational failure.

Specimens G-1 and G-2 had respectively 16 mm and 33 mm thick drop panels. The size of drop panels in both tests was 600 x 600 mm. The loaded length of the radial strips, as bond model predicts, is smaller than the dimensions of the drop panels. Therefore, the overall thickness of slab and drop panel is used to determine w_x and w_y . Negative flexural capacities of the radial strips are also calculated based on the overall thickness of the slab and drop panel. However, when determining the positive flexural capacities of the radial strips, the thickness of the slab has been used.

Torsion along side faces of the column, M_{tc} is estimated ignoring the thickness of the drop panel mainly because of the level of the bottom bars. Torsional moment along side faces of the interior radial strip, M_{tx} , is estimated by the negative flexural capacity of the adjacent radial strip. The width of this strip (1.5 h) and its flexural depth are calculated based on the overall thickness including the thickness of the drop panel.

C5.3 Lamb ; Two of the Lamb's tests had edge beams and are excluded from this study. Specimens L-1 and L-2 had the same extremely light reinforcement lay out. Specimen L-1 was described as having a punching failure at the edge column, proceeding extensive cracking in the slab. Specimen L-2 failed by punching at the interior column but the condition at the edge connection was near failure.

C6 - Regan, Walker, and Zakaria

Regan et al. (1979) conducted an extensive test program which included interior, edge, and corner connections plus wall supported slabs. Fourteen tests on edge connections are considered here. Specimens SE3 and SE18 are excluded from this study due to the presence of shear reinforcement. Specimens SE16 and SE17 are excluded from this study due to non-orthogonal reinforcement. All tests were double column tests with load applying on the slab. A unique feature of tests SE1 through SE11 was the absence of any bottom reinforcement parallel to the free edge. All edges of the specimens were free to rotate, and no edge restraining system was provided. Therefore, M_y^+ , in all tests is equal to zero.

At failure, knowing the values of column reaction, applied point load, and the negative moment at column center, positive moment at the mid span, M_{test}^+ , is calculated using equations of equilibrium. The positive moment at the interior radial strips, M_{sx}^+ , is calculated based on the smaller value of the positive yield moment and the M_{test}^+ .

The yield stress or 0.2 percent proof stress of the reinforcement used was a variable of bar size; 480 MPa for 8 and 12 mm bars, 500 MPa for 10 mm bars, 595 MPa for 6 mm hot-rolled bars, and 800 MPa for 6 mm cold-worked steel.

The average test to calculated value for Regan's tests is 1.27 with a coefficient of variation of 10.4 percent. The specimens were grouped in three series;

C6.1 Series SE1 through SE8; Specimens SE1 through SE8 were all 125 mm thick, 1.3 m wide, and 3.05 m long, with 8 loading points. The variables in this group were column dimensions and the amount and detailing of the slab reinforcement.

C6.2 Series SE9 through SE11; The slab thickness of 125 mm was retained for these specimens but the plan dimensions were increased to 2.08 & 3.91 m. The number of load points was increased from 8 to 10 loading points. Details of reinforcement were also the same for SE9 through SE11. The only parameter varied was the degree of restraint provided at the plate-column connection.

C6.3 Series SE12 through SE15; All tests in this group were 80 mm thick, with four point loads. The width and the clear span of all specimens were respectively 1.22 m and 1.83 m. In slab SE 14, like slabs SE1 through SE 11, the slab edges were flushed with the outer face of the column.

In test SE15, the slab edge was at the inner face of the column. The absence of spandrel strips in this test, makes it an interesting case since it directly examines the mechanics of shear transfer in an interior radial strip.

Slabs SE12 and SE13 had respectively 370 and 160 mm overhangs beyond the outer face of the columns. Since no Jack load is applied to the overhangs, these tests have been treated like tests on edge connections with two spandrel strips and one interior radial strip.

**Table C1 Summary of Test Results, Geometry, and Material Properties of
Edge Connections Reported in the Literature**

Mark	h	c _x	c _y	f _{cu}	f' _c	f _y	P _{test}	M _{test}	M ⁺ _{test}	e
	mm	mm	mm	MPa	MPa	MPa	kN	kNm	kNm	mm
Stamenkovic and Chapman										
V/E/1	76	127	127	35.8	28.6	495	74.7	0	0	0
C/E/1	76	127	127	38.4	30.7	448	73.1	5.59	0	76.47
C/E/2	76	127	127	32.4	25.9	495	54.7	9.17	0	167.6
C/E/3	76	127	127	34	27.2	495	24.9	10.05	0	403.6
C/E/4	76	127	127	34.3	27.4	495	10.9	8.83	0	810.1
M/E/2	76	127	127	33.1	26.5	495	0	8.35	0	INF
Kane / Hanson & Hanson										
K1	51	68	100	38.5	30.8	480	24	2.38	0	99.17
K2	48	75	114	45	36	480	20.9	2.07	0	99.04
K3	48	75	114	51	40.8	480	25.1	2.48	0	98.8
K4	48	75	114	35.3	28.24	480	18.2	1.8	0	98.9
D-15	76.2	152	152		31.06	365.1	12.03	10.51	0	873.4
Afhami										
North	152	305	254		34.8	420	176.1	51.1	134	290.2
South	152	305	254		34.8	420	222	88	138	396
Scavuzo / Gosselin / lamb										
S-1	63	102	152		38.09	379	35.6	4.66	6.46	130.8
G-1	63	150	225		38.09	375	41.5	7.23	5.03	174.2
G-2	63	150	225		39	375	47.1	11.16	3.65	236.9
L-1	63	150	225		34.7	395	31.1	3.49	7.39	112.2
L-2	63	150	225		43.8	395	34.2	5.12	6.41	149.7
Zaghlool										
Z-IV(1)	152	178	178		27.31	475.3	122.1	44.96	0	368.2
Z-V(1)	152	267	267		34.3	473.2	214.9	84.5	0	393.2
Z-V(2)	152	267	267		40.43	473.2	246.4	93.44	0	379.2
Z-V(3)	152	267	267		38.71	474.6	267.7	103.5	0	386.4
Z-V(4)	152	267	267		34.78	436.7	0	81.25	0	INF
Z-V(5)	152	267	267		35.13	475.3	278.8	0	0	0
Z-V(6)	152	267	267		31.27	476	116.8	88.02	0	753.8
Z-VI(1)	152	356	356		25.97	475.3	264.6	106.7	0	403.3

Table C1 Continued										
Mark	h	c _x	c _y	f _{cu}	f' _c	f _y	P _{test}	M _{test} ⁻	M _{test} ⁺	e
	mm	mm	mm	MPa	MPa	MPa	kN	kNm	kNm	mm
Regan, Walker, Zakaria (1979)										
SE1	125	200	300	44.6	35.68	480	198	39.5	51.58	199.5
SE2	125	200	300	54.6	43.68	480	192	34	54.32	177.1
SE4	125	300	200	34.3	27.44	480	152	30.5	47.02	200.7
SE5	125	300	200	55.2	44.16	480	164	38.5	45.14	234.8
SE6	125	300	200	40	32	500	149	27.5	48.49	184.6
SE7	125	300	200	49.5	39.6	500	129	31.7	34.09	245.8
SE8	125	100	300	52	41.6	480	136	33.7	28.86	247.8
SE9	125	250	250	51.8	41.44	480	123	35.7	54.34	290.2
SE10	125	250	250	50.9	40.72	480	114	36	47.45	315.8
SE11	125	250	250	62.5	50	480	138	39.5	61.52	286.2
SE12	80	160	160	63.1	50.48	480	69	17.9	13.63	259.4
SE13	80	160	160	51.8	41.44	480	60	14.7	12.72	245
SE14	80	160	160	55.6	44.48	480	46	12.2	8.82	265.2
SE15	80	160	160	53.2	42.56	480	48	7.4	14.54	154.2

Table C2 Information Regarding Reinforcement of Tests on the Edge Connection

Mark	Bars normal to the free edge						Bars parallel to the free edge					
	Top			Bottom			Top			Bottom		
	ϕ	s_{avg}	d	ϕ	s_{avg}	d	ϕ	s_{avg}	d	ϕ	s_{avg}	d
Stamenkovic and Chapman												
V/E/1	7.94	76	60	7.94	76	60	7.94	76	52	7.94	76	52
C/E/1	7.94	76	60	7.94	76	60	7.94	76	52	7.94	76	52
C/E/2	7.94	76	60	7.94	76	60	7.94	76	52	7.94	76	52
C/E/3	7.94	76	60	7.94	76	60	7.94	76	52	7.94	76	52
C/E/4	7.94	76	60	7.94	76	60	7.94	76	52	7.94	76	52
M/E/2	7.94	76	60	7.94	76	60	7.94	76	52	7.94	76	52
Kane / Hanson & Hanson												
K1	6	67	44	6	67	44	6	60	38	6	60	38
K2	6	92	41	6	92	41	6	85	35	6	85	35
K3	6	67	41	6	67	41	6	62	35	6	62	35
K4	6	131	41	6	131	41	6	109	35	6	109	35
D-15	9.53	76	62.15	9.53	76	62.15	9.53	76	52.2	9.53	76	52.2
Afhami												
North	11.3	102	126	See Figure 3.9			16	175	110	See Figure 3.9		
South	16	102	124	See Figure 3.10			16	175	108	See Figure 3.10		
Scavuzo / Gosselin / lamb												
S-1	5.74	66	52.5	5.74	66	52.5	5.74	63.5	46.5	5.74	125	46.5
G-1	5.74	100	68	5.74	125	52	5.74	75	62	5.74	100	46
G-2	5.74	100	84	5.74	125	52	5.74	75	78	5.74	100	46
L-1	5.74	125	52	5.74	125	52	5.74	100	46	5.74	165	46
L-2	5.74	125	52	5.74	125	52	5.74	100	46	5.74	165	46
Zaghlool												
Z-IV(1)	12.7	76.2	127	12.7	76.2	127	12.7	58.2	114	12.7	58.2	114
Z-V(1)	12.7	63.5	127	12.7	63.5	127	12.7	69.9	114	12.7	69.9	114
Z-V(2)	12.7	59.2	127	12.7	59.2	127	12.7	58.4	114	12.7	58.4	114
Z-V(3)	12.7	59.2	127	12.7	59.2	127	12.7	59.2	114	12.7	59.2	114
Z-V(4)	12.7	59.2	127	12.7	59.2	127	12.7	69.9	114	12.7	69.9	114
Z-V(5)	12.7	63.5	127	12.7	63.5	127	12.7	69.9	114	12.7	69.9	114
Z-V(6)	12.7	63.5	127	12.7	63.5	127	12.7	69.9	114	12.7	69.9	114
Z-VI(1)	12.7	87.6	127	12.7	87.6	127	12.7	82.6	114	12.7	82.6	114

Table C2 Continued												
Mark	Bars normal to the free edge						Bars parallel to the free edge					
	Top			Bottom			Top			Bottom		
	ϕ	s_{avg}	d	ϕ	s_{avg}	d	ϕ	s_{avg}	d	ϕ	s_{avg}	d
Regan, Walker, Zakaria (1979)												
SE1	12	100	104	12	90	104	12	125	92	0	0	0
SE2	8	200	105	12	90	105	12	125	95	0	0	0
SE4	12	100	104	12	175	104	12	125	92	0	0	0
SE5	12	120	104	12	210	104	12	125	92	0	0	0
SE6	10	150	104	12	140	104	12	125	93	0	0	0
SE7	10	100	104	10	250	104	12	125	93	0	0	0
SE8	12	120	104	12	210	104	12	125	92	0	0	0
SE9	12	200	104	12	290	104	12	125	92	0	0	0
SE10	12	200	104	12	290	104	12	125	92	0	0	0
SE11	12	200	104	12	290	104	12	125	92	0	0	0
SE12	8	75	66	8	140	66	8	100	58	0	0	0
SE13	8	75	66	8	140	66	8	100	58	0	0	0
SE14	8	75	66	8	140	66	8	100	58	0	0	0
SE15	8	75	66	8	140	66	8	100	58	0	0	0

Table C3 Parameters Required for Constructing Interaction Diagram of the Edge Connections Reported in Literature

Mark	w_x	w_y	M_{sx}^-	M_{sy}^-	M_{sx}^+	M_{sy}^+	M_{tc}	M_{tx}
	kN/m	kN/m	kNm	kNm	kNm	kNm	kNm	kNm
Stamenkovic and Chapman								
V/E/1	46.2	53.3	2.19	1.86	0	0	1.64	1.64
C/E/1	47.84	55.2	2.02	1.72	0	0	1.66	1.66
C/E/2	43.95	50.71	2.16	1.83	0	0	1.52	1.52
C/E/3	45.02	51.95	2.17	1.84	0	0	1.59	1.59
C/E/4	45.22	52.17	2.17	1.85	0	0	1.61	1.61
M/E/2	44.42	51.25	2.16	1.84	0	0	1.55	1.55
Kane / Hanson & Hanson								
K1	35.01	40.54	0.55	0.76	0	0	0.49	0.49
K2	34.86	40.84	0.43	0.59	0	0	0.52	0.41
K3	37.11	43.47	0.58	0.79	0	0	0.53	0.53
K4	30.88	36.17	0.3	0.46	0	0	0.51	0.29
D-15	48.25	57.5	2.9	2.38	0	0	1.91	1.91
Afhami								
North	107.72	123.39	15.01	12.5	9.57	5.92	7.5	7.5
South	105.76	121.43	27.86	12.2	9.86	6.34	12.74	12.74
Scavuzo / Gosselin / lamb								
S-1	47.67	53.82	0.76	1.04	0.45	0.39	1.25	0.7
G-1	63.52	69.67	0.97	1.75	0.4	0.44	1.9	0.76
G-2	80.86	87.08	1.2	2.21	0.29	0.44	1.9	1.14
L-1	44.98	50.85	0.62	1.02	0.59	0.63	1.82	0.39
L-2	50.54	57.13	0.62	1.03	0.51	0.63	1.91	0.39
Zaghlool								
Z-V(1)	99.16	110.17	15.44	16.93	0	0	8	8
Z-V(1)	111.13	123.47	27.89	22.78	0	0	12.5	12.5
Z-V(2)	120.65	134.05	30.31	27.18	0	0	12.63	12.63
Z-V(3)	118.05	131.17	30.21	26.77	0	0	12.6	12.6
Z-V(4)	111.9	124.34	27.71	21.3	0	0	12.51	12.51
Z-V(5)	112.46	124.95	28.09	22.95	0	0	12.52	12.52
Z-V(6)	106.1	117.89	27.63	22.57	0	0	12.41	12.41
Z-VI(1)	96.69	107.43	27.21	25.35	0	0	15.21	15.21

Table C3 Continued								
Mark	w_x	w_y	M_{sx}^-	M_{sy}^-	M_{sx}^+	M_{sy}^+	M_{tc}	M_{tx}
	kN/m	kN/m	kNm	kNm	kNm	kNm	kNm	kNm
Regan								
SE1	91.22	103.12	10.32	11.05	7.64	0	9.73	9.67
SE2	104.23	115.2	2.49	11.61	8.05	0	7.47	2.34
SE4	80	90.43	15.04	7.18	5.37	0	6.23	6.23
SE5	101.49	114.72	13.29	7.48	7.79	0	6.57	6.57
SE6	87.33	97.66	7.79	7.38	10.39	0	6.39	4.87
SE7	97.15	108.64	11.56	7.51	4.79	0	6.49	6.49
SE8	98.5	111.35	4.41	11.18	1.96	0	9.83	8.28
SE9	98.31	111.14	6.79	9.32	4.74	0	8.19	5.09
SE10	97.45	110.17	6.79	9.3	4.74	0	8.18	5.09
SE11	107.99	122.07	6.84	9.43	4.76	0	8.27	5.13
SE12	68.41	77.84	3.2	2.13	1.76	0	2.22	2.22
SE13	61.98	70.53	3.16	2.11	1.75	0	2.19	2.19
SE14	64.21	73.07	3.18	2.11	1.26	0	2.2	2.2
SE15	62.81	0	3.17	0	1.75	0	0	0

Table C4 Analytical Results (Points on Interaction Diagram, Failure Load, and Test to Calculated Ratio) for Edge Connection

Tests - Strip Model

Mark	P ₁	P ₂	P _{3a}	P _{3b}	M ₄	e _{test}	e ₂	e _{3a}	e _{3b}	Region	P _v	P _y	P _{test}	Test / Cal.	Failure Mode
	kN	kN	kN	kN	kNm	mm	mm	mm	mm		kN	kN	kN		
Stamenkovic and Chapman															
V/E/1	46.57	48.24	31.81	31.81	5.47	0	71.7	235.6	235.6	1	46.57		74.7	1.6	P
C/E/1	45.98	47.2	31.95	31.95	5.33	76.5	69.1	230.4	230.4	23	46.2		73.1	1.58	P
C/E/2	44.96	46.71	30.21	30.21	5.19	167.6	72.6	235.4	235.4	23	35.42		54.7	1.54	P
C/E/3	45.74	47.45	31.06	31.06	5.36	403.6	72.2	236	236	34	15.75		24.9	1.58	P
C/E/4	45.88	47.58	31.22	31.22	5.39	810.1	72.1	236.1	236.1	34	7.22		10.9	1.51	P
M/E/2					5.26	INF				4	M _{test} = 8.35		0	1.59	
Kane / Hanson & Hanson															
K1	24.98	24.51	14.69	14.69	1.54	99.2	40.5	154.9	154.9	23	18.26	21.9	24	1.31	P & B
K2	22.69	21.59	13.18	13.18	1.47	99	40.1	168.6	168.6	23	16.7	15.7	20.9	1.33	B & P
K3	26.77	25.89	15.56	15.56	1.63	98.8	42.7	161.8	161.8	23	19.72	21.9	25.1	1.27	P & B
K4	19.02	17.64	10.43	10.43	1.33	98.9	36.8	184.1	184.1	23	13.66	15.7	18.2	1.33	P & B
D-15	55.57	56.76	36.04	36.04	6.73	873.4	82.9	263	263	34	8.44		12.03	1.43	P
Afhami															
North	212.2	237.7	185.31	130.59	30	290.2	118.2	251.4	356.8	3	160.6	197	176	1.1	P
South	210	260.6	217.22	163.5	52.3	396.4	168.4	341.1	453.2	3	186.9	206.5	222	1.19	P & B

Table C4 Continued

Mark	P ₁	P ₂	P _{3a}	P _{3b}	M ₄	e _{test}	e ₂	e _{3a}	e _{3b}	Region	P _v	P _y	P _{test}	Test / Cal.	Failure Mode
	kN	kN	kN	kN	kNm	mm	mm	mm	mm		kN	kN	kN		
Scavuzo / Gosselin / Lamb															
S-1	38.03	39.95	28.59	22.34	3.26	130.8	47.9	173.7	222.3	23	31.66	37.6	35.59	1.12	P
G-1	57.26	53.56	33.38	27.14	4.76	174.2	57.3	234	287.8	23	38.26	39.26	41.5	1.09	P & B
G-2	71.29	64.97	40.49	34.94	5	236.9	56.5	220.5	255.5	3	37.68	42.15	47.1	1.25	P & B
L-1	40.53	40.63	27.96	18.94	4.26	112.2	56.2	228.6	337.5	23	35.41	26.97	31.1	1.15	B
L-2	43.58	42.66	29.02	19.72	4.45	149.7	54.6	229.7	338.2	23	33.99	27.11	34.2	1.26	B & P
Zaghloul															
Z-IV(1)	192.32	200.41	111.67	111.67	31.4	368.2	111.8	370.5	370.5	23	112.1		122.1	1.09	P
Z-V(1)	245.08	261.35	153.32	153.32	52.9	393.2	163.5	478.3	478.3	23	172.6		214.9	1.25	P
Z-V(2)	277.21	291.69	163.77	163.77	55.6	379.2	159.2	472.7	472.7	23	188.42		246.42	1.31	P
Z-V(3)	272.02	287.05	161.75	161.75	55.4	386.4	160.7	475.9	475.9	23	184.63		267.73	1.45	P
Z-V(4)	239.03	256.94	153.63	153.63	52.7	INF	165.6	476.6	476.6	4	M _{test} = 81.25		0	1.54	P
Z-V(5)	247.51	263.86	154.59	154.59	53.1	0	163.3	477	477	1	247.51		278.83	1.13	P
Z-V(6)	237.75	254.17	149.2	149.2	52.5	753.8	165.5	484.9	484.9	34	84.54		116.77	1.38	P
Z-VI(1)	246.94	250.19	149.3	149.3	57.6	403.3	181.7	563.8	563.8	23	179.76		264.62	1.47	P

Table C4 Continued

Mark	P ₁	P ₂	P _{3a}	P _{3b}	M ₄	e _{test}	e ₂	e _{3a}	e _{3b}	Region	P _v	P _y	P _{test}	Test / Cal.	Failure Mode
	kN	kN	kN	kN	kNm	mm	mm	mm	mm		kN	kN	kN		
Regan															
SE1	155.64	176.42	116.66	116.66	29.77	199.5	127.3	405.2	405.2	23	155.7	292.68	198	1.27	P
SE2	169.32	169.73	79.64	79.64	17.43	177.1	73.3	368.9	368.9	23	121.47	277.81	192	1.58	P
SE4	129.05	152.88	102.55	102.55	27.49	200.7	151.2	368.1	368.1	23	137.49	238.32	152	1.11	P
SE5	151.63	175.4	117.89	117.89	26.44	234.8	128.5	324.3	324.3	23	138.68	138.14	164	1.19	B & P
SE6	136.69	155.62	98.74	98.74	20.58	184.6	101.2	308.4	308.4	23	126.34	160.6	149	1.18	P
SE7	146.88	160.52	106.76	106.76	24.54	245.7	121.7	329.9	329.8	23	123.47	90.28	129	1.43	B & P
SE8	152.27	149.92	95.04	95.04	24.07	247.8	79.6	403.2	403.2	23	115.32	178.75	136	1.18	P
SE9	156.48	158.35	92.42	92.42	23.17	290.2	96.1	375.7	375.6	23	105.89	99.28	123	1.24	B & P
SE10	155.6	157.58	91.99	91.99	23.14	315.8	96.3	376.6	376.6	23	101.12	105.32	114	1.13	P & B
SE11	166.23	166.75	97.16	97.16	23.38	286.2	94.1	365.7	365.7	23	110.67	98.88	138	1.4	B & P
SE12	63.95	73.28	50.73	50.73	9.41	259.4	84	265.4	265.4	23	51.25	62.64	69	1.35	P & B
SE13	60.03	69.37	48.02	48.02	7.55	245	85.8	237.2	237.2	34	45.75	58.02	60	1.31	P & B
SE14	61.42	68.92	47.66	47.66	7.59	265.2	85.3	239.1	239.1	34	40.95	64.29	46	1.12	P
SE15	without spandrel strip				3.17	154.2			90.1	34	35.16	40.65	48	1.37	P & B

Table C5 Analytical Results (Points on Interaction Diagram, Failure Load, and Test to Calculated Ratio) for Edge

Connection Tests - North American Standards

Mark	P _a	P _b	P _c	M _d	e _{test}	e _b	e _c	Region	P _v	P _y	P _f	P _{test}	Test / Cal.	Failure Mode
	kN	kN	kN	kNm	mm	mm	mm		kN	kN	kN	kN		
Stamenkovic and Chapman														
V/E/1	30.53	49.2	18.26	3.44	0	42.77	301.04	a	30.53			74.7	2.45	P
C/E/1	31.62	50.96	18.91	3.56	76.47	42.77	301.04	bc	41.73		269.79	73.1	1.75	P
C/E/2	29.04	46.81	17.37	3.27	167.64	42.77	301.04	bc	25.73		77.9	54.7	2.13	P
C/E/3	29.75	47.95	17.8	3.35	403.61	42.77	301.04	cd	11.52		27.13	24.9	2.16	P
C/E/4	29.88	48.16	17.88	3.37	810.09	42.77	301.04	cd	4.83		12.77	10.9	2.26	P
M/E/2	29.35	47.31	17.56	3.31	INF	42.77	301.04	d	M _f = 9.756		M _{test} = 8.35		2.52	
Kane / Hanson & Hanson														
K1	17.08	26.52	8.26	1.39	99.17	29.01	249.91	bc	15.58	21.9	43.54	24	1.54	P&B
K2	18.93	28.78	8.58	1.62	99.04	29.33	275.01	bc	17.25	15.7	30.8	20.9	1.33	B&P
K3	20.16	30.63	9.13	1.73	98.8	29.33	275.01	bc	18.39	21.9	41.88	25.1	1.36	P&B
K4	16.77	25.49	7.6	1.44	98.9	29.33	275.01	bc	15.29	15.7	21.82	18.2	1.19	P&B
D-15	38.11	60.62	22.23	4.87	873.39	47.47	347.05	cd	6.54		14.23	12.03	1.84	P
Afhami														
North	147.65	243.16	98.05	34.81	290.2	92.61	590.79	bc	153.2	197	287.39	176.1	1.15	P
South	144.78	238.13	95.93	33.92	396.4	91.85	587.9	bc	124.67	206.5	349.06	222	1.78	P&B

Table C5 Continued

Mark	P _a	P _b	P _c	M _d	e _{test}	e _b	e _c	Region	P _v	P _y	P _f	P _{test}	Test / Cal.	Failure Mode
	kN	kN	kN	kNm	mm	mm	mm		kN	kN	kN	kN		
Zaghlool														
Z-IV(1)	97.52	162.66	62.66	18.52	368.22	76.03	485.38	bc	76.04		300.61	122.1	1.61	P
Z-V(1)	151.72	245.05	91.15	36.25	393.22	90.98	636.57	bc	126.61		403.17	214.9	1.7	P
Z-V(2)	164.72	266.04	98.96	39.35	379.19	90.98	636.57	bc	140.62		459.59	246.42	1.75	P
Z-V(3)	161.18	260.32	96.83	38.51	386.43	90.98	636.57	bc	135.98		446.83	267.73	1.97	P
Z-V(4)	152.79	246.76	91.78	36.5	INF	90.98	636.57	d	M _f = 36.5		M _{test} = 81.25	2.23		
Z-V(5)	153.54	247.98	92.24	36.68	0	90.98	636.57	a	153.54			278.83	1.82	P
Z-V(6)	144.87	233.97	87.03	34.61	753.8	90.98	636.57	cd	67.21		182.12	116.77	1.74	P
Z-VI(1)	169.73	267.81	97.5	49.07	403.26	105.88	792.36	bc	152.46		338.99	264.62	1.74	P
Scavuzo / Gosselin / Lamb														
S-1	33.9	51.45	15.38	3.86	130.8	38.87	365.04	bc	30.98	37.6	40.57	35.59	1.15	P
G-1	64.94	97.52	28.72	10.53	174.22	54.17	528.73	bc	60.72	39.26	35.97	41.5	1.15	F
G-2	83.78	128.36	38.91	14.59	236.94	60.49	549.18	bc	70.14	42.15	33.85	47.1	1.39	F
L-1	45.75	67.09	19.13	6.88	112.22	47.82	509.84	bc	49.71	26.97	38.03	31.1	1.15	B
L-2	51.4	75.38	21.49	7.73	149.71	47.82	509.84	bc	48.54	27.11	24.18	34.2	1.41	F&B

Table C5 Continued

Mark	P _a	P _b	P _c	M _d	e _{test}	e _b	e _c	Region	P _v	P _y	P _f	P _{test}	Test / Cal.	Failure Mode
	kN	kN	kN	kNm	mm	mm	mm		kN	kN	kN	kN		
Regan														
SE1	127.86	194.15	58.09	28.73	199.49	76.71	719.22	bc	134.12	292.68	415.78	198	1.48	P
SE2	144.67	220.08	66.02	32.72	177.08	77.5	721.79	bc	161.75	277.81	123.8	192	1.55	F&P
SE4	90.44	153.17	68.04	17.63	200.66	79.8	453.93	bc	109.08	238.32	427.53	152	1.39	P
SE5	114.74	194.31	86.31	22.36	234.76	79.8	453.93	bc	127.98	138.14	294.74	164	1.28	P&B
SE6	98.25	166.44	73.94	19.18	184.56	79.99	454.65	bc	123.36	160.6	255.86	149	1.21	P
SE7	109.29	185.15	82.25	21.34	245.74	79.99	454.65	bc	119.19	90.28	239.66	129	1.43	B&P
SE8	129.35	188.59	41.68	25.96	247.79	63.06	823.75	bc	101.61	178.75	213.92	136	1.34	P
SE9	124.5	198.73	73.11	26.49	290.24	79.5	575.23	bc	114.84	99.28	130.37	123	1.24	B&P
SE10	123.41	197	72.47	26.26	315.79	79.5	575.23	bc	108.3	105.32	116.2	114	1.08	B&P
SE11	136.75	218.3	80.3	29.1	286.23	79.5	575.23	bc	127.17	98.88	133.77	138	1.4	B&P&F
SE12	55.56	88.6	32.56	7.54	259.42	50.6	367.14	bc	41.5	62.64	62.05	69	1.66	P&F&B
SE13	50.34	80.28	29.51	6.83	245	50.6	367.14	bc	39.03	58.02	65.78	60	1.54	P&B
SE14	52.15	83.17	30.57	7.08	265.22	50.6	367.14	bc	38.39	64.29	59.89	46	1.2	P

Appendix D Tests in Literature - Eccentrically Loaded Interior Connections

Similar to appendix C, information regarding tests used in this appendix is summarized in five tables. Table D1 provides a summary of test results, geometry of the connections, and the material properties. In Table D2, the required information regarding the reinforcement of the specimens are summarized. Table D3 shows the calculated parameters required for constructing the moment shear interaction diagrams. In Table D4, analytical results required to construct the moment-shear interaction diagrams according to the Strip Model are presented, as well as the region in which the test specimen failed. Finally, in Table D5, analytical results required to construct the interaction diagrams using the North American codes are presented, as well as the test to calculated ratios and the predicted governing mode of failure.

D1 - Regan, Walker, and Zakaria

Regan et al. (1979) conducted fourteen tests on interior connections under unbalanced moments, all considered here. Three different test setups were used.

D1.1 SM Series ; Eleven tests belong to SM series. All slabs in this series were 2.0 m square and 80 mm thick. The slabs were simply supported only in the downward direction by lines of tie bars positioned at all four edges. The load was applied to the column at a fixed eccentricity.

The main top reinforcement was the same in all specimens. Specimen SM 10 was the only specimen with bottom reinforcement. Extra steel passing through column was placed in top mat of specimens SM 11 and SM12.

In addition to the details of reinforcement, size and shape of the column, load eccentricity, and in one instance the arrangement of the supports were the variables of series SM tests.

D1.2 Slab SRI ; One test on a 2.05 m square and 65 mm thick slab is reported. Vertical load was applied on the slab at 16 equally spaced point loads. Two horizontal loads were applied to the column to generate the unbalanced moment. The slab was heavily reinforced with 6 mm cold-worked deformed bars with a 0.2 % proof stress of 800 MPa.

D1.3 SI1 and SI2 ; Two 2 mm wide and 125 mm thick strips with simple supports across their ends and an interior column dividing the length into two spans were loaded at 12 load points simulating a uniform loading.

The layout of the reinforcement were the same for both slabs but specimen SI1 had larger bars. Both slabs developed considerable yielding before failure. The punching of slab SI2 is regarded as somewhat secondary.

D2 - Stamenkovic and Chapman

Stamenkovic and Chapman (1974) conducted 12 tests on interior connections. Based on the size and the shape of the column, specimens are divided into two groups; 6 slabs with 127 mm square column in group I, and 6 slabs with 76 x 152 mm rectangular columns in group Ir.

The moment to shear ratio ranged from 0 to ∞ in each group. The slabs were quite small; 914 mm square and 76 mm thick. All edges were supported by 38.1 mm rods, in

the same way as described for the edge connections. Vertical load was applied to the column end and distributed by the slab to the edges. Unbalanced moment was caused by two horizontal forces applied to the column.

The average test to calculated ratio is 1.628 with a coefficient of variation of 8.7 percent. The high test to calculated ratios are related to the high torsional moments generated in the plate due to line support at edges, and also to the positive bending moments generated because of the supporting rods being clamped to the slab.

D3 - Hanson and Hanson

Hanson and Hanson (1968) conducted 16 tests on interior connections under unbalanced loading. Only 7 tests are considered here, since others had some kind of perforations right at the column face. The average test to calculated ratio for these 7 tests is 1.42 with a coefficient of variation of 7.5 percent.

All slabs were 1220 x 2135 mm and 76 mm thick with free edges. Type A had 152 mm square columns. Type B and C both had 152 x 305 mm rectangular columns. Unlike type C, longer size of the column in type B slabs was in the direction of the eccentricity.

Two line loads were applied to the slab by means of a steel beam bearing on the slab one on each side of the column. In slabs A1, A2, B7, and C8, both loads were downward. In these slabs, the eccentricity was caused by the difference in the magnitude of the loads. In slabs A12, B16, and C17, however, one load was upward and the other one downward, causing very large eccentricities.

D4 - Moe

Moe (1961) conducted 12 tests on interior connections with unbalanced loading. Slabs M4 and M5 did not have top reinforcement and were under large eccentricities. They failed in bending before plate-column connection reached its capacity, and therefore are excluded from this study. All other specimens failed in punching at the plate-column connection.

All slabs were 1830 mm square with an overall thickness of 152 mm. Slabs were simply supported along all four edges with the corners free to lift. Load was applied to the column at a fixed eccentricity. Specimens M8 and M10 were the only specimens with two layer of steel in each direction. Therefore, for other slabs, the value of M_{sup}^+ equals to zero. Slabs M1A through M3 had 305 mm square columns, and slabs M6 through M10 had 252 mm square columns.

Eccentricity in applied load, column size, and steel strength were the main variables. Average test to calculated ratio for these tests is 1.17 with a coefficient of variation of 10.3 percent.

Table D1 Summary of Test Results, Geometry, and Material Properties of Interior Connections Reported in the Literature

Mark	h	c _x	c _y	f _{cu}	f' _c	f _y	P _{test}	M _{test}	e
	mm	mm	mm	MPa	MPa	MPa	kN	kNm	mm
Moe									
M1A	152.4	304.8	304.8		20.8	480.3	432.01	0	0
M2A	152.4	304.8	304.8		15.5	480.3	212.23	39.44	185.8
M3A	152.4	304.8	304.8		17.63	480.3	143.41	62.49	435.7
M2	152.4	304.8	304.8		25.69	480.3	291.71	57.18	196
M3	152.4	304.8	304.8		22.7	480.3	206.9	70.17	339.2
M6	152.4	254	254		26.45	327.18	238.87	40.23	168.4
M7	152.4	254	254		24.93	327.18	310.8	18.98	61.1
M8	152.4	254	254		24.59	327.18	149.18	65.31	437.8
M9	152.4	254	254		23.21	327.18	266.4	33.9	127.3
M10	152.4	254	254		21.08	327.18	177.6	54.81	308.6
Stamenkovic and Chapman									
V/I/2	76.2	127	127	32.37	27.52	433.94	117.22	0	0
C/I/1	76.2	127	127	44.98	38.23	433.94	84.36	7.32	86.7
C/I/2	76.2	127	127	37.06	31.5	433.94	62.16	10.48	168.6
C/I/3	76.2	127	127	31.89	27.11	433.94	33.74	13.64	404.3
C/I/4	76.2	127	127	31.34	26.64	433.94	20.87	16.66	798.2
M/I/1	76.2	127	127	35.13	29.86	433.94	0	18.37	INF
V/Ir/2	76.2	76.2	152.4	31.41	26.7	413.28	108.42	0	0
C/Ir/1	76.2	76.2	152.4	28.24	24	413.28	85.51	7.31	85.5
C/Ir/2	76.2	76.2	152.4	36.51	31.03	413.28	67.13	10.87	161.9
C/Ir/3	76.2	76.2	152.4	35.68	30.33	413.28	39.78	15.72	395.1
C/Ir/4	76.2	76.2	152.4	33.2	28.22	413.28	21.58	16.8	778.7
M/Ir/1	76.2	76.2	152.4	32.51	27.63	413.28	0	18.61	INF
Hanson & Hanson									
A1	76.2	152.4	152.4		30.24	365.06	5.73	22.33	3898
A2	76.2	152.4	152.4		31.27	375.4	4.8	24.3	5067
B7	76.2	152.4	304.8		32.92	354.04	4.88	35.71	7311
C8	76.2	304.8	152.4		32.79	410.52	5.59	31.4	5613
A12	76.2	152.4	152.4		33.2	371.95	26.82	20.5	764.4
B16	76.2	152.4	304.8		30.38	340.27	34.32	27.35	796.8
C17	76.2	304.8	152.4		35.96	340.96	31.44	24.71	786.2

Table D1 Continued									
Mark	h	c _x	c _y	f _{cu}	f' _c	f _y	P _{test}	M _{test}	e
	mm	mm	mm	MPa	MPa	MPa	kN	kNm	mm
Regan, Walker, Zakaria (1979)									
SM1	80	240	240	30.2	24.16	480	122	0	0
SM3	80	240	240	41.6	33.28	480	95	20.9	220
SM4	80	120	240	32.9	26.32	480	101	0	0
SM5	80	120	240	40	32	480	72	15.84	220
SM6	80	120	240	37.2	29.76	480	67	14.74	220
SM7	80	120	120	35.7	28.56	480	105	0	0
SM8	80	120	120	32.4	25.92	480	49	10.78	220
SM9	80	120	240	47.1	37.68	480	97	10.67	110
SM10	80	120	240	47.1	37.68	480	88	19.36	220
SM11	80	240	240	46.1	36.88	480	91	20.02	220
SM12	80	240	240	39.9	31.92	480	88	19.36	220
SR1	65	130	130	?	40	800	95	8.46	89
SI1	125	200	300	57.4	45.92	480	187	36.5	195.2
SI2	125	200	300	77.3	61.84	500	142	28.7	202.1

Table D2 Information Regarding Reinforcement -Tests on the Interior Connections

Mark	Top bars; strip x			Bottom bars; strip			Top bars; strip y			Bottom bars; strip		
	ϕ	s_{avg}	d	ϕ	s_{avg}	d	ϕ	s_{avg}	d	ϕ	s_{avg}	d
Moe												
M1A	19.05	152.4	123.8	0	0	0	19.05	177.8	104.8	0	0	0
M2A	19.05	152.4	123.8	0	0	0	19.05	177.8	104.8	0	0	0
M3A	19.05	152.4	123.8	0	0	0	19.05	177.8	104.8	0	0	0
M2	19.05	152.4	123.8	0	0	0	19.05	177.8	104.8	0	0	0
M3	19.05	152.4	123.8	0	0	0	19.05	177.8	104.8	0	0	0
M6	15.88	120.6	123.8	0	0	0	15.88	139.7	104	0	0	0
M7	15.88	120.6	123.8	0	0	0	15.88	139.7	104.8	0	0	0
M8	15.88	120.6	123.8	15.88	304.8	123.8	15.88	139.7	104.8	15.88	304.8	104.8
M9	15.88	120.6	123.8	0	0	0	15.88	139.7	104.8	0	0	0
M10	15.88	120.6	123.8	15.88	304.8	123.8	15.88	139.7	104.8	15.88	304.8	104.8
Stamenkovic and Chapman												
V/I/2	7.94	76.2	59.53	7.94	76.2	59.53	7.94	76.2	51.59	7.94	76.2	51.59
C/I/1	7.94	76.2	59.53	7.94	76.2	59.53	7.94	76.2	51.59	7.94	76.2	51.59
C/I/2	7.94	76.2	59.53	7.94	76.2	59.53	7.94	76.2	51.59	7.94	76.2	51.59
C/I/3	7.94	76.2	59.53	7.94	76.2	59.53	7.94	76.2	51.59	7.94	76.2	51.59
Stamenkovic and Chapman (continued)												
C/I/4	7.94	76.2	59.53	7.94	76.2	59.53	7.94	76.2	51.59	7.94	76.2	51.59
M/I/1	7.94	76.2	59.53	7.94	76.2	59.53	7.94	76.2	51.59	7.94	76.2	51.59
V/Ir/2	7.94	76.2	59.53	7.94	76.2	59.53	7.94	76.2	51.59	7.94	76.2	51.59
C/Ir/1	7.94	76.2	59.53	7.94	76.2	59.53	7.94	76.2	51.59	7.94	76.2	51.59
C/Ir/2	7.94	76.2	59.53	7.94	76.2	59.53	7.94	76.2	51.59	7.94	76.2	51.59
C/Ir/3	7.94	76.2	59.53	7.94	76.2	59.53	7.94	76.2	51.59	7.94	76.2	51.59
C/Ir/4	7.94	76.2	59.53	7.94	76.2	59.53	7.94	76.2	51.59	7.94	76.2	51.59
M/Ir/1	7.94	76.2	59.53	7.94	76.2	59.53	7.94	76.2	51.59	7.94	76.2	51.59
Hanson & Hanson												
A1	9.53	76.2	61.91	9.53	76.2	61.91	9.53	76.2	52.39	9.53	76.2	52.39
A2	9.53	76.2	61.91	9.53	76.2	61.91	9.53	76.2	52.39	9.53	76.2	52.39
B7	9.53	76.2	61.91	9.53	76.2	61.91	9.53	76.2	52.39	9.53	76.2	52.39
C8	9.53	76.2	61.91	9.53	76.2	61.91	9.53	76.2	52.39	9.53	76.2	52.39
A12	9.53	76.2	61.91	9.53	76.2	61.91	9.53	76.2	52.39	9.53	76.2	52.39
B16	9.53	76.2	61.91	9.53	76.2	61.91	9.53	76.2	52.39	9.53	76.2	52.39
C17	9.53	76.2	61.91	9.53	76.2	61.91	9.53	76.2	52.39	9.53	76.2	52.39

Table D2 Continued												
Mark	Top bars; strip x			Bottom bars; strip x			Top bars; strip y			Bottom bars; strip y		
	ϕ	s_{avg}	d	ϕ	s_{avg}	d	ϕ	s_{avg}	d	ϕ	s_{avg}	d
Regan, Walker, Zakaria (1979)												
SM1	8	80	64	0	0	0	8	80	56	0	0	0
SM3	8	80	64	0	0	0	8	80	56	0	0	0
SM4	8	80	64	0	0	0	8	80	56	0	0	0
SM5	8	80	64	0	0	0	8	80	56	0	0	0
SM6	8	80	64	0	0	0	8	80	56	0	0	0
SM7	8	80	64	0	0	0	8	80	56	0	0	0
SM8	8	80	64	0	0	0	8	80	56	0	0	0
SM9	8	80	64	0	0	0	8	80	56	0	0	0
SM10	8	80	64	6	80	64	8	80	56	6	80	56
SM11	8	45	64	0	0	0	8	80	56	0	0	0
SM12	8	80	64	0	0	0	8	45	56	0	0	0
SR1	6	43	54	6	85	54	6	43	48	6	85	48
SI1	12	100	107	12	190	107	12	200	95	0	0	0
SI2	10	100	108	10	190	108	10	200	98	0	0	0

Table D3 Parameters Required for Constructing Interaction Diagram of the Interior Connections Reported in Literature

Mark	w_x	w_y	M_{sx}^+	M_{sy}^+	M_{sup}^+	M_{tc}	M_{tx}
	kN/m	kN/m	kNm	kNm	kNm	kNm	kNm
Moe							
M1A	79.33	93.75	26.94	19.47	0	11.3	20.2
M2A	68.47	80.92	24.56	17.72	0	8.42	18.42
M3A	73.04	86.31	25.69	18.55	0	9.58	19.27
M2	88.16	104.19	28.26	20.44	0	13.96	21.2
M3	82.86	97.92	27.52	19.9	0	12.33	20.64
M6	89.45	105.71	15.25	11.12	0	11.98	13.72
M7	86.85	102.64	15.15	11.04	0	11.29	13.63
M8	86.25	101.93	15.12	11.03	6.4	11.13	13.61
M9	83.8	99.03	15.02	10.95	0	10.51	13.52
M10	79.85	94.37	14.83	10.81	6.36	9.54	13.35
Stamenkovic and Chapman							
V/I/2	44.93	51.84	1.91	1.63	1.91	1.64	1.72
C/I/1	52.96	61.1	1.97	1.69	1.97	1.73	1.78
C/I/2	48.07	55.46	1.94	1.66	1.94	1.7	1.75
C/I/3	44.59	51.45	1.91	1.63	1.91	1.62	1.72
C/I/4	44.2	51.01	1.91	1.62	1.91	1.59	1.72
M/I/1	46.8	54	1.93	1.65	1.93	1.68	1.74
V/Ir/2	44.25	51.06	1.1	1.87	1.1	1.91	1.64
C/Ir/1	41.96	48.42	1.08	1.84	1.08	1.72	1.62
C/Ir/2	47.71	55.05	1.11	1.9	1.11	2.03	1.67
C/Ir/3	47.17	54.42	1.11	1.9	1.11	2.03	1.67
C/Ir/4	45.5	52.5	1.1	1.88	1.1	2.01	1.65
M/Ir/1	45.02	51.95	1.1	1.88	1.1	1.98	1.65
Hanson & Hanson							
A1	47.82	56.52	2.87	2.38	2.87	1.92	2.16
A2	48.63	57.47	2.96	2.45	2.96	1.93	2.22
B7	49.9	58.97	2.82	4.69	2.82	3.87	2.12
C8	49.8	58.85	6.44	2.66	6.44	1.93	2.41
A12	50.11	59.22	2.95	2.45	2.95	1.94	2.22
B16	47.93	56.64	2.7	4.48	2.7	3.84	2.03
C17	52.15	61.63	5.51	2.29	5.51	1.95	2.07

Table D3 Continued							
Mark	w_x	w_y	M_{sx}^-	M_{sy}^-	M_{sup}^+	M_{tc}	M_{tx}
	kN/m	kN/m	kNm	kNm	kNm	kNm	kNm
Regan, Walker, Zakaria (1979)							
SM1	45.69	52.22	4.1	3.52	0	2.91	2.05
SM3	53.63	61.29	4.24	3.67	0	3.43	2.12
SM4	47.69	54.5	2.07	3.56	0	3.17	2.07
SM5	52.59	60.1	2.11	3.65	0	3.42	2.11
SM6	50.71	57.96	2.1	3.62	0	3.39	2.1
SM7	49.68	56.78	2.09	1.8	0	1.69	2.09
SM8	47.33	54.09	2.07	1.78	0	1.56	2.07
SM9	57.06	65.21	2.14	3.71	0	3.47	2.14
SM10	57.06	65.21	2.14	3.71	1.53	3.47	2.14
SM11	56.45	64.52	7.13	3.7	0	3.46	3.57
SM12	52.52	60.02	4.23	5.93	0	3.42	2.11
SR1	50.39	56.69	3.16	2.75	1.73	1.15	2.37
SI1	106.86	120.36	10.86	7.45	0	9.14	10.18
SI2	127.93	140.98	8.18	5.66	0	8.78	7.67

Table D4 Analytical Results (Points on Interaction Diagram, Failure Load, and Test to Calculated Ratio) for Interior Connection Tests - Strip Model

Mark	P ₁	P ₂	P ₃	M ₄	e	e ₂	e ₃	Reg ion	P _v	P _y	P _{test}	Test / Calculated	
	kN	kN	kN	kNm	mm	mm	mm		kN	kN	kN		
Moe													
M1A	355.8	263.4	146.2	84.1	0	156	491	1	355.8		432	1.21	P
M2A	315.5	233.5	129.7	72	186	159	472	23	218.4		212.2	0.97	P
M3A	333.3	246.7	137	77.2	436	158	480	23	145.9		143.4	0.98	P
M2	384.3	284.4	157.8	93.4	196	153	508	23	259.2		291.7	1.13	P
M3	367.6	272.1	151	87.8	339	155	498	23	190.1		206.9	1.09	P
M6	284.9	211	123.6	64.4	168	117	444	23	189.8		238.9	1.26	P
M7	279.8	207.2	121.4	62.4	61.1	118	438	12	236.7		310.8	1.31	P
M8	278.6	206.3	120.9	71.2	438	149	489	23	129		149.2	1.16	P
M9	273.6	202.7	118.7	60.2	127	119	431	23	198.8		266.4	1.34	P
M10	265.4	196.6	115.2	66.4	309	152	477	23	146.6		177.6	1.21	P
Stamenkovic and Chapman													
V/I/2	73.86	55.32	31.03	11.1	0	90.5	293	1	73.86		117.2	1.59	P
C/I/1	81.56	61.1	34.22	11.8	86.7	85.9	280	23	60.9		84.36	1.39	P
C/I/2	76.99	57.67	32.33	11.4	169	88.6	288	23	43.9		62.16	1.42	P
C/I/3	73.52	55.06	30.89	11	404	90.7	292	34	23.47		33.74	1.44	P
C/I/4	73.12	54.76	30.73	10.9	798	90.9	291	34	12.64		20.87	1.65	P
M/I/1				11.3	INF			4	M _{test} = 18.37		0	1.63	
V/Ir/2	66.92	52.99	27.86	10.3	0	61.4	292	1	66.92		108.4	1.62	P
C/Ir/1	64.72	51.24	26.96	9.71	85.5	62.3	284	23	46.82		85.51	1.83	P
C/Ir/2	70.07	55.5	29.15	10.7	162	60.1	292	23	39.72		67.13	1.69	P
C/Ir/3	69.59	55.11	28.95	10.7	395	60.3	292	34	22.67		39.78	1.76	P
C/Ir/4	68.07	53.91	28.33	10.5	779	60.9	296	34	12.32		21.58	1.75	P
M/Ir/1				10.4	INF			4	M _{test} = 18.61		0	1.78	
Hanson & Hanson													
A1	93.28	69.83	37.07	15.2	3898	108	335	34	3.83		5.73	1.49	P
A2	95.42	71.43	37.93	15.5	5066	108	334	34	3.02		4.8	1.59	P
B7	114	90.25	37.54	24.8	7311	103	509	34	3.33		4.88	1.47	P
C8	121.7	85.86	47.36	24	5613	182	430	34	4.21		5.59	1.33	P
A12	96.84	72.5	38.47	15.6	764	107	331	34	18.61		26.82	1.44	P
B16	109.3	86.49	35.99	24.1	797	103	516	34	25.34		34.32	1.35	P
C17	115.3	81.42	44.84	21.8	786	167	409	34	25.22		31.44	1.25	P

Table D4 Continued													
Mark	P ₁	P ₂	P ₃	M ₄	e	e ₂	e ₃	Reg ion	P _v	P _y	P _{test}	Test / Calculated	
	kN	kN	kN	kNm	mm	mm	mm		kN	kN	kN		
Regan, Walker, Zakaria (1979)													
SM1	109	81.61	38.71	16.48	0	90.5	376	1	109		122	1.12	P
SM3	120.3	90.13	42.67	18.35	220	87.3	380	23	59.93		95	1.59	P
SM4	95.51	75.63	34.43	15.15	0	58.9	364	1	95.51		101	1.06	P
SM5	101.4	80.34	36.53	16.1	220	57.8	365	23	49.19		72	1.46	P
SM6	99.21	78.58	35.74	15.89	220	58.2	368	23	48.36		67	1.39	P
SM7	81.21	60.83	35.3	8.93	0	54.5	215	1	81.21		105	1.29	P
SM8	78.8	59.01	34.27	8.54	220	55.2	211	34	33.11		49	1.48	P
SM9	106.5	84.35	38.32	16.6	110	56.9	357	23	69.57		97	1.39	P
SM10	106.5	84.35	38.32	19.4	220	75.1	397	23	54.75		88	1.61	P
SM11	142.1	102	56.75	23.7	220	117	368	23	76.84		91	1.18	P
SM12	135.1	105.3	42.15	18.2	220	74.1	382	23	61.62		88	1.43	P
SR1	100.5	75.21	39.92	11.9	89	86.9	245	23	74.34		95	1.28	P
SI1	256	187.9	115.5	57.1	195	112	402	23	159.3	182	187	1.17	P&B
SI2	242.3	177.7	109.7	52.3	202	101	385	23	145.5	137	142	1.04	B

Table D5 Analytical Results (Points on Interaction Diagram, Failure Load, and Test to Calculated Ratio) for Interior Connection Tests - North American Standards

Mark	P _a	M _b	M _f	e	P _v	P _y	P _f	P _{test}	Test / Calcul.	Failure mode
	kN	kNm	kNm	mm	kN	kN	kN	kN		
Moe										
M1A	291.02	103.53	112.24	0	291.02			432.01	1.48	P
M2A	251.19	89.36	102.33	185.82	165		550.71	212.23	1.29	P
M3A	267.94	95.32	107.04	435.73	120.43		245.65	143.41	1.19	P
M2	323.42	115.06	117.75	196.01	208.53		600.73	291.71	1.4	P
M3	303.98	108.14	114.66	339.16	155.62		338.06	206.9	1.33	P
M6	288.38	90.64	71.15	168.41	187.77		422.51	238.87	1.27	P
M7	280	88	70.69	61.08	234.44		1157	310.8	1.33	P
M8	278.06	87.39	70.58	437.81	116.2		161.21	149.18	1.28	P
M9	270.16	84.91	70.1	127.25	192.3		550.85	266.4	1.39	P
M10	257.43	80.91	69.22	308.59	129.9		224.32	177.6	1.37	P
Stamenkovic and Chapman										
V/I/2	70.88	11.03	8.93	0	70.88			117.22	1.65	P
C/I/1	83.54	13	9.21	86.72	53.65		106.25	84.36	1.57	P
C/I/2	75.83	11.8	9.06	168.59	36.4		53.74	62.16	1.71	P&F
C/I/3	70.35	10.95	8.92	404.33	19.55		22.05	33.74	1.73	P&F
C/I/4	69.74	10.86	8.9	798.17	11.38		11.15	20.87	1.87	F&P
M/I/1	73.83	11.49	9.01	INF	$M_{test} = 18.37$			0	2.04	
V/Ir/2	64.96	8.99	8.06	0	64.96			108.42	1.67	P
C/Ir/1	61.59	8.52	7.96	85.52	38.06		93.03	85.51	2.25	P
C/Ir/2	70.03	9.69	8.18	161.93	32.27		50.52	67.13	2.08	P&F
C/Ir/3	69.23	9.58	8.16	395.11	17.96		20.66	39.78	2.22	P&F
C/Ir/4	66.78	9.24	8.1	778.7	10.08		10.41	21.58	2.14	P&F
M/Ir/1	66.09	9.14	8.09	INF	$M_{test} = 18.61$			0	2.3	
Hanson & Hanson										
A1	87.72	15.6	11.98	3899	3.83		3.07	5.73	1.86	F&P
A2	89.2	15.87	12.32	5067	3.03		2.43	4.8	1.97	F&P
B7	124.82	28.2	13.25	7311	3.74		1.81	4.88	2.7	F&P
C8	124.55	29.65	16.98	5613	5.07		3.02	5.59	1.85	F&P
A12	91.91	16.35	12.31	764.4	17.35		16.1	26.82	1.67	F&P
B16	119.89	27.09	12.67	796.8	26.49		15.91	34.32	2.16	F&P
C17	130.43	31.05	14.53	786.2	30.32		18.48	31.44	1.7	F&P

Table D5 Continued										
Mark	P _a	M _b	M _f	e	P _v	P _y	P _f	P _{test}	Test / Calcul.	
	kN	kNm	kNm	mm	kN	kN	kN	kN		
Regan, Walker, Zakaria (1979)										
SM1	117.85	29.76	13.66	0	117.85			122	1.04	P
SM3	138.31	34.92	14.15	220	73.91		64.31	95	1.48	F&P
SM4	98.4	18.88	11.56	0	98.4			101	1.03	P
SM5	108.5	20.82	11.8	220	50.55		53.65	72	1.42	P&F
SM6	104.64	20.08	11.72	220	48.74		53.27	67	1.37	P&F
SM7	76.88	11.85	10.45	0	76.88			105	1.37	P
SM8	73.24	11.29	10.34	220	30.18		46.99	49	1.62	P&F
SM9	117.74	22.59	11.97	110	74.84		108.84	97	1.3	P
SM10	117.74	22.59	11.97	220	54.85		54.42	88	1.62	F&P
SM11	145.6	36.76	23.77	220	77.81		108.06	91	1.17	P
SM12	135.46	34.2	14.09	220	72.39		64.06	88	1.37	F&P
SR1	77.76	11.96	13.18	89	49.26		148.05	95	1.93	P
SI1	319.99	93.13	55.23	195.19	191.54	182	282.98	187	1.03	B
SI2	380.85	111.56	41.62	202.11	225.36	137	205.94	142	1.04	B